COMPUTATIONAL STUDY OF THE TRANSPORT MECHANISMS OF MOLECULES AND IONS IN SOLID MATERIALS

A Dissertation

by

YINGCHUN ZHANG

Submitted to the Office of Graduate Studies of
Texas A&M University
in partial fulfillment of the requirements for the degree of

DOCTOR OF PHILOSOPHY

May 2006

Major Subject: Chemical Engineering

COMPUTATIONAL STUDY OF THE TRANSPORT MECHANISMS OF MOLECULES AND IONS IN SOLID MATERIALS

A Dissertation

by

YINGCHUN ZHANG

Submitted to the Office of Graduate Studies of
Texas A&M University
in partial fulfillment of the requirements for the degree of

DOCTOR OF PHILOSOPHY

Approved by:

Chair of Committee,	Perla B. Balbuena
Committee Members,	Tahir Cagin
	Yue Kuo
	Hung-Jue Sue
Head of Department,	Kenneth R. Hall

May 2006

Major Subject: Chemical Engineering

ABSTRACT

Computational Study of the Transport Mechanisms of Molecules and Ions in Solid Materials. (May 2006)

Yingchun Zhang, B.S., Xiamen University, Xiamen, China;

M.S., Xiamen University, Xiamen, China

Chair of Advisory Committee: Dr. Perla B. Balbuena

Transport of ions and molecules in solids is a very important process in many technological applications, for example, in drug delivery, separation processes, and in power sources such as ion diffusion in electrodes or in solid electrolytes. Progress in the understanding of the ionic and molecular transport mechanisms in solids can be used to substantially increase the performance of devices. In this dissertation we use ab initio calculations and molecular dynamics simulations to investigate the mechamisn of transport in solid.

We first analyze molecular transport and storage of H_2. Different lightweight carbon materials have been of great interest for H_2 storage. However, pure carbon materials have low H_2 storage capacity at ambient conditions and cannot satisfy current required storage capacities. Modification of carbon materials that enhance the interaction between H_2 and absorbents and thus improve the physisorption of H_2, is needed for hydrogen storage. In this dissertation, corannulene and alkali metal-doped corannulene are investigated as candidate materials for hydrogen storage. Molecular modifications of corannulene, which provides large pore volume for H_2 adsorption, is

also investigated. Using computational chemistry, we predict enhanced H_2 adsorption on molecular systems with modification and hydrogen uptake can reach DOE target of 6.5wt% at at 294 bar at 273 K, and 309 bar at 300 K.

In the second part of this dissertation, we study the lithium ion transport from a solid electrolyte phase to a solid electrode phase. Improvement of ionic transport in solid electrolytes is a key element in the development of the solid lithium ion batteries. One promising material is dilithium phthalocyanine (Li_2Pc), which upon self-assembly may form conducting channels for fast ion transport. Computational chemistry is employed to investigate such phenomena: (1) to analyze the crystalline structure of Li_2Pc and formation of conducting channels; (2) to understand the transport of Li ions inside channels driven by an electric field; (3) to study the continuity of the conducting channels through interface. The study shows Li_2Pc has higher conductivity than PEO as electrolyte.

ACKNOWLEDGEMENTS

Looking back over past four years working on my Ph.D. degree, I have received so much help from many people. This dissertation would not be possible without the contribution of many people.

I would like to express my sincere gratitude to my advisor, Dr. Perla B. Balbuena. It has been my good fortune to have the opportunity to work with Dr. Balbuena for the past four years. Dr. Balbuena continuously enlightened my mind with her broad knowledge and intelligence and encouraged me with her infinite patience whenever I met difficulties. Dr. Balbuena's enthusiasm for science always inspired my working spirit. Besides, not only being a wonderful research advisor with financial support, Dr. Balbuena is also a great mentor for my life. From her, I learned to be a researcher and a mature human being as well.

I want to acknowledge Dr. Cagin. His knowledge on computational chemistry helped me understand and solved a lot of puzzles in this field. The conversations with Dr. Cagin were always instructive on my research. I am thankful to Dr. Kuo, Dr. Grunlan, Dr. Sue for providing insightful advice to my research and for serving on my committee.

I am deeply grateful to Dr. Lawrence Scanlon. His contribution to this dissertation is unique. The collaboration and communication on this dissertation were very insightful with him. His advice and suggestion made this dissertation much easier.

I am thankful to Dr. Yixuan Wang for his suggestions and discussions since I joined the group. Dr. Wang always patiently answered questions I had and gave advice on the research I have worked on. I would like to thank all members of Dr. Balbuena's group. They created a friendly climate in the office and shared their interesting culture from their own countries. Staying in this group has given me a feeling of a big international family.

I am thankful to Mr. Jeff Polasek and Dr. Lisa M. Perez for their computer and cluster support. Computer resources from Artie McFerrin, Department of Chemical Engineering, Texas A&M University, the National Center for Supercomputing Applications (NCSA), and National Energy Research Scientific Computing Center (NERSC) are highly appreciated.

I want to express my sincere appreciation to my family for their unconditional support in my school life. The spirit of hard working and never giving-up from my parents, Mr. Yuzao Zhang and Ms. Meizhu He, have been inspired me since I was a kid. They taught me the lessons of their lives and how to become a better person. I have been blessed to have Dr. Hong Wu as my wife. She is not only a wife with her love to help in my life, but also has constantly given me suggestions on my research. I often learn something new from the conversation with her. Her idea and revision on this dissertation made it much better. I would like to express my special thanks to my parents-in-law, Mr. Daolin Wu and Ms. Chunying Yuan, for their love and support. I want to thank my sister, Ms. Yinglian Zhang, my brother, Mr. Yingliu Zhang, and their families. They have taken care of our parents all these years.

And last but not least, I would like to thank all my friends at University of South Carolina and Texas A&M University for their friendships. They have made my life more joyful and happy.

TABLE OF CONTENTS

CHAPTER Page

CHAPTER Page

Page

LIST OF TABLES

Page

Page

LIST OF FIGURES

Page

Page

Page

Page

Page

Page

CHAPTER I

INTRODUCTION – MOLECULAR TRANSPORT IN SOLID MATERIALS

1.1 History of hydrogen as energy carrier

Hydrogen, first on the periodic table of the all elements, is the least complex and most abundant element in the universe. Hydrogen has the highest energy content of any common fuel by weight, but the lowest energy content by volume due to the fact of the lightest element.

As an energy source, the first use of hydrogen can be dated back to early 1820s.[1] On November 27, 1820, Rev. W. Cecil, M.A., Fellow of Magdalen College and of the Cambridge Philosophical Society, presented "the Application of Hydrogen Gas to Produce Moving Power in Machinery" and described an engine operated by the pressure of the atmosphere upon a vacuum caused by explosions of hydrogen gas and atmospheric air.[1] Cecil pointed out the disadvantages of the water-driven engines, which could be used only where water is abundant, and of the steam engines, which were slow in getting underway. He proposed that a hydrogen-powered engine would solve these two problems by combing the advantages of water and steam to produce moving force of capability of acting in any place without the delay and labor of preparation.[1]

This dissertation follows the style of *the Journal of Physical Chemistry B*.

In the following 150 years or so, hydrogen's properties were discussed with increasing attention by scientists and by writers of early science fiction. One of the most famous examples is in one of Jules Verne's, The Mysterious Island in 1874, of how hydrogen would become the world's chief fuel.[2] In a part of his book, Verne describes the discussions of five Americans. They were "learned, clear-headed and practical" engineer Cyrus Harding, his servant Neb, the "indomitable, intrepid" reporter Gideon Spillett, a sailor named Pencroft, and young Herbert Brown (an orphan and Pencroft's protégé). They discussed what would happen to commerce and industry if the coal supply were to run out and the following was the remarkable conversation between these five Americans: [2]

"Without coal there would be no machinery, and without machinery there would be no railways, no steamers, no manufactories, nothing of that which is indis-pensable to modern civilization!"
"But what will they find?" asked Pencroft. "Can you guess, captain?"
"Nearly, my friend."
"And what will they burn instead of coal?"
"Water," replied Harding.
"Water!" cried Pencroft, "water as fuel for steamers and engines! Water to heat water!"
"Yes, but water decomposed into its primitive elements," replied Cyrus Harding, "and decomposed doubtless, by electricity, which will then have become a powerful and manageable force, for all great discoveries, by some inexplicable laws, appear to agree and become complete at the same time. Yes, my friends, I believe that water will one day be employed as fuel, that hydrogen and oxygen which constitute it, used singly or together, will furnish an inexhaustible source of heat and light, of an intensity of which coal is not capable. Some day the coalrooms of steamers and the tenders of locomotives will, instead of coal, be stored with these two condensed gases, which will burn in the furnaces with enormous calorific power.
There is, therefore, nothing to fear. As long as the earth is inhabited it will supply the wants of its inhabitants, and there will be no want of either light or heat as long as the productions of the vegetable, mineral or animal kingdoms do not fail us. I believe, then,

that when the deposits of coal are exhausted we shall heat and warm ourselves with water. Water will be the coal of the future."
"I should like to see that," observed the sailor.
"You were born too soon, Pencroft," returned Neb, who only took part in the discussion with these words.

Although Verne did not explain where the primary energy for the decomposition of water could come from, his foresight is very impressive based on the 19th century scientific knowledge.

Interest in hydrogen as fuel started to get attention in the 1920s and the 1930s around the world.[1,3] In 1934 Ontario Hydro utility in Canada built a 400-kilowatt electrolysis plant and planed to heat buildings with hydrogen and even to run test vehicles.[4] In 1923, John Burden Sanderson Haldane, a physiologist turned geneticist, lectured at Cambridge University and described on the conceptual level that hydrogen, derived from wind power via electrolysis, liquefied and stored, would be the fuel of the future, in industry, transportation, heating, and lighting.[5] In the 1930s, Franz Lawaczeck in Germany first suggested that energy could be transported via hydrogen-carrying pipelines.[6] In 1937 an article by engineer A. Beldimano in Italy mentioned the experimental efforts to adapt liquid hydrogen for use in aircraft engines.[7] In 1938, Igor Sikorski in the United States predicted that hydrogen fueled aircraft engine would permit planes to fly at speeds of 500-600 MPH and altitudes of 30,000-50,000 feet. [8]

Rudolf Erren, [6] a brilliant and visionary German engineer, was one of the best-known hydrogen advocates of the 1930s and the 1940s formed Erren Motoren GmbH Spezialversuchsanstalt in Berlin and the Erren Engineering Company in London and worked on hydrogen engine that would permit hydrogen to be used alone as a fuel or as

a clean-up additive to normal fuels. As the result, the Erren system achieved much better combustion of hydrocarbons with higher output and lower specific fuel consumption and less pollution in trucks, buses, German tested railway system. His other two inventions, the "oxy-hydrogen" submarine and the trackless torpedo, attracted some attention in Britain in 1942, by using hydrogen as the fuel.

After Francis T. Bacon, a British scientist, developed the first practical hydrogen-air fuel cell, and Eduard Justi, a German electrochemist, developed the new, more efficient fuel cells, interest in hydrogen was picked up again in 1950s.[9] In the next two decades, the idea and development of using solar energy to produce hydrogen started to grow in Germany and other countries. The term "Hydrogen economy" was first coined by John Bockris, an Australian electrochemist, in 1970 during a discussion at the General Motors Technical Center in Warren, Michigan.[10] Replacing gasoline by other fuels to help eliminating pollution began to creep into the public consciousness and many scientists concluded that hydrogen would be the fuel for all types of transports. The oil shock of 1973 announced that the age of cheap, convenient liquid fuel would be coming to an end at some sense and that substitutes for liquid fuel would have to be found.[11] The desire for energy and the environmental concern speeded up the further investigation of hydrogen as a substitution for fossil fuels.

In March 1974, The Hydrogen Economy Miami Energy (THEME), the first major international hydrogen conference, was hold in Miami Beach.[12] It was agreed " that hydrogen was a permanent solution to the depletion of conventional fuels, it was the permanent solution to the global environmental problem."[12] Governments and other

organizations around the world began showing the concerns. However, before people realized that the real hydrogen economy and hydrogen technique related hardware would not appear rapidly within a few years, the development of hydrogen as energy carrier had been slow before late 1990s. A few highlights of the international hydrogen activities during the late last century are listed below. [7,9,10]

1988

• A 164-passenger TU-154 commercial jet was partially fueled by liquid hydrogen, developed by the Soviet Union's Tupolev Design Bureau. One of the three engines was operated on the rocket fuel. The 21-minute maiden flight took place on April 15.

• In May, in Fort Lauderdale, William Conrad became the first person to fly an airplane (a four-seat Grumman American Cheetah) exclusively fueled by liquid hydrogen.

• In Germany, a submarine powered by a hydrogen-fueled alkaline fuel cell, which was developed by Siemens, was tested underwater.

1989

• After trying for more than 10 years, Ho-Kwang Mao and Russell Hemsley at the Geophysical Laboratory of the Carnegie Institution in Washington announced they had produced hydrogen in a metallic state. They obtained metallic hydrogen by compressing the gas under ambient conditions to pressures of more than 2.5 megabars (2.5 million atmospheres).

1991

• In Bavaria, an experimental liquid-hydrogen refueling device for cars and buses was used at Solar-Wasserstoff-Bayern's prototype solar hydrogen plant. The goal was to refuel a car in a few minutes, competitively to refuel a car with gasoline.

1992

• The Fraunhofer Institute first designed a grid-independent solar house that used hydrogen for long-term energy storage in Freiburg, Germany.

1994

• Under the effort of the Euro-Quebec Hydro-Hydrogen Pilot Project, hydrogen-powered buses were developed and tested in Geel, Belgium.

1995

• Hydrogen fueled or partially hydrogen fueled vehicles were exhibited at the sixth annual US Hydrogen Meeting, organized by the National Hydrogen Association in Alexandria, Virginia.

1997

• At the Detroit Auto Show, the Chrysler Corporation displayed the mockup of a PEM-fuel-cell passenger car that would be fueled by hydrogen with the aid of an onboard processor developed by Arthur D. Little, Inc.

1999

• Europe's first hydrogen gas stations were opened in Hamburg and Munich. A similar station was opened at Ford's research labs in Dearborn, Michigan.

2000

• A collaboration of the National Renewable Energy Laboratory and the University of California at Berkeley developed an experimental renewable hydrogen-production technique based on the action of green algae.

As it turned into the 21st century, the desire of hydrogen as energy carrier has been continuously increased.[13,14] In the U.S., a National Hydrogen Vision and Roadmap process was initiated by the U.S. Department of Energy, in partnership with key hydrogen energy and transportation organizations.[15] On January 28, 2003, the speech of " President's Hydrogen Fuel Initiative: A Clean and Secure Energy Future" stated,

> A simple chemical reaction between hydrogen and oxygen generates energy, which can be used to power a car producing only water, not exhaust fumes. With a new national commitment, our scientists and engineers will overcome obstacles to taking these cars from laboratory to showroom so that the first car driven by a child born today could be powered by hydrogen, and pollution-free. Join me in this important innovation to make our air significantly cleaner, and our country much less dependent on foreign sources of energy.
> — President Bush, State of the Union Address, January 28, 2003

As a key component of the President's clean air and climate change strategies, President Bush announced $1.2 billon to develop the necessary technologies for commercially viable hydrogen-powered fuel cells, which produce no pollution and no greenhouse gases and can reduce America's growing dependence on foreign oil import. The aim of the President's Hydrogen Fuel Initiative is to develop hydrogen, fuel cell, and infrastructure technologies and make it practical and cost-effective for large numbers of Americans to choose to use fuel cell vehicles by 2020.[16] Other important highlights since 2000 are listed as following.[12]

2001

• BMW announced their 750hLs sedans Clean Energy World Tour by hydrogen-powered.

2003

• Quantum supplied fuel injector for Ford's new environmentally friendly Hybrid Model U.

• In Barth, Germany, Proton Energy Systems' HOGEN® Hydrogen Generator was installed for hydrogen fuel cell bus program.

• Shell Hydrogen, a global business of the Royal Dutch/Shell Group of Companies, developed the design for a hydrogen station in Iceland and started to put into use in April.

• Chemists at the University of Massachusetts discovered a way to double the efficiency of a solar-powered process to generate hydrogen fuel.

2004

• Clean Energy, Inc. has completed the acquisition of an international exclusive license from HPA, LLC for a turnkey hydrogen delivery system for internal combustion engines. Hydrogen Internal Combustion Engines are used to provide alternative to gasoline.

• A hydrogen fuel-propelled car entirely built with Korean technology has been developed in December.

2005

• Hydrogen Buses to Fuel China Modernization. As part of China's march toward modernization, the Hythane Company started to demonstrate its low-emission vehicle fuel system in support of Chinese national air quality program. The company has signed

memos of understanding with five major cities to test and convert as many as 10,000 diesel buses to be powered by Hythane(TM) fuel, a blend of natural gas and hydrogen that reduces emissions by up to 50 percent compared to traditional natural gas. The project targets full conversion prior to the 2008 Olympic Games in Beijing.

• Dynetek Delivers Hydrogen Fuel Storage Solutions to TUG Technologies. This demonstration project utilizes Dynetek's Hydrogen Fuel Storage System solutions by providing hydrogen to tow tractors powered by a Ford Motor Company internal combustion engine. The Hydrogen Internal Combustion Engine (H2 ICE) vehicle platform provides the reliability necessary for the adoption of Hydrogen as an alternative vehicle fuel.

• Mazda develops hybrid with electric motor, hydrogen-powered engine. YOKOHAMA, Japan (AP) - Mazda Motor Corp. has developed a new type of hybrid car that runs by switching between an electric motor and a hydrogen-powered engine, and then automatically shifts to gasoline when it runs out of hydrogen.

• Toyota unveils hydrogen-powered fuel cell hybrid bus. (Kyodo) -Toyota Motor Corp. unveiled next-generation hydrogen-powered fuel cell hybrid-electric bus.

This January, a report titled "The Hydrogen House: Fueling a Dream" said that Bryan Beaulieu recently built a $2 million solar-and-hydrogen-powered "dream" house in the northernmost reaches of Scottsdale, Arizona.[17] The 6,000-square-foot luxury home has total integral design and is, by far, the most environmentally sustainable. Each function is taken care of either by design or natural law. "This is the opposite of a fossil-fuel-dependent lifestyle, says Roy McAlister, president of the American Hydrogen

Association in Mesa, Arizona. 'And that lifestyle jeopardizes billions of people and creates inflation, pollution and conflict.'"

1.2 Roadmap to hydrogen economic

So far our world depends on fossil fuels as the primary energy source and this global dependence has many serious consequences over recent years. Now people realize that it is the root cause of contemporary problems, such as air pollution, global warming, etc.[18-21] Moreover, the reserves of fossil fuels are finite and consumption of fossil fuels is increasing with both population and industrialization. Finding alternatives to fossil fuels is inevitable. On the other hand, hydrogen is abundant in the universe and its conversion into energy is clean, efficient, non-toxic, and renewable since during the process energy is released when hydrogen reacts with oxygen to produce water as the only byproduct. Hydrogen has been proposed as the nearly ideal energy carrier for our future.[22,23] Using hydrogen as fuel can fundamentally change our relationship with the natural environment. Figure 1.1 shows the schematic diagram of the hydrogen energy system. The diagram is taken from the internet at www.unido-ichet.org. We can see that as an energy carrier, with the primary energy sources such as solar energy, nuclear energy, wind energy, and so on, hydrogen is sustainable. Hydrogen can play am important role in a new, decentralized energy infrastructure that can provide power to different transportations which include vehicles, trains, and airplanes, residential and commercial industry.

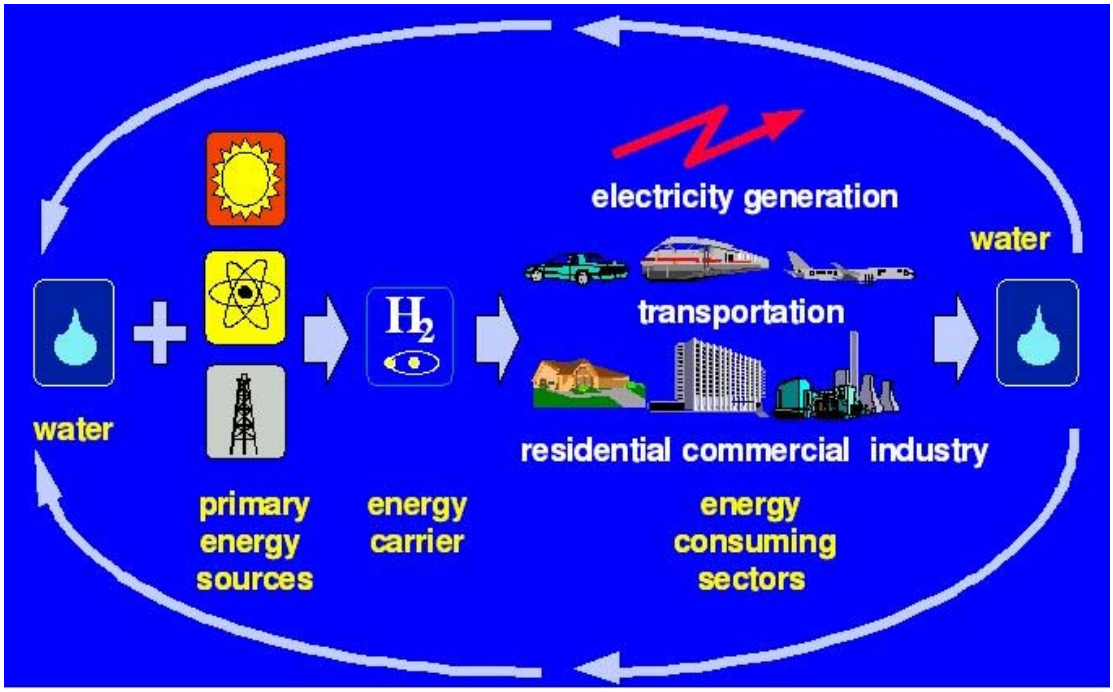

Figure 1.1. The schematic diagram of the hydrogen energy system [24]

As the energy carrier, hydrogen has many important advantages.[25] These advantages include, (1) Health and environmental safety. Hydrogen is non-toxic and safe to breathe to human beings. (2) Problems of use of fossil fuels. Burning of conventional fuels, including gasoline, diesel, natural gas and coal, produces carbon dioxide (CO_2), which is the cause of global warming. Also, combustion of fossil fuels at high temperatures either inside an internal combustion (IC) engine or in an electric power plant produces other toxic emissions, for example, carbon monoxide (CO), oxides of nitrogen and sulfur (NO_x and SO_x), volatile organic chemicals, and fine particulates, which could cause ecosystem damage, and increase lung disease and cancer. (3) Superior efficiency. Most of IC engines only obtain 15-20 percent of the energy in

gasoline, while the rest is lost as waste heat and vibrational noise. However, hydrogen-powered fuel cells can convert 40-65 percent of hydrogen's energy into electricity via a chemical reaction. (4) Decarbonization: the trend towards clean renewables. Less carbon content in fuels with higher concentration of hydrogen has a much greater specific energy density and burns cleanlier. For the future energy, the aim of the trend is to use pure hydrogen fuel. (5) Renewable energy carrier. Hydrogen can be made from electrolytic decomposition of water and becomes water again when reacted with oxygen in a fuel cell. With all these advantages, we believe that hydrogen economy will happen in the coming years with more advanced techniques.

At a meeting on November 15-16, 2001, 53 senior executives representing energy and transportation industries, universities, environmental organizations, Federal and State government agencies, and National Laboratories discussed the potential role of hydrogen systems in America's energy future.[22] The meeting agreed that hydrogen is America's clean energy choice for the future and concluded five major findings so far on the development of hydrogen as fuel. [22]

(1) Hydrogen has the potential to solve two major energy challenges that confront America today: reducing dependence on petroleum imports and reducing pollution and greenhouse gas emissions.

(2) Hydrogen could play an increasingly important role in America's energy future. Hydrogen is an energy carrier that provides a future solution for America. The complete transition to a hydrogen economy could take several decades.

(3) The transition toward a so-called “hydrogen economy” has already begun. We have a hydrocarbon economy, but we lack the know-how to produce hydrogen from hydrocarbons and water, and deliver it to consumers in a clean, affordable, safe, and convenient manner as an automotive fuel or for power generation.

(4) The “technology readiness” of hydrogen energy systems needs to be accelerated, particularly in addressing the lack of efficient, affordable production processes; lightweight, small volume, and affordable storage devices; and cost-competitive fuel cells.

(5) There is a "chicken-and-egg" issue regarding the development of a hydrogen energy infrastructure. Even when hydrogen utilization devices are ready for broad market applications, if consumers do not have convenient access to hydrogen as they have with gasoline, electricity, or natural gas today, then the public will not accept hydrogen as “America’s clean energy choice.”

The development of hydrogen energy technologies represents a potential long-term energy solution for America. However, it could take several decades before the real hydrogen economy is coming and all partners must work together to overcome the technical, economic, and institutional challenges.[26] Table 1.1 shows the overview of the transition to the hydrogen economy according to the report titled “ A National Vision of America’s Transition to a Hydrogen Economy – to 2030 and Beyond”.[22]

Table 1.1: Overview of the transition to the hydrogen economy [22]

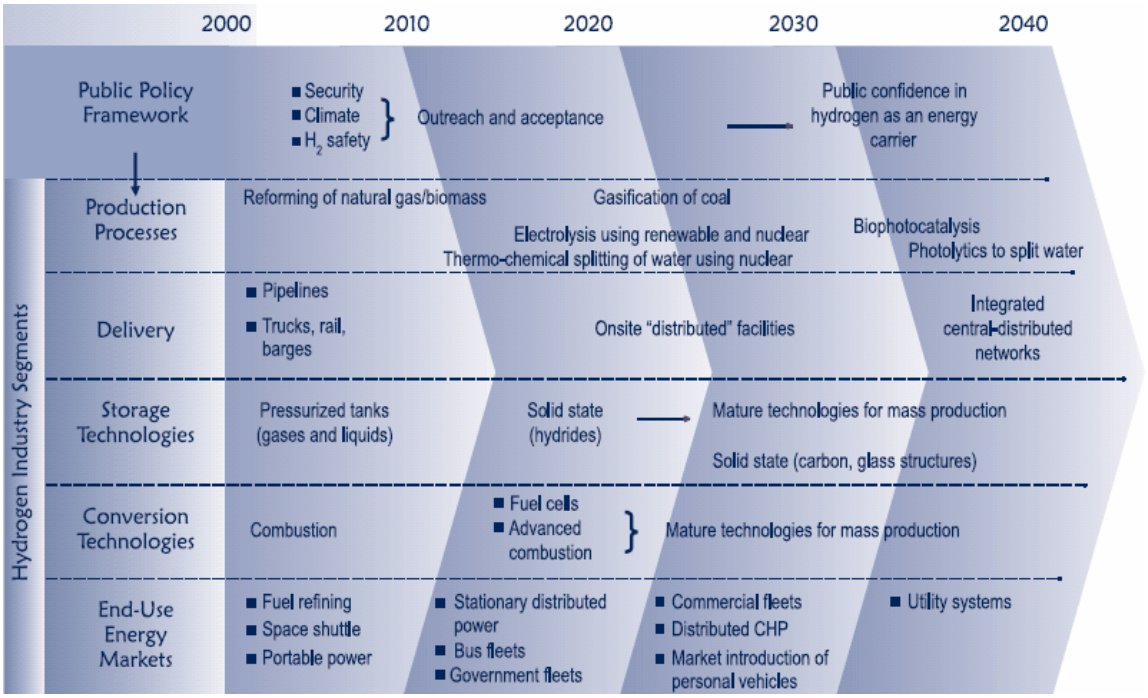

Currently, the development is at the phase one of the transition to the hydrogen economy according to DOE's projection.[22] During this first transition phase, most of the related work focuses on four aspects.[22] Hydrogen economy should achieve significant progress and expand more and build the strong and reliable foundation for the next stages. First, most of research on hydrogen production and hydrogen storage, aiming at reducing the cost and enhancing the safety, is still on the level of laboratory work. In this part of dissertation, the research work is focused on the storage material for hydrogen adsorption. In next section, an overview on the materials of hydrogen storage will be provided. At the current status, no material is found to reach DOE target of the capacity of 6.5 wt% at ambient conditions. These research techniques should be making

a further significant progress to support industry's pre-commercial efforts. Second, current hydrogen production options include solar, nuclear, and traditional fossil-fuel steam reforming with underground sequestration of the carbon dioxide. Innovative techniques need to be developed for massive hydrogen production at affordable for market readiness. Third, different devices need to be developed, including hydrogen-fueled internal combustion engines, hydrogen fuel cells for portable power devices, and hydrogen fuel cells for combined heat and power applications in buildings. With improved techniques in these fields and more reliable and higher efficient devices, we can build solid support for infrastructure development, which is one key step for hydrogen economy. Last, the creation of hydrogen-related policies on energy and the environment should be completed. Only these specific and strict policies, including liability, permitting, and codes and standards can provide a framework and guide the commercial development. So following these policies will be more effective for the reduction of energy imports, managing greenhouse gas emissions, and strengthening the control of air pollution. Table 1.2 [22] summerizes the key drivers affecting hydrogen energy development and provides what need to be accomplished on for the coming hydrogen economy.

Table 1.2: Summary of key krivers affecting hydrogen energy development [22]

Factor	Reasons
Support	(1) National security and the need to reduce oil imports (2) Global climate change and the need to reduce greenhouse gas emissions and pollution (3) Global population and economic growth and the need for new clean energy supplies at affordable prices, as hydrogen is potentially available in virtually unlimited quantities (4) Air quality and the need to reduce emissions from vehicles and power plants
Inhibit	(1) The inability to build and sustain national consensus on energy policy priorities (2) Lack of hydrogen infrastructure and the substantial costs of building one (3) Lack of commercially available, low-cost hydrogen production, storage and conversion devices, such as fuel cells (4) Hydrogen safety issues
Both Support and Inhibit	(1) Rapid pace of technological change in hydrogen and competing energy sources and technologies (2) The current availability of relatively low-cost fossil fuels, along with the inevitable depletion of these resources (3) Simultaneous consumer preferences for both a clean environment and affordable energy supplies

With the foundation and successful development of the phase one, the hydrogen economy will be facing the phase two, transition to the marketplace. During the process the federal and state government facilities will play a critical role to facilitate such transition, through serving as first use sites for hydrogen energy systems, especially for public transportation services.[22] During the second phase, development of more advanced technologies on hydrogen production and storage, and manufacture of fuel cells should be achieved to reduce the cost for marketing.

With the competitive cost of hydrogen fuel compared to the traditional liquid fuels, hydrogen economy will be facing the phase three, massive production of hydrogen and convenient delivery system, most importantly, the expansion of markets and a nation wide hydrogen infrastructure.[26] During this period, we will see the widespread use of hydrogen fueled powered buses, mini-trucks and sedans. Hydrogen storage advanced materials will become more reliable for commercialization. In this phase, policies made at phase one will regulate and guide the hydrogen economy to the direction of more economical and environmentally friendly.

Finally, hydrogen as an energy carrier will overcome most of the barrier and take over fossil fuels for most energy market applications before the coming of the end of the oil age. According to DOE's projection, a national comprehensive system for the use of hydrogen for fuel and electricity production will be built.[26] People will start to enjoy the economic benefits as well as the environmental benefits of the clean energy systems. The hydrogen economy will become reality.

1.3 Overview on hydrogen storage

Table 1.3 summarizes the elements of today's hydrogen energy system.[22] For the successful hydrogen economy on a large scale, there are several scientific and technological bundles to be solved. As we know that one popular and attractive option of hydrogen energy is that hydrogen is used as a transportation fuel. To achieve this goal, hydrogen needs to be accessible and easily stored onboard on different transportation tools in reasonable amount, for example, different transportation fueled by

hydrogen can travel about 300 miles and get refueled in a few minutes, competitive with the high density by weight and volume and ease of use of traditional liquid fuel.[22] On the other hand, cost and safety are two key factors of the marketing. At this point, finding a cost effective, compact, and safe storage solution is the key enabling technology for the further development of hydrogen economy. Hydrogen storage is important to all other aspects of hydrogen usage, including production, delivery, and end-use applications. Finding suitable hydrogen materials is long-term task and might take decades.[23] To follow the roadmap of hydrogen economy on the application of hydrogen energy in transportation, DOE has set specific targets for the suitable amount of hydrogen contained in storage medias, about 4 kg of hydrogen for cars and 5 to 10 kg of hydrogen for light-duty trucks for a distance of about 300 miles.[26] Also, on-board energy storage requires compact and safe hydrogen fuel, which put a big challenge for using hydrogen on board. For the development of the hydrogen economy step by step, DOE's 2010 target for hydrogen storage system is with an energy density of 7.2 MJ/kg and 5.4 MJ/L, which is about 6 wt% of hydrogen and 45 kg of hydrogen per cubic meter.[26] As following the roadmap, at 2015, the target of hydrogen storage system is 9 wt% of hydrogen and 81 kg of hydrogen per cubic meter, which is greater than the density of liquid hydrogen, about 70 kg/m3 at 20 K and 1 atm. [26]

Table 1.3: Elements of today's hydrogen energy system [22]

Hydrogen Industry Segment	Explanation
Production	(1) production of hydrogen from fossil fuels, biomass, or water (2) thermal, electrolytic, and photolytic processes
Delivery	(1) distribution of hydrogen from production and storage sites (2) pipelines, trucks, barges, and fueling stations
Storage	(1) confinement of hydrogen for delivery, conversion and use (2) tanks for both gases and liquids at ambient and high pressures (3) reversible and irreversible metal hydride systems
Conversion	(1) production of electricity and/or thermal energy (2) combustion turbines, reciprocating engineers, and fuel cells
End-Use Energy Application	(1) use of hydrogen for portable power in devices such as mobile phones and computers (2) use of hydrogen for transportation systems such as fuel additives, fuel-cell vehicles, internal combustion engines, and in propulsion systems for the space shuttle (3) use of hydrogen as stationary energy generation systems, including mission critical, emergency, and combined heat and power applications

From Table 1.3 we can see that hydrogen storage is the bridge between production and application. Hydrogen storage plays an important role in hydrogen economy. Generally speaking, there are mainly four categories of methods for hydrogen storage. To get a brief idea of the importance of compatibility of hydrogen in different ways of storage, Figure 1.2 shows the volume of 4 kg hydrogen compacted in different ways, with size relative to the size of the car, these storage methods include currently mature technologies, high-pressure gas-storage system, cryogenic liquid hydrogen, metal hydride.[27] This figure clearly shows that the volume to be occupied by the same amount of hydrogen greatly depends on the method used to store hydrogen. Among these

storage methods, packing hydrogen in high-pressure gas container occupies the largest volume, while has the smallest volume in Mg_2NiH_4 hydride. The importance of the storage method can be seen from the comparison of these occupied volume needed by different ways of storage methods. To decrease the volume occupied by hydrogen as much as possible is a must for on-board techniques of hydrogen-fueled transportation and our ultimate goal. Current worldwide research is to find more advanced materials to storage enough hydrogen energy at moderate conditions.

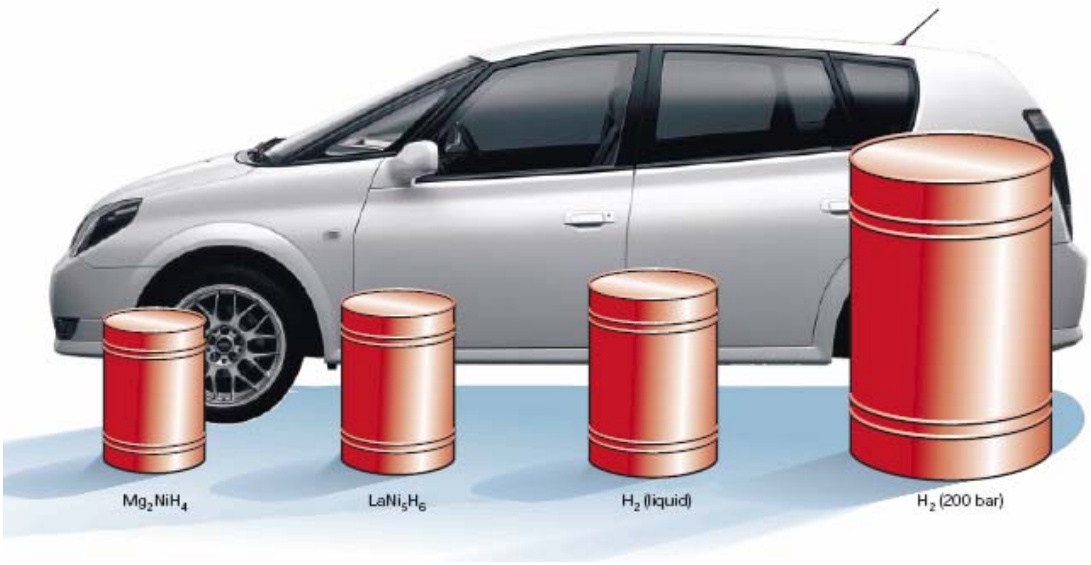

Figure 1.2. Volume of 4 kg of hydrogen compacted in different ways, with size relative to the size of a car. (Image of car courtesy of Toyota press information, 33rd Tokyo Motor show, 1999) (Adapted by permission from Macmillan Publishers Ltd: Nature, 414, 2001, 353-358 [27], copyright 2001)

Other than the methods of high-pressure gas-storage system, cryogenic liquid hydrogen, and metal hydride system, hydrogen adsorption on solids of large surface area or large pore volume of light materials is currently one of the most intensive investigated field. Figure 1.3, [27]demonstrates the ability of hydrogen storage per mass as well as per volume of specific compounds, including traditional pressurized hydrogen, liquid hydrogen, metal hydrides, carbon nanotubes, alanates. In the following sections, a brief overview of the advantages and disadvantages will be discussed considering these different storage methods.

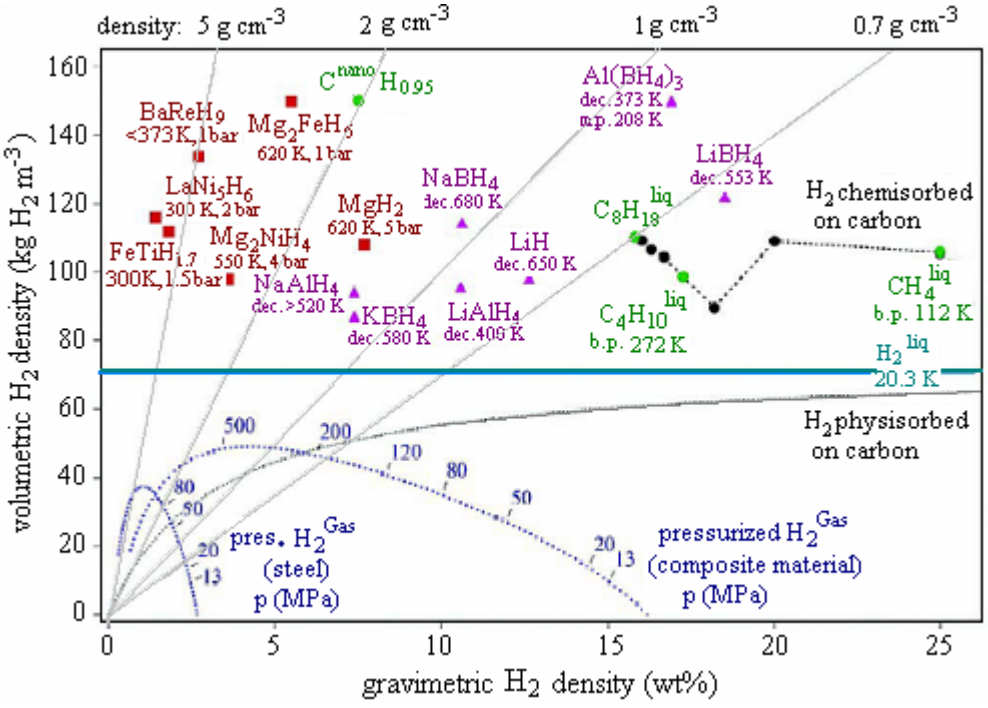

Figure 1.3. Stored hydrogen per mass and per volume. Comparison of metal hydrides, carbon nanotubes, petrol and other hydrocarbons. (Adapted by permission from Macmillan Publishers Ltd: Nature, 414, 2001, 353-358 [27], copyright 2001)

1.3.1 Conventional hydrogen storage

Conventional hydrogen storages include high-pressure gas-storage system and cryogenic liquid hydrogen at very low temperature. They are mature techniques for hydrogen storage.[28-31] For high-pressure gas-storage system, cylindrical shape of containers is mainly used and the container materials include fairly cheap steel, carbon-fiber-reinforced composite, and inert aluminum with external carbon-fiber coatings. In steel high-pressure tanks, hydrogen is normally filled up to 300 bar, while at carbon-fiber-reinforced composite tanks, with inert inner coating to prevent reaction of high-pressure hydrogen with the polymer, hydrogen can be filled up to 600 bar. Figure 1.3 demonstrates that hydrogen densities on the mass base is less than 4 wt% in steel high-pressure tanks and up to 15 wt% in the carbon-fiber-reinforced composite tanks. But this method has significant disadvantages and cannot satisfy long-term storage goals. These disadvantages include high energy input for pressurization of hydrogen, considerable risk due to the high-pressure vessels, and additional pressure control for the release of hydrogen from tanks. Also, it usually occupies the largest volume for same amount of hydrogen, which is the limitation factor for on-board application.

Another way of conventional hydrogen storage is that hydrogen is stored in the form of liquid hydrogen through condensation at low temperature. Hydrogen stored as liquid has higher mass of hydrogen per volume and the density of liquid hydrogen is 70.8 kg/m^3. With cryotechniques, liquid hydrogen has been used as a fuel in the launching process of the space shuttle. However, the condensation temperature of hydrogen is very low, -252 ^oC at 1 bar. The liquid hydrogen has to be kept in a very

good heat insulation container to maintain at very low temperature. Another fact is that the critical temperature of hydrogen is -241 ^{o}C, above which hydrogen is in gas state. In order to avoid strong overpressure, the liquid hydrogen containers have to be open systems. Although large containers with small surface to volume ratio are used to reduce the loss of hydrogen, due to heat transfer through the container, hydrogen losses up to 1 % a day by boiling at 20 K. Another disadvantage is that, the liquefaction of hydrogen costs large amount of electric power, roughly one-third of the energy value of the hydrogen. This decreases the overall energy density of hydrogen as fuel.

1.3.2 Hydrogen storage by metal hydride

Numerous research groups have examined a large number of metal hydrides over decades and the list of materials includes hydrides of nickel and other transition metals, rare-earth alloys, and related materials.[32-40] Metal hydrides have been commercialized for battery applications and extensively evaluated in combination with combustion engines for storage applications.[37] The essential of the storage of hydrogen is that molecular hydrogen is dissociated at metal surface before absorption, and two hydrogen atoms recombine to form molecular hydrogen during the desorption process. The formation of metal hydrides is described by pressure-composition isotherms, as shown in Figure 1.4.[27] First, hydrogen molecules dissociate on metal surface and some hydrogen atoms start to dissolve in the metal. A solid solution (α-phase) starts to form. As the pressure of hydrogen in gas phase increases, more and more hydrogen molecules dissociate. With the diffusion of H atom into metal, the concentration of H in the metal increases and the interaction between metal-H becomes locally important. At certain

point, the metal hydride (β-phase) starts to form. After the formation of the β-phase, the system contains two coexisted phases and isotherm shows a flat plateau, as observed in Figure 1.4. The plateau or equilibrium pressure depends strongly on the temperature and is related to the changes ΔH and ΔS, respectively.[27] The length of the plateau is the indication of the amount of hydrogen can be stored reversibly with small pressure variations. The longer of the plateau is desired regarding the amount of hydrogen stored, but it requires lower temperature.

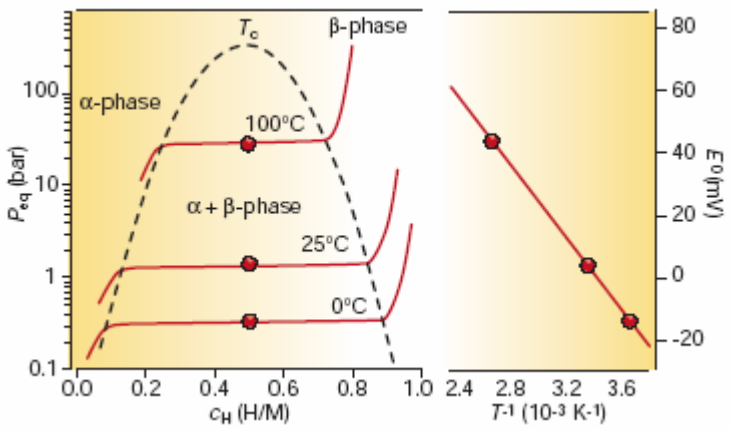

Figure 1.4. Pressure-concentration-temperature plot and a van't Hoff curve (logarithm of the equilibrium or plateau pressure against the reciprocal temperature). Values are for $LaNi_5$. The vertical axes indicate the corresponding hydrogen pressure or the equivalent electrochemical potential. (Adapted by permission from Macmillan Publishers Ltd: Nature, 414, 2001, 353-358 [27], copyright 2001)

Metal hydrides generally have two types. One is Fe-Ti transition metal system. This system includes elemental type, like Pd; AB_5 type, like $LaNi_5$; AB_2 type, like ZrV_2; AB type, like FeTi; A_2B type; body-centered cubic type, like TiV_2.[41] The progress had

been made on these metal hydrides in 1990s, such as fast and reversible sorption at room temperature and good cycling life, but the maximum hydrogen storage capacity at room temperature alloys is still lower than 2 wt%, which is too low for the economic support of hydrogen fuel for transportation system and cannot meet DOE target of 6.5 wt%. The other metal hydride materials are based on magnesium and Mg alloys. Due to the lighter weight of metal itself, hydrogen storage can reach up to 7.6 wt% in case of pure MgH_2. However, the formation of hydride from bulk Mg and gaseous hydrogen is very slow and also requires high temperature at 300 ^oC, because the sorption kinetics is mainly controlled by diffusion.[42] Using various binary and ternary Mg alloys to reducing the binding interaction of Mg-H, [43] ball milling to increase the defect concentration and shorten the diffusion path, and fluorination treatments [44] to obtain the surface active sites are used to improve the slow kinetics. Formation of hydrides at 150 ^oC has been achieved, but hydrogen uptake is much lower than pure MgH_2, for example 3.59 wt% in Mg_2NiH_4. This high temperature required to evolve hydrogen and relatively low hydrogen storage capacity limit the use of metal hydride, especially in transportation applications.

1.3.3 Alanates and other light hydride materials

A novel group of reversible hydrogen storage materials, alanates (alkali metal aluminum hydrides), have been extensively studied recently.[45-47] Although hydrogen content in these compounds can be very high and up to 18 wt%, these light elements form stable and ionic compounds with hydrogen. The desorption temperature is normally higher than 500 ^oC, as shown in Figure 1.3. At present the only material which

seems to be promising is sodium alanate, $NaAlH_4$.[48-52] Theoretically, sodium alanate decomposes in two steps and produces about 5.5 wt% of hydrogen. During first decomposition step, sodium alanate decomposes to Na_3AlH_6, Al, and 3.7 wt% of hydrogen with an equilibrium pressure of 0.1 MPa; while at the second step, Na_3AlH_6 continues to decompose to NaH, Al, and 1.8 wt% of hydrogen.[53] However, the reversible conditions for sodium alanate system were reported to be at temperatures of 200-400 ^oC and pressures of 10-40 MPa.[53-55] These conditions are not practical considering the melting point of 183 ^oC. While a small amount of titanium doped $NaAlH_4$ system can improve the slow kinetics of rehydrogenation and the reversible reaction can be performed at temperature lower than the melting point of 183 ^oC and around 100 MPa.[45] For the dehydrogenation process, the graphite-titanium combination sodium alanate can lower the dehydrogenation temperature by about 15 ^oC compared with only titanium doped sodium alanate.[47] Although these progresses are promising, the hydrogen storage capacity is decreased and only about 3.0 – 3.7 wt%. Also, other problems still exist, especially related to engineering problems. First of all, the heat released when reloading hydrogen is a severe problem and needs to be efficiently removed to keep the material system below the melting point. Second, the volume changes during dehydrogenation and rehydrogenation and the change can be as high as 15 %, which would affect the cycle stability of the materials. Last, $TiNaAlH_4$ is a very reactive solid and can ignite with air or moisture. New safety issue has to be considered.

1.3.4 Hydrogen storage on large surface area or large pore volume materials

Generally, these materials with large surface area or large pore volume include a range of carbon-based materials such as carbon nanotubes (both single wall nanotubes and multi wall nanotubes), aerogels, nanofibers (including metal doped hybrids), activated carbon, as well as metal-organic frameworks (MOF), conducting polymers and clathrates. In these materials, hydrogen is adsorbed as a molecular state by the virtue of their high surface area and microporosity, through the weak van der Waals forces, i.e., physisorption; or as an atom state by dissociation of hydrogen molecule at the surface, i.e., chemisorption. The adsorption of hydrogen in these materials is greatly depended on the applied pressure and the temperature. Carbon nanotubes and metal-organic frameworks are two main categories as hydrogen storage materials. Figure 1.5 shows the structures and micrographs of various carbon allotropes, including a single-wall nanotube, nanotube-bundle, cup-stacked carbon nanofiber, nanohorns, and metal-organic frameworks.[56]

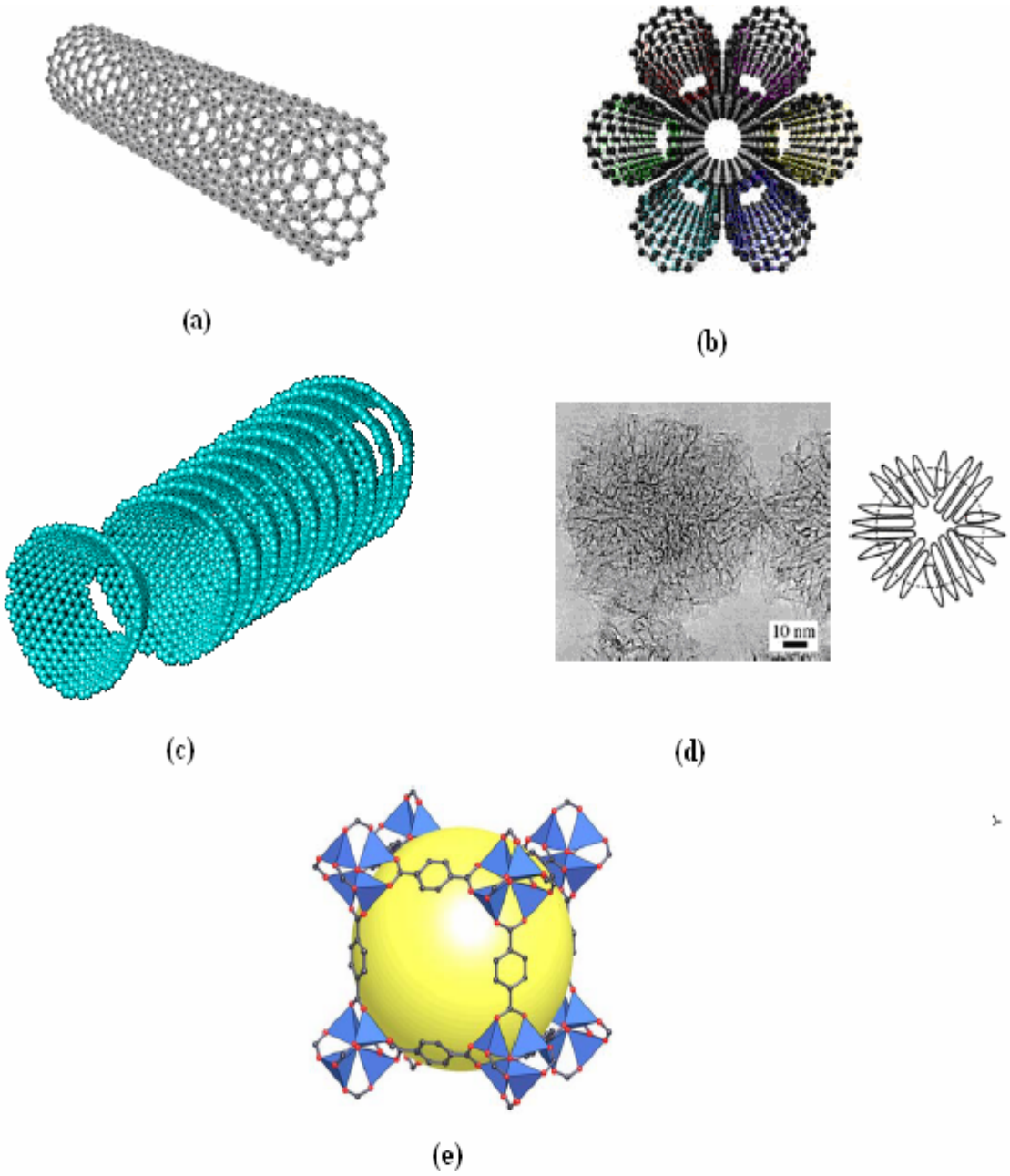

Figure 1.5. Structures and micrographs of selected carbon allotropes and nanostructures. (a) single-wall carbon nanotube, (b) nanotube-bundle, (c) cup-stacked carbon nanofiber, (d) nanohorns, (e) metal-organic framework (Adapted from report by Argonne National Laboratory, as in REF [56]; source of (e): Li, H., [57])

1.3.4.1 Carbon materials

Carbon nanotubes have shown tremendous promise for impressive performance as hydrogen storage materials since 1997 in many laboratories around the world. However, the hydrogen storage capacities of these materials remain controversial considering the poor reproducibility in sample preparation, measurement, and thus the capabilities. At some point, this controversy is caused by insufficient characterization of the carbon materials used by different research groups. As we know that carbon nanotubes are often mixtures of opened and unopened, single-walled and multi-walled tubes of various diameters and helicities together with other carbonaceous species, depending on the methods of preparation of the samples. Even though this uncertainty, carbon nanotubes and doping to nanotubes are still considered the important candidates for hydrogen storage application because these materials are well-packed nanoporous solids and have electronic properties that may be controlled through nanotube geometry such as diameter and open or close cap, nanotube defects, dopants or catalytic species.[22,23,26] Synthesizing single-wall nanotubes at the National Renewable Energy Laboratory (NREL) showed a 3.00 to 3.13 wt% hydrogen storage capacity on 8 different samples.[58] The studies of hydrogen adsorption on carbon materials are carried out extensively experimentally and theorectically.

Experimental investigations. Dillon et al. [59] first reported the study of hydrogen storage on single-wall nanotubes (SWNTs). They estimated hydrogen storage capacity in the range of 5-10 wt% for pure SWNTs and predicted that SWNTs with diameter of 1.63 and 2 nm could store about 6.5 wt% at room temperature, which is the target set by

DOE for on-board applications. With a large mean diameter of about 1.85 nm of SWNTs after the ultrasonic cutting procedure, a maximum adsorption capacity of 7 wt% was reported by Dillon et al.[60,61] Ye et al. [62] reported a hydrogen storage capacity of more than 8 wt% on crystalline ropes SWNTs at a cryogenic temperature of 80 K and pressure higher than 12 MPa. The high adsorption capacity was attributed to the occurrence of a phase transition when pressure was higher than 40 bar at 80 K, which provided a tube-tube cohesive energy. Liu et al. synthesized of SWNTs with a large mean diameter of about 1.85 nm by a semicontinuous hydrogen arc discharge method, followed by post-treatment of soaking in hydrochloric acid and heat-treated in vacuum.[63] The SWNTs showed a reproducible hydrogen storage capacity of 4.2 wt% at room temperature under 10 MPa.[63] More recently, Gao et al. [64] investigated different carbon materials, including high specific surface area activate carbon, open-tipped MWNTs, close-tipped MWNTs and SWNTs at room temperature and 77 K. They found that open-tiped MWNTs had the highest hydrogen storage capacity of 6.46 wt% at 77 K and 1.12 wt% at room temperature. Gundiah et al. [65] observed a maximum hydrogen storage capacity of 3.7 wt% at 300 K and 145 bar on the sample of MWNTs after acid treatment. Other hydrogen storage capacities of 0.6 wt% ~ 8.6 wt% were reported for different carbon nanotube materials with different treatments in a wide range of temperature and pressure. [66-73]

Theoretically investigations. So far, no general conclusion could be drawn from experimental results on the adsorption of hydrogen on carbon nanotubes, especially the mechanism of adsorption. This lack of understanding of the mechanism affects both the

nature of these materials and the improvement of their storage capacity. On the other hand, theoretical calculations and modeling could explain what and why is happening in the experiments at the molecular or atomic level. Theoretical calculations can be very useful for understanding the elementary steps of the adsorption procedure and giving insight into the adsorption phenomenon.[74,75] Based on the theoretical approximation of these calculations, there are mainly three methodologies used to study the adsorption of hydrogen, including the grand canonical Monte Carlo (GCMC) method, molecular mechanics (MM) classical algorithms, ab initio / DFT or semiempirical quantum techniques.

Johnson and coworkers studied [76-79] the adsorption isotherms of hydrogen in SWNT arrays, isolated SWNTs and idealized carbon slit pores. Their results showed that curvature of the nanotubes increased the number of the nearest neighbor carbon atoms to interact with hydrogen and the packing geometry of the SWNTs plays an important role in hydrogen storage, and idealized graphitic nanofibers (slit pores) gave better performance than SWNT arrays did. They then predicted that (9,9) SWNT triangular arrays with an intertube spacing of 0.9 nm had gravimetric and volumetric densities close to the DOE targets at 77 K and 5 MPa. Gauy et al. [80] used GCMC method to investigate the hydrogen storage capacities in pure SWNTs, DWNTs, and CNFs or with metallic impurities in an SWNT network. Their simulation results indicated that hydrogen storage capacity was significantly affected by the structural porosity and a maximum capacity of 1.4 wt% was achieved for the nanostructured carbons with optimum pore diameter of about 0.7 nm at 293 K and 10 MPa. The

presence of metallic particles enhanced the attractive interaction to hydrogen and increased the hydrogen storage capacity, but was not able to reach the DOE target. Yin et al. [81] investigated hydrogen storage capacity in a triangular array of SWNTs and in slit pores at 298 K and 77 K using GCMC method and they obtained 4.7 wt% hydrogen adsorption capacity at 298 K and 10 MPa for the large diameter SWNTs (6.0 nm) with large intertube spacing of 1.0 nm. Cao et al. [82] performed GCMC simulations to study hydrogen storage of graphitic carbon inverse opal (GCIO) at 298 K and 30.25 MPa. An adsorption value of 5.9 wt%, which was close to the DOE target, was predicted at the conditions studied when the diameter of the spherical cavity in the GCIO materials was 1.78 nm.

Ma et al. [83] studied the hydrogen storage behavior of an armchair (5,5) SWNT using ab initio calculations and molecular dynamics simulations. They used a many-body Tersoff-Brenner potential simulate low-energy collision of atomic H on the side-wall of SWNT, and minimal HF/STO-3G ab initio calculations on selective configurations from molecular dynamics simulations. They obtained a maximum capacity of 5 wt% when hydrogen atoms with a kinetic energy of 16-30 eV penetrated and were trapped inside the tube of SWNT. Dubot and Cenedese [84] used semi-empirical AM1 method to study adsorption of lithium and molecular hydrogen in SWNTs. They predicted that lithium could be adsorbed on zig-zag nanotubes and these adsorbed lithium allowed the anchoring of molecular hydrogen on the carbon nanotube with a binding energy in a chemisorption regime, which would enhance hydrogen storage capacity compared to those adsorption through weak physisorption. Based on the

assumption of the chemisorption of hydrogen adsorption in SWNTs, Lee et al. [85] used DFT calculations to study the stability, mechanism and hydrogen storage capacity and their results indicated that hydrogen storage capacity of (10,10) SWNTs with diameter of 1.3 nm could reach 14.3 wt%. Bauschlicher [86] investigated the binding energy of hydrogen to a (10,0) SWNT at different coverage rates. He obtained the most stable state with the binding energy of –57.3 kJ/mol, which corresponded to about 4 wt% hydrogen storage capacity.

As pointed out previously, hydrogen storage capacities on carbon materials have been in the wide range of discrepancy. Scientists have tried to identify factors such as effect of structural characteristics of materials, effect of synthesis method and post-treatment, and effect of the surface area of materials, measurement methodology, that influence the hydrogen storage capacities of different materials. So far, hydrogen storage of carbon materials still remains open and needs to be further investigated. Table 1.4 and Table 1.5 list the of newly reported experimental and theoretical results for hydrogen storage in carbon materials.[87]

Table 1.4: Summary of newly reported experimental results for hydrogen storage in carbon materials

Sample	Synthesis technique	Diameter (nm)	Pressure and temperature	Result (wt%)	Ref.
SWNT	HiP_{CO}	-	8 MPa, RT	0.43 (A)	71
MWNT	CVD	20-30	100 bar, 298 K	3.3 (A)	88
SWNT	HiP_{CO}	-	48 bar, RT	1.2 (A)	89
MWNT	CVD	-	145 bar, 300 K	3.7 (A)	65
MWNT	CVD	10-60	10 MPa, RT	3.98 (A)	90
MWNT	CVD	53	13.59 MPa, RT	4.6 (A) 3.2 (R)	91
MWNT	CVD	30	10 Mpa, 77 K	0.45 (A)	92
MWNT (tip closed)	CVD (anodized Al_2O_3 template)	40	10 Mpa, 77 K 10 MPa, RT	6.46 (A) 1.12 (A)	64
CNF	CVD	-	69 bar, RT	3.8 (R)	93
SWNT	Arc discharge	1.2-1.5	1 bar, RT 1 bar, 77 K	0.02 (A) 1.58	94
Mixed SWNT and DWNT	CVD	-	10 MPa, RT	0.51 (A)	95
MWNT	CVD	10	Desorbed up to 2000^{o}C	8.6 (R)	66
SWNT	Laser ablation	1.4	9 MPa, RT	0.3 (A)	96
SWNT	HiP_{CO}	-	1 bar, 295 K 1 bar, 77 K	0.2 (A) 1.7 (A)	67
SWNT	Arc discharge	1.2-1.5	300 Torr, 77 K	3.0 (A)	97
SWNT	HiP_{CO}	-	3.5 MPa, 303 K	0.25 (A)	98
SWNT	HiP_{CO}	-	300 atm, 294 K	0.91 (A)	99
SWNT	Arc discharge	1.2	25 bar, 77 K	2.4 (A)	100
MWNT	CVD	25-30	9 MPa, RT	0.69 (A)	101
SWNT	Arc discharge	0.7-1.2	2 MPa	0.60 (R)	68
MWNT	CVD	60-100	10 MPa, RT	5.0	102
MWNT	CVD	10-30	10.61 MPa, RT	0.272 (R)	103
CNF	CVD	250	80 atm, RT	17 (A)	104

Notes: RT. Room temperature; A. adsorption; R. release.

Table 1.5: Summary of newly reported theoretical results for hydrogen storage in carbon materials

Sample	Diameter (nm) or (n,m) indices	ITD (nm)	Method	Pressure and temperature	Result (wt%)	Ref.
CNT and CNF			GCMC	10MPa,293K	0.6	80
Graphite slitlike			GCMC	80MPa,303K	1.4	105
SWNT	2.719	Isolated	Classical potential and DFT	4 MPa, 77 K	9.5	106
Alkali doped SWNT	(10,10)	0.3-1.2	NVT MC	100 atm, RT	3.95[a] 4.21[b]	107
SWNT	2.719	Isolated	Classical potential and DFT	20MPa,300K	1.0	106
SWNT	1.17	0.7	Tight-binding MD and GCMC	10MPa,293K	3.4	108
Li-doped pillared SWNT	(10,10) and 1:3 Li:C doping	0.9	Developed DFT and GCMC	50 bar, RT	6.0	109

Note: RT, Room temperature. [a], K-doping. [b], Li-doping.

1.3.4.2 Metal-organic frameworks

Recently, metal-organic frameworks have been of interest as candidates for hydrogen storage materials.[110-121] Metal-organic frameworks (MOFs) are crystalline solids which are assembled by connection of metal ions or clusters through different organic linkers. MOFs have features of large apparent surface areas, high porosity, reproducible and facile syntheses, amenability to scale-up, and chemical modification for targeting desired properties.[115] Chae et al. demonstrated that MOF-177 (Zn_4O(1,3,5-benzenetribenzoate)$_2$) had surface area of 4500 m^2g^{-1} and micropore volume of 0.69

cm^3cm^{-3}. [122] The framework had cavities of 10.9-11.8 Å in diameter connected in all directions by channels. MOF-177 showed about 2.0 wt% hydrogen storage capacity at room temperature. Hydrogen uptake at the level of 2.0 wt% in IRMOF-8 at 293 K and 10 bar was also been obtained by the same group in IRMOF-8 (Zn_4O(naphthalene-2,6-dicarboxylate)).[121] At low temperature, Yildirim and Hartman found that hydrogen molecules form unique interlinked high-sysmetry nanoclusters with intermolecular distances as small as 3.0 Å and hydrogen storage capacity reached up to 11.0 wt% in MOF5.[119] Other hydrogen storage capacities of MOFs are shown in Table 1.6, which is adapted from Rowsell.[115]

Table 1.6: Summary of hydrogen storage in MOFs

Materials*	Accessible volume fraction	Apparent surface area (m^2/g)	Pore vol. (cm^3/g)	Results (wt%)	Conditions	Ref.
$Zn_4O(bdc)_3$, IRMOF-1	0.59	3362	1.19	1.32	77 K, 1 atm	121
				1.0	RT, 20 bar	110
				1.65	RT, 48 atm	123
$Zn_4O(R^6\text{-bdc})_3$, IRMOF-6	0.50	2630	0.93	1.0	RT, 10 bar	110, 124
$Zn_4O(ndc)_3$, IRMOF-8	0.66	1466	0.52	1.5	77 K, 1 atm	121
				2.0	RT, 10 atm	110
$Zn_4O(hpdc)_3$, IRMOF-11	0.40	1911	0.68	1.62	77 K, 1 atm	121
$Zn_4O(tmbdc)_3$, IRMOF-18	0.42	1501	0.53	0.89	77 K, 1 atm	121
$Zn_4O(btb)_2$, MOF-177	0.63	4526	0.61	1.25	77 K, 1 atm	121
Al(OH)(bdc), MIL-53(Al)	0.29	1590,1020	-	3.8	77 K, 16 bar	125, 126
Cr(OH)(bdc), MIL-53(Cr)	0.29	1500,1026	-	3.1	77 K, 16 bar	125, 126
$Mn(HCO_2)_2$	0.10	297	-	0.9	77 K, 1 atm	127

Table 1.6 Continued

Materials*	Accessible volume fraction	Apparent surface area (m^2/g)	Pore vol. (cm^3/g)	Results (wt%)	Conditions	Ref.
$Cu_2(hfipbb)_2(H_2hfipbb)$	0.03	-	-	1.0	RT, 48 atm	123
Ni(cyclam)(bpydc)	0.18	817	0.37	1.1	77 K, 1 atm	128
$Zn_2(bdc)_2(dabco)$	0.45	1450	-	2.0	77 K, 1 atm	129
$Ni_2(bpy)_3(NO_3)_4$(M)	0.05	-	0.181	0.8	77 K, 1 atm	130
$Ni_2(bpy)_3(NO_3)_4$(E)	0.05	-	0.149	0.7	77 K, 1 atm	130
$Ni_3(btc)_2(3\text{-pic})_6(pd)_3$	0.30	-	0.63	2.1	77 K, 14 bar	130
$Zn_4O(L^1)_3$	0.21	502	0.20	1.12	RT, 48 atm	112
$Zn_4O(L^2)_3$	0.17	396	0.13	0.98	RT, 48 bar	112
$Cu_2(pzdc)_2(pyz)$, CPL-1	0.04	-	-	0.2	89 K, 1 atm	131
$Cu_2(bptc)$, MOF-505	0.37	1646	0.63	2.48	77 K, 1 atm	132

* Acronyms: bdc=benzene-1,4-dicarboxylate
R^6-bdc=1,2-dihydrocyclobutylbenzene-3,6-dicarboxylate
ndc=naphthalene-2,6-dicarboxylate
hpdc=4,5,9,10-tetrahydropyrene-2,7-dicarboxylate
tmbdc=2,3,5,6-tetramethylbenzene-1,4-dicarboxylate
btb=benzene-1,3,5-tribenzoate
hfipbb=4,4'-(hexafluoroisopropylidene)bisbenzoate
cyclam=1,4,8,11-tetraazacyclotetradecane
bpydc=2,2'-bipyridyl-5,5'-dicarboxylate
dabco =1,4-diazabicyclo[2.2.2]octane
bpy=4,4'-bipyridine
btc =benzene-1,3,5-tricarboxylate
3-pic=3-picoline
pd =1,2-propanediol
L^1=6,6'-dichloro-2,2'-diethoxy-1,1'-binaphthyl-4-4'-dibenzoate
L^2=6,6'-dichloro-2,2'-dibenzyloxy-1,1'-binaphthyl-4,4'-dibenzoate
bptc =biphenyl-3,3',5,5'-tetracarboxylate

Although MOFs at ambient conditions have not yet shown to be able to reach DOE target, the large surface area and high pore volume together with the flexible modification of the structure have made them promising materials for hydrogen storage. With the optimization of pore size, adsorption energy by linker modification, impregnation, catenation and inclusion of open metal sites and lighter metals, [115] MOFs are expected to further increase hydrogen storage capacities.

1.4 Objectives of this project

From the point of view of the energy density, light-weight materials are a promising choice for hydrogen storage. Carbon materials have been extensively investigated for hydrogen adsorption, because of their light weight. Physisorption of hydrogen on these carbon materials is most likely the mechanism of storage, especially at ambient temperature. Van de Waals intermolecular interactions between hydrogen molecules and carbon adsorbents are important factors for adsorption. In this project, we investigate a new carbon material, corannulene, [133-141]as adsorbent for hydrogen adsorption at ambient temperature. Corannulene has the bowl-shaped curvature and represents the polar cap of the C_{60} sphere. Corannulene is very stable and hollow because of the arrangement of the six-member rings and five-member ring. The curvature structure of corannulene is similar to that of carbon nanotubes, being more attractive to hydrogen molecules compared to planar graphite structure. Besides, as the polar cap of the C_{60} sphere, corannulene has a dipole moment, which can induce a dipole

moment on hydrogen molecules. The induced dipole-dipole interaction can thus enhance the attraction of hydrogen molecules with corannulene.

Pure carbon materials may not be sufficient for hydrogen storage to reach the DOE target of 6.5 wt%. Doping of alkali metal on carbon materials has been studied for hydrogen adsorption, both experimentally and theoretically.[142-149] Doping of alkali metal shows enhanced hydrogen storage, compared to the pure carbon materials. In this project, we study the role that lithium atoms adsorbed on corannulene have on the hydrogen adsorption on corannulene molecules. With the understanding of lithium doping on corannulene for hydrogen adsorption, we expect that this project provides guidelines to improve hydrogen storage by doping of alkali metal.

Other than doping of alkali metal, molecular modification provides another way to improve hydrogen storage. Different corannulene derivatives have been reported and predicted. [150-155] This project will characterize a new modification of corannulene, which has potential of providing a larger adsorbent capacity for hydrogen adsorption. Modification of corannulene provides a general idea for other materials to obtain an improved feature for gas adsorption.

Corannulene has been chosen to model the curved carbon lattice with carbon-hydrogen interactions. This can also help to gain an understanding of the increased hydrogen storage capability in different carbon nanotubes over other carbon materials, and even general gas storage on gas industry.

CHAPTER II

METHODOLOGY AND COMPUTATIONAL / SIMULATIONAL DETAILS

2.1 Overview

Theoretical studies have been playing very important role on the investigation of hydrogen adsorption at the level of molecular or atomic scale. These studies explain the mechanism of hydrogen adsorption and the details of what are happening, such as hydrogen binding sites on different materials, adsorption isotherms, and density profiles. Other than developing an understanding of the elementary steps in the adsorption process, theoretical studies can also predict an upper limit on hydrogen storage capacity and guide the direction of experiments by studying ideal and complex systems. In this section, the methods used for this project and the details described the simulation procedures are provided.

2.2 Ab initio / DFT calculations

Gaussian 03 [156] is used for ab initio / DFT calculations. Cerius^2 3.0 package [157] and GaussView 03W [158] are used for visualization of calculation results.

Previous theoretical studies on corannulene indicated that a hybrid DFT method combined with double-ξ plus polarization basis sets would well reproduce the structural

parameters of corannulene [159,160] and protonation and lithium cation binding on corannulene.[161,162]

In this project, we use B3LYP/6-31G(d,p) for geometry optimization of corannulene and lithium atom doped corannulene complexes. The optimized geometries are then followed by frequency calculations at the same level to make sure they are local minima. Details of charge distribution and geometry configurations, as well as the electronic energies of different molecular systems are analyzed. From these studies, we are able to predict the molecular properties of these systems and as the candidates for hydrogen storage applications.

In order to find the favorable binding sites for hydrogen adsorption and see the interaction strength between hydrogen molecular and corranluene and different lithium atoms doped corannulene complexes, we perform potential energy surface scana at B3LYP/6-311G(d,p) with hydrogen molecule approaching each molecular system from different directions. During the potential energy surface scan, the geometries of hydrogen molecule, corannulene, and different lithium atoms doped corannulene complexes are fixed as the optimized geometry obtained at the level of B3LYP/6-31G(d,p). Only the distance between hydrogen molecule and specific site of corannulene or lithium atoms doped corannulene complexes is changed.

With previous potential energy surface of the systems of hydrogen molecule with corannulene and lithium atoms doped corannulene complexes at the level of B3LYP/6-311G(d,p), the favorable adsorption sites for hydrogen molecule at different molecular systems are clear. Since hydrogen storage on these adsorbent materials are in the region

of physisorption through the weak van del Waals interactions and DFT methods have limitation to describe weak van del Waals interactions, we perform single point calculations using second order Moller Plesset perturbation theory (MP2) to account for weak van der Waals forces that are responsible for the hydrogen molecule and corannulene or lithium atoms doped corannulene complex interaction based on physisorption at the minima of B3LYP based potential energy surface scan, with the basis set of 6-31G(d,p). Based on the energy obtained from MP2/6-31G(d,p), the interaction energy between hydrogen molecule and adsorbent molecules can be calculated precisely. This interaction energy is one of the important criteria to evaluate the potential performance as hydrogen storage materials.

Our final aim is to predict the hydrogen storage capacity of corannulene and lithium atoms doped corannulene complexes at ambient conditions. To achieve this goal, we use classical molecular dynamics simulations to study hydrogen adsorption on different adsorbent molecular systems, which will be described in details in next section. Before we move on to the classic molecular dynamics simulations, we are interested in the possible assembly of these molecules. Here, we use DFT calculations for full or partial optimization of dimer of corannulene molecules, dimer of most favorable lithium atoms doped corannulene complexes at specific lithium doping concentrations. Full optimizations at the level of B3LYP/6-311G(d,p) are performed for dimer of corannulene molecules in different orientations. While, partial optimizations at the same level of theory are performed for dimer of lithium atoms doped corannulene molecular complexes. During the partial optimizations, each of these two lithium doped

corannulene complex is treated as rigid molecule and two molecules are only allowed to move in one direction until the dimers reach the most stable states. These partial optimizations give us the separation between molecules and the results are used as reference for later molecular dynamics simulations. These results yield intermolecular distance (IMD) and interlayer distance (ILD). The details of the definitions of IMD and ILD will be explained later. Other than DFT calculations of dimers, we also perform semi-empirical calculations of 4, 8, and 12 corannulene molecules using AM1 method.

2.3 Classical molecular dynamics (MD) simulations

2.3.1 Essentials of MD simulations

The ultimate goal of this project is to predict hydrogen storage capacities of corannulene and lithium atoms doped corannulene complexes at ambient conditions. With the necessary information obtained from ab initio / DFT calculations in previous section, most of the work on this project is focused on molecular dynamics simulations at desired temperatures and pressures of interest. Molecular dynamics simulations have been useful as the tool for the understanding the properties of assemblies of molecules in terms of their structure and the microscopic interactions between them.[163,164] Molecular dynamics simulation has acted as a bridge both for, (i) between microscopic length (Å) and time scales (pico-second) and the macroscopic world of the laboratory, and (ii) between experiment and theory, through a good model with precise molecular interactions. Figure 2.1 shows the role of molecular dynamics simulation.[165] With molecular dynamics simulations, we can observe the phenomena of chemical process at

molecular level and predict the bulk properties of materials given the interactions between molecules. Also, with the model, molecular dynamics simulation can test a theory and compare with experimental results as well. In this project, we will perform molecular dynamics simulations with our model of interactions between hydrogen molecules and adsorbents and compare with known experimental results, and more importantly, predict and guide the direction of the experiments.

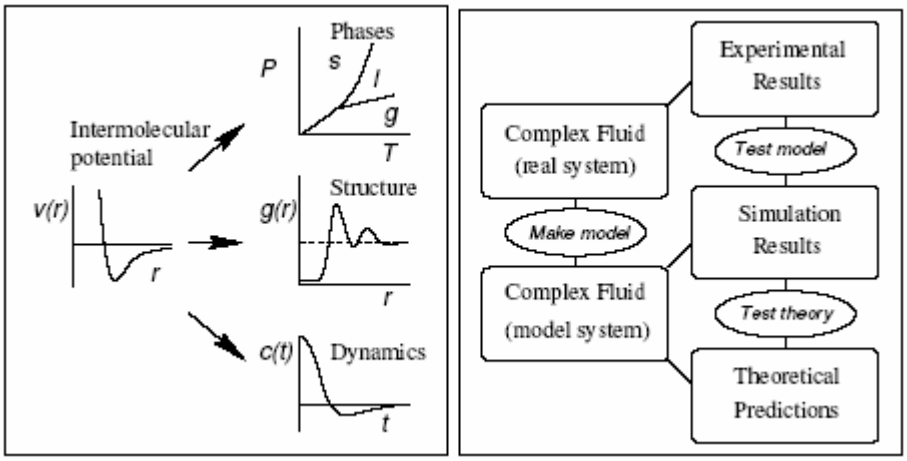

(a) (b)

Figure 2.1. Role of molecular dynamics simulations. As a bridge between, (a) microscopic and macroscopic; (b) theory and experiment. (Reproduced with permission from John von Neumann Institute for Computing. Copyright 2004) [165]

The essential of the molecular dynamics simulation is to numerically solve the classical equation of motion, which for a simple atomic system may be written as

$$m_i \ddot{r}_i = f_i$$
$$f_i = -\frac{\partial}{\partial r_i} U \qquad (2.1)$$

With the potential energy $U(r^N)$ we define in the input, where $r^N = (r_1, r_2, \cdots, r_N)$ represents the complete set of $3N$ atomic coordinates, we are able to calculate the forces acting on each atom, then finally we are able to solve the of velocity and position of each atom changing with the simulation time.

The program we use for molecular dynamics simulations is DL_POLY program, version 2.14.[166] In this project, MD simulations are carried out in the NVT ensemble with Evans thermostat. A total simulation time of 800 ps at either 273 K or 300 K under different pressures is used for hydrogen adsorption, with equilibration runs of 300 ps and production runs of 500 ps. Hydrogen uptake capacities of different systems at various conditions are evaluated as the average value during the production period. So does the corresponding pressure in the gas phase, by counting the average number of hydrogen molecules in the gas phase above the adsorbent molecules. Periodic boundary conditions (PBC) in all three dimensions are used. The cutoff radius, beyond which intermolecular interactions of the van der Waals potentials are set to zero, is chosen as 11.0 Å, which corresponding the half of the minimum simulation cell length.

Initially N hydrogen molecules are located in the gas phase above the adsorbent phase. As simulations start, H_2 molecules move from the gas phase to the adsorbent phase until they reach an equilibrium state, which is monitored by counting N_g, the number of H_2 molecules in gas phase as a function of time. The pressure in the gas phase is evaluated after the system reaches the equilibrium state. Hydrogen uptake is calculated by the equations

$$N_a = N - N_g \tag{2.2}$$

$$\rho_w = \frac{N_a m_{H_2}}{N_a m_{H_2} + N_{adsorbent} m_{adsorbent}} \times 100 wt\% \quad (2.3)$$

where N_a is the number of adsorbed molecules. For a given N, the molecules in the gas phase N_g are estimated by counting those that are located at distances greater than 4 Å from the surface of the adsorbent. N_g is used to calculate the pressure, based on the ideal gas approximation, taking the average value obtained during the last 500 ps simulation period. We find that N_a reaches an equilibrium value at about 100 ps. Longer simulation times up to 1200 ps do not change the number of H_2 adsorbed.

2.3.2 Arrangement of adsorbent molecules

2.3.2.1 Corannulene systems

To investigate possible structural arrangements of corannulene dimers, we carried out DFT calculations at the level of B3LYP/6-311G(d,p). Calculations yielded sandwich and T-shaped conformers of the corannulene dimer, shown in next chapter. The T-shaped conformer is the global minimum, and the sandwich is a local minimum, higher in 0.08 eV with respect to the T-shaped conformer. These structures somehow resemble those found for the benzene dimer, [167]although an additional dimer in parallel-displaced arrangement was not found for corannulene. Thus, two alternative structures were tested as corannulene adsorbent materials for the MD simulations, corresponding to the two dimer configurations, one where the molecules form T-shaped assemblies, as in the corannulene crystal,[168] and another with a simple stack of corannulene molecules arranged as in the sandwich configuration.

The crystalline structure of corannulene is monoclinic with space group of $P2_1/c$ (a = 13.260 Å, b = 11.859 Å, c = 16.520 Å, and $\beta = 120.69^{o}$) at $20^{o}C$.[168] In this structure, corannulene molecules are arranged as T-shaped conformers. To represent such structure, we use an MD simulation cell containing 32 corannulene molecules, located at the bottom of the cell of dimensions $26.520 \times 23.718 \times c$ $Å^3$, and an angle $\beta = 120.69^{o}$. The value of the c parameter for each simulation is estimated on the basis of the number of H_2 molecules, N_g, at a temperature T needed to obtain a given pressure P according to the ideal gas law.

In the second structural configuration tested for the adsorbent material, the simulation cell contains two layers of corannulene, with 16 molecules per layer, distributed at the bottom of the simulation cell. In this cell, corannulene molecules are arranged as sandwich conformers and also located at the bottom of the simulation cell. The cell dimensions are depended on the arrangement of adsorbent molecules, which will be provided individually at the discussion section.

In the MD simulations, the dynamics of the corannulene molecules is not included, thus the adsorbent molecules are kept fixed in their initial positions, and their distribution in each layer is determined by two parameters: the interlayer distance (ILD) and the intermolecular distance (IMD). As shown in Figure 2.2, the ILD is defined as the distance between two overlap molecules and the IMD is that between the centers of two parallel molecules. Values for IMD and ILD were obtained from DFT calculations described in the next section.

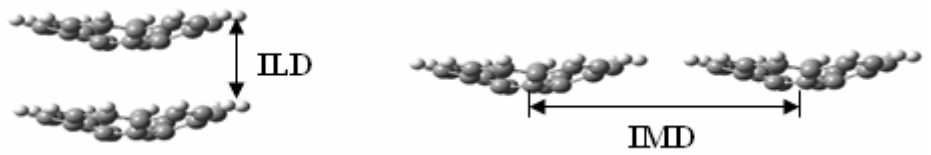

Figure 2.2. Definition of interlayer distance (ILD) and intermolecular distance (IMD)

2.3.2.2 Lithium atoms doped corannulene complexes

From DFT calculations, we are able to investigate the energetically favorable configuration of lithium atoms doped complexes at each specific lithium concentration. Here, we take the most stable configuration at each lithium doping concentration as the adsorbent for the investigation of hydrogen adsorption. We assume that lithium-atom doped corannulene arranges in a stack configuration as discussed in previous section for the case of undoped corannulene systems. Each simulation cell contains 16 lithium-atom doped corannulene molecules, with 8 molecules in one layer and distributed at the bottom of the simulation cell. In the MD simulations, the dynamics of the adsorbent molecules is not included, thus the adsorbent molecules are kept fixed in their initial positions, and their distribution in each layer is also determined by two parameters: ILD and IMD. Here, the ILD is defined as the distance between two overlap lithium atoms doped molecules and the IMD is between the centers of two parallel lithium atoms doped molecules, as similar in previous section as shown in Figure 2.2. The values of IMD and ILD will be discussed in the next sections.

2.3.3 Estimation of the IMD and ILD parameters

DFT calculations at the level of B3LYP/6-311G(d,p) are performed for the characterization of corannulene dimer and six lithium atoms doped (at the concave side) of a corannulene dimer. In order to investigate available space and collective effects on H_2 adsorption, it is fair to assume that lithium atoms doped corannulene molecules arrange in a simple stack. In this case, we can adjust the ILD and IMD variables, performing analyses similar to those reported by other researchers using CNT bundles and GNF[79,109,169,170]. To have a reference, we compute the optimum ILD and IMD distances for a corannulene dimer and a six lithium atoms doped (at the concave side) corannulene dimer using partial optimization calculations which provide estimates of the IMD (11.4 Å) and the ILD (6.5 Å) parameters for six lithium atoms doped (at the concave side) corannulene dimer, and of the ILD (4.8 Å) for corannulene dimer. To determine the optimum ILD value, only the z coordinates of the dimer are allowed to change, whereas only the x coordinates of dimer are allowed to change to investigate the optimum IMD value. In our MD simulations, the IMD is fixed to 11.0 Å for all the adsorbent systems, and additional values of ILD of 8.0 and 10.0 Å are used for a simple stack of two different lithium doped corannulene systems; and additional values of ILD of 6.0 and 8.0 Å for a simple stack of corannulene molecules. Such systems are chosen to investigate the potential H_2 uptake capacity, assuming that substitution of H with bulky alkyl function groups to the rim carbons, for example, t-butyl, isopropyl, [171]or bridging of lithium atoms doped corannulene molecules might increase the ILD.

2.3.4 Force fields

To study hydrogen at temperatures lower than 150 K, one must consider quantum effects on hydrogen adsorption.[77,170] However, at temperatures higher than 150 K, the quantum effects decrease significantly and may be reasonably neglected.[172] At temperatures in the 273 to 300 K range, it is expected that the adsorption of hydrogen molecules is mainly due to van der Waals interactions between hydrogen and corannulene. The pair interaction between hydrogen molecules is represented by a simple spherical 12-6 Lennard-Jones (LJ) potential, with ε = 2.97 meV, σ = 2.96 Å, [172]which is able to reproduce the vapor-liquid phase behavior of hydrogen gas over a broad range of conditions.[173] We have also tested a two-site model for H-H intermolecular interactions; [174] however, the model fails to reproduce the correct minima found in ab initio calculations for the potential energy of H_2.[175] Figure 2.3 shows the potential energy of two simple spherical hydrogen molecules with parameters of ε = 2.97 meV, σ = 2.96 Å.

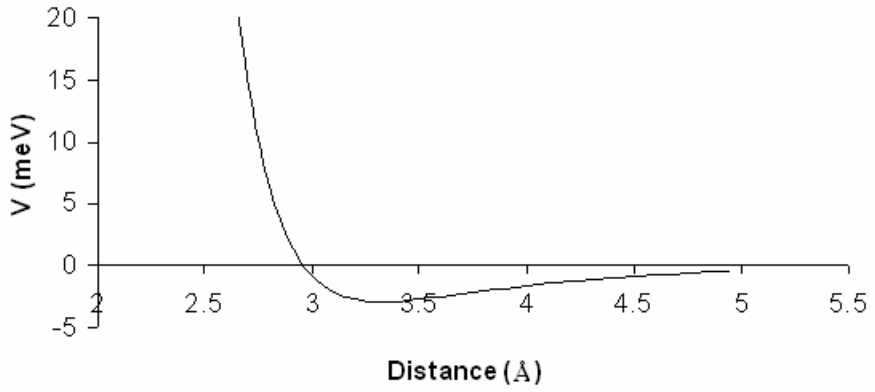

Figure 2.3. The potential energy of two simple spherical hydrogen molecules: ε = 2.97 meV, σ = 2.96 Å

Carbon nanotubes have been intensively studied for hydrogen storage both theoretically and experimentally. Studies suggest that carbon nanotubes have an advantage for hydrogen storage compared to other planar carbon materials, because of their curved structures offering additional attractive interaction sites to hydrogen molecules.[176] Corannulene is a bowl-shaped molecule and this curved structure can therefore be expected to increase the adsorption energy of hydrogen, similarly to carbon nanotubes. Thus, for the interaction potential between H_2 and the carbon atoms of corannulene, we use a one site 12-6 LJ potential, with parameters initially derived following the procedure described by Cheng et al, [177]to introduce curvature effects of the corannulene molecule. The curvature in the corannulene molecule could be compared with that of a cap of a 10 Å diameter carbon nanotube. Therefore, taking a value of 5 Å is for the corannulene radius, the parameters $\varepsilon_{C\text{-}H}$ = 3.35 meV, $\sigma_{C\text{-}H}$ = 2.78 Å are calculated for a curvature-dependent 2-site model. The interaction is then refitted to that of a single site model, yielding $\varepsilon_{C\text{-}H}$ = 2.52 meV, $\sigma_{C\text{-}H}$ = 2.95 Å. The potential energy of this result between C and one-site hydrogen molecule is shown in Figure 2.4 (a).

However, additional interactions need to be included since the corannulene molecule is polar with an dipole moment of 2.07 D determined experimentally, and of 2.15 D calculated at the MP2/6-31G(d) level,[178] although H_2 does not have a permanent dipole moment. The permanent dipole moment of corannulene creates an induced dipole moment on H_2, enhancing the adsorption of hydrogen molecules on the corannulene system. The general Debye formula for the mean potential energy due to induction by permanent dipoles is, [179]

$$\overline{\Gamma}_{ij} = -\frac{(\alpha_i \mu_j^2 + \alpha_j \mu_i^2)}{(4\pi\varepsilon_0)^2 r^6} \tag{2.4}$$

where i and j refer to hydrogen and corannulene, α is the molecular polarizability, and μ as the dipole moment. Polarizabilities are usually reported in units of volume using the relation,

$$\alpha' = \frac{\alpha}{4\pi\varepsilon_0} \tag{2.5}$$

Values of α' are 8.1×10^{-25} cm^3 for hydrogen [180] and 2.55×10^{-23} cm^3 for corannulene.[181] To calculate the mean potential energy, we first estimate the value of the induced dipole moment of hydrogen in the electric field created by corannulene. The field strength *E* around corannulene molecules is evaluated using the equation

$$E = \frac{\mu}{\alpha} \tag{2.6}$$

Equation (2.4) thus can be simplified to

$$\overline{\Gamma}_{ij} = -\frac{2236.04}{r^6}\ meV \tag{2.7}$$

This mean potential energy due to dipole and induced-dipole interactions is added to the L-J potential for C-H interactions. The overall potential of the sum of dipole-induced interaction and VDW interaction between C and one site hydrogen molecule is plotted in Figure 2.4 (b). Finally, the resulting potential energy is refitted yielding a new set of 12-6 interaction parameters that include the effects of curvature of the adsorbent molecule and the dipole and induced-dipole interactions, as in Figure 2.4 (c). As a result, the new

12-6 LJ parameters $\varepsilon_{C\text{-}H}$ = 4.02 meV and $\sigma_{C\text{-}H}$ = 2.80 Å are used in the reported MD simulations. Figure 2.4 shows the fitting results of VDW parameters for C-H interaction.

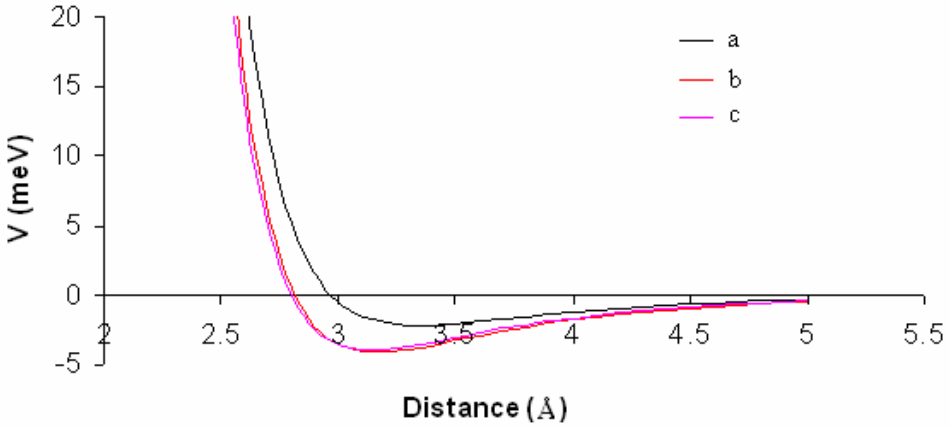

Figure 2.4. Fitting results of VDW parameters for C-H interaction. (a) potential energy of VDW interaction C and one-site hydrogen molecule, $\varepsilon_{C\text{-}H}$ = 2.52 meV, $\sigma_{C\text{-}H}$ = 2.95 Å; (b) sum of dipole-induced interaction and potential energy of VDW interaction C and one-site hydrogen molecule; (c) fitting of potential energy of VDW interaction C and one-site hydrogen molecule, $\varepsilon_{C\text{-}H}$ = 4.02 meV, $\sigma_{C\text{-}H}$ = 2.80 Å

Now we need to obtain the interaction between Li and one-site hydrogen molecule. The 12-6 LJ parameters for the Li-H pair are derived using published van der Waals parameters for Li atom in the form,

$$E_{vdw} = D_{IJ}\left\{-2\left[\frac{x_{IJ}}{x}\right]^{6} + \left[\frac{x_{IJ}}{x}\right]^{12}\right\} \tag{2.8}$$

where D_{Li}= 0.025 kcal/mol, and x = 2.451 Å.[182] The parameters are then refitted to the equivalent form,

$$E_{vdw} = 4\varepsilon\left\{\left[\frac{\sigma_{IJ}}{r}\right]^{12} - \left[\frac{\sigma_{IJ}}{r}\right]^{6}\right\} \quad (2.9)$$

with ε=0.0275 kcal/mol and σ=2.18 Å. The Lorentz-Berthelot mixing rules are applied to get the cross parameters $\varepsilon_{\text{Li-H}}$=1.87 meV and $\sigma_{\text{Li-H}}$=2.57 Å. For the dipole-induced interaction, we take the dipole moment of Li_3-$C_{20}H10$-Li_2 complex of 3.856 De calculated at the level of B3LYP/6-311G(d,p) and lithium polarizability of 2.43×10^{-23} cm^3.[183] An average pair interaction is calculated as:

$$\bar{\Gamma}_{ij} = -\frac{7759.74}{r^6}\ meV \quad (2.10)$$

With addition of the dipole induced interaction between Li and H, the non-bonded interaction parameters for Li-H used in Equation (2.9) are $\varepsilon_{\text{Li-H}}$ = 39.06 meV and $\sigma_{\text{Li-H}}$ = 2.00 Å. The fitting process and results are shown in Figure 2.5.

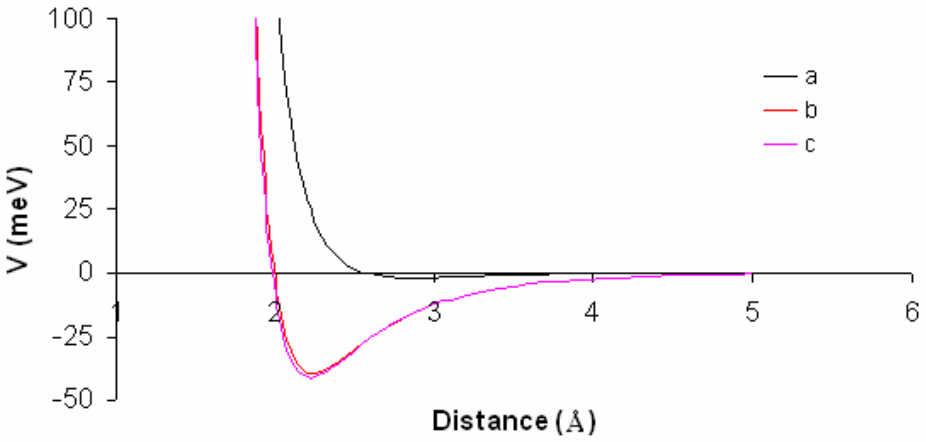

Figure 2.5. Fitting results of VDW parameters for Li-H interaction. (a) potential energy of VDW interaction Li and one-site hydrogen molecule, $\varepsilon_{\text{Li-H}}$ = 1.87 meV, $\sigma_{\text{Li-H}}$ = 2.95 Å; (b) sum of dipole-induced interaction and potential energy of VDW interaction Li and one-site hydrogen molecule; (c) fitting of potential energy of VDW interaction Li and one-site hydrogen molecule, $\varepsilon_{\text{Li-H}}$ = 39.06 meV, $\sigma_{\text{Li-H}}$ = 2.00 Å

CHAPTER III

AB INITIO/DFT STUDIES OF CORANNULENE AND LITHIUM ATOMS DOPED CORANNULENE SYSTEMS

3.1 Doping of lithium atoms on corannulene

3.1.1 Characterization of corannulene

Corannulene is a bowl-shape molecule with C_{5v} symmetry. There are three types of carbon in corannulene molecule. In this paper, the notation used is as follows. The outmost ten carbons bonding to one hydrogen each are donated as rim carbons (C_r), the innermost five carbons on the five-member ring as hub carbons (C_h); while the remaining five carbons connecting between rim carbon and hub carbon as "bridge" carbons (C_b). Figure 3.1 shows the optimized structure of corannulene at the level of B3LYP/6-311G(d,p). The calculation shows that rim carbon atoms posses more electron density than hub and "bridge" carbon atoms and corannulene is polar with the negative dipole moment at the end of the five-member ring. The dipole moment of corannulene is 2.18 D at the level of calculation, which is close to the experimental data of 2.07 D[184]. The structural information and Mulliken charge distribution of corannulene are shown in Table 3.1.

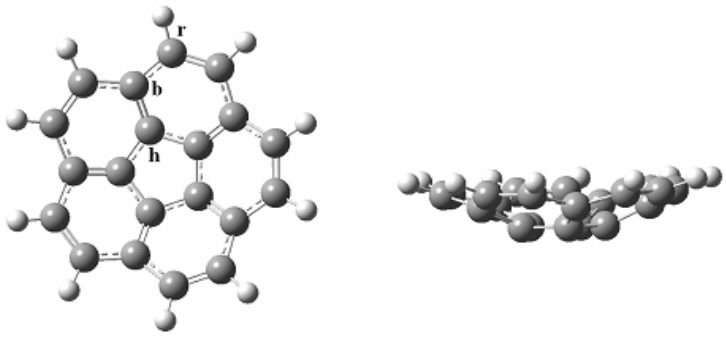

Figure 3.1. Optimized structure of corannulene at the level of B3LYP/6-311G(d,p)

Table 3.1: Structural parameters and Mulliken charge distribution in corannulene

atom	charge	atom pair	bond distance (Å)	atom group	bond angle (^{O})
C_h	-0.036	C_h-C_h	1.416	C_h- C_h-C_b	122.88
C_b	-0.004	C_h-C_b	1.383	C_h- C_b-C_r	114.43
C_r	-0.072	C_b-C_r	1.446	C_b- C_r-C_r	121.96
H	+0.092	C_r-C_r	1.396	C_r- C_b-C_r	129.78

3.1.2 Doping of lithium atom on corannulene

3.1.2.1 Doping of single lithium atom

Experimentally, ball milling has been proved to effectively increase the lithium doping concentration in carbon materials and this technique is ready to be extended to industrial scales.[185] Kang [186] found the stable complex of pyrene-Li_4 where the ratio of Li to C is 1:4. Deng et al. [109]found the most stable ratio of Li:C is 1:6 and 1:8 for Li-GIC at the equilibrium interlayer distance, while 1:3 for Li-PGS (Li pillared graphene sheet) for ILD > 8 Å.

In this study, we investigate the doping of different concentration of lithium atoms to corannulene molecule. We first study doping of single lithium ion/atom to

corannulene and confirm the method used is reliable. Then we study five and six lithium atoms doped on corannulene molecule, which brings the ratio of Li to C between 1:3 and 1:4, consistent with other groups' results.[109,186]

Recently, Kang [186] used density functional theory to study lithium – aromatic sandwich compounds, R-nLi-R, where R is benzene, naphthalene, pyrene. Lithium atom was preferentially adsorbed over the six-member ring, instead of over individual or pair carbon atoms. On a separate study, for a single Li ion, it was found that lithium cation was more energetically favorable binded over six-member ring than five-member ring, and it was more stable to bind on the convex side over six-member ring of corannulene than that of on the concave side over the six-member ring at the level of B3LYP/6-311G(d,p)//B3LYP/6-31G(d,p).[161] On this study, we want to investigate the favorable doping position of lithium atoms on the corannulene. With previous two studies, it is fair to assume that lithium atom would be more stable to dope over the six-member ring. But we need to find out on which side of the six-member ring, concave side or convex side. We dope either a single lithium atom or a single lithium ion on the concave/convex side over the six-member ring of corannulene at the level of B3LYP/6-31G(d,p), which brings to a total of combination of four systems. Table 3.2 shows the difference of the complexes of corannulene with lithium cation or lithium atom on the concave/convex side over the six-member ring. The data in table 3.2 indicate that for lithium ion, complex of lithium ion at convex side is more stable than at the concave side, which is in agreement with the result of Frash et al.[161] The result indicates that the level of theory we use for optimization is reliable. For lithium atom, however, the doping situation is

different. The complex with lithium atom at the concave side is more stable than at the convex side over the six-member ring. The complex with lithium atom at the concave side is -1.2 kcal/mol lower in the energy than that of at the convex side. The range of distance between Li ion/atom and C corresponds to the distance of Li ion/atom and C atoms of the six-member ring, where Li ion/atom is doped. The smallest value of distance is that of Li ion/atom to C_r and the largest value of distance corresponds to that of Li ion/atom to C_h. When Li ion or atom is doped on the concave side, the difference between the smallest and largest distance of Li-C is smaller than that of when Li ion or atom doped on the convex side. The difference is 0.027 Å for Li ion doped at the concave side, 0.033 Å for Li atom doped at the concave side. While, the difference increases to 0.151 Å for Li ion doped at the convex side, and 0.230 Å for Li atom doped on the convex side.

Table 3.2: Complexes of corannulene with lithium cation/atom at the level of B3LYP/6-31G(d,p)

Complex of corannulene	Li-C (Å)	Electronic energy (Hatrees)
Li^+ on the concave side of 6-member ring	2.282-2.309	-775.52514
Li^+ on the convex side of 6-member ring	2.293-2.444	-775.52700
Li on the concave side of 6-member ring	2.215-2.248	-775.68264
Li on the convex side of 6-member ring	2.140-2.374	-775.68073

3.1.2.2 Doping of multiple lithium atoms

For multiple lithium atoms, they can be doped either at concave side or at convex side, depending on the interactions between lithium atoms and corannulene molecule.

We first dope five lithium atoms on a single corannulene molecule at different positions, with choice of concave / convex side and six-member ring, then we study the sixth lithium doping on corannulene. In order to differentiate the different doping positions of lithium atoms doping, we use formula to Li_n-$C_{20}H_{10}$-Li_m to name the lithium atoms doped corannulene systems, while the sum of (n+m) means the total number of lithium atoms doped on each corannulene molecule, n the number of lithium atom on the concave side over the six-member ring, and m the number of lithium atom on the convex side of the six-member ring. For example, Li_3-$C_{20}H_{10}$-Li_2 is the complex that have three lithium atoms doped on the concave side, two lithium atoms on the convex side, and the total number of lithium atoms doped is five. Figure 3.2 show the different doping of five lithium atoms on corannulene at the level of B3LYP/6-31G(d,p), followed by the frequency calculation at the same level. Symbols and labels are all clear marked to make our discussion more clear. Considering the effect of charge transfer from lithium atom to carbon atoms and thus the repulsion between two lithium atoms, we only dope lithium atoms over the outer six-member rings on either side, and no lithium atom is doped over the five-member ring. With initial of all five lithium atoms doped at the same side, either the concave side or convex side, the optimized structures both become the same conformation, shown as in Figure 3.2 (a), with all five lithium atoms doped at the concave side over the six-member rings. This inversion of curvature of corannulene molecule regarding lithium atoms, which leads to the final configurations with lithium atoms located at the concave side of corannulene molecule, agrees with our previous calculation of the complex of single lithium atom doped on corannulene, which is

lithium atom energetically located at the concave side of corannulene over the six-member ring. Frequency calculations indicate that this complex is at local minima.

We then dope with two lithium atoms on one side and three lithium atoms on the other side, either with two lithium atoms on the concave side and three lithium atoms on the convex side, or with three lithium atoms on the concave side and two lithium atoms on the convex side. The results agree with previous studies. The energetically favorable optimized conformations contain more lithium atoms on the concave side, that is, three lithium atoms on the concave side and the other two lithium atoms on the convex side. In this conformation, five lithium atoms are more separated from each other and so the repulsion between lithium atoms decreases. It has lower energy than the conformation of five lithium atoms all doped at concave side. The comparison of the energy is shown in Table 3.3. From previous calculations, we see that energetically the concave side dopes more lithium atoms than the convex side does. The other relative structural information is also shown in Table 3.3.

The optimized conformations indicate that both the complexes of Li_5-$C_{20}H_{10}$ and Li_3-$C_{20}H_{10}$-Li_2 have symmetry of σ_v as shown in Figure 3.2. The symmetric plane can be pictured as the plane perpendicular to the plane of the paper and with the labeled 1Li atom on the symmetric plane in both configurations.

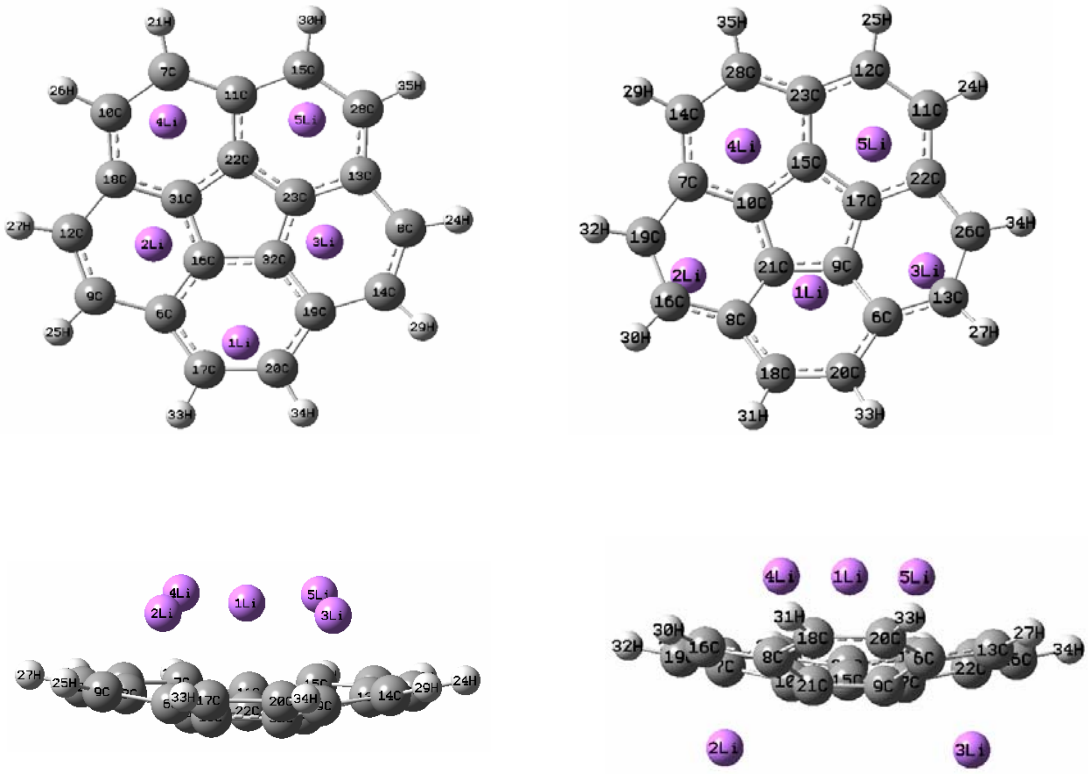

(a) (b)

Figure 3.2. Optimized conformations of corannulene with five lithium atoms doped at different positions at the level of B3LYP/6-31G(d,p). (a) five lithium atoms doped at concave side over six-member rings, Li_5-$C_{20}H_{10}$, (b) three lithium atoms doped at concave side and two at convex side over six-member rings, Li_3-$C_{20}H_{10}$-Li_2

From Table 3.3 we can see that charge transfer from lithium atoms to corannulene molecules, resulting positive charge on lithium atoms in both complexes of Li_5-$C_{20}H_{10}$ and Li_3-$C_{20}H_{10}$-Li_2. Overall, the total charge on lithium atoms at the complex of Li_3-$C_{20}H_{10}$-Li_2 is higher than that of at the complex of Li_5-$C_{20}H_{10}$. Thus, carbon atoms of corannulene possess more negative charge. Besides the charge distribution, we observe that lithium atoms each is generally closer to a six-member ring of corannulene in the complex of Li_3-$C_{20}H_{10}$-Li_2 that in the complex of Li_5-$C_{20}H_{10}$. For 1Li, 4Li and 5Li in the

complex of Li_5-$C_{20}H_{10}$, they are more close to rim carbon atoms, as we can see from the distance of Li-C shown in Table 3.3. Same labels of these three lithium atoms on the concave side of the complex of Li_3-$C_{20}H_{10}$-Li_2 are move closer to the center of six-member ring, where each lithium atom is doped. For 2Li and 3Li, they are also more closer to the six-member ring when doped at the convex side of corannulene complex Li_3-$C_{20}H_{10}$-Li_2 than that of the same labels on the concave side of corannulene complex Li_5-$C_{20}H_{10}$, although these two lithium atoms in the latter complex are located relatively at the center over the six-member ring, compared to in the complex of Li_3-$C_{20}H_{10}$-Li_2. Due to the fact that in the complex of Li_3-$C_{20}H_{10}$-Li_2, more charges transfer from lithium atoms to corannulene and closer distance of lithium atoms to the six-member ring where they are doped in general, the attraction interaction between lithium atoms and corannulene is stronger than in the complex of Li_5-$C_{20}H_{10}$. We can expect that complex Li_3-$C_{20}H_{10}$-Li_2 will be more stable than the complex Li_5-$C_{20}H_{10}$. This can be seen from the energy information of these two complexes, also shown in Table 3.3. The results of B3LYP/6-31G(d,p) show that Li_3-$C_{20}H_{10}$-Li_2 is about –4.00 kcal/mol stable than Li_5-$C_{20}H_{10}$ and the binding energy is –23.91 kcal/mol-Li in Li_3-$C_{20}H_{10}$-Li_2 and –23.11 kcal/mol-Li in Li_5-$C_{20}H_{10}$. The binding energy is calculated with the reference the total energies of isolated corannulene and n number of Li atoms, n is 5 in this case, as zero energy. The binding energy is calculated based on per mole lithium atom. The magnitude of the binding energies in both complexes indicate that these two complexes can be stable.

Table 3.3: Five lithium doped corannulene complexes structural information and electronic energy (Hatrees) and binding energy of per mole Li to corannuele (kcal/mol-Li) at the level of B3LYP/6-31G(d,p)

complex	Label of Li	Charge of Li	Distance Li-C *		
			Li-Cr	Li-Cb	Li-Ch
	1	0.316	2.145	2.650	3.070
Li_5-$C_{20}H_{10}$	2,3	0.139	2.226	2.299	2.319
			2.242	2.332	2.337
	4,5	0.251	2.143	2.511	2.823
			2.165	2.549	2.859
	1	0.451	2.205	2.291	2.363
Li_3-$C_{20}H_{10}$-Li_2	2,3	0.479	2.126	2.268	2.175
			2.185	2.532	2.409
	4,5	0.223	2.125	2.252	2.424
			2.221	2.469	2.506

* each value represents two pairs of the distance of Li-C in σ_v symmetric complexes

	Electronic Eenergy	Binding Energy
Li	-7.49098	
$C_{20}H_{10}$	-768.16483	
Li_5-$C_{20}H_{10}$	-805.80384	-23.11
Li_3-$C_{20}H_{10}$-Li_2	-805.81022	-23.91

We then study possible doping conformations of six lithium atoms on corannulene based on the previous studies of five lithium atoms doped corannulene complexes, Li_5-$C_{20}H_{10}$ and Li_3-$C_{20}H_{10}$-Li_2. Same procedure has been followed as in previous section. Figure 3.3 shows the conformations of doping of lithium atoms on four different combinations. Take the complex of Li_5-$C_{20}H_{10}$, we can doped the sixth lithium atom on the concave side or the convex side. These two conformations are showed in Figure 3.3 (a) and (b). With all six lithium atoms doped on the same side, forming the complex Li_6-$C_{20}H_{10}$, the conformation becomes with first five lithium atoms doped over six-member ring on the concave side, and the sixth lithium atom in the middle over these five lithium

atoms. With the sixth lithium atom doped at the convex side, we obtain Li_5-$C_{20}H_{10}$-Li complex. The complex Li_6-$C_{20}H_{10}$ and Li_5-$C_{20}H_{10}$-Li both have the symmetry of σ_v, with labeled 1Li and 6Li on the symmetry plane. The last two complexes we dope is that first five lithium atoms are doped as the same way in the complex Li_3-$C_{20}H_{10}$-Li_2 and the sixth lithium atom is doped either on the concave side or the convex side over the six-member ring where the other labeled Li is doped on the opposite side of the six-member ring, forming the complexes Li_4-$C_{20}H_{10}$-Li_2 and Li_3-$C_{20}H_{10}$-Li_3. The complexes Li_4-$C_{20}H_{10}$-Li_2 and Li_3-$C_{20}H_{10}$-Li_3 are no longer symmetric as other complexes after the optimization. Partial structural information, including the charge distribution of lithium atoms and distance between lithium atom to carbon of the six-member ring where lithium atom is doped, and the related energies are shown in Table 3.4 as well.

Frequency calculations at the level of B3LYP/6-31G(d,p) on the optimized structures of these complexes also indicate that complexes are at local minima, while the complex Li_6-$C_{20}H_{10}$ is -9.00 kcal/mol more stable than the complex Li_3-$C_{20}H_{10}$-Li_3. The binding energy per mole lithium is -25.03 and -23.53 kcal/mol-Li for the complex Li_6-$C_{20}H_{10}$ and Li_3-$C_{20}H_{10}$-Li_3, respectively. Same reference state is used to calculate binding energy, with n as 6 in this case. Compared to binding energies in the complexes of five lithium atoms doped, which we discussed previously, we see that binding energies per mole lithium are similar as those in five lithium doped complexes. Again, the relatively large binding energies might indicate the stable lithium doping concentration on corannulene, with the ratio of Li:C in between 1:4 and 1:3. The lithium doping concentration is agreed with other groups' results.[109,186]

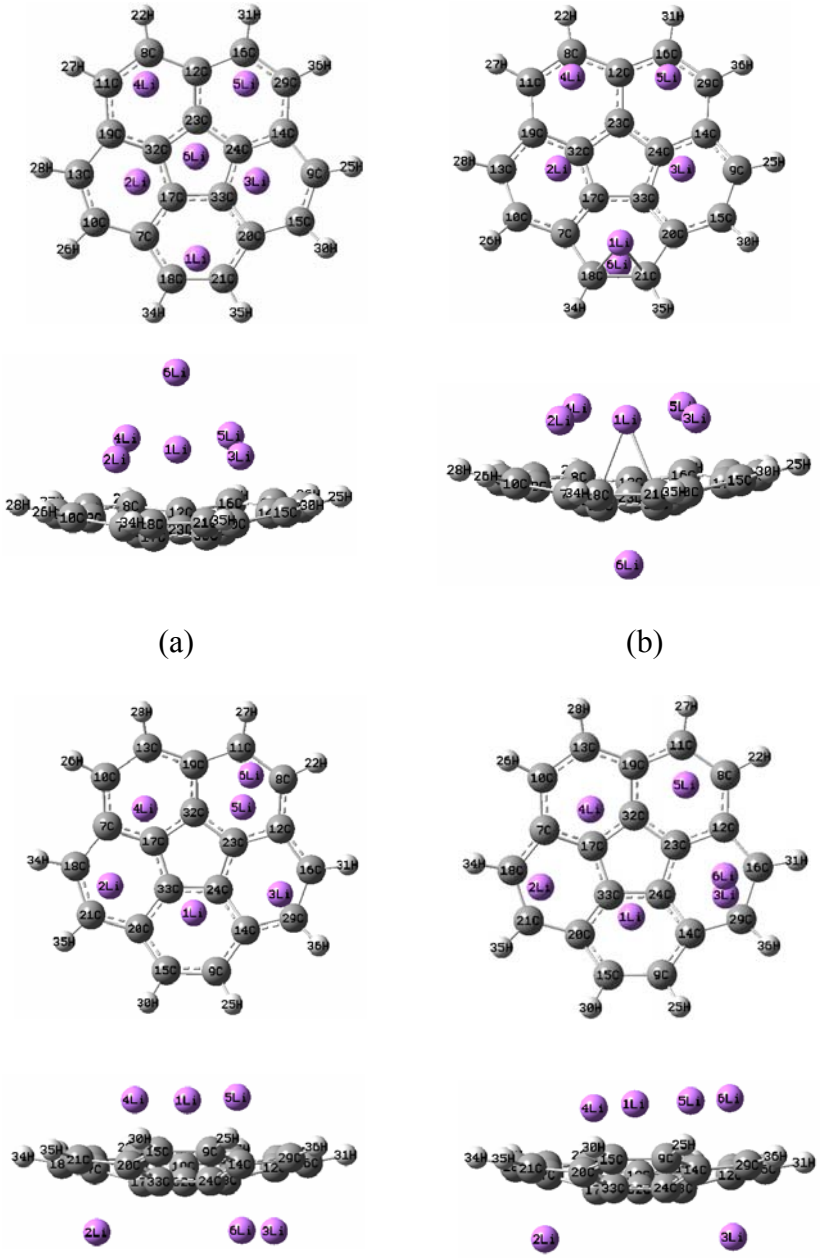

(a) (b)

(c) (d)

Figure 3.3. Optimized conformations of corannulene with six lithium atoms doped at different positions at the level of B3LYP/6-31G(d,p). (a) six lithium atoms doped at concave side, Li_6-$C_{20}H_{10}$ (b) five lithium atoms doped at concave side and one lithium doped at the convex side, Li_5-$C_{20}H_{10}$-Li (c) four lithium atoms doped at concave side and two at convex side, Li_4-$C_{20}H_{10}$-Li_2 (d) three lithium atoms doped at concave side and three at convex side, Li_3-$C_{20}H_{10}$-Li_3

Table 3.4: Six lithium doped corannulene complexes structural information and electronic energy (Hatrees) and binding energy of per mole Li to corannulene (kcal/mol-Li) at the level of B3LYP/6-31G(d,p)

complex	Label of Li	Charge of Li	Distance Li-C *		
			Li-Cr	Li-Cb	Li-Ch
Li_6-$C_{20}H_{10}$	1	0.220	2.160	2.674	3.161
	2,3	0.311	2.188	2.274	2.338
			2.204	2.306	2.355
	4,5	0.258	2.136	2.545	2.969
			2.180	2.638	3.020
	6	-0.230			
Li_5-$C_{20}H_{10}$-Li	1	0.454	2.099	2.565	3.052
	2,3	0.137	2.173	2.310	2.434
			2.215	2.398	2.442
	4,5	0.205	2.070	2.458	2.749
			2.149	2.485	2.788
	6	0.511	2.149	2.417	2.250
Li_4-$C_{20}H_{10}$-Li_2	1	0.258	2.215	2.329	2.444
			2.275	2.449	2.517
	2	0.470	2.137	2.274	2.207
			2.192	2.505	2.326
	3	0.453	2.123	2.360	2.240
			2.126	2.429	2.313
	4	0.147	2.227	2.227	2.371
			2.371	2.546	2.509
	5	0.048	2.176	2.508	2.810
			2.181	2.520	2.836
	6	0.493	2.149	2.518	2.915
			2.157	2.585	2.981
Li_3-$C_{20}H_{10}$-Li_3	1	0.301	2.321	2.350	2.360
			2.366	2.455	2.416
	2	0.453	2.165	2.313,2.	2.206
			2.215	499	2.328
	3	0.198	2.134	2.256	2.236
			2.249	2.626	2.460
	4	0.145	2.169	2.290	2.504
			2.275	2.544	2.645
	5	0.349	2.167	2.314	2.568
			2.328	2.615	2.749
	6	0.386	2.169	2.396	2.287
			2.170	2.409	2.321

Table 3.4 Continued

	Electronic Energy	Binding Energy
Li	-7.49098	
$C_{20}H_{10}$	-768.16483	
Li_6-$C_{20}H_{10}$	-813.35008	-25.03
Li_5-$C_{20}H_{10}$-Li	-813.34599	-24.61
Li_4-$C_{20}H_{10}$-Li_2	-813.34763	-24.78
Li_3-$C_{20}H_{10}$-Li_3	-813.33568	-23.53

* each value in σ_v symmetric complexes, Li_6-$C_{20}H_{10}$ and Li_5-$C_{20}H_{10}$-Li, represents two pairs of the distance of Li-C; while in non-symmetric complexes, Li_4-$C_{20}H_{10}$-Li_2 and Li_3-$C_{20}H_{10}$-Li_3, only represents a single pair of the distance of Li-C.

3.2 Optimization of corannulene dimer

Among the various types of nonbonded interactions between molecules, π···π interactions have been realized as the key roles in molecular recognition, crystal packing, self-assembly. Zhao and Truhlar [187] recently used multicoefficient extrapolated density functional theory to study aromatic π···π interactions of benzene dimer and obtained three conformers of benzene dimer, sandwich (S), T-shaped (T), and parallel-displaced (PD). When comes to corannulene, it is not surprising that π···π interactions also play important roles in molecular self-assembly, because of the 5 six-member ring of corannulene molecule. Here, we use DFT to study the geometry configurations of corannulene dimer at the level of B3LYP/6-311G(d,p). The optimizations yield sandwich and T-shaped conformers of corannulene dimer, as shown in Figure 3.4. The T-shaped conformer is the global minimum, and the sandwich is a local minimum, higher in 0.08 eV with respect to the T-shaped conformer. These structures somehow resemble those found for the benzene dimer by Zhao and Truhlar[187], although we do not find an additional dimer in parallel-displaced arrangement for corannulene dimer.

Another point that is worthy to be mentioned is the separation in sandwich corannulene dimer. The optimization yields 4.80 Å between these two corannulene molecules, which is significantly larger than separation in graphite layers of 3.45 Å. This is very interesting when corannulene is used for hydrogen adsorption. Larger separation indicates that corannulene has more space available for hydrogen molecules to be adsorbed, compared to graphite, if we assume corannulene can arrangement as sandwich structure at the conditions of desired. Later in this project, we will discuss hydrogen adsorption in corannulene materials, where two arrangements are used as adsorbents.

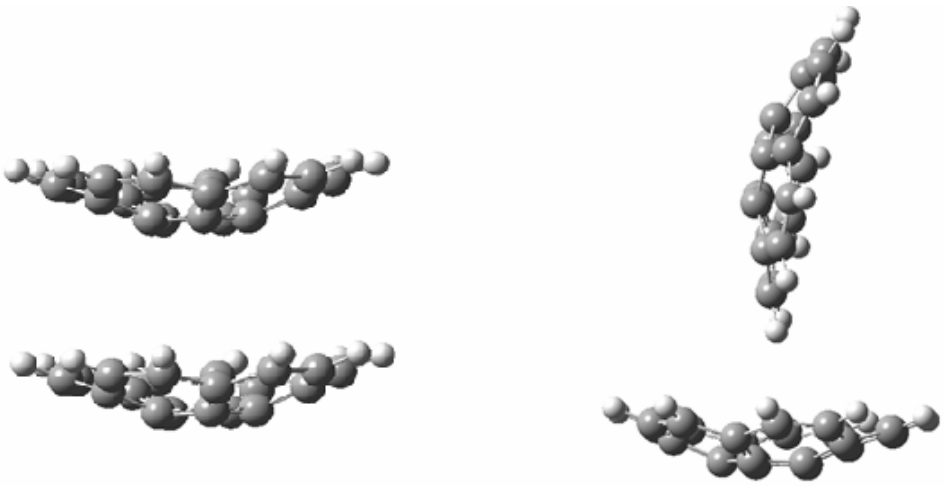

(a) (b)

Figure 3.4. Conformations of corannulene dimer: (a) sandwich; (b) T-shaped

3.3 AM1 studies of corannulene clusters

With the idea of sandwich and T-shaped corannulene dimer, we investigate the possible conformations of clusters of more corannulene molecules. Due to the limitation of the computation cost, we choose semi-empirical method, AM1 (Austin Model 1),[188] instead of DFT calculations. Optimization of 4 corannulene molecules arranged in sandwich conformation fails to converge. 4, 8, and 12 corannulene molecules arranged in T-shaped conformation converge successfully. Figure 3.5 show the structures of these 4, 8, and 12 corannulene molecular systems, with every two corannulene in T-shaped. In the structure of $(C_{20}H_{10})_4$ every two neighbor corannulene molecules are well assembled in T-shaped, as we observed in previous DFT study. In the $(C_{20}H_{10})_8$ and $(C_{20}H_{10})_{12}$ systems, deformed T-shaped conformers are observed. Instead of perpendicular of two neighbor corannulene molecules, every two neighbor corannulene molecules are inclined one to the other in certain angle.

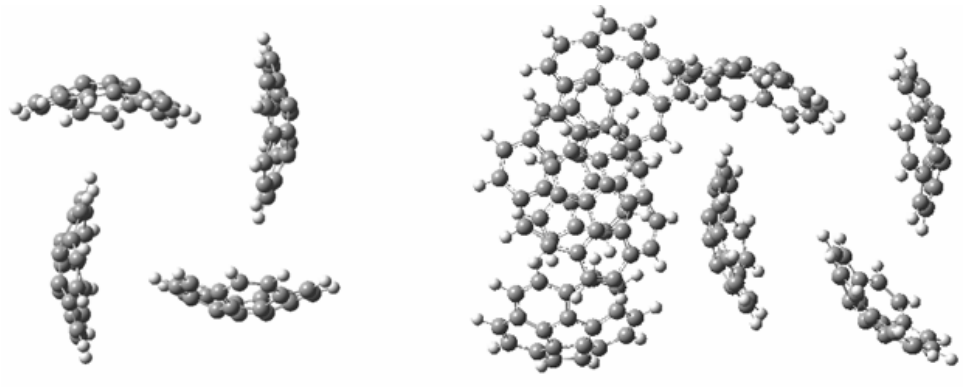

(a) (b)

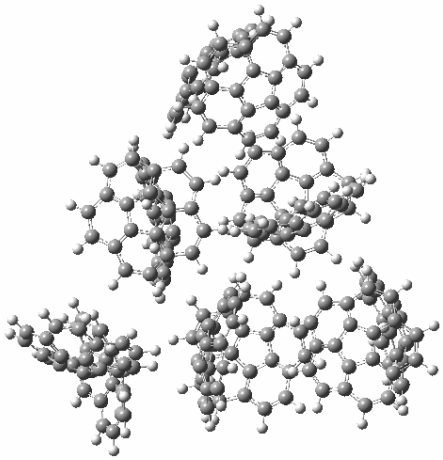

(c)

Figure 3.5. Optimized structures of n corannulene molecules using AM1. (a) n=4; (b) n=8; (c) n=12

Optimizations of lithium atom doping on corannulene molecule are also investigated with AM1. We study doping of a single lithium atom, five lithium atoms, and six lithium atoms on corannulene molecule. Unfortunately, these studies failed to agree with doping of lithium atom(s) on corannulene using B3LYP/6-31G(d). Optimization involving metal atoms using AM1 is not reliable. Further optimization for

the systems containing more than two lithium atoms doped corannulene molecules are not considered in this project.

3.4 Partial optimization of Li_6-$C_{20}H_{10}$ dimer

There are two reasons that we only perform partial optimization for lithium atoms doped corannulene complex. One is due to the limitation of the expense computational cost. More importantly, as we discuss previously, we assume a simple stack of lithium atoms doped corannulene complex when comes to the study of hydrogen adsorption. In such simple stack configuration of adsorbent molecules, ILD and IMD are two important parameters that we are looking for. The partial optimizations for the values of ILD and IMD are performed at the level of B3LYP/6-31G. For value of ILD, only z-coordinates of the two overlap Li_6-$C_{20}H_{10}$ complexes are allowed to change and the calculation yields the value of 6.5 Å, the figure is shown in Figure 3.6 (a). It is found that binding energy of the dimer is -18.9 kcal/mol. For value of IMD, only x-coordinates of the two parallel Li_6-$C_{20}H_{10}$ complexes are allowed to change and the calculation yields the value of 11.4 Å, as shown in Figure 3.6 (b). The values of ILD and IMD provide a reference of the arrangement of adsorbent molecules in our molecular dynamics simulations.

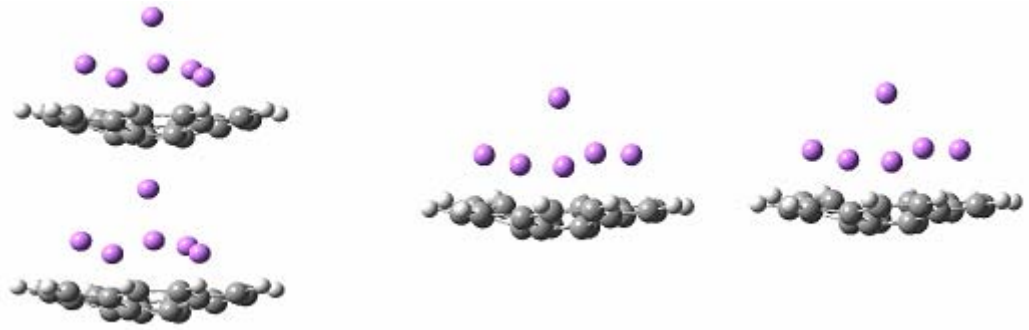

(a) (b)

Figure 3.6. ILD and IMD of two Li_6-$C_{20}H_{10}$ complexes

3.5 Adsorption of hydrogen

3.5.1 Potential surface scan

Ab initio/DFT calculations are performed for the adsorption of hydrogen on corannulene and lithium diped corannulene complexes. Studies of adsorption of hydrogen molecule on lithium doped corannulene complexes are only performed on the energetically favorable doping complex of each doping concentration, i.e., on the complex Li_6-$C_{20}H_{10}$ for six lithium atoms doped corannulene, and the complex Li_3-$C_{20}H_{10}$-Li_2 for five lithium atoms doped corannulene. In this section, we perform three different studies. First, we investigate the potential energy surface of the systems when hydrogen molecule approaches corannulene or lithium atoms doped corannulene complexes, using DFT calculations. Then, we study interaction of hydrogen molecule with adsorbent molecule with MP2/6-31G(d,p), to account the weak VDW interactions. For hydrogen in corannulene system, two orientations of hydrogen are used and full geometry optimizations are performed. For hydrogen in two lithium atoms doped

corannulene complexes, only single point calculations are performed, due to the expensive computation cost. Last, we use DFT method to study adsorption of 18 hydrogen molecules on Li_3-$C_{20}H_{10}$-Li_2.

Figure 3.7 shows the different approaches of hydrogen molecule to corannulene, Li_6-$C_{20}H_{10}$ and Li_3-$C_{20}H_{10}$-Li_2 complex. These approaches include hydrogen molecule to the center of five-member ring from concave side of corannulene (path a), hydrogen molecule to the center of five-member ring from convex side of corannulene (path b), hydrogen molecule to the center of six-member ring from concave side of corannulene (path c), hydrogen molecule to the center of six-member ring from convex side of corannulene (path d), hydrogen molecule to the top lithium of Li_6-$C_{20}H_{10}$ complex (path e), and hydrogen molecule to one of lithium on the convex side of Li_3-$C_{20}H_{10}$-Li_2 complex (path f). The molecular structures of corannulene, Li_6-$C_{20}H_{10}$ complex, and Li_3-$C_{20}H_{10}$-Li_2 complex are the optimized results at the level of B3LYP/6-31G(d,p) and the whole molecular structures are kept fixed during the potential energy surface scan. The potential energy surfaces of these different approaches are shown in Figure 3.8. When hydrogen molecule approaches to corannulene, not an attractive interaction between hydrogen and corannulene molecule is detected at this level of theory for all these four different approaches. The most repulsive interaction appears when hydrogen molecule approaches from the convex side to the six-member ring of corannulene, path d, and the least repulsive when approached from the concave side to the center five-member ring, path a. However, when a hydrogen molecule approaches Li_6-$C_{20}H_{10}$ or Li_3-$C_{20}H_{10}$-Li_2 complexes, an clear and relatively strong attractive interaction between

H_2 and the lithium atom doped complex is shown in Figures 3.8 (e) and (f), which hydrogen molecule approached to the labeled 6Li of the complex Li_6-$C_{20}H_{10}$ and the labeled 2Li (or 3Li) of the complex Li_3-$C_{20}H_{10}$-Li_2, respectively. The strongest attraction appears when the center of hydrogen molecule is 2.47 Å from corresponding lithium atom and the attraction energies were -0.47 and -2.06 kcal/mol with complex Li_6-$C_{20}H_{10}$ and Li_3-$C_{20}H_{10}$-Li_2, respectively. The attractive interaction between hydrogen molecule and complex Li_6-$C_{20}H_{10}$ or Li_3-$C_{20}H_{10}$-Li_2 confirms that doping of lithium enhances the interaction between hydrogen molecule and adsorbent molecule, compared to the repulsive interaction between hydrogen molecule and undoped adsorbent molecule. The enhanced interaction between hydrogen molecule and lithium atoms doped corannulene complexes, and together with the more available space due to the increasing ILD caused by lithium doping, are the reasons that hydrogen uptake capacity in higher in lithium atoms doped corannulene systems, as will be discussed in the coming sections.

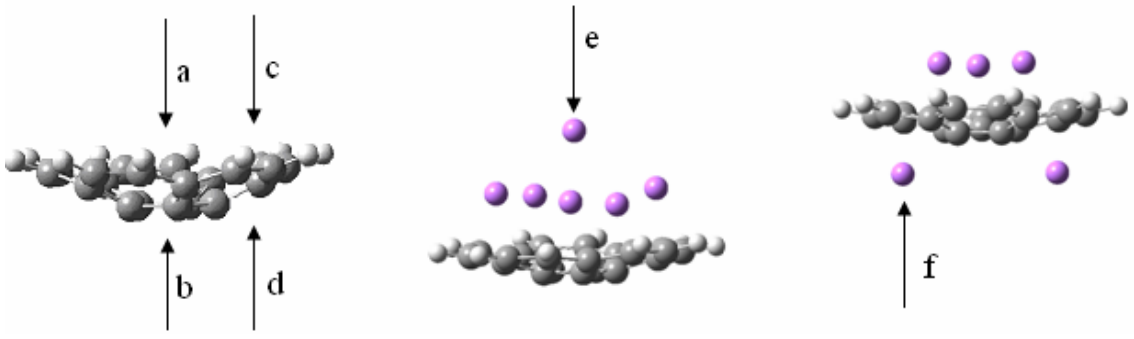

Figure 3.7. Indication of approaches of hydrogen molecule to different adsorbent molecule

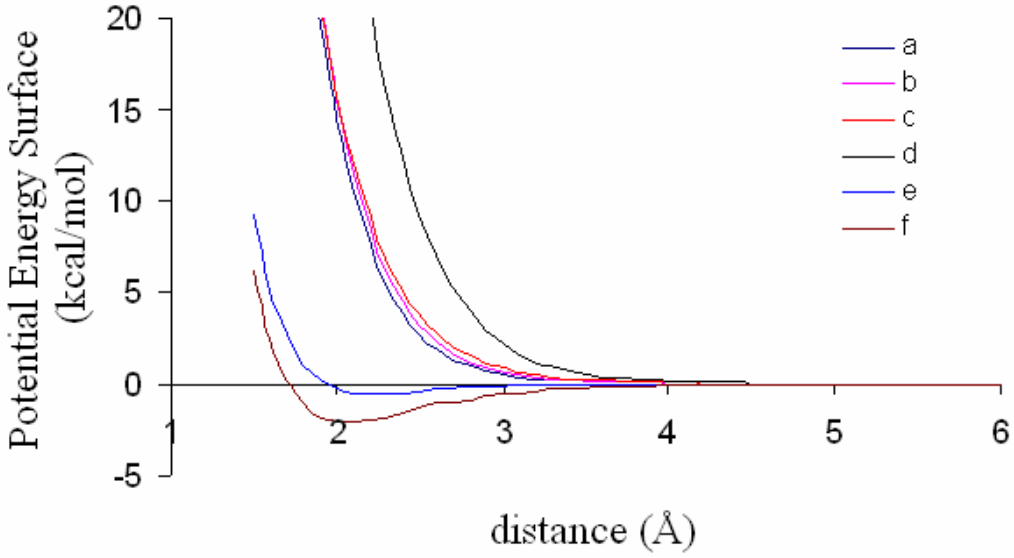

Figure 3.8. Potential energy surface of H_2 approaching to corannulene and lithium-doped corannulene at the level of B3LYP/6-311G(d,p). In each curve H_2 approaches corannulene at: (a) the center five-member ring at the concave side, (b) the center five-member ring at the convex side, (c) the center of a six-member ring at the concave side, (d) the center of a six-member ring at the convex side, (e) the top Li atom in Li_6-$C_{20}H_{10}$, (f) the Li atom on the convex side in Li_3-$C_{20}H_{10}$-Li_2

3.5.2 Single point calculations of binding energy with MP2 theory

Scanlon et al. [189] calculated the binding energies of hydrogen adsorption via physisorption on corannulene. Geometry optimization of a single hydrogen molecule on the concave side and convex side of corannulene with MP2(full)/6-31G(d) yielded binding energies of -0.94 and -0.83 kcal/mol for hydrogen molecule on the concave side and the convex side, respectively. Single point calculation at higher level with MP2(full)/6-311++G(3df,2p) at the optimized geometries with MP2(full)/g-31G(d)

yielded -2.81 and -1.38 kcal/mol, respectively. Okamoto [176] calculated the potential energy curve of corannulene-H_2 by using MP2 with the 6-31G(d) basis set for corannulene and the 6-311G(d,2p) basis set for H_2 molecule and obtained 3.05 kcal/mol of binding energy with H_2 molecule adsorbed on the concave side of the corannulene. Geometry optimization of hydrogen molecule on the concave side of corannulene at lower level of B3LYP/6-311G(d,p) does not yield a negative binding energy as obtained with MP2 calculations.

Here, we study the interaction of hydrogen molecule with corannulene molecule using MP2/6-31G(d,p). Figure 3.9 show the top view and side view of the optimized structures of H_2-$C_{20}H_{10}$ systems, one with end-on hydrogen adsorbed (Figure 3.9 (a)), and the other with head-on hydrogen adsorbed (Figure 3.9 (b)). At the same level of method, adsorption of hydrogen on other position, such as six-member ring, C_r, C_h, C_b, yield higher energy than adsorption of hydrogen on five-member ring, both for head-on and end-on orientation. Considering the length of H-H bond of 0.74 Å, in the head-on orientation, the distance from the center of mass of hydrogen molecule to the center of the five-member ring is 3.01 Å, which equals to the sum of 2.64 Å and half of H-H bond of 0.74 Å. This distance is same as the distance from the center of mass of hydrogen molecule in the end-on orientation to the center of the five-member ring, as shown in Figure 3.9 (a). But one hydrogen atom in the head-on orientation is much closer to center of the five-member ring and the distance is 2.64 Å. In end-on orientation, both hydrogen atoms have zero charge; while in head-on orientation, the hydrogen close to five-member ring has charge of +0.014 and the other hydrogen on the top has charge of

–0.015. The binding energies of hydrogen molecule to corannulene are –1.13 kcal/mol and –1.24 kcal/mol for end-on orientation and head-on orientation, respectively. Adsorption of hydrogen in head-on orientation is more stable. This is in agreement with Scanlon et al. studies, where single or multiple hydrogen molecules are all adsorbed to corannulene in head-on orientation.

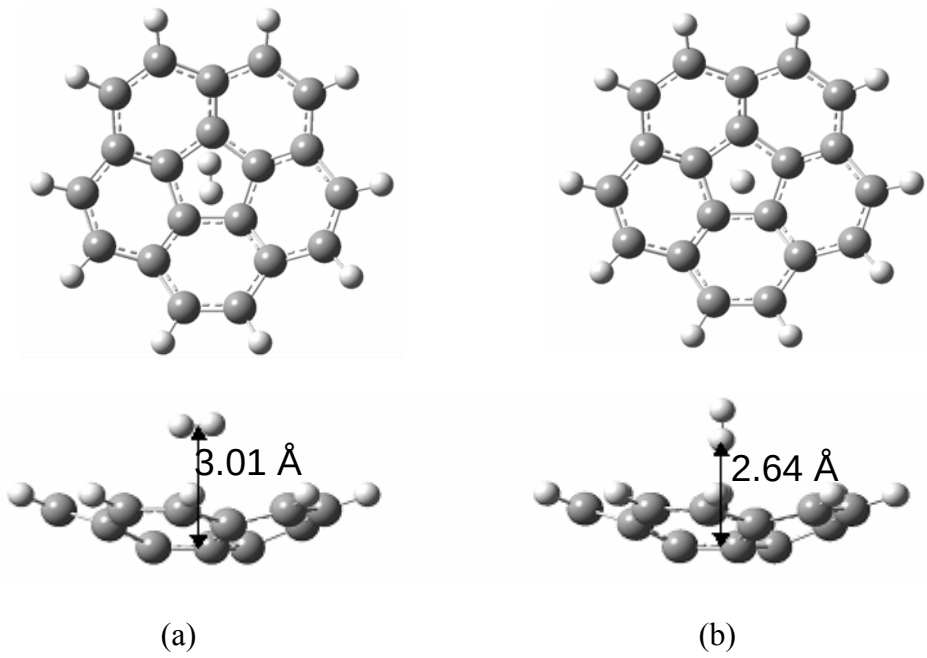

Figure 3.9. Adsorption of hydrogen molecule on corannulene, MP2/6-31G(d,p). (a) end-on orientation; (b) head-on orientation

Figure 3.10 shows the structures of hydrogen molecule with these two lithium-atoms doped complexes at the most attractive point on the potential surface curves in Figure 3.8, where the closer distance of hydrogen atom to corresponding lithium is 2.10Å (this corresponds to a distance of 2.47 Å from the center of mass of hydrogen

molecule to the lithium atom where hydrogen molecule is adsorbed). In order to account for weak van der Waals forces that are responsible for the hydrogen molecule/lithium doped corannulene complex interaction we use second order Moller Plesset perturbation theory to calculate the single point calculation of hydrogen molecule with these two complexes individually with the basis set of 6-31G(d,p). Calculations of the single point energy yield the binding energies of -1.83 and -2.82 kcal/mol for H_2-(Li_6-$C_{20}H_{10}$) system and H_2-(Li_3-$C_{20}H_{10}$-Li_2) system, respectively, as shown in Table 3.5. Compared to the binding energies of hydrogen molecule adsorbed on the center five-member ring of corannulene molecule, binding energies increase quite much, especially in the H_2-(Li_3-$C_{20}H_{10}$-Li_2) system, where binding energy is more than double of that in the H_2-($C_{20}H_{10}$) system. The interaction is indeed stronger between of hydrogen and lithium atom than between of hydrogen and carbon atom according to the value of binding energies. As a result, this enhanced binding energy between hydrogen molecule and lithium atom doped complexes results higher hydrogen uptake capacity, as we will discuss in later sections.

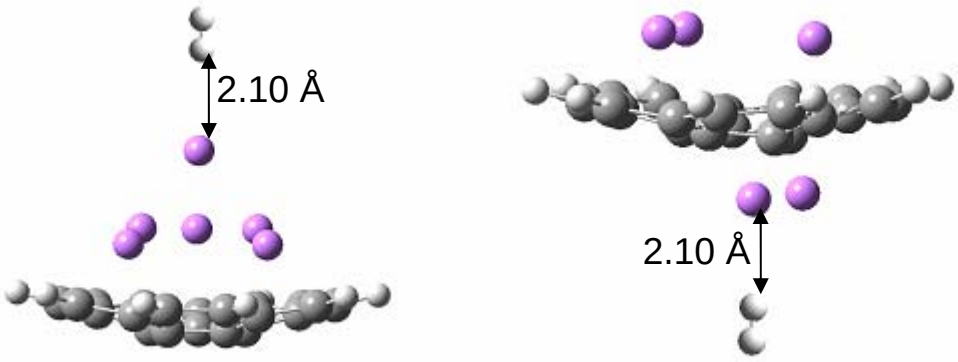

(a) (b)

Figure 3.10. The structures of hydrogen molecule with different lithium atom doped corannulene complexes. (a) complex Li_6-$C_{20}H_{10}$ (b) complex Li_3-$C_{20}H_{10}$-Li_2

Table 3.5: Hydrogen adsorption via physisorption on lithium doped complexes. Binding energies (kcal/mol) are calculated doing a single point calculation with MP2/6-31G(d,p) on the geometries of such systems on the lowest potential surface curves, corresponding to curves on Figure 3.8 (e) and (f)

	Electronic Energy	Binding Energy
H_2	-1.15759	
Li_6-$C_{20}H_{10}$	-810.63407	
Li_3-$C_{20}H_{10}$-Li_2	-803.18090	
H_2-(Li_6-$C_{20}H_{10}$)	-811.79457	-1.83
H_2-(Li_3-$C_{20}H_{10}$-Li_2)	-804.34299	-2.82

3.5.3 Adsorption of multiple hydrogen on Li_3-$C_{20}H_{10}$-Li_2

From previous study, we found that binding of hydrogen molecule to lithium atom selected was larger in Li_3-$C_{20}H_{10}$-Li_2 than in Li_6-$C_{20}H_{10}$. Here, we want to study adsorption of multiple hydrogen molecules. It will be interesting to find out the maximum number of hydrogen molecules that can be doped. We choose Li_3-$C_{20}H_{10}$-Li_2 complex and a total of 18 hydrogen molecules, with 10 molecules on the concave side

and 8 molecules on the convex side. Due to the computation cost, we use DFT method at the level of B3LYP/6-31G(d,p) to study interaction of multiple hydrogen molecules on adsorbent. The calculation yields a total of –11.30 kcal/mol for the system of 18 hydrogen molecules and Li_3-$C_{20}H_{10}$-Li_2 complex. By carefully examination on the optimized geometry of the system, as shown in Figure 3.11, we find 16 of 18 hydrogen molecules are adsorbed on the first shell around Li_3-$C_{20}H_{10}$-Li_2 complex, among these 16 hydrogen molecules, 8 on the concave side, and the other 8 on the convex side. If we calculate the binding energy based on 16 adsorbed molecules, the value is –0.71 kcal/mol-H_2. On the two lithium atoms on the convex side, 6 of 8 hydrogen molecules are surrounded around on lithium atoms. The distance between hydrogen molecules and Li_3-$C_{20}H_{10}$-Li_2 complex is in the range of 2.14-2.42 Å, which is in consistent with previously study of the potential energy surface scan of hydrogen molecule on Li_3-$C_{20}H_{10}$-Li_2 complex. On the concave side, it also has 6 hydrogen molecules adsorbed on three lithium atoms. Most of hydrogen molecules adsorbed on lithium atoms. For each lithium atom, up to 3 hydrogen molecules can be adsorbed. Also, we notice that hydrogen molecules are in head-on orientation adsorbed to the complex.

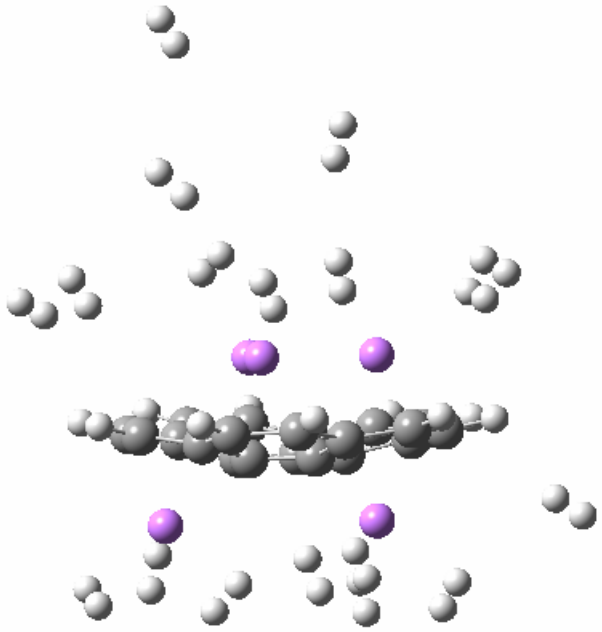

Figure 3.11. Optimization geometry of 18 hydrogen molecules with Li_3-$C_{20}H_{10}$-Li_2 complex at B3LYP/6-31G(d,p)

3.6 Conclusions

Corannulene molecule is a bowl-shape molecule and has a permanent dipole moment. The features of bowl-shape structure and permanent dipole moment provide the potential advantages as hydrogen storage material, with enhanced intermolecular attraction to hydrogen molecules. Doping of lithium atom on carbon materials is stable through the interaction of lithium atom with carbon atoms, due to the charge transfer from lithium atom to carbon atoms. The energetically favorable site of doping of single lithium atom on corannulene is over the six-member ring on the concave side. For doping of multiple lithium atoms on corannulene, the energetically favorable configuration of doping complex has more lithium atoms on the concave side than on the

convex side. Complexes of Li_6-$C_{20}H_{10}$ and Li_3-$C_{20}H_{10}$-Li_2 are two most stable configurations of six and five lithium atoms doped systems, calculated by B3LYP/6-31G(d,p).

Potential surface scan of hydrogen molecule approaching to corannulene and lithium atoms doped complexes, at the level of B3LYP/6-311G(d,p), indicate that lithium atoms doped complexes are more attractive to hydrogen molecules. Based on these potential surface scans, binding energies calculated by single point energy with MP2/6-31G(d,p) of these systems show doping of lithium atoms increase the interaction between hydrogen and lithium atoms doped corannulene complexes. Adsorption of multiple hydrogen on Li_3-$C_{20}H_{10}$-Li_2 indicate that each lithium atom can adsorb three hydrogen molecules.

CHAPTER IV

MD SIMULATIONS OF HYDROGEN ADSORPTION ON CORANNULENE SYSTEMS

4.1 Hydrogen adsorption on crystalline corannulene

4.1.1 Crystalline structure of corannulene

The first study of hydrogen adsorption focuses on crystalline corannulene systems at different temperatures and pressures. Figure 4.1 shows the crystalline cell of corannulene, containing 32 molecules with every two molecules arranged in T-shaped conformer. For adsorption of hydrogen molecules, these 32 corannulene molecules are put at the bottom of a simulation cell with dimensions 26.520 × 23.718 × c $Å^3$, and an angle $\beta = 120.69^o$. Hydrogen molecules are all randomly distributed on the gas phase above these corannulene adsorbents. The parameter c used is decided by the predicted desirable gas phase pressure and the temperature of interest. The temperatures of 273 K and 300 K, and pressure of between 50 bar and up to 250 bar are studied for the adsorption. As simulation starts, hydrogen molecules in the gas phase begin to diffuse and get adsorbed on corannulene adsorbent. The simulation process during the production period, the last 500 ps, is recorded in the trajectory file. The evaluation of hydrogen uptake and gas phase pressure are based on average value of the whole trajectory file.

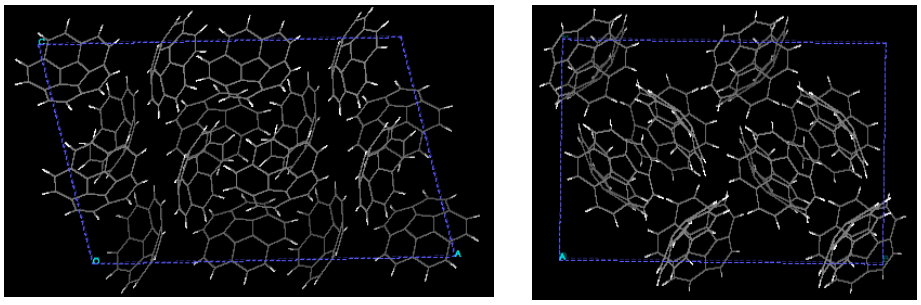

Figure 4.1. Crystalline structure of corannulene, containing 32 molecules

4.1.2 Hydrogen adsorption

Figure 4.2 shows the hydrogen uptake on crystalline corannulene at different temperatures as a function of the gas phase pressure. Plot a shows hydrogen adsorption at 300 K and plot b at 273 K. Over all, the predicted H_2 adsorption shows a linear relation with pressure in the range of pressure studied, and the amount of H_2 adsorbed is higher at the lower temperature 273 K than at 300K. At the temperature of 300 K, the hydrogen uptake capacity is 0.55 wt% at 50 bar. It increases to 1.25 wt% at 170 bar, and 1.45 wt% at 215 bar. At the temperature of 273 K, the hydrogen uptake capacity is 0.65 wt% at 50 bar. It increases to 1.35 wt% at 165 bar, and 1.70 wt% at 210 bar. According to the projection of the hydrogen uptake capacity with the relationship of pressure, Figure 4.2 predicts about 0.79 % wt at 72 bar at 273 K and 0.68 % wt at 300 K. This prediction is in very good agreement with 0.8 wt% of H_2 adsorption on crystalline corannulene found experimentally at 72 bar at 298 K. This agreement between the experimental data and simulation data validates the parameters for H-H and C-H

interactions used in our MD simulations. According the projection, at 250 bar, H_2 adsorption reaches 1.95 wt% at 273 K and 1.69 wt% at 300 K.

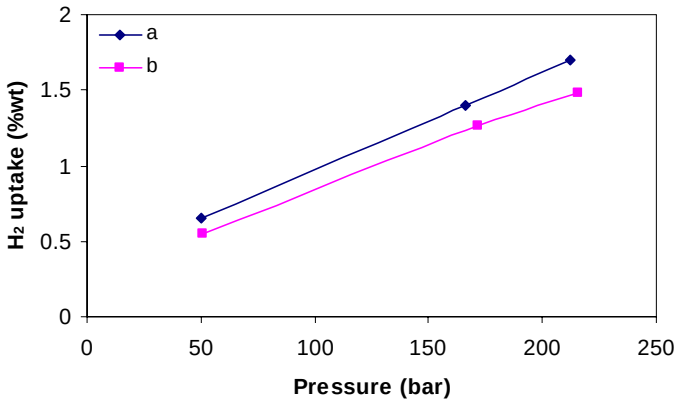

Figure 4.2. MD results of H_2 adsorption on crystalline corannulene. (a) at 273 K, (b) at 300 K

4.2 Hydrogen adsorption on corannulene assembled in stack arrays

4.2.1 Arrangement of corannulene adsorbent molecules

The second assembly of corannulene studied is in a simple stack, in a tetragonal simulation cell. As we mentioned before, the arrangement of corannulene molecules in the stack arrays depends on the parameters of IMD and ILD. For IMD, a value of 11.0 Å is used in all our MD simulations. Regarding to ILD, we obtained a separation distance of 4.8 Å for corannulene dimer from full optimization at the level of B3LYP/6-311G(d,p). Other than the optimum separation for ILD, we also test the ILD values of 6.0 and 8.0 Å, to investigate the effect of the available space on the capacity of hydrogen storage. The arrangement of 32 molecules are evenly distributed in two layers, each

layer of 16 molecules is in the same XY plane. The cell parameters are 38.4×22×c $Å^3$ for ILD value of 4.8 Å, 24×44×c $Å^3$ for ILD value of 6 Å, 32×44×c $Å^3$ for ILD value of 8 Å, where parameter c is depends on desired temperature (273 K or 300 K) and pressure (up to 250 bar) of the system. The distribution of hydrogen molecules in the simulation cell at the beginning of the simulation and the evaluation of hydrogen uptake and equilibrium gas phase pressure are the same as described in previous section of hydrogen adsorption in crystalline corannulene systems.

To get the idea of the distribution of corannulene molecules and the adsorption of hydrogen molecules on these systems, two systems of final configurations of hydrogen adsorption on corannulene adsorbents are shown in Figure 4.3. Figure 4.3 (a) shows final configuration of two different views of adsorbent layers with hydrogen molecules adsorbed, corresponding to the condition of ILD value of 4.8 Å at 300 K and 139 bar. A hydrogen uptake of 1.04 wt% is predicted in this system. Figure 4.3 (b) shows final configuration of two different views of adsorbent layers with hydrogen molecules adsorbed, corresponding to the condition of large ILD value of 8.0 Å at 300 K and 92 bar. A hydrogen uptake of 2.79 wt% is obtained in this system. The more discussion regarding the distribution of hydrogen molecules distributed in adsorbent layers will be provided next.

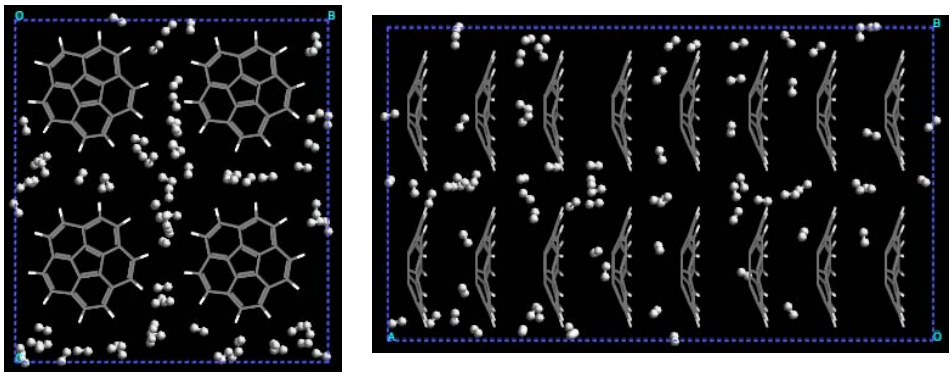

(a)

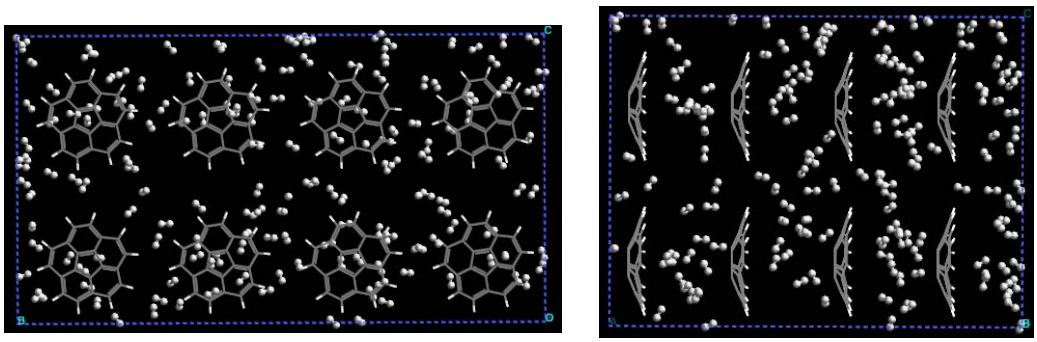

(b)

Figure 4.3. Final configurations of systems of adsorbent layers with hydrogen adsorbed. (a) ILD = 4.8 Å, 300 K and 139 bar; (b) ILD = 8.0 Å, 300 K and 92 bar

4.2.2 Hydrogen adsorption

Figure 4.4 shows the predicted hydrogen uptake on corannulene systems assembled in a stack configuration, at various ILDs (4.8 Å, 6.0 Å, and 8.0 Å) and temperatures (273 K and 300 K) as a function of the pressure. Similar to hydrogen adsorption in crystalline corannulene, we again observe the linear adsorption behavior of hydrogen uptake vs. pressure (in the range up to 250 bar) at a certain value of ILD at each temperature studied, also the enhanced hydrogen uptake capacity at low

temperature is found at the same ILD and pressure. Besides, it is observed that as ILD increases from 4.8 Å to 6.0 and 8.0 Å, the hydrogen uptake increases significantly. At ILD of 4.8 Å, hydrogen uptake capacities are 0.55 wt% at 273 K and 63 bar, and 0.50 wt% at 300 K and 65 bar. As ILD increases to 6.0 Å, hydrogen uptake capacities are 1.36 wt% at 273 K and 58 bar, 1.11 wt% at 300 K and 60 bar. When ILD further increases to 8.0 Å, hydrogen uptakes at two temperatures continue to increase, respectively. At ILD of 8.0 Å, hydrogen uptakes reach 2.10 wt% at 273 K and 47 bar, 1.77 wt% at 300 K and 50 bar. The degree of enhancement in hydrogen uptake regarding to the higher gas phase pressure is larger at higher ILD, which can be seen from larger slope of adsorption isotherm of higher ILD. Take the adsorption of hydrogen at 300 K, we obtain (1) at ILD of 4.8 Å, 0.50 wt% at 65 bar and 1.67 wt% at 231 bar; (2) at ILD of 6.0 Å, 1.11 wt% at 60 bar and 2.96 wt% at 180 bar; (3) at ILD of 8.0 Å, 1.77 wt% at 50 bar and 3.89 wt% at 139 bar. The increases in weight percentage are 0.0067 per bar for ILD value of 4.8 Å, 0.0154 per bar for ILD value of 6.0 Å, and 0.0238 per bar for ILD value of 8.0 Å. Also, Figure 4.4 shows that the adsorption difference due to temperature is higher for a specific ILD when ILD increases from 4.8 Å to 6.0 and 8.0 Å. For example at 100 bar, the adsorption differences between 273 K and 300 K are 0.07 wt%, 0.37 wt%, and 0.47 wt% for ILD values of 4.8, 6.0, and 8.0 Å, respectively. This, on the other hand, might indicate that desorption of hydrogen from adsorbent is easier at a higher value of ILD as T increases. So if we can increase the ILD value of corannulene by substituting H with bulky functional alkyl groups, we might be able to get larger amount of hydrogen adsorbed and more friendly conditions for these

adsorbed hydrogen molecules to get desorbed. If the substitution of H with bulky functional alkyl groups can increase the ILD to 6.0 Å, the hydrogen uptake will reach DOE target of 6.5 wt% at the pressure of 410 bar with temperature of 300 K. Further increased ILD to 8.0 Å and at 300 K, the pressure needed to reach the same DOE target can be drown down to 300 bar.

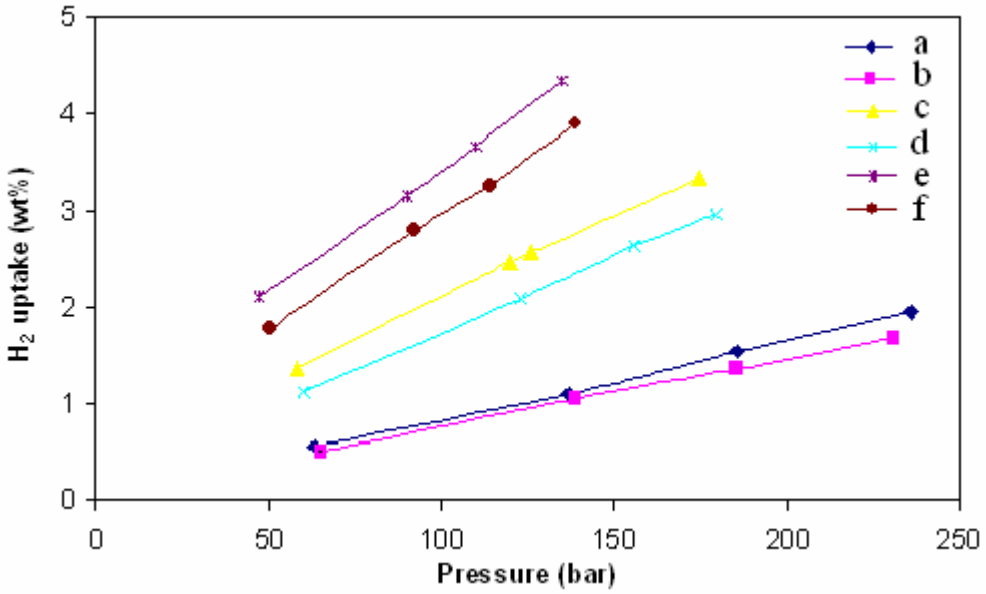

Figure 4.4. Hydrogen uptake capacity at different temperatures and ILD values. The intermolecular distance IMD is kept at 11.0 Å. (a) ILD = 4.8 Å, 273 K; (b) ILD = 4.8 Å, 300 K; (c) ILD = 6.0 Å, 273 K; (d) ILD = 6.0 Å, 300 K; (e) ILD = 8.0 Å, 273 K; (f) ILD = 8.0 Å, 300 K

After careful examination, we find that predicted H_2 adsorption, at the optimized value of ILD of 4.8 Å and pressure of 100 bar, is about 0.75 wt% at 300 K and 0.83 wt% at 273 K, respectively. Guay et al. [80] obtained about 0.75 % for SWNT and 0.40 % for GNF at a value of VDW gap around 4.8 Å with simulations performed at 293K and 100

bar. Based on the effect of temperature and pressure on the H_2 uptake observed above, our MD results indicate that corannulene may have some advantages over SWNT or GNF, which may be due to the dipole induced interaction between H_2 and corannulene, as we discussed in the section of force field section. With increasing values of ILD, the space available for H_2 to anchor to the assembled corannulene increases, leading to enhanced H_2 adsorption. The distribution of hydrogen molecules in the adsorbent layers is very interesting to look at. Two examples of final configurations of hydrogen adsorption are shown in Figure 4.3. At an ILD of 4.8 Å, almost none of the adsorbed H_2 molecules are anchored in the regions between two overlapped corannulene molecules, instead they are located at the region in the middle of 4 corannulene molecules (4-fold interstice) or between two parallel corannulene molecules (2-fold interstice), as can be seen in Figure 23 (a). As the ILD increases to 6 and 8 Å, the space between two overlap corannulene molecules increase and H_2 molecules start to fill the space between two overlapped corannulene molecules, as shown in Figure 4.3 (b) for the case of ILD = 8.0 Å. More adsorption sites for hydrogen molecules are the reason of the increased H_2 uptake at higher ILD values. Similar results had been found when H_2 adsorbed on the Li pillared graphene sheet system and Li pillared SWNT as a function of interlayer distance and intertube distance, respectively.[109]

4.2.3 Radial distribution functions

A radial distribution function (RDF) of C atoms surrounded by H_2 molecules, $g_{C\text{-}H}(r)$, is defined as the ratio of the local density of H_2 molecules located in concentrical spherical shells at distances r from a C atom, to the bulk density (i.e., the number of H_2

molecules that would be found in the same volume in gas phase). The RDFs provide molecular level insights about structural features of the adsorbed phase. Analysis of $g_{C\text{-}H}(r)$ indicates that at the same value of ILD, RDFs at different temperatures and different pressures have similar shape, but differ on the peak intensities, which are higher at lower temperatures. Figure 4.5 illustrates $g_{C\text{-}H}(r)$ functions corresponding to H_2 adsorption of 1.09 wt% (a), 2.46 wt% (b), and 3.15 wt% (c), respectively. As we can see, at ILD of 4.8 Å, no clear peaks are observed at distances below 5.0 Å. When ILD increases to 6.0 Å, a relatively sharp peak appears around 3.3 Å. This short-range peak mainly corresponds to the H_2 molecules adsorbed between two overlapped corannulene molecules. This, on the other hand, confirms that H_2 starts to fill in the space between overlapped molecules provided by the increasing ILD, and also explains the jump of H_2 adsorption from 1.09 wt% to 2.46 wt% shown in Figure 4.4. The second peak around 9 Å corresponds to the pair of C atoms interacting with H_2 in a second layer. For an ILD of 8 Å, the first peak becomes broader and the peak intensity decreases, due to the fact that the distribution of H_2 in between two overlapped molecules is changing from a relatively thin single layer as in the 6 Å ILD to a relatively thick single layer or to the formation of two layers. Similar distribution of H_2 has been found on SWNTs, DWNTs, and especially GNFs as the VDW gaps increase in these systems by Guay et al.[80]

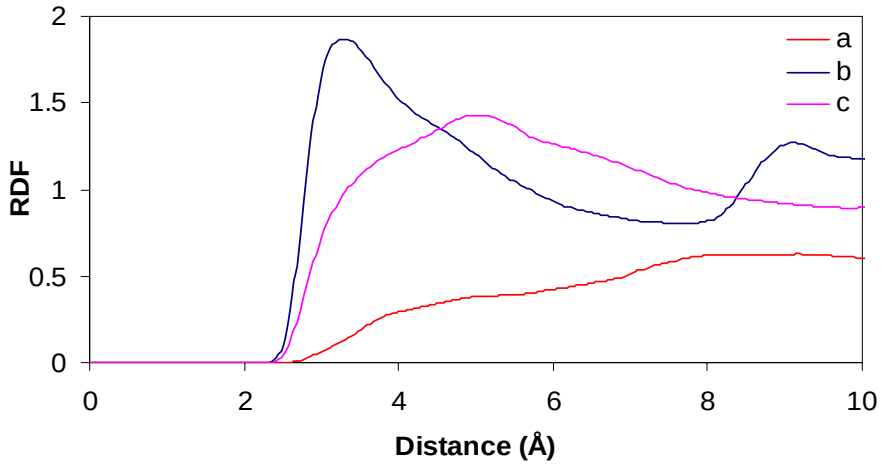

Figure 4.5. Radial distribution functions of C atoms surrounded by H_2 molecules at 273 K. (a) ILD = 4.8 Å, P = 137 bar; (b) ILD = 6.0 Å, P = 120 bar; (c) ILD = 8.0 Å, P = 90 bar. Comparison of the RDFs corresponding to the two lowest ILD values illustrates the adsorption enhancement in between corannulene molecules, forming two well defined shells at ILD = 6.0 Å, whereas a broader adsorption distribution is observed at the highest ILD value

4.3 Conclusions

MD simulations predict the capacities of hydrogen adsorption on simple stack of corannulene with various values of ILD. Hydrogen adsorption isotherms indicate the linear relation between hydrogen uptake capacity and applied pressure on the system, higher adsorption at lower temperature. At the ILD of optimum value of 4.8 Å, hydrogen uptake cannot meet the target set by DOE. Without modification, corannulene does not show enough capacity as hydrogen storage material. With increasing ILD, hydrogen uptake capacity is enhanced and DOE target of 6.5 wt% is projected at the conditions of 300 bar and 300 K with ILD value of 8.0 Å.

CHAPTER V

MD SIMULATIONS OF HYDROGEN ADSORPTION ON LITHIUM ATOMS DOPED CORANNULENE SYSTEMS

5.1 Advantages of Li doping

In pure carboneous materials, it is difficult to have capacity of hydrogen storage to reach DOE target of 6.5 wt% at room temperature. For corannulene system, it would require the increasing ILD to 8.0 Å and at the pressure of 300 bar in order to reach 6.5 wt% at 300 K, assuming all the adsorbed hydrogen molecules get desorbed at moderate conditions. On the other hand, doping of alkali metal has been investigated and shows enhanced hydrogen storage capacities.[75,109,142,190-194] Generally, the role of alkali metal has been attribute to three factors. First, doping of lithium atoms on carbon materials leads to charge transfer from metal atom to carbon, which creates an enhanced dipole induced interaction with hydrogen molecules. Second, the VDW interaction between Li-H_2 is stronger than that of C-H_2. Third, doping of lithium atoms provides more space in the adsorbent materials for hydrogen molecules to get adsorbed. According to our potential energy surface scan using DFT calculations and ab initio calculations of single point interaction energies with MP2, we found enhanced interaction between hydrogen molecule and lithium atoms doped corannulene complexes. Besides, an increasing ILD value, as suggested by the partial optimization of $(Li_6\text{-}C_{20}H_{10})_2$, was obtained as the result of doping of lithium atoms, which could provide more space for hydrogen to get

adsorbed in the adsorbent layers. Based on these factors, higher hydrogen uptake capacity can be expected in the systems of lithium atoms doped corannulene complexes under the same conditions of temperature and pressure, compared to undoped corannulene system. In this section, we will investigate the hydrogen uptake capacities in two different lithium atoms doped complexes, Li_6-$C_{20}H_{10}$ and Li_3-$C_{20}H_{10}$-Li_2. We will discuss the effect of lithium doping as well as the effect of doping concentration.

5.2 Hydrogen adsorption in Li_6-$C_{20}H_{10}$ systems

5.2.1 Arrangement of Li_6-$C_{20}H_{10}$ adsorbent molecules

The arrangement of Li_6-$C_{20}H_{10}$ complex in the simulation cell is in a simple stack, which depends on the parameters of ILD and IMD. IMD value of 11.0 Å is used in MD simulations. As for ILD, we obtained an optimum value of 6.5 Å from partial optimization of Li_6-$C_{20}H_{10}$ dimer. Higher values of ILD at 8.0 and 10.0 Å are tested for hydrogen adsorption. In each simulation cell, there are total of 16 Li_6-$C_{20}H_{10}$ molecules distributed in two layers, with 8 molecules in each layer. The cell parameters are 28×22×c $Å^3$ for ILD value of 6.5 Å, 32×22×c $Å^3$ for ILD value of 8.0 Å, and 40×22×c $Å^3$ for ILD value of 10.0 Å, where parameter c is depends on desired temperature (273 K or 300 K) and pressure (up to 250 bar) of the system. The distribution of hydrogen molecules in the simulation cell at the beginning of the simulation and the evaluation of hydrogen uptake and equilibrium gas phase pressure are the same as described before as hydrogen adsorption in undoped corannulene systems.

In order to see the different behavior of hydrogen adsorption on lithium atoms doped system and the distribution of hydrogen molecules on these systems, two systems of final configurations of hydrogen adsorption on Li_6-$C_{20}H_{10}$ adsorbents are shown in Figure 5.1. In such systems, Li_6-$C_{20}H_{10}$ adsorbents are arranged as in simple stack. The arrangement is decided by IMD and ILD. As mentioned in Chapter II, IMD value of 11.0 Å and different values of ILD are used in MD simulations. ILD values include optimum separation value of 6.5 Å, as well as two larger values at 8.0 and 10.0 Å. Figure 5.1 (a) shows final configuration of two different views of adsorbent layers with hydrogen molecules adsorbed, corresponding to the condition of ILD value of 6.5 Å at 300 K and 75 bar. A hydrogen uptake of 2.36 wt% is predicted in this system. Figure 5.1 (b) shows final configuration of two different views of adsorbent layers with hydrogen molecules adsorbed, corresponding to the condition of large ILD value of 10.0 Å at 300 K and 57 bar. A hydrogen uptake of 2.39 wt% is obtained in this system. The more discussion regarding the distribution of hydrogen molecules distributed in adsorbent layers will be provided next.

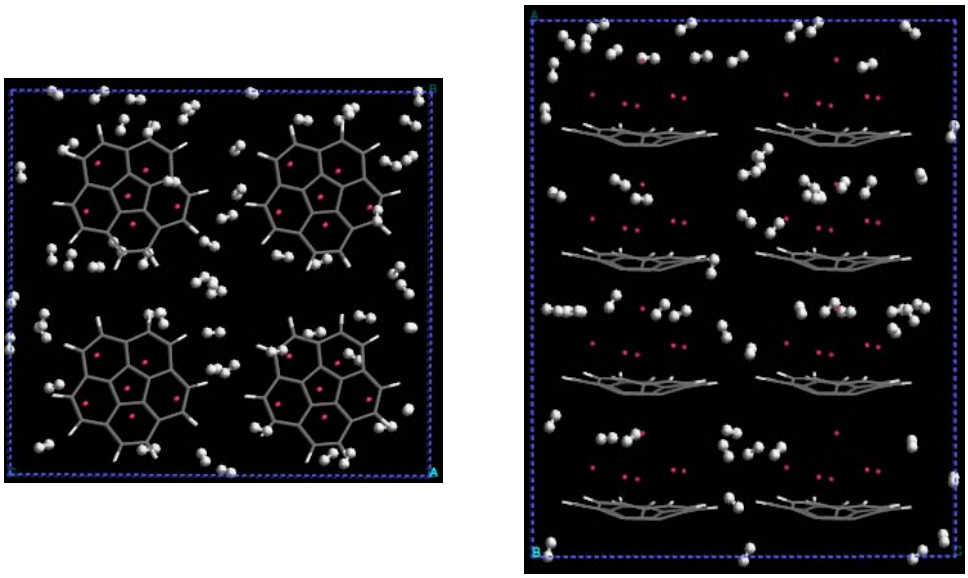

(a)

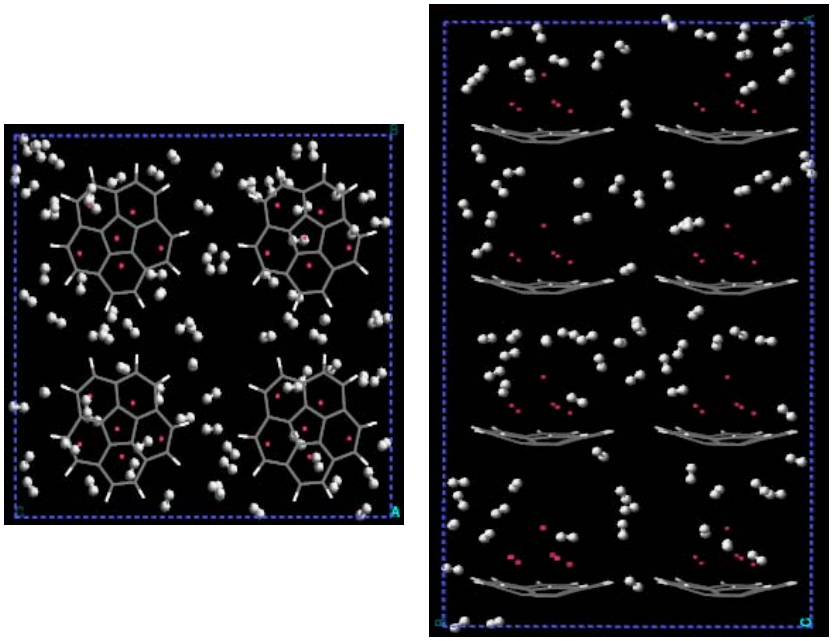

(b)

Figure 5.1. Final configurations of Li_6-$C_{20}H_{10}$ systems of adsorbent layers with hydrogen adsorbed. (a) ILD = 6.5 Å, 300 K and 75 bar; (b) ILD = 10.0 Å, 300 K and 57 bar

5.2.2 Hydrogen adsorption

Figure 5.2 shows the predicted H_2 uptake at 273 K and 300 K and various ILD for $Li_6C_{20}H_{10}$ as a function of H_2 pressure. Overall, our MD simulations predict (1) at all the conditions studied, the H_2 uptake is higher than 2 wt%; (2) the H_2 uptake at a given ILD and temperature is almost linear with the increase of pressure in the pressure region studied; (3) adsorption decreases as temperature increases, and H_2 uptake is lower at 300 K than in 273 K while kept other conditions the same according to the adsorption isotherm; (4) increasing ILD while keeping the same T and P, significantly increases the H_2 uptake, especially changing ILD from 8.0 to 10.0 Å. At the optimum equilibrium ILD of 6.5 Å, the predicted H_2 uptake values are 2.75 wt% to 5.08 wt% corresponding to 70 bar to 225 bar at 273 K, and 2.38 wt% to 4.58 wt% corresponding to 75 bar to 230 bar at 300 K. According the projection, H_2 uptake would reach the DOE target of 6.5 wt% at 300 K under the pressure of 315 bar. Compared to the undoped corannulene in the simple stack at the optimum ILD value of 4.8 Å, for H_2 uptake to reach DOE target of 6.5 wt% at 300 K, the pressure needed in the gas phase will be higher than 900 bar, assuming that the linearity can extend to 900 bar. The dropping of pressure from more than 900 bar to 315 bar indicates the great potential of enhancement of hydrogen uptake upon the doping of lithium atoms.

On the other hand, these simulation results indicate that at pressures lower than 250 bar, there is not enough H_2 uptake to reach DOE target at the optimum equilibrium ILD of 6.5 Å and temperatures above 273 K. This is due to the limited space available around the Li dopants. In order to enhance the H_2 uptake at low pressures, one possible

way is to increase the ILD of lithium atoms doped complex, by substituting hydrogen atoms attached to rim carbon atoms with bulky alkyl functional groups. With the substitution, we can expect that more space will available for hydrogen to get adsorbed. In our simulations, we assume that ILDs of 8.0 and 10.0 Å can be obtained by such substitution reactions. Figures 5.2 (c) to (f) show the H_2 uptake at ILDs of 8.0 and 10.0 Å as a function of pressure at different temperatures; the predicted H_2 uptake increases significantly as ILD increases at the same conditions of T and P, especially from 8.0 to 10.0 Å. Take the adsorption of hydrogen on Li_6-$C_{20}H_{10}$ complex at 300 K, we obtain (1) at ILD of 6.5 Å, 2.36 wt% at 75 bar and 4.58 wt% at 230 bar; (2) at ILD of 8.0 Å, 2.22 wt% at 58 bar and 4.85 wt% at 199 bar; (3) at ILD of 10.0 Å, 2.39 wt% at 57 bar and 5.62 wt% at 184 bar. The increases in weight percentage are 0.0142 per bar for ILD value of 6.5 Å, 0.0187 per bar for ILD value of 8.0 Å, and 0.0255 per bar for ILD value of 10.0 Å. According to the projection of our molecular dynamics simulations, for the ILD of 8.0 Å, the hydrogen uptake reaches DOE target at pressure of 287 bar at 300 K; while for ILD of 10.0 Å, the pressure needed continues to decrease to 215 bar at 300 K. The pressures required for reaching the same target at 273 K are 317 bar for ILD of 6.5 Å, 256 bar for ILD of 8.0 Å, and 187 bar for ILD of 10.0 Å. These values of predicted pressures are significantly lower than pressures needed for the case of undoped corannulene at increasing ILD values, to achieve the same target at the same given temperature.

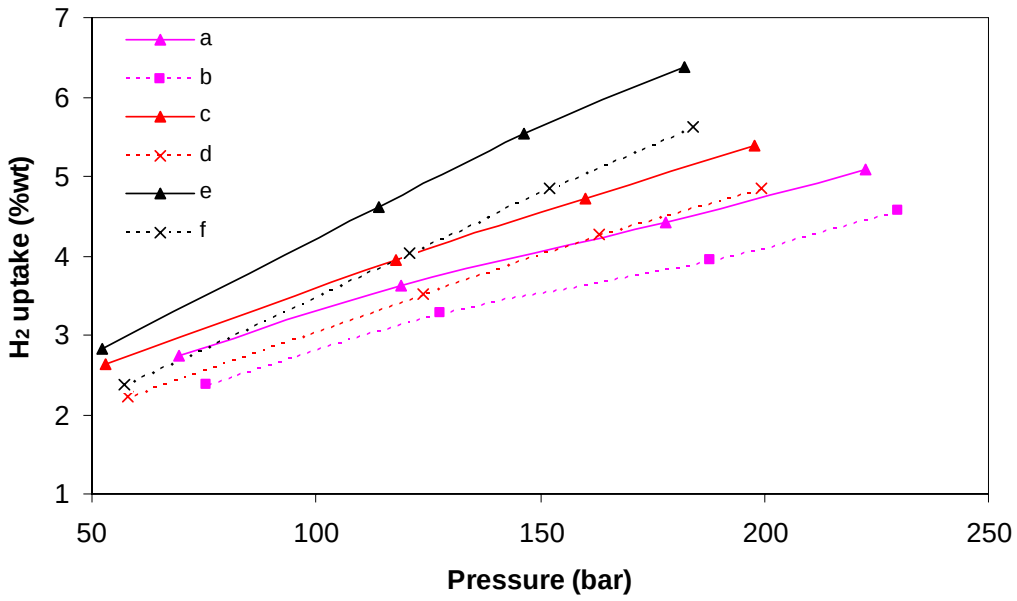

Figure 5.2. Hydrogen uptake capacity of $Li_6C_{20}H_{10}$. (a) ILD = 6.5 Å, 273 K; (b) ILD = 6.5 Å, 300 K; (c) ILD = 8 Å, 273 K; (d) ILD = 8 Å, 300 K; (e) ILD = 10 Å, 273 K; (f) ILD = 10 Å, 300 K

5.2.3 Radial distribution functions

The increased uptake regarding the increasing values of ILD is mainly due to the enhanced space available to H_2 adsorption. The difference of hydrogen uptake is higher for ILDs changing from 8.0 to 10.0 Å than that of ILDs changing from 6.5 to 8.0 Å. For example, from our predictions, we can obtain that at 100 bar, the H_2 uptake increases from 3.26 wt% (ILD = 6.5 Å) to 3.56 wt% (ILD = 8 Å), and to 4.19 wt% (ILD = 10 Å) at 273 K; and that from 2.78 wt% (ILD = 6.5 Å) to 3.03 wt% (ILD = 8 Å), and 3.49 wt% (ILD = 10 Å) at 300 K. The difference is 0.30 wt% at 273 K from ILD of 6.5 Å to ILD of 8.0 Å; while at the same temperature when ILD changes from 8.0 Å to 10.0 Å, the

difference is 0.63 wt%. At 300 K, these two differences are 0.25 wt% and 0.46 wt%, respectively. The differences are about double in two given temperature. This could be attributed to the adsorption of hydrogen molecules and the distribution of hydrogen molecules in between adsorbent molecules, as seen from radial distribution functions (RDFs) between C and H_2, shown in Figure 5.3. At an ILD of 6.5 Å, a relatively sharp peak is observed at a distance lower than 4.0 Å, with a shoulder appearing at a larger distance. This relatively sharp peak indicates that the H_2 molecules located in between adsorbent molecules are distributed in a relatively thin layer. As the ILD increases to 8 Å, a broader peak appears at a distance larger than 4.0 Å, which indicates that the space accessible to hydrogen molecules is increasing and that the thin layer becomes thicker. At an ILD of 10 Å, two peaks are evident; one located at a distance less than 5 Å and the other at a distance greater than 6 Å, indicating the formation of two adsorption layers of hydrogen molecules in between adsorbent molecules. The formation of two adsorption layers might explain the large increase in H_2 uptake when ILD increases from 8 to 10 Å. Similar H_2 distribution has been found in single-wall and double-wall carbon nanotubes, and especially in GNFs as the VDW gaps increase in these systems.[169]

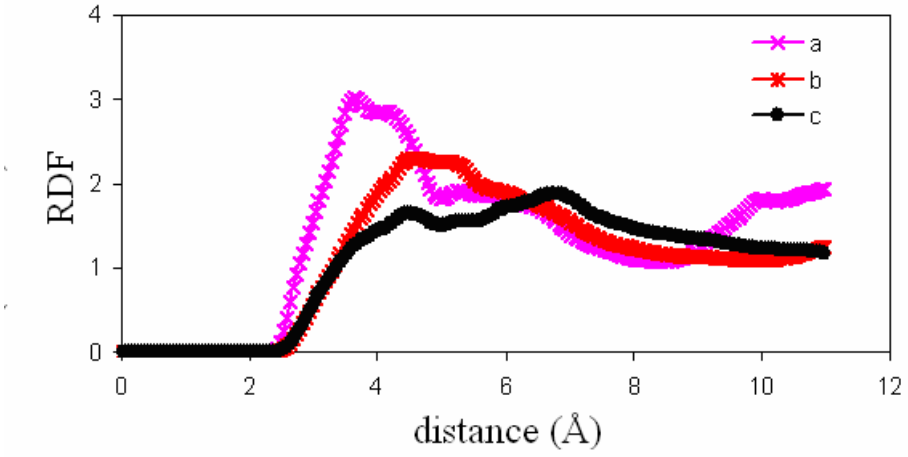

Figure 5.3. Radial distribution function of C-H in the Li_6-$C_{20}H_{10}$ complex. (a) ILD = 6.5 Å, 273 K, P = 119 bar and H_2 uptake of 3.63 wt%, (b) ILD = 8 Å, 273 K, P=118 bar and H_2 uptake of 3.95 wt%, (c) ILD =10 Å, 273 K, P = 114 bar and H_2 uptake of 4.61 wt%

As we discussed in Chapter II about the way we evaluated the hydrogen uptake capacity and the equilibrium gas phase pressure, we stated that 300 ps is long enough for system to get equilibrium, and 500 ps enough for calculating hydrogen adsorption. This can be explained from Figure 5.4, which shows the number of hydrogen molecules adsorbed in Li_6-$C_{20}H_{10}$ adsorbent layers during the whole molecular dynamics simulations for the systems of ILD value of 6.5 Å at 273 K and various pressures. A total simulation time of 1200 ps is performed. From Figure 5.4, it is clear that the number of hydrogen adsorbed in the adsorbent layers fluctuated around the average value at the given conditions at about 150-200 ps in the equilibration period. In the production period, from 300-1200 ps, the number of adsorbed hydrogen molecules is about the average. Longer simulation time does not increase the number of hydrogen

molecules adsorbed. This validates the total simulation time of 800 ps is enough for our MD simulations.

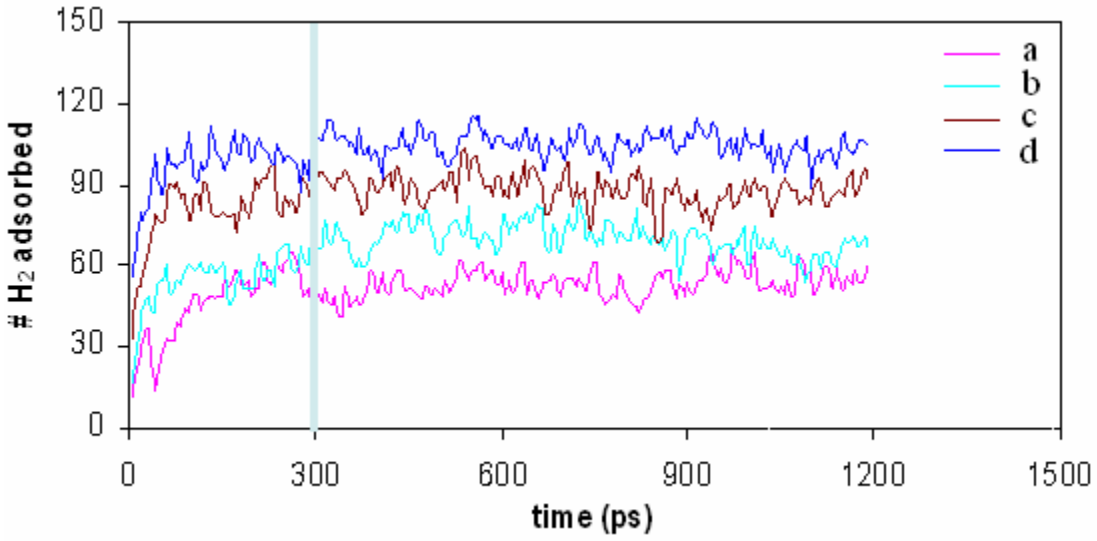

Figure 5.4. Number of hydrogen adsorbed in Li_6-$C_{20}H_{10}$ adsorbent layers for ILD value of 6.5 Å at 273 K. (a) P = 69 bar with H_2 uptake of 2.75 wt%; (b) P = 119 bar with H_2 uptake of 3.63 wt%; (c) P = 178 bar with H_2 uptake of 4.42 wt%; (d) P = 223 bar with H_2 uptake of 5.08 wt%

5.3 Hydrogen adsorption in Li_3-$C_{20}H_{10}$-Li_2 systems

5.3.1 Arrangement of Li_3-$C_{20}H_{10}$-Li_2 adsorbent molecules

The arrangement of Li_3-$C_{20}H_{10}$-Li_2 complex in the simulation cell is in a simple stack, which also depends on the parameters of ILD and IMD. IMD value of 11.0 Å is used in MD simulations. As for ILD, same values of ILD at 6.5, 8.0, and 10.0 Å are tested for hydrogen adsorption as used for Li_6-$C_{20}H_{10}$ complex. In each simulation cell, there are total of 16 Li_3-$C_{20}H_{10}$-Li_2 molecules distributed in two layers, with 8 molecules

in each layer. The cell parameters are 28×22×c $Å^3$ for ILD value of 6.5 Å, 32×22×c $Å^3$ for ILD value of 8.0 Å, and 40×22×c $Å^3$ for ILD value of 10.0 Å, where parameter c is depends on desired temperature (273 K or 300 K) and pressure (up to 250 bar) of the system. The distribution of hydrogen molecules in the simulation cell at the beginning of the simulation and the evaluation of hydrogen uptake and equilibrium gas phase pressure are the same as described before as hydrogen adsorption in previous systems.

For the same purpose of seeing the different behavior of hydrogen adsorption on lithium atoms doped system and the distribution of hydrogen molecules, two systems of final configurations of hydrogen adsorption on Li_3-$C_{20}H_{10}$-Li_2 adsorbents are shown in Figure 5.5. Figure 5.5 (a) shows final configuration of two different views of adsorbent layers with hydrogen molecules adsorbed, corresponding to the condition of ILD value of 6.5 Å at 300 K and 131 bar. A hydrogen uptake of 2.87 wt% is predicted in this system. Figure 5.5 (b) shows final configuration of two different views of adsorbent layers with hydrogen molecules adsorbed, corresponding to the condition of large ILD value of 10.0 Å at 300 K and 127 bar. A hydrogen uptake of 3.35 wt% is obtained in this system. Both left side views of Figure 5.5 (a) and (b) show that hydrogen molecules can be adsorbed in the region between two overlap Li_3-$C_{20}H_{10}$-Li_2 complexes. As the ILD increases, more hydrogen molecules are adsorbed in these regions around lithium atoms and the ratio of hydrogen molecules adsorbed in these regions to hydrogen molecules adsorbed in 2-fold or 4-fold interstice increases.

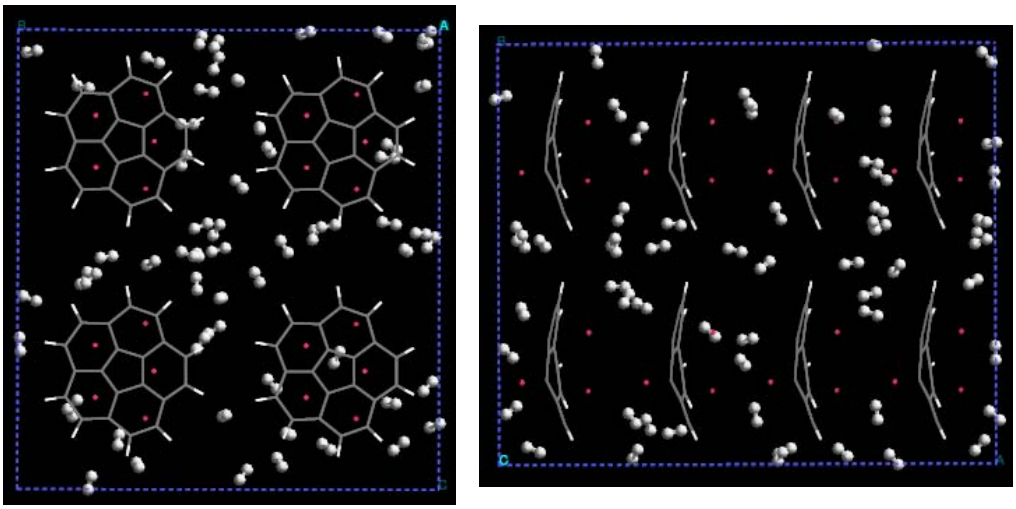

(a)

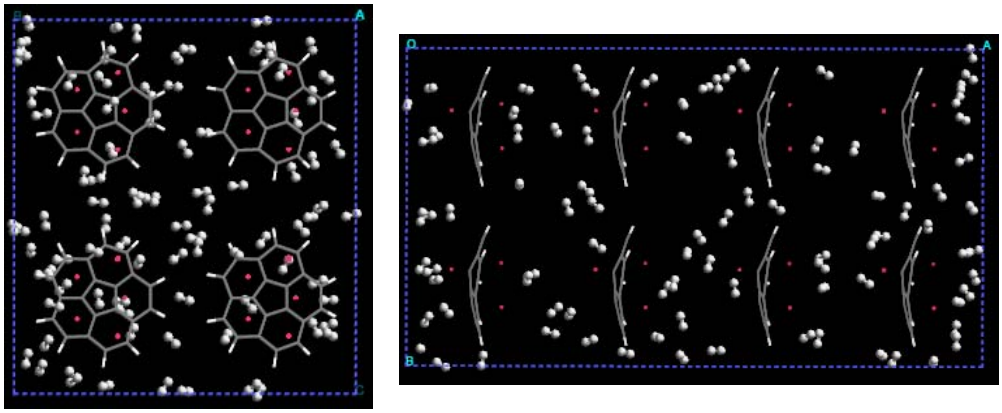

(b)

Figure 5.5. Final configurations of Li_3-$C_{20}H_{10}$-Li_2 systems of adsorbent layers with hydrogen adsorbed. (a) ILD = 6.5 Å, 300 K and 131 bar; (b) ILD = 10.0 Å, 300 K and 127 bar

5.3.2 H_2 adsorption and radial distribution functions

Figure 5.6 shows the predicted H_2 uptake on Li_3-$C_{20}H_{10}$-Li_2 adsorbent systems at temperatures of 273 K and 300 K, and various ILDs as a function of H_2 pressure in gas

phase. The overall hydrogen uptake behavior of Li_3-$C_{20}H_{10}$-Li_2 adsorbent systems is similar to that of Li_6-$C_{20}H_{10}$ adsorbent systems, which includes the linearity of H_2 uptake vs. gas phase pressure at a given temperature and ILD of adsorbent system, higher H_2 uptake ability of the same system at lower temperature, and clearly significantly increased H_2 uptake as increasing value of ILD. The MD simulations predict that at the temperature of 300 K H_2 uptake capacities are (1) at ILD of 6.5 Å, 1.85 wt% at 81 bar and 4.14 wt% at 235 bar; (2) at ILD of 8.0 Å, 1.93 wt% at 64 bar and 4.07 wt% at 203 bar; (3) at ILD of10.0 Å, 1.68 wt% at 63 bar and 4.77 wt% at 186 bar. The increases in weight percentage at 300 K are 0.0151 per bar for ILD value of 6.5 Å, 0.0181 per bar for ILD value of 8.0 Å, and 0.251 per bar for ILD value of 10.0 Å. The jump of H_2 uptake when the ILD increases from 8.0 to 10.0 Å is higher than that of from 6.5 to 8.0 Å. Again, this can be attributed to the arrangement of hydrogen molecules in between adsorbent molecules and can be explained from the RDFs of the C-H pair, shown in Figure 5.7. The RDF at an ILD of 6.5 Å clearly shows one peak about 4 Å. Similarly, this peak at an ILD of 8.0 Å becomes broader at distances larger than 4 Å, with a shoulder at an even larger distance, which might indicate the formation of one thick adsorption layer or a transition of one thick adsorption layer to two adsorption layers. At an ILD of 10 Å, two peaks are located at 4.2 and 7.2 Å, respectively. The radial distribution functions also suggest a relatively ordered adsorbed state.

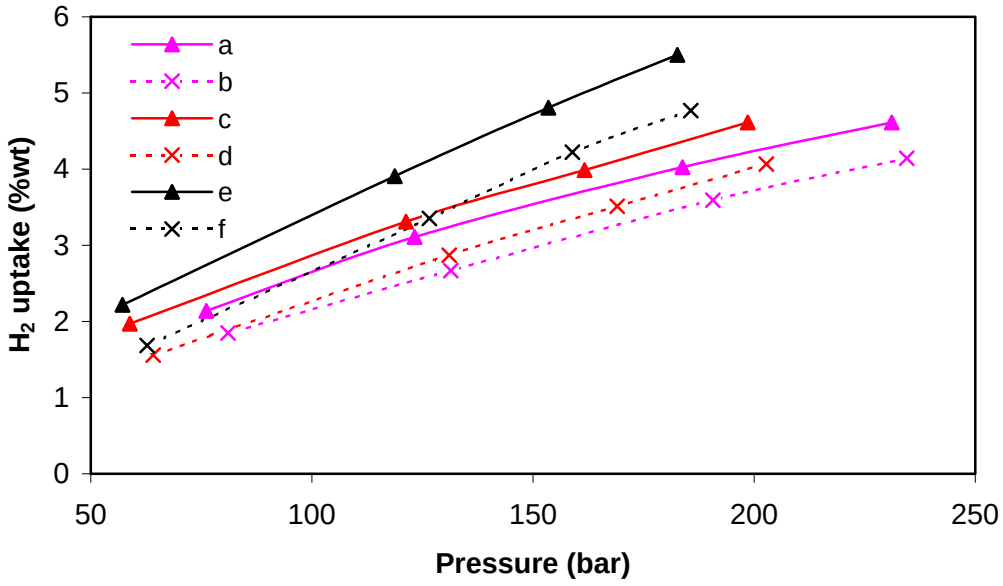

Figure 5.6. Hydrogen uptake capacity of $Li_3C_{20}H_{10}Li_2$. (a) ILD = 6.5 Å, 273 K; (a) ILD = 6.5 Å, 300 K; (a) ILD = 8 Å, 273 K; (a) ILD = 8 Å, 300 K; (a) ILD = 10 Å, 273 K; (a) ILD = 10 Å, 300 K

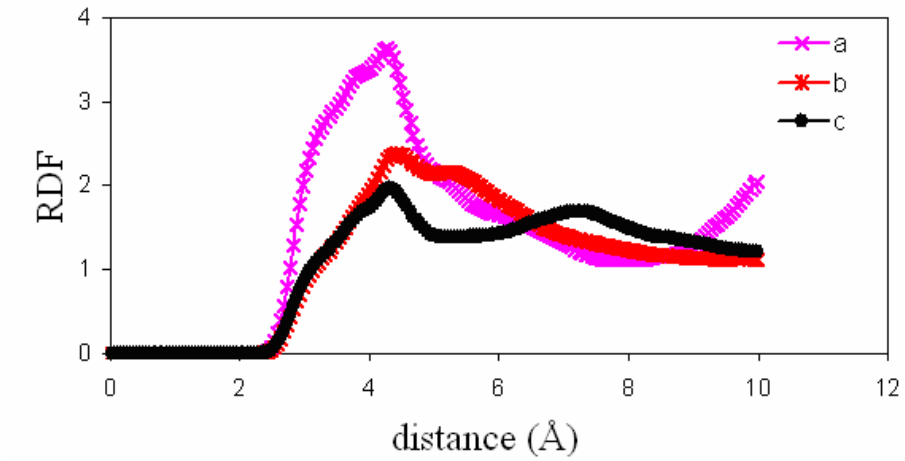

Figure 5.7. Radial distribution function of C-H in the Li_3-$C_{20}H_{10}$-Li_2 complex. (a) ILD=6.5 Å, 273 K, P=123 bar and H_2 uptake of 3.11 wt%, (b) ILD = 8 Å, 273 K, P = 121 bar and H_2 uptake of 3.31 wt%, (c) ILD = 10 Å, 273 K, P = 119 bar and H_2 uptake of 3.91 wt%

5.4 Effect of lithium doping

According to the projection of MD simulation results at 300 K, DOE target of 6.5 wt% can be met at pressure of 385 bar for ILD value of 6.5 Å, 335 bar for ILD of 8.0 Å, and 251 bar for ILD of 10.0 Å in Li_3-$C_{20}H_{10}$-Li_2 adsorbent systems. At these same adsorbent systems and temperature of 273 K, this target can be met at lower pressures, 344 bar, 295 bar, and 219 bar for ILD values of 6.5 Å, 8.0 Å, and 10.0 Å, respectively. These pressures are higher than those corresponding pressures at the same value of ILD and temperature in Li_6-$C_{20}H_{10}$ adsorbent systems, in which concentration of lithium atoms doped is higher.

In order to analyze the role of the concentration of lithium atoms doped on the H_2 physisorption, we analyze the H_2 uptake behavior on these two different lithium atoms doped corannulene systems. Since the relationship of H_2 uptake capacity is almost linear to the pressure in the region studied, it is fair to take only one pressure, for example, 100 bar, to explain the effect of lithium concentration on H_2 uptake. The data in other pressure should follow the same ratio, though the absolute values will not be the same.

At 100 bar, in the Li_3-$C_{20}H_{10}$-Li_2 adsorbent system, the H_2 uptake increases from 2.63 wt% (with ILD of 6.5 Å) to 2.81 wt% (with ILD of 8.0 Å), and 3.38 wt% (with ILD of 10.0 Å) at 273 K; and that of from 2.17 wt% (with ILD of 6.5 Å) to 2.24 wt% (with ILD of 8.0 Å), and 2.65 wt% (with ILD of 10.0 Å) at 300 K. While, at 100 bar, in the Li_6-$C_{20}H_{10}$ adsorbent system, the H_2 uptake increases from 3.26 wt% (with ILD of 6.5 Å) to 3.56 wt% (with ILD of 8.0 Å), and 4.19 wt% (with ILD of 10.0 Å) at 273 K; and that of from 2.78 wt% (with ILD of 6.5 Å) to 3.03 wt% (with ILD of 8.0 Å), and 3.49 wt%

(with ILD of 10.0 Å) at 300 K. These data are shown in Table 5.1. Li_6-$C_{20}H_{10}$ adsorbent systems have higher H_2 uptake capacity than Li_3-$C_{20}H_{10}$-Li_2 adsorbent system and the difference at 100 bar is about 0.61 to 0.84 wt%, depending on the temperature and the values of ILD. This difference is most likely caused by the lower lithium concentration in the Li_3-$C_{20}H_{10}$-Li_2 adsorbent system. Table 5.1 also shows that the ratio of the H_2 uptake to the number of Li atoms per corannulene molecule for each system at the same ILD, temperature, and pressure, yield very close values for these two systems, a consequence of the linear dependence of H_2 uptake on lithium doping concentration. For example, at ILD of 6.5 Å, the ratios of the H_2 uptake to the number of lithium atoms are 0.54 in Li_6-$C_{20}H_{10}$ system and 0.53 in Li_3-$C_{20}H_{10}$-Li_2 system at 273 K and 100 bar. The ratios decrease to 0.46 in Li_6-$C_{20}H_{10}$ system and 0.43 in Li_3-$C_{20}H_{10}$-Li_2 system at 300 K and 100 bar. Similar behavior of the dependence of H_2 uptake on lithium atom concentration was found in Li-pillared graphene sheets.[109]

Table 5.1: Comparison of H_2 uptake at 100 bar on Li-doped corannulene systems. The number in parenthesis is the ratio of the H_2 uptake to the number of Li atoms per corannulene molecule.

ILD	273 K		300 K	
(Å)	Li_6-$C_{20}H_{10}$	Li_3-$C_{20}H_{10}$-Li_2	Li_6-$C_{20}H_{10}$	Li_3-$C_{20}H_{10}$-Li_2
6.5	3.26 (0.54)	2.63 (0.53)	2.78 (0.46)	2.17 (0.43)
8.0	3.56 (0.59)	2.81 (0.56)	3.03 (0.51)	2.24 (0.45)
10.0	4.19 (0.70)	3.38 (0.68)	3.49 (0.58)	2.65 (0.53)

5.5 Conclusions

Li_6-$C_{20}H_{10}$ and Li_3-$C_{20}H_{10}$-Li_2 complexes are used as adsorbents for hydrogen uptake. MD simulations of hydrogen adsorption on these complex systems at temperatures of 273 K and 300 K predict significantly enhanced hydrogen uptake capacities, compared to undoped corannulene system. The higher adsorption is caused by three reasons, enhanced dipole moment on lithium atoms doped complexes, strong interaction between hydrogen molecule and lithium atoms, and increased available space in adsorbent layers. Linear relation of hydrogen uptake vs. pressure and other hydrogen adsorption behaviors are similar to hydrogen adsorption on corannulene.

CHAPTER VI

MODIFICATION OF CORANNULENE AND MD SIMULATIONS OF HYDROGEN ADSORPTION

6.1 Motivation of modification of corannulene

In previous two chapters on the hydrogen adsorption on corannulene systems, or lithium atom doped corannulene systems, it is clearly that the available space in the adsorbent layers plays an important role on hydrogen uptake capacity. Here, the objective is to find a method to chemically modify the molecule of corannulene. With the modification, the new material can expect to have more space available when it is assembled and used as an adsorbent for hydrogen adsorption. Aylon et al. reported two different complex sandwich dimmers of corannulene derivatives, tert-butylcorannulene and isopropylcorannulene, where one H was substituted by tert-butyl group and isopropyl group, respectively.[171] Besides, the dimmers of monosubstituted corannulene exhibited supramolecular stereochemistry, a meso dimer and a *d,l* dimer. Seiders et al. successfully synthesized different alkyl derivatives of corannulene, for example methylcorannulene, dimethylcorannulene, tetramethylcorannulenes, acecorannulene, C_{5h} symmetric pentamethylcorannulene, and decamethylcorannulene, by substituting H group with methyl group.[139,155] Sygula et al. used addition of various alkyllithium reagents to obtain 1-alkyl-1,2-dihydrocorannulenes. X-ray diffraction studies showed the exo-pseudoaxial conformation in the solid state of different derivatives.[195] Recently,

they reported a clean and quick synthesis of discorannulenosemibullvalene dimethyl dicarboxylate with the exo-endo conformer of the semibullvalene as the most stable conformer.[196] Other groups also reported the substitutions of different functional groups to H attached on the rim carbon atoms of corannulene.[197,198] With the bulky functional groups and self-assembly of these derivatives, more available space in these materials can be expected. The potential increased free space of these materials justifies the use of higher values of ILD in previous two chapters for the adsorption of hydrogen.

Other than substitution of H with bulky function groups, bridging of two corannulene molecule can also change available space of the materials. Linkers have been successfully used in MOFs to increase the internal surface and porosity of MOFs. Shabtai et al. reported that the use of an octamethylene chain could join two corannulene molecules to form 1,8-dicorannulenyloctane.[199] This is very interesting as it provides another way of modification to corannulene molecules, by bridging two molecules with certain linkers in certain way to obtain more porous materials. These new materials potentially with more available space can increase the adsorption of hydrogen. Based on this idea, 1,5-biscorannulenecyclophane ($C_{52}H_{20}$) is synthesized by collaborate in Air Force Research Laboratory.[200] The molecular structure of 1,5-biscorannulenecyclophane is shown as in Figure 6.1. The molecule has the jaw shape with the mirror plane of the symmetry element in σ_v group.

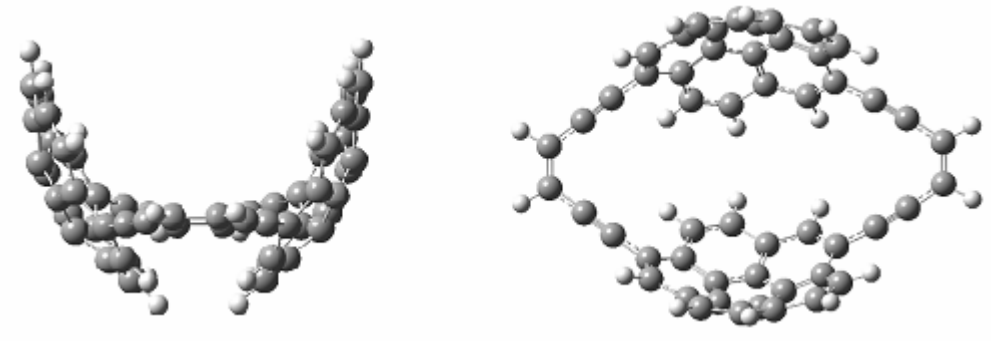

Figure 6.1. Molecular structure of 1,5-biscorannulenecyclophane

6.2 Characterization of 1,5-biscorannulenecyclophane

Figure 6.2 shows another view of molecular structure, overlooked from one convex side of the molecule, optimized at the level of B3LYP/6-31G. From this view, only half of the atoms on the front can be seen, labeled from C1 through H36. The other half of atoms on the back cannot be seen. But we can label these atoms from C1' through H36', corresponding to symmetric positions of the mirror plane. Table 6.1 shows the distance between two symmetric carbon atoms through the mirror plane. These values of distance somehow are similar to ILD values as we studied in previous chapters. The bridging of two corannulene molecules leads to open-jaw shape, with bottom pairs of atoms closer to each other. Compared to the optimum ILD distance of 4.8 Å of two sandwich corannulene molecules optimized at the level of B3LYP/6-311G(d,p), only three pairs of Cr-Cr distance are smaller. These three pairs of Cr-Cr are 3.88 Å, 4.26 Å, 4.44 Å for C3-C3', C2-C2', C4-C4', respectively. Other pairs of Cr-Cr, Cb-Cb, and Ch-Ch are all larger than the optimum ILD value of sandwich corannulene dimer. The

distance ranges from 5.23 Å to 9.57 Å, depending on the positions of each pair in the molecule. If taking the average distance of these pairs, the value is about 7.22 Å. The distance is between ILD values of 6 Å and 8 Å for the simple stack corannulene configurations. At this point, we could expect that the adsorption of hydrogen molecules on 1,5-biscorannulenecyclophane would show clear improvement compared with adsorption of hydrogen molecules in the system of simple stack with ILD of 4.8 Å. The distance of pairs C23-C26 and C23'-C26' is 12.85 Å, and the distance of pairs H35-H36 and H35'-H36' is 14.74 Å. These distances are pointed out because they are much larger than the diameter of corannulene molecule, which can also increase the space between intermolecules. Other than the potentially more available space for hydrogen molecules to get adsorbed, the dipole moment of 1,5-biscorannulenecyclophane is also larger than corannulene molecule (2.07 D experimentally, 2.15 D theoretically). DFT calculations with B3LYP yield 3.45 D at the level of 3-21G, and 2.69 D at the level of 6-31G. The higher dipole moment of 1,5-biscorannulenecyclophane can create a stronger dipole induced interaction between hydrogen and 1,5-biscorannulenecyclophane molecule, thus increases the hydrogen uptake capacity. Charge distribution on 1,5-biscorannulenecyclophane is also shown in Table 6.1.

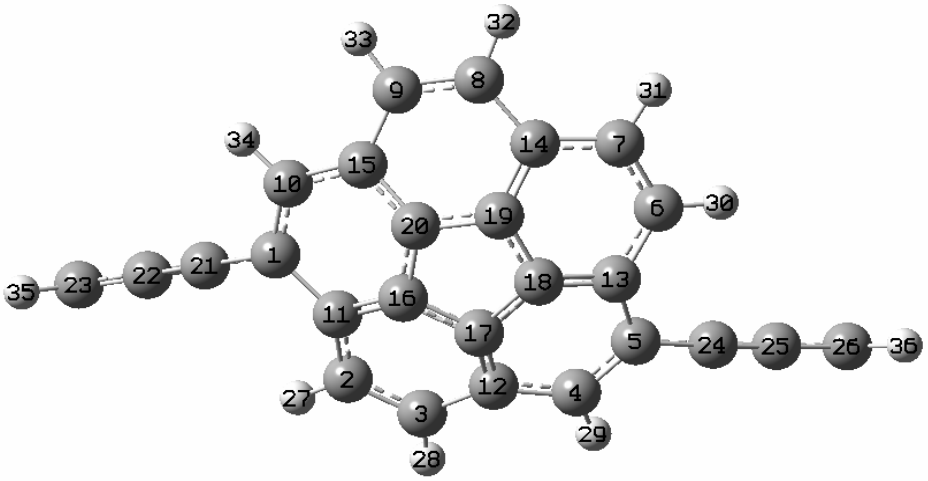

Figure 6.2. Labeled 1,5-biscorannulenecyclophane, optimized with B3LYP/6-31G

Table 6.1: Selective structure parameters (Å) and Mulliken charge distribution of 1,5-biscorannulenecyclophane* at B3LYP/6-31G

Cr-Cr		Cr-Cr		Cb-Cb		Ch-Ch	
C1-C1’	6.04	C6-C6’	7.72	C11-C11’	6.05	C16-C16’	7.65
C2-C2’	4.26	C7-C7’	8.76	C12-C12’	5.23	C17-C17’	7.25
C3-C3’	3.88	C8-C8’	9.57	C13-C13’	7.24	C18-C18’	8.21
C4-C4’	4.44	C9-C9’	9.21	C14-C14’	9.38	C19-C19’	9.25
C5-C5’	5.35	C10-C10’	7.32	C15-C15’	8.63	C20-C20’	8.89

atoms	Q	atoms	Q	atoms	Q	atoms	Q
C1,C1’	0.178	C10,C10’	-0.130	C19,C19’	-0.078	H28,H28’	0.127
C2,C2’	-0.120	C11,C11’	0.149	C20,C20’	-0.052	H29,H29’	0.145
C3,C3’	-0.146	C12,C12’	0.109	C21,C21’	-0.225	H30,H30’	0.138
C4,C4’	-0.123	C13,C13’	0.140	C22,C22’	-0.232	H31,H31’	0.129
C5,C5’	0.170	C14,C14’	0.121	C23,C23’	-0.023	H32,H32’	0.130
C6,C6’	-0.122	C15,C15’	0.106	C24,C24’	-0.211	H33,H33’	0.131
C7,C7’	-0.148	C16,C16’	-0.084	C25,C25’	-0.230	H34,H34’	0.145
C8,C8’	-0.147	C17,C17’	-0.062	C26,C26’	-0.024	H35,H35’	0.165
C9,C9’	-0.144	C18,C18’	-0.079	H27,H27’	0.141	H36,H36’	0.160

*The atom numbers correspond to Figure 6.2.

6.3 Intermolecular interaction

As we discussed in previous chapters that the adsorption of hydrogen in different adsorbent systems is attributed to VDW and dipole induced interactions between hydrogen molecules and adsorbent molecules. In chapter II, we have obtained the VDW interaction parameters between C atom and a single site model of hydrogen molecule, yielding $\varepsilon_{C\text{-}H}$ = 2.52 meV, $\sigma_{C\text{-}H}$ = 2.95 Å. The same VDW parameters will be used in MD simulations.

Similarly, additional interactions need to be included because although H_2 does not have a permanent dipole moment, the 1,5-biscorannulenecyclophane molecule is polar with theoretical of 2.69 D calculated at the B3LYP/6-31G level, as we mentioned in previous section. This permanent dipole moment of 1,5-biscorannulenecyclophane creates an induced dipole moment on H_2, enhancing the adsorption of hydrogen molecules on the 1,5-biscorannulenecyclophane system. Follow the same procedure of in chapter II, we can obtain the induced dipole interaction between hydrogen and 1,5-biscorannulenecyclophane. Equation (2.4) thus can be simplified to

$$\bar{\Gamma}_{ij} = -\frac{3727.98}{r^6}\ meV \tag{6.1}$$

This mean potential energy due to dipole-induced dipole interactions is added to the L-J potential for C-H_2 interactions. The overall potential of the sum of dipole-induced interaction and VDW interaction between C and one site hydrogen molecule is plotted in Figure 6.3 (b). Finally, the resulting potential energy is refitted yielding a new set of 12-6 interaction parameters that included the effects of curvature of the adsorbent molecule and the dipole-induced dipole interactions, as in Figure 6.3 (c). As a result, the 12-6 LJ

parameters ε_{C-H} = 6.15 meV and σ_{C-H} = 2.75 Å are used in the reported MD simulations. Figure 6.3 shows the fitting results of VDW parameters for C-H_2 interaction.

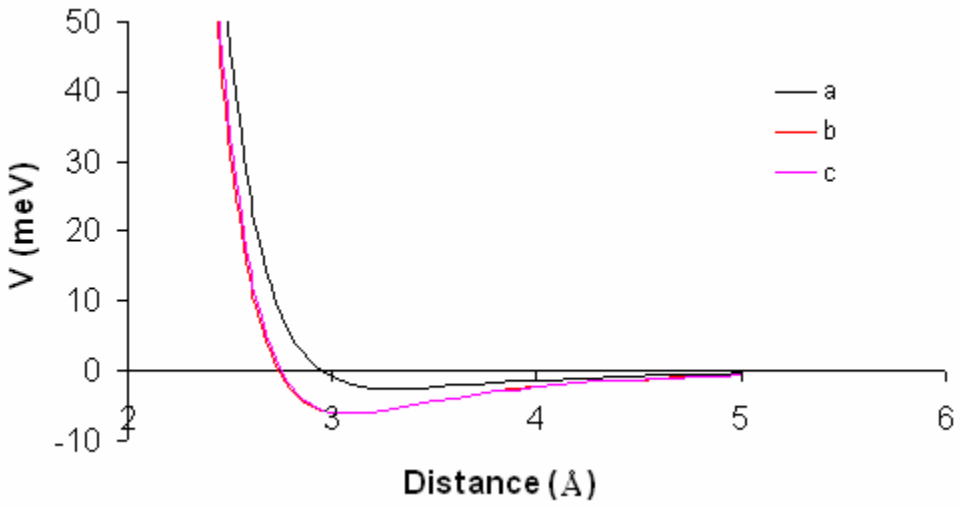

Figure 6.3. Fitting results of VDW parameters for C-H_2 interaction for adsorbent 1,5-biscorannulenecyclophane. (a) potential energy of VDW interaction C and one-site hydrogen molecule, ε_{C-H} = 2.52 meV, σ_{C-H} = 2.95 Å; (b) sum of dipole-induced interaction and potential energy of VDW interaction C and one-site hydrogen molecule; (c) fitting of potential energy of VDW interaction C and one-site hydrogen molecule, ε_{C-H} = 6.15 meV, σ_{C-H} = 2.75 Å

6.4 Partial optimizations of 1,5-biscorannulenecyclophane dimer

Before we perform MD simulations of adsorption of hydrogen molecules on 1,5-biscorannulenecyclophane system, we still need the information about the arrangement of 1,5-biscorannulenecyclophane molecules. Unfortunately, there is not such experimental data available yet. Here we are going to use the simple stack of 1,5-biscorannulenecyclophane molecules. By performing the partial optimization of 1,5-

biscorannulenecyclophane dimer we can get some idea about the possible arrangement of molecules, which will be adopted in later MD simulations of hydrogen adsorption.

Figure 6.4 (a) through (d) show the partial optimization results of 1,5-biscorannulenecyclophane dimer at the level of B3LYP/3-21G. On these partial optimizations, only x-coordinates, in (a) and (b), or y-coordinates, in (c) and (d) of dimer are allowed to change. The difference between (a) and (b) is that, in (a) one jaw opens up and the other down, while in (b) both jaw open up. The energies are –3964.64602 Hatrees and –3964.64471 Hatrees for (a) and (b), respectively. Energetically, dimer in (a) is more favorable and the distance between the center of mass of two molecules is 13.54 Å. In (c) and (d), only y-coordinates are allowed to change. In (c) two molecules are totally overlap in along Y-axis, while in (d) two molecules are jaw-to-jaw. The optimized structures of these two dimers have electronic energies of –3964.64942 Hatrees and –3964.64741 Hatrees. Conformation (c) is more stable than conformation (d) and the distance between the centers of mass of these two molecules in (c) is 8.24 Å. For the purpose of the MD simulations of adsorption of hydrogen on 1,5-biscorannulenecyclophane system, we will build a cell with PBC in three dimensions. The arrangements of molecules depend on our partial optimization results. Along X-axis, molecules arrange repeatedly as shown in (a). Along Y-axis, molecules arrange totally overlapped, as shown in (c).

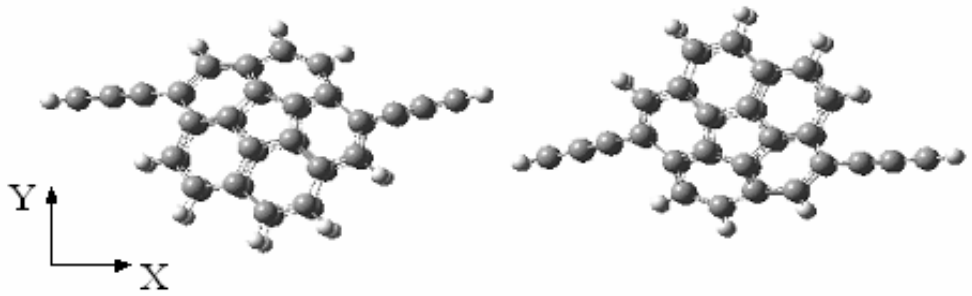

(a)

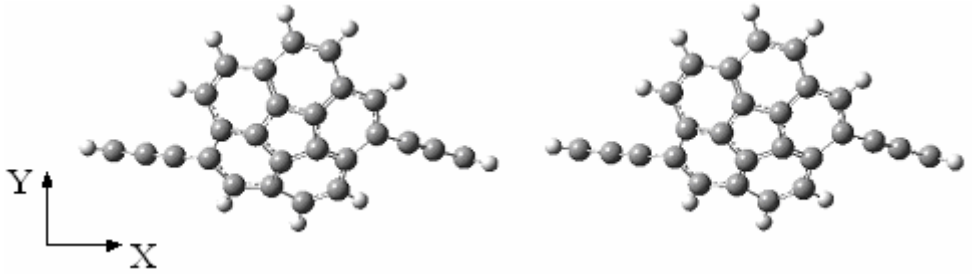

(b)

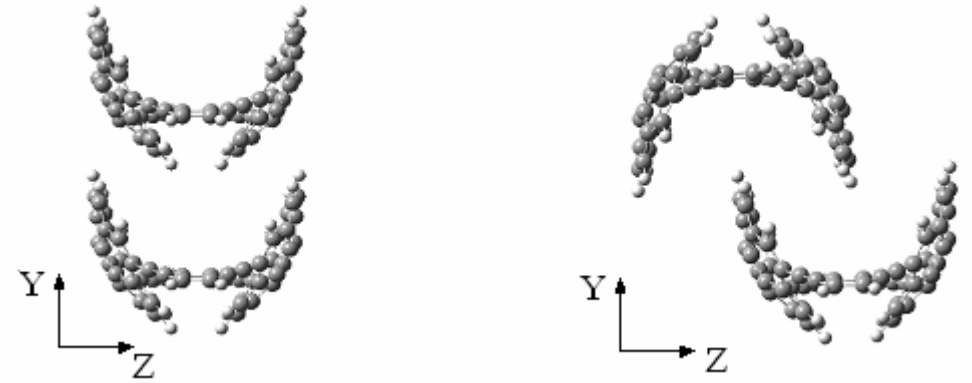

(c) (d)

Figure 6.4. Partial optimization of 1,5-biscorannulenecyclophane dimer with B3LYP/3-21G. (a) x-coordinates allowed to change, one jaw up and the other down, (b) x-coordinates allowed to change, both jaws up, (c) y-coordinates allowed to change, both jaws up and two molecules overlapped along Y-axis, (d) y-coordinates allowed to change, two jaws open to each other

For the simulation cell, the arrangement in Z-axis needs to be determined. Figure 6.5 shows the arrangement of 1,5-biscorannulenecyclophane in YZ plane. Along Z-axis, the molecules are arranged with jaw of the molecule toward to up and down repeatedly. Based on previous ab initio calculation of corannulene dimer, which yielded an ILD value of 4.8 Å at the level of B3LYP/6-311G(d,p), the separation between the center mass of 1,5-biscorannulenecyclophane dimer along Z-axis is 14.0 Å, and at this value of separation, the distance between two center five-member rings from two neighbor molecules is 4.8 Å, as shown in Figure 6.5.

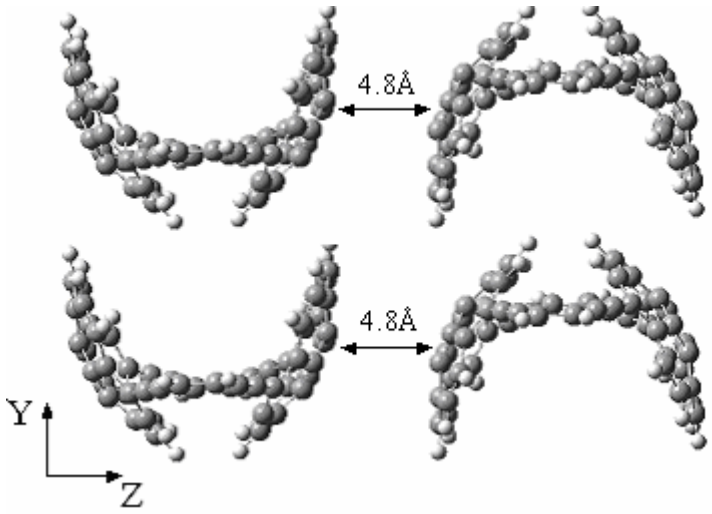

Figure 6.5. Arrangement of 1,5-biscorannulenecyclophane in YZ plane of the MD simulation cell

Overall, we now are able to build our MD simulation cell for the distribution of adsorbent molecules. A tetragonal cell with 27.08 × 16.48 × 56 $Å^3$ containing 16 1,5-biscorannulenecyclophane molecules is built. These 16 molecules are distributed in two

layers along Y-axis, with 8 molecules in each layer. When used these molecules as adsorbent for hydrogen adsorption, the dimension of b parameter is changed according to the predicted desired pressure in the gas phase. In other word, the cell has the dimensions of 27.08 × b × 56 $Å^3$, with 16 1,5-biscorannulenecyclophane molecules located at the bottom of the cell. Initially, hydrogen molecules are distributed above the adsorbent layers randomly. The simulation produce is same as in previous sections as hydrogen adsorption in corannulene and Li-doped corannulene complex.

6.5 MD simulations of hydrogen adsorption

6.5.1 Snapshot of hydrogen adsorption

Figure 6.6 shows one snapshot of hydrogen adsorption on 1,5-biscorannulenecyclophane adsorbent layers, at the temperature of 273 K and pressure of 127 bar. The hydrogen adsorption isotherms at temperature of 273 K and 300 K are shown in Figure 6.7.

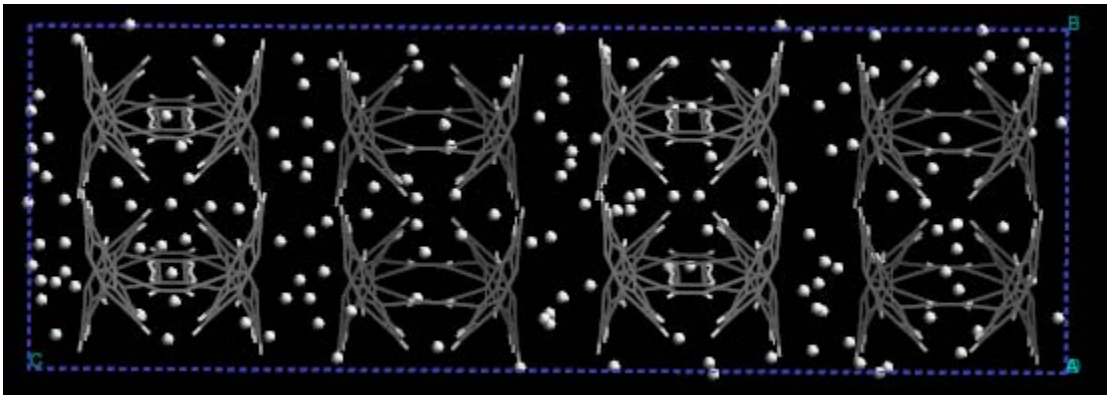

Figure 6.6. Snapshot of hydrogen adsorption on 1,5-biscorannulenecyclophane adsorbent layers at 273 K and 127 bar

6.5.2 Hydrogen adsportion

6.5.2.1 Hydrogen adsportion

Overall, hydrogen adsorption behaviors on 1,5-biscorannulenecyclophane are similar to what we have observed on corannulene and lithium atoms doped corannulene complexes. We can see that, (1) at a given temperature of either 273 K or 300K, hydrogen uptake is almost linear response to the increase of the gas phase pressure; (2) 1,5-biscorannulenecyclophane adsorbent system at low temperature has higher uptake capacity than at high temperature. At 273 K, hydrogen uptake capacities are 1.87 wt% at 62 bar, 2.42 wt% at 90 bar, 2.74 wt% at 105 bar, and 3.16 wt% at 127 bar. At 300 K, hydrogen uptake capacities are 1.55 wt% at 67 bar, 2.15 wt% at 92 bar, 2.37 wt% at 107 bar, and 2.76 wt% at 125 bar. According to the prediction, the hydrogen uptake at 100 bar is about 2.63 wt% at 273 K and 2.26 wt% at 300 K. If the linearity can extend to higher pressure, DOE target of 6.5 wt% can be reached at 294 bar at 273 K, and 309 bar at 300 K.

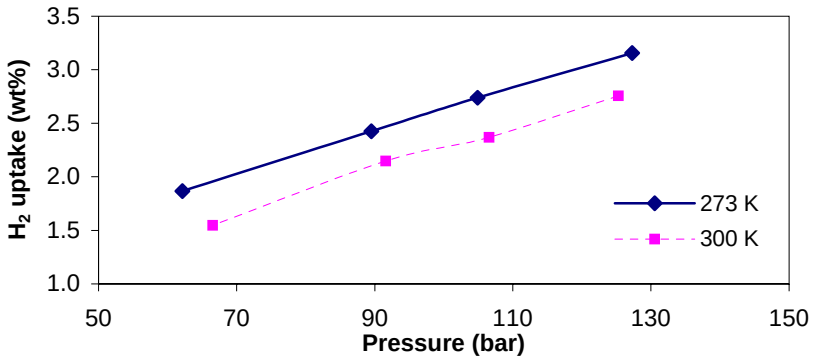

Figure 6.7. Hydrogen adsorption isotherm on 1,5-biscorannulenecyclophane adsorbent

6.5.2.2 Distribution of hydrogen on 1,5-biscorannulenecyclophane adsorbent

Table 6.2 shows the ratio of hydrogen adsorbed in the open jaw of 1,5-biscorannulenecyclophane at different conditions. About 60% of adsorbed hydrogen at different conditions of temperatures and pressures are distributed in the open jaw region of 1,5-biscorannulenecyclophane. Two reasons might contribute to this situation. One is that the jaw region has more available volume for hydrogen to get adsorbed, and the other is that the region inside the jaw is more attractive to hydrogen molecules due to the curvature of 1,5-biscorannulenecyclophane molecule.

Table 6.2: Ratio of hydrogen adsorbed in the open jaw region of 1,5-biscorannulenecyclophane at different conditions

Conditions	Total number of H_2 adsorbed	Number of H_2 in open jaw region	Percentage of H_2 in open jaw region
273 K, 127 bar	168	96	0.57
273 K, 105bar	145	86	0.59
273 K, 90 bar	128	75	0.59
273 K, 62 bar	98	58	0.59
300 K, 125 bar	146	88	0.60
300 K, 107 bar	125	75	0.60
300 K, 92 bar	113	69	0.61
300 K, 67 bar	81	50	0.62

6.5.3 Comparison of hydrogen adsorption

As we mentioned previously, the idea of the molecular modification is to enhance hydrogen adsorption on adsorbents. Here we can see the effect of the molecular modification to corannulene on the hydrogen adsorption. Figure 6.8 shows the comparison of hydrogen uptake on 1,5-biscorannulenecyclophane system with hydrogen

uptake on different values of ILD of corannulene system at 273 K and 300 K. All solid curves are adsorption isotherms at 273 K, and dot curves are adsorption isotherms at 300 K. Figure 6.8 (a) shows the comparison with the optimum ILD of corannulene (4.8 Å). It is very clear that hydrogen uptake capacities on 1,5-biscorannulenecyclophane system are much higher that on corannulene with optimum ILD of 4.8 Å at the same conditions of temperature and pressure. According to the prediction, the hydrogen uptake capacities for corannulene with ILD of 4.8 Å are 0.83 wt% at 273 K and 0.75 wt% at 300 K. The hydrogen adsorption on 1,5-biscorannulenecyclophane at 100 bar is three times or more as on corannulene (with ILD of 4.8 Å). The differences are 1.80 wt% and 1.51 wt% at 273 K and 300 K respectively.

The reason that 1,5-biscorannulenecyclophane has significant higher hydrogen adsorption capacity is that modification leads to large volume inside the molecule. The linker ($-C \equiv C - CH = CH - C \equiv C -$) connects two pairs of rim carbons of corannulene at C1-C1' and C5-C5', respectively. This leads to the jaw shape of molecule. The distance between two symmetry carbon atoms of the σ_V plane is listed in Table 6.1. Most of the distance of these pair carbons is larger than 7 Å, except for those pairs at the bottom of the jaw, which average at 4.99 Å. Even this value is larger than the optimum value of separation of corannulene dimer. The largest separation of pair carbons is about 9.57 Å. According to the shape of the molecule of 1,5-biscorannulenecyclophane, we can estimate the average separation of two corannulene molecules of 1,5-biscorannulenecyclophane by averaging the distance of all five pairs of Cb-Cb, which is 7.3 Å. This value is about 2.5 Å larger than the optimum separation distance of

corannulene dimer. Recall that in Chapter IV, we have studied hydrogen adsorption on larger separation distance of corannulele (with ILD of 6.0 and 8.0 Å), we can expect that hydrogen adsorption capability on 1,5-biscorannulenecyclophane might be between hydrogen adsorption on these two systems at the same condition of pressure and temperature, since the volume of the jaw of 1,5-biscorannulenecyclophane is open to hydrogen adsorption.

Figure 6.8 (b) shows the comparison of hydrogen adsorption on 1,5-biscorannulenecyclophane with those of on corannulene with ILD of 6.0 and 8.0 Å both at 273 K and 300 K. It is clear that in the range of pressure studied at both temperatures, hydrogen adsorption capabilities of 1,5-biscorannulenecyclophane are indeed in between of hydrogen adsorption capabilities of corannulene with ILD of 6.0 and 8.0 Å. For example, at pressure of 100 bar, hydrogen adsorption capabilities are, (1) 2.63 wt% on 1,5-biscorannulenecyclophane, 2.10 wt% for corannulene with ILD of 6.0 Å, and 3.41 wt% for corannulene with ILD of 8.0 Å, at 273K; and (2) 2.26 wt% on 1,5-biscorannulenecyclophane, 1.72 wt% for corannulene with ILD of 6.0 Å, and 2.95 wt% for corannulene with ILD of 8.0 Å, at 300 K. On the other hand, to reach DOE target of 6.5 wt%, the pressures needed at 273 K are 294 bar for 1,5-biscorannulenecyclophane, 361 bar for corannulene with ILD of 6.0 Å, and 228 bar for corannulene with ILD of 8.0 Å; and at 300 K 309 bar for 1,5-biscorannulenecyclophane, 408 bar for corannulene with ILD of 6.0 Å, and 253 bar for corannulene with ILD of 8.0 Å.

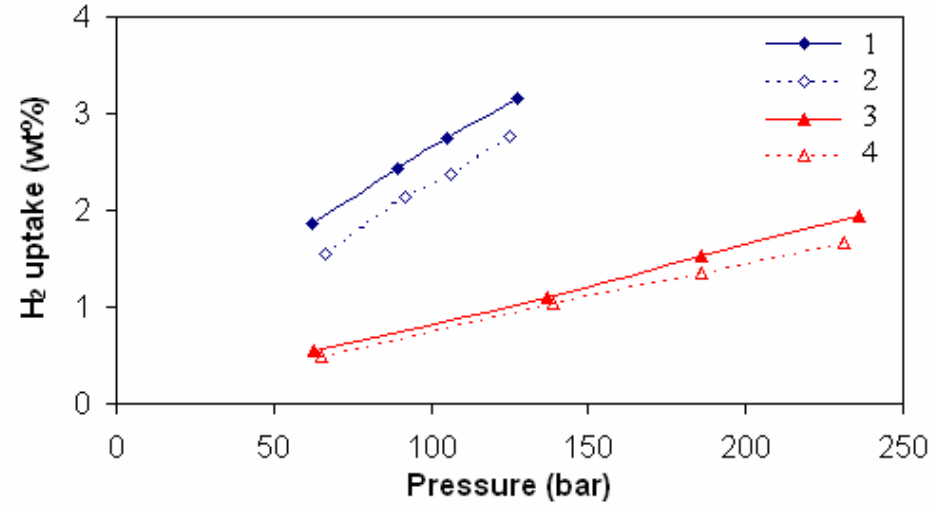

(a)

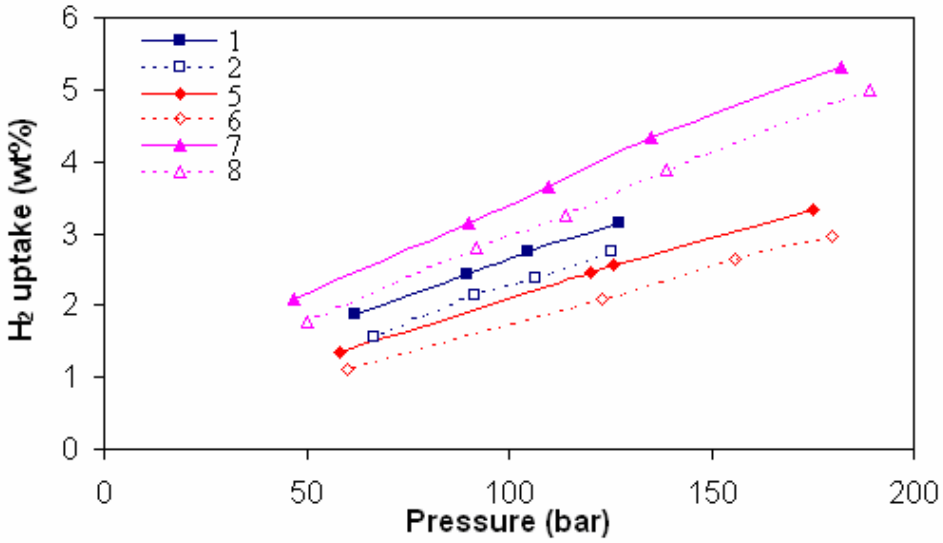

(b)

Figure 6.8. Comparison of hydrogen uptake on 1,5-biscorannulenecyclophane with hydrogen uptake on undoped corannulene at different values of ILD at temperatures of 273 K and 300 K. (a) comparison with optimum value of ILD of $C_{20}H_{10}$, (b) comparison with higher values of ILD of $C_{20}H_{10}$

Curve 1: 273 K, H_2 uptake on 1,5-biscorannulenecyclophane
Curve 2: 300 K, H_2 uptake on 1,5-biscorannulenecyclophane
Curve 3: 273 K, H_2 uptake on $C_{20}H_{10}$ with ILD=4.8 Å
Curve 4: 300 K, H_2 uptake on $C_{20}H_{10}$ with ILD=4.8 Å
Curve 5: 273 K, H_2 uptake on $C_{20}H_{10}$ with ILD=6.0 Å
Curve 6: 300 K, H_2 uptake on $C_{20}H_{10}$ with ILD=6.0 Å
Curve 7: 273 K, H_2 uptake on $C_{20}H_{10}$ with ILD=8.0 Å
Curve 8: 300 K, H_2 uptake on $C_{20}H_{10}$ with ILD=8.0 Å

6.6 Conclusions

1,5-biscorannulenecyclophane is modification of corannulene by bridging two corannulene molecules with organic linkers. The modified molecule has symmetry of σ_v. The average distance between the symmetric carbon pair is about 7.3 Å. 1,5-biscorannulenecyclophane has large intramolecular volume which is available for hydrogen adsorption. MD simulations of hydrogen adsorption is predicted to show enhanced hydrogen adsorption capacities compared to the hydrogen adsorption on corannulene at the similar conditions of temperature and pressure. Hydrogen adsorption on 1,5-biscorannulenecyclophane has capacity that is similar to the system of corannulene with ILD value of between 6.0 Å and 8.0 Å. According to the prediction, DOE target of 6.5 wt% can be reached at 294 bar at 273 K, and 309 bar at 300 K. On the adsorbed hydrogen molecules, about 60 % are adsorbed in the region of intramolecular area.

CHAPTER VII

INTRODUCTION – ION TRANSPORT IN SOLID MATERIALS

Ionic transport is important not only in power source devices such as batteries and fuel cells, but also in biological systems where ion channels are among the most common vehicles for ion transport. In this study we focus on understanding mechanisms of ion transport for electrolyte materials useful for lithium-ion batteries.

7.1 Development of lithium ion batteries

7.1.1 Comparison of various rechargeable batteries

Electricity is one of the most important discoveries in the last 400 years. However, electricity only became useful to humanity in late 1800s after Alessandro Volta's experiment of generating electricity by creating a static charge. Table 7.1 show the main history of battery development till the early of this century.[201] A battery is a system of changing chemical energy to electric energy. Normally, a battery is composed of several electrochemical cells that are connected in series and/or in parallel to provide voltage and capacity. Each cell has three components, which are the positive electrode, the negative electrode, and electrolyte solution. When these two electrodes are connected externally, the chemical reactions proceed at both electrodes and provide electric energy for the external device. Although battery development has been a long history, it did not become widely commercialization until past 60 years.

Table 7.1: History of battery development [201]

Time	Researcher	Achievement
1600	Gilbert (England)	Establishment of electrochemistry study
1791	Galvani (Italy)	Discovery of 'animal electricity'
1800	Volta (Italy)	Invention of the voltaic cell
1802	Cruickshank (England)	First electric battery capable of mass production
1820	Ampère (France)	Electricity through magnetism
1833	Faraday (England)	Announcement of Faraday's Law
1836	Daniell (England)	Invention of the Daniell vell
1859	Planté (France)	Invention of the lead acid battery
1868	Leclanché (France)	Invention of the Leclanché cell
1888	Gassner (USA)	Completion of the dry cell
1899	Jungner (Sweden)	Invention of the nickel-cadmium battery
1901	Edison (USA)	Invention of the nickel-iron battery
1932	Shlecht & Achermann (Germany)	Invention of the sintered pole plate
1947	Neumann (France)	Successfully sealing the nickel-cadmium battery
Mid 1960	Union Carbide (USA)	Development of primary alkaline battery
Mid 1970		Development of valve regulated lead acid battery
1990		Commercialization nickel-metal hydride battery
1992	Kordesch (Canada)	Commercialization reusable alkaline battery
1999		Commercialization lithium-ion polymer
2002		Limited production of proton exchange membrane (PEM) fuel cell

Advances in materials science and engineering design technology greatly improve the development and application of primary and secondary batteries.[202] The applications of batteries at home have greatly expanded to different purposes, for example, household as telephones, detectors, and so on, entertainment as compact disk players, ipod, etc, personal hygiene and health as toothbrushes, blood pressure monitors etc, and portable electronic devices, watches, cameras, cell phones, laptop computers. Also large size battery packs have been used as the uninterruptible power supply in public building,

factories, office blocks, telephone exchanges. More recently, large primary or rechargeable batteries have been widely used in the defense field, including submarine traction batteries, missiles, in space vehicles like satellites and space probes, in solar energy storage for remote area power supplies and navigation beacons, and in electric and hybrid vehicles.[202]

Different battery systems can be used for the purposes of these applications if we do not consider the weight, volume, safety and other issues of these systems. However, the development of new information technology has greatly changed our society and now we have to look for lighter and smaller battery systems for the mobile electronic appliances in order to put them in our pocket. Lighter and smaller battery systems require more advanced battery systems. New materials and improved engineering design technologies need to be investigated and invented for such battery systems. In the view of economy and material saving, rechargeable batteries are more desirable than primary batteries. Figure 7.1 shows the energy density per unit volume (Wh l^{-1}) and per unit weight (Wh kg^{-1}) of various rechargeable batteries. [203] Table 7.2 shows the detailed information of the electrodes, electrolyte, battery reaction mechanism and nominal voltage of these different rechargeable batteries.[202]

7.1.1.1 Lead-acid batteries

Although continuous improvement in materials of construction, design and manufacture has been made to lead-acid batteries, lead-acid batteries still have low energy density. The theoretical specific energy of the lead-acid battery is 170 Wh kg^{-1}, while in practice they can only deliver 30-50 Wh kg^{-1}, as shown in Figure 7.1. Two

main reasons cause the low practical specific energy, (1) the mass of the inactive components, such as cell case, grids, current collector bars, separators, terminals, and so on; (2) slow diffusion processes in the porous reactants and low conductivity of the discharge product ($PbSO_4$). Also, low recycling life, storage problem (cannot be stored in a discharged condition), environmentally unfriendly, and potential spillage of lead acid have made lead-acid battery unfavorable for the future advanced battery systems.

7.1.1.2 Nickel-cadmium batteries

In practical use, nickel-cadmium batteries have similar or slight higher specific energy as/than lead-acid batteries, depending on the manufactures and applications. Also, these batteries have better performance at high rate and low temperature conditions, longer recycling life, lower maintenance, compared to lead-acid batteries. However, the disadvantages of nickel-cadmium batteries hinder them as the choice for the future advanced batteries. These disadvantages include the low energy density, memory effect, high cost (up to 10 times that of lead-acid), high self-discharge, and more importantly environmentally unfriendly concern, due to toxic cadmium content.

7.1.1.3 Nickel-metal hydride batteries

The basic principle of nickel-metal hydride batteries is that hydrogen may be stored reversibly in the form of a metal hydride as the negative electrode. Nickel-metal hydride batteries have been steadily improved since the development of advanced hydride alloys in the 1980s. Since then, nickel-metal hydride batteries have been successful and been replacing nickel cadmium batteries in markets due to the advantages they have. These advantages include high specific energy of up to 100 Wh kg^{-1}, less

memory effect, simple storage and transportation, and use of environmentally friendly metals, flat discharge curve. However, shortcomings are also significant since nickel-metal hydride batteries are nickel based technology. Also, these batteries have disadvantages of limited load ability, high self-discharge rate.

7.1.1.4 Lithium ion/polymer batteries

Rechargeable lithium ion/polymer batteries are an entirely new class of battery system, which was first developed with high energy density and high discharge voltage (3.7 V) and introduced into the market place as early as in 1991 in Japan.[204] They are replacing alkaline batteries for a wide range of applications both in the portable electronics field and much larger cells and modules. A little bit more detailed information will be provided next.

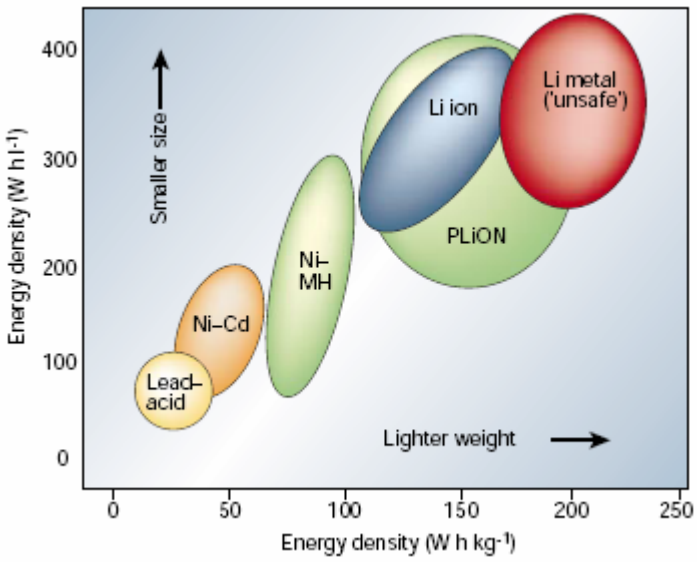

Figure 7.1. Comparison of the different battery technologies in terms of volumetric and gravimetric energy density. (Adapted by permission from Macmillan Publishers Ltd: Nature, 414, 2001, 359-367[203], copyright 2001)

Table 7.2: Various secondary batteries and their characteristics

Battery system	Reaction*/electrolyte	Nominal voltage (V)
Lead-acid	cathode : PbO_2 $PbO_2 + 4H^+ + SO_4^{2-} + 2e^- \leftrightarrow PbSO_4 + 2H_2O$ anode : Pb $Pb + SO_4^{2-} \leftrightarrow PbSO_4 + 2e^-$ total reaction : $PbO_2 + 2H_2SO_4 + Pb \leftrightarrow 2PbSO_4 + 2H_2O$ electrolyte : H_2SO_4 aqueous solution	2
Ni-Cd	cathode : NiOOH $2NiOOH + 2H_2O + 2e^- \leftrightarrow 2Ni(OH)_2 + 2OH^-$ anode : Cd $Cd + 2OH^- \leftrightarrow Cd(OH)_2 + 2e^-$ total reaction : $2NiOOH + Cd + 2H_2O \leftrightarrow 2Ni(OH)_2 + Cd(OH)_2$ electrolyte : KOH aqueous solution	1.2
Ni-MH	cathode : NiOOH $2NiOOH + 2H_2O + 2e^- \leftrightarrow 2Ni(OH)_2 + 2OH^-$ anode : Hydrogen adsorbed alloy $H_2 + 2OH^- \leftrightarrow 2H_2O + 2e^-$ total reaction : $2NiOOH + H_2 \leftrightarrow 2Ni(OH)_2$ electrolyte : KOH aqueous solution	1.2
Lithium ion	cathode : CoO_2 $Li^+ + CoO_2 + e^- \leftrightarrow LiCoO_2$ anode : C + Li $Li(C) \leftrightarrow Li^+ + e^-$ total reaction : $Li(C) + CoO_2 \leftrightarrow LiCoO_2$ electrolyte : Organic electrolyte and Li salt	3.7

* Discharge process from left to right; charge process from right to left.

7.1.2 Lithium ion batteries

7.1.2.1 Principle of lithium ion batteries

Rechargeable lithium ion batteries have been considered as a choice for the alternative energy storage technology after the first successfully commercial lithium ion secondary battery was introduced by SONY about 15 years ago.[205] Compared to the long period of the development and evolution of other types of rechargeable batteries, the history for the development and optimization of lithium ion/polymer batteries, especially lithium polymer batteries and newly other rechargeable lithium solid state batteries, is very short. So the improvement of rechargeable lithium batteries will definitely occurs in the near future, with the development of more advanced materials for electrodes and electrolyte, as well as the engineering design.[206]

Typically, commercialized lithium ion batteries are consisted of a lithium metal oxide cathode, e.g. $LiCoO_2$, a graphite anode, and a separator soaked with a liquid organic solution of a lithium salt, e.g. $LiPF_6$, in an organic solvent mixture, e.g. an ethylene carbonate-dimethylcarbonate, EC-DEC.[207] These light and compact lithium ion batteries have an operating voltage of around 3.7 V with the energy density up to 250 Wh kg^{-1}. The principle and mechanism of the operation of the lithium ion batteries are shown in Figure 7.2, [208] where both the charge and discharge processes are included. The electrochemical charge/discharge reactions are given in Table 7.2. Lithium ions are shuttled between anode and cathode during charge and discharge processes. During discharge process, lithium ions intercalate into cathode, $LiCoO_2$ in this case, from electrolyte liquid, and simultaneously an equivalent amount of lithium ions deintercalate

from anode, graphite in this case into electrolyte liquid. The process reverses during the charge process. Electrolyte is not consumed by the charge-discharge reaction in lithium ion batteries.

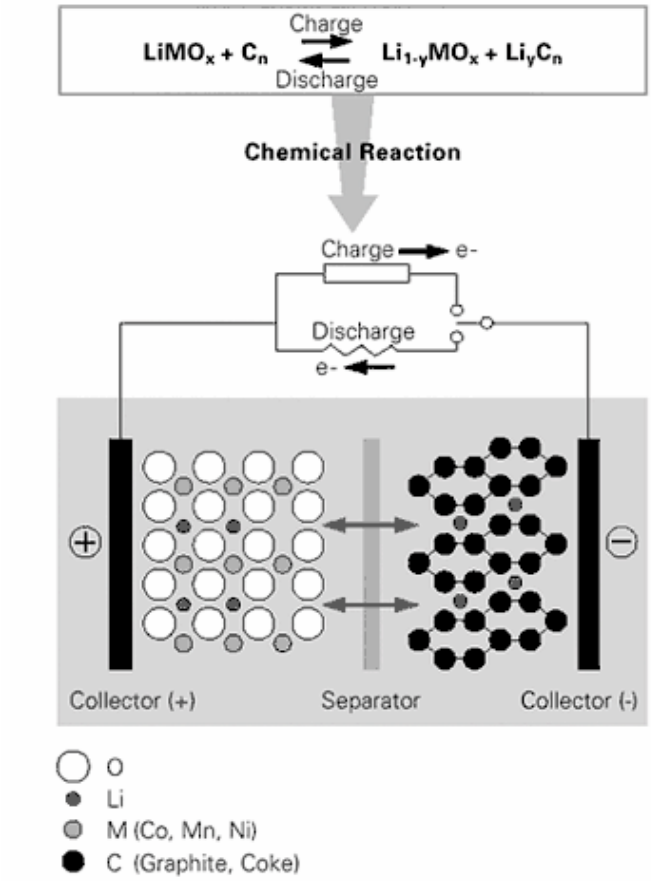

Figure 7.2. Principle and mechanism of lithium ion battery [208]

Applications of lithium ion batteries can be divided into two distinct areas. First, small batteries are needed for the consumer market for portable electronic devices, including cellular phones, laptops, PDAs, and so on, because of the characteristics of

high-energy, high-power, long-life power sources. Second, larger battery systems and modules are requested for electric vehicles (EV) or hybrid-type electric vehicles (HEV) and dispersed energy storage, where the cost of the active components, i.e. electrodes, will be a much more significant factor than in first category. Demand and competition drive the quest of the advanced batteries for higher storage capacity, longer operating times, faster recharging times, wider operating temperature range, easier storage and transportation, better safety, and other optimization of performance. To reach these goals, directions and solutions for the research and development of more advanced lithium ion batteries include that, (i) advances in nanostructured materials provide a chance to improve both cathode and anode performance, especially the capacity of anode; (ii) new in situ characterization techniques are helping to identify material problems in a way of rapid assessment of possible solutions to replace existing materials; and (iii) advanced computational modeling and simulation rapidly predict and guide the new combinations of materials and designs.[205] Here, information about the development of cathode and anode will be brief overviewed, while the development of the electrolyte will be provided in next section.

7.1.2.2 Cathode

For cathode materials in lithium ion batteries, materials should posses some principal characteristics. These features include high discharge voltage (large negative Gibbs free energy of discharge reaction), high energy capacity (low molecular weight of the host structure while accommodating large amount of lithium), high power density (high lithium diffusion coefficient in host structure), long cycle life (small structural

modifications during intercalation and deintercalation), as well as chemically stable, non-toxic and inexpensive.[204] Cathode materials studied include TiS_2, [209] layered $LiCoO_2$ with α-$NaFeO_2$ structure, [210-212] Li_xMnO_2 and $Li_x(Mn_{0.9}Co_{0.1})O_2$, [213-215] $Li_xMn_2O_4$, [216-223] crystalline/amorphous V_2O_5, [224-227] $Li_xFe_yO_z$, [228] iron phosphates, [229,230] and so on.

Among these different types of materials, $LiCoO_2$ has been successfully utilized for commercial batteries in spite of its high price.[210,231,232] $LiCoO_2$ produces a high and up to about 4.3 V vs. Li/Li^+ when it is oxidized during charge. The specific capacity is close to 140 Ah kg^{-1}, and capacity density of 690 Ah l^{-1}.[233] $LiNiO_2$ has a large capacity (up to 200 Ah kg^{-1}) with a high operating voltage and is far cheaper than $LiCoO_2$, as a cathode candidate in commercial batteries.[231,232] However, the drawbacks of less stable in the overcharge state [233] and serious issue of electrolyte decomposition [234] hinder its practical use, unless these problems can be solved. Another candidate for cathode of lithium ion batteries is the spinel-manganese oxide, $LiMn_2O_4$, which has also been extensively studied.[216-223] The main advantages of $LiMn_2O_4$ include the high working voltage, high stability of the electrolyte and the expected low price. However, the disadvantages are also significant compared to $LiCoO_2$, including the small discharge capacity, low chemical stability itself, and a shorter recycling life.

Research for next generations of the cathode materials has continuously performed and $LiCo_xNi_yO_2$ (x = 0.1-0.3, y = 0.9-0.7), or incorporation of certain amount of Al to these materials (to improve the performance) is proposed.[212,235-237] Low price while high capacity and flat operating voltage of some phosphates, sulfates or amorphous

hydroxides of Fe are also attractive.[230,238,239] Another class of layer structure compound like $LiNi_xMn_yO_z$ are also attractive due to their high operating voltage (so-called "5 V class materials") while with no or small sacrifice in capacity.[233,234] However, for the last two classes of materials, the decomposition of electrolyte has to be prevented when incorporated, due to the high oxidizing potential during the charge process.

7.1.2.3 Anode

Normally, anode is the limiting material for the capacity of lithium ion batteries. The first used anode for lithium ion batteries is lithium metal, which can be plated with high efficiency. However, there exist serious issues with lithium metal anode. Lithium metal is very reactive element and brings the likely solvable safety issue when cycled. Lithium ion batteries with lithium metal anode experience loss of some of the plated lithium grains and reduce the energy capacity. Also, formation of dendrite might lead to short circuits, and the cell may overheat because of the highly exothermic passivation reaction, more worse thermal runaway may occur due to the low melting point of lithium metal.[206]

To solve the safety issue of the lithium batteries, replacement for lithium metal anode has been greatly studied. Different materials have been proposed as anode. These materials include polyacenes, [240,241] hard carbons, [232] low-temperature mesophase carbons, [242,243] metallic silicon, [232] metal nitrides, [244] tin oxides and related materials, [232] silicon-containing carbons, [245,246] and so on. These materials in some point enhance the safety of lithium ion batteries, but major problems still exist. For example, volume significantly changes during charge and discharge, which produces enormous constraints

on the metal grains and induces heavy fragmentation and poor cyclability. Or they have issues of low working voltage, low power, and low conductivity.

On the other hand, carbon materials have been successfully used as anode materials in lithium ion batteries.[217,247-257] These carbon materials have theoretical capacity of 372 Ah kg^{-1} and are categorized into (i) graphite, (ii) hard carbon (non-graphitized glass-like carbon), and (iii) soft carbon (easily changeable with heat treatment). The advantages include high negative operating potential, which is close to that of Li^+/Li, flat discharge performance, high-power availability, low initial charging capacity loss and safety. However, carbon nodes generally are capacity limited factor of lithium ion batteries and the diffusion of lithium ion between carbon layers is not fast enough.[204] Search for more advanced anode materials is one important factor for the development of lithium ion batteries. These works lead to the development of $Li_{2.6}Co_{0.4}N$ and its modification, [258-261] alloy anodes based on Sn, and Si, tin oxides, $InVO_4$, $FeVO_4$, and Brannerite-type MnV_2O_6.[262-274] Unfortunately, the factor of the working voltage of these alternative anodes that is significantly higher than Li metal anode makes them not very competitive, since the cell potential is reduced and so does the energy density. Also, stabilization of the structures of these oxide materials and improvement of the large capacity fade on cycling must be solved for practice use.[264]

7.2 Development of electrolytes for lithium ion/polymer batteries

7.2.1 Organic liquid electrolyte

Although the main characteristics of lithium ion batteries such as operating voltage, theoretical energy density, etc., are decided by the properties of the active materials used as the cathode and anode, the chemistry of the electrolyte often affects the performance of lithium ion batteries. An aqueous electrolyte does not work in lithium ions batteries because of two reasons. First, water will decompose as the charge or discharge voltage is higher than 3 V. Second, water will react with lithium in anode when lithium ions are reduced. As a result, various inorganic salts, for example, $LiClO_4$, $LiPF_6$, dissolved in organic liquids with electrochemical stability over a wide range of potential have been used as electrolytes. Organic electrolytes play two important roles in lithium ion batteries. First, organic electrolyte should provide fast transport of lithium ions in a wide range of temperature. Second, organic electrolyte should also form suitable surface films, solid electrolyte interface (SEI), especially on the surface of anode. The importance of the first role is straight. While, the properties of SEI , including porosity, electronic and ionic conductivity, are also important and relate to the organic solvents chosen. SEI also determines the kinetics of lithium ion intercalation and thus the performance of the anode and battery. Protection of anode by SEI from contact with organic solvents improves the recycling life of batteries.[275] Table 7.3 summarizes the physico-chemical properties of major solvents.[204,276,277]

Table7.3: Physical properties of solvents at 25°C

Solvent	mp(°C, 1atm)	bp(°C, 1atm)	Relative permittivity	Viscosity (cP)	Dipole moment (D)	DN[a]	AN[b]
Acetonitrile (AN)	-45.72	81.77	38	0.345	3.94	14.1	18.9
γ-Butyrolactone (BL)	-42	206	39.1	1.751	4.12	-	-
Diethylether (DEE)	-116.2	34.6	4.27	0.224	1.18	19.2	3.9
1,2-Dimeth-oxyethane (DME)	-58	84.7	7.2	0.455	1.07	24	-
Dimethylsulfoxide (DMSO)	18.42	189	46.45	1.991	3.96	29.8	19.3
1,3-Dioxolane (DOL)	-95	78	6.79[c]	0.58	-	-	-
Ethylene carbonate (EC)	39-40	248	89.6[d]	1.86[c]	4.8	16.4	-
Methylformate (MF)	-99	31.5	8.5[e]	0.33	1.77	-	-
2-methyltetra-hydrofuran (MeTHF)	-	80	6.24	0.457	-	-	-
3-Methylox-azolidin-2-one (MO)	15.9	-	77.5	2.45	-	-	-
Propylene carbonate (PC)	-49.2	241.7	64.6	2.53	5.21	15.1	18.3
Sulfolane (S)	28.86	287.3	42.5[c]	9.87[c]	4.7	14.8	19.3
Tetrahydrofuran (THE)	-108.5	65.0	7.25[c]	0.46[c]	1.71	20	8.0

[a] Donicity
[b] Acceptor number
[c] At 30°C
[d] At 40°C
[e] At 20°C

Choosing a good electrolyte is very important for lithium ion batteries. A good electrolyte should have good solubility of lithium salt, high ionic conductivity and low electronic conductivity, high chemical stability, high safety, low price, and good performance at low temperature and ambient temperature.

The performance of organic electrolytes is decided by the properties of the solvents listed in Table 7.3. For example, melting point (m.p.) and boiling point (b.p.) of the solvent relate to the operating temperature of the battery systems, and relative permittivity (dielectric constant) and viscosity of the solvent decides the ionic conductance of the electrolyte solution, [278] while donicity and acceptor number are indication of the interactions between solvent and cation, solvent and anion, respectively.[279] Based on these solvent properties, criteria of good electrolyte, and operating temperature of lithium ion batteries of between -20 and 60^{o}C, cyclic esters, such as propylene carbonate (PC) and ethylene carbonate (EC), and linear esters like dimethyl carbonate (DMC), diethyl carbonate (DEC), and 1,2-dimethoxyethane (DME) have been widely used in combination as liquid electrolyte. The molecular structures of these solvents are shown in Figure 7.3.

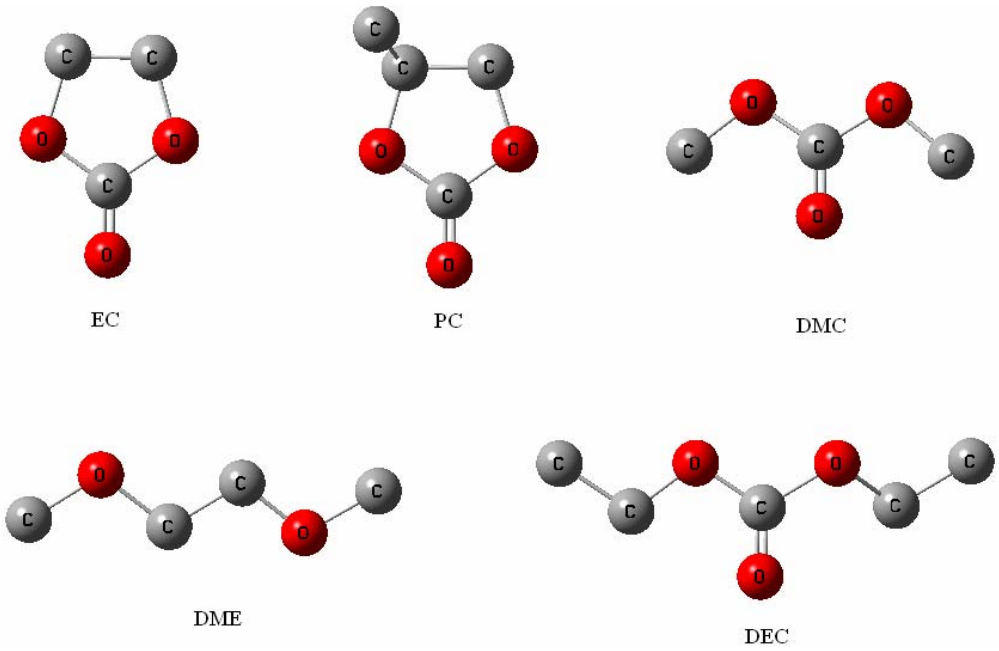

Figure 7.3. Structures of main organic solvents (hydrogen atom not shown)

EC has higher dielectric constant and lower viscosity than PC. EC is considered a better solvent. However, m.p. of EC is about 39-40^{o}C and is a solid in the lower operating temperature range. Mixtures of EC with other liquid solvents such as linear carbonates are required for practical applications of lithium ion batteries at low temperature. The choices of co-solvent are based on two factors, as we mentioned previously that electrolyte has two roles in lithium ion batteries. The considerations of ionic conductance and formation of SEI layer are important. Extensive studies of different combinations have been performed and Table 7.4 shows the conductivity of EC-based electrolytes at 25^{o}C.[204,276]

Table 7.4:Conductivity of EC-based electrolytes (EC:co-solvent, 1:1 by volume) at 25°C [204,276]

Electrolytic salt (1mol/dm^3)	Co-solvent	Specific conductivity (mS/cm)
$Li(CF_3SO_2)_2N$	DME	13.3
	DMC	9.2
	DEC	6.5
	MP	10.8
$LiCF_3SO_3$	DME	8.3
	DMC	3.1
	DEC	2.1
	MP	3.7
$LiPF_6$	DME	16.6
	DMC	11.2
	DEC	7.8
	MP	13.3

PC also has high dielectric constant for superior ionic conductivity over the wide range of the operating temperature of lithium ion batteries. But in the current commercialized lithium ion batteries using carbon anode, PC alone cannot form effective SEI films to separate anode and electrolyte.[280] PC solvent tends to co-intercalate into anode, resulting in large irreversible charge consumption and (partial) electrode destruction. In order to use PC in commercialized batteries, studies of liquid additives to PC have been investigated. These additives include chloroethylene carbonate (CEC), derivatives of halogen-substituted carbonates, various of unsaturated carbonates like vinylene carbonate, and ethylene/propylene sulfide.[281-286] These additives effectively improve the properties of SEI films.

In order to overcome the shortcomings of individual solvent, mixtures of various solvents with different characteristics are used in practical battery system. Different

compositions of electrolyte affect both the ionic conductivity of solvents and the electrode reaction in battery as well. [287-289] The ionic conductivity of these mixed solvents is less than 2×10^{-2} $S\cdot cm^{-1}$ in the range of operating temperature. From different investigations, including thermal stability and cyclic voltammetry, $LiPF_6$-based organic electrolyte has been chosen as the best performance in the commercialized batteries.[204]

Organic liquid electrolyte in lithium ion batteries now is a well-established technology. Mixtures of organic electrolytes show various advantages, including a wider usable liquid range of operating temperature, voltage windows up to about 5 V, good solubility of lithium salt, and better chemical stability and thermal stability, appropriate ionic conductivity. On the other hand, the disadvantages are also significant and these include the issues of potential gassing and leakage problems in batteries, the higher effort in assembling battery systems using metal can, toxicity and inflammability of organic solvents, as well as the expensive separator. The fundamental solutions to these issues are to substitute these organic liquid solvents with non-liquid solvents and now studies on non-liquid electrolytes have therefore become much more extensive in order to improve the high reliability of lithium ion batteries.

7.2.2 Polymer electrolytes

7.2.2.1 Features of polymer electrolytes

Polymer electrolytes have attracted extensive attraction because they can enable us to be free from electrolyte leakage and to provide a very thin battery. The development of polymer electrolyte has been in progress for last decades. So far, different kinds of polymer electrolytes have been proposed, which have been reviewed in several papers,

[290-294] but only a few of them are utilized in practical lithium battery systems, for example, mixtures of polyethylene oxide (PEO) and polyacrylamide gel (PAA) containing $LiPF_6$ and some liquid solvents. In a polymer based rechargeable battery, it normally contains a polymer electrolyte membrane, which acts both as the electrolyte and the separator. Free of liquid solvents implies that lithium polymer batteries can be more easily packed in light-weight plastic containers in any shape desired, unlike conventional batteries which require metallic casing.[204] Compared to liquid electrolyte assembled lithium ion batteries, lithium polymer batteries have several advantages.[295] First, manufacture of battery system is easier and simpler. Second, the battery system can be designed to various shapes and sizes in plastic containers as desired. Third, the battery system has higher energy density because of lighter total weight of the whole system. Forth, the battery system possesses higher safety, without leaking of corrosive or explosive liquids. Finally, the battery is expected to be less expensive and more easily scaled up.

In order to replace liquid solvent filled lithium ion batteries, the key component of lithium polymer batteries is the polymer electrolyte membrane. The development of the polymer electrolyte membrane should direct towards, (i) good mechanical properties in order for easy battery manufacture, (ii) compatible ionic conductivity for low internal resistance, (iii) high lithium ion transport to avoid concentration polarization, (iv) wide electrochemical stability to be compatible with high voltage cathode, (v) relatively low cost in order to get the market share, and (vi) non-toxic chemical composition for friendly environmental.[296] While, not any polymer electrolyte membrane has been found

to have all these features yet and a lot of research work has been performed in recent years to reach this goal. The development of polymer electrolytes can be divided into two categories, (i) solvent-free membranes, formed by mixing PEO together with a lithium salt, LiX, where X is preferably a large soft anion, and (ii) gel-type membranes, formed by trapping certain amount of liquid solutions in a polymer matrix, for example, poly(vinylidene fluoride) (PVDF) matrix.[295]

7.2.2.2 PEO based polymer electrolyte

Polymer electrolyte was first discovered by Wright et al. [297] and they made the first measurement of ionic conductivity in PEO in which certain amount of sodium salt had been dissolved. A few years later, Armand et al. [298] examined and developed lithium ion conductivity of mixed lithium salts in PEO and applied as practical battery components. This class of polymer electrolytes is intrinsic solid polymer electrolytes without liquid content and several reviews have been published describing the properties and modifications to these polymer electrolytes.[290-294] Figure 7.4 shows the segmental motion of the intrinsic solid polymer chain in the amorphous state and the mechanism of lithium ion conduction in polymer electrolyte.[299] In these polymer electrolytes, lithium ions are coiled by polymer chains and the anions are more loosely coordinated. It has been in agreement that diffusion of lithium ion is regulated by the lithium ion and polymer interaction involving cation ether oxygen coordination bonds, and local relaxation and segmental motion of the host polymer chains are the factors of the conductivity of the solid polymer electrolyte.[204,300,301]

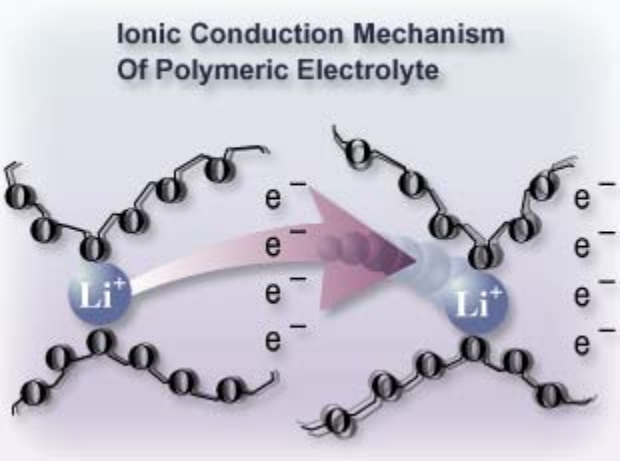

Figure 7.4. Mechanism of lithium ion conduction in intrinsic solid polymer electrolyte[299]

Unfortunately, lithium ions can only be released and diffuse to other sites when unfolding of the coordinating PEO chains occurs. Fast ion transport is not possible at temperature lower than glass-transition temperature, T_g, typical value of about 60^{o}C, because low temperatures lead to crystallization of the polymer in intrinsic solid polymer electrolyte. At temperature lower than melting point of polymer, ionic conductivity falls below 10^{-8} S cm^{-1} and does not have practical use.[294] Also, the lithium transference number is very low and typically of the order of 0.25.[302] Low transference number leads to the concentration polarizations and build-ups of lithium ions since the intercalation process is based on the transfer of lithium ions. Modification and improvement of solid polymer electrolyte have been studied to develop elastic and self-supporting polymer electrolytes. These methods include use of nanoparticulate fillers in minor proportions (<10 wt%), [303-310] bridging of PEO chains, [311] introduction of side chains, [312-319] blending

of different kinds of polymers, [320,321] and improvement of lithium salts.[315] With these methods, crystallinity of polymer at temperature lower than melting point can be suppressed in some degree. The conductivity can be orders-of-magnitude enhancements at temperature lower than melting point and 10^{-5}~10^{-4} S cm^{-1} at ambient temperature has been achieved. However, ionic conductivity is still far smaller than liquid electrolyte and cannot be used in practical. On the other hand, enhanced ionic conductivity is based on the loss of the crystallinity. Thus, the way to provide additional mechanical integrity, or incorporation of a secondary component to aggregate into distinct domains needs to be considered.[314,318,319]

7.2.2.3 Gel-type polymer electrolyte

Gel-type polymer electrolyte is the second generation with higher conductivity. Gel-type polymer electrolyte was first proposed by Perche et al.[322] The applications of gel-type polymers to polymer batteries were fully recognized by Abraham and Alamgir [323,324], and Nagasubramanian et al.[325] In gel-type polymer electrolyte, a certain amount of conventional non-aqueous electrolytes (up to 80 %) are incorporated and trapped within the structural polymeric network.[326] Solvents or solvent mixtures used are cyclic or linear carbonates such as PC, EC, DMC, and their derivatives, or cyclic esters such as γ-butyrolactone. Lithium ion transport in gel-type polymer electrolytes is different from the transport mechanism in dry polymer electrolyte, where it depends on the segmental motion of polymer. The lithium ion transport somehow resembles that of in organic liquid electrolyte due to the trapped organic solvent in the polymer matrix. The ionic conductivity as high as 10^{-3} S cm^{-1} has been achieved in several types at room

temperature or even lower.[204,295] Organic liquid solvents play dual roles to enhance the ionic conductivity: (1) they make segmental motion of polymer easier, and (2) they provide liquid-like feature of the liquid electrolytes. Besides the high ionic conductivity, gel-type polymer electrolyte batteries improve the transference number to the order of about 0.5. Typical examples of such gel-type polymer electrolytes such as mixtures of $LiPF_6$-PC-EC solution trapped into a poly(vinylidene fluoride) (PVdF) matrix, and $LiPF_6$-EC-DMC solution with Al_2O_3 (6 %) trapped into a poly(acrylonitrile) (PAN) matrix are well developed.[327]

A second approach for preparation of gel-type polymer electrolyte involves the idea of lithium ion transport inside the pores and is referred to as the Bellcore process.[328-330] Such gel-type polymer electrolyte contains two polymers, while one polymer have good affinity for the liquid solvent, which is trapped in the polymer network and the other has no affinity, but improve the mechanical properties. As an example of such gel-type polymer electrolyte, an inert-matrix copolymer system, poly(vinylidene fluoride-co-hexafluoropropylene) (PVdF-HFP), supports a two-phase morphology of solvent-swollen polymer and pores of "free" solvent.[331] A conductivity of 3.7×10^{-3} S cm^{-1} at 25°C for PC-EC-DMC-$LiPF_6$-PVdF-HFP of the Sony gel was reported, which was about an order less than that of liquid electrolytes.[331] The lithium ion transport mechanism is similar to previous gel-type polymer electrolyte. The pore size has significantly effect on the lithium ion transport. Boudin et al. [332] studied ionic conductivity in microporous PVdF gel and found that increasing pore size from nanopores to micropores could improve the ionic conductivity. However, the high ionic

conductivity has been achieved because of the compromise of mechanical stability of such gel complexes, due to the fact of the relatively large amount of liquid solvent contents. During the preparation process, addition nanoparticulate silica is added to enhance the mechanical stability. With Bellcore gel electrolyte in the cell, the cell fabrication has the advantage of that individual electrodes are internally bonded together to form an integral unit and the whole cell system is less sensitive to shock and vibration.[333] Bellcore process technique is not yet ready for implementation in large-scale production.

Both types of gel polymer electrolytes possess higher ionic conductivity in the order of 10^{-3} S cm^{-1} at room temperature, which is not very far away from that of liquid electrolyte. However, such types of gel polymer electrolytes contain large amount of liquid solvents. Other than the compromise of the mechanical stability, the issues of cell fabrication, device safety of solvent leakage, electrochemical stability of the solvents, and potential flammability at higher operating temperature also hinder the further development, especially practical applications in the market.

Figure 7.5 is adapted from Tarascon and Armand's publication, [203] which shows the Arrhenius plots of conductivity for representatives of various solid electrolytes discussed previously. Figure 7.5 gives the overview of the features of these various electrolytes and guides the direction of the future technology improvement for electrolytes. Together with previous discussion sections of various polymer electrolytes, several factors, which affect the ionic conductivity of electrolyte, can be observed. First, effect of different salts: curve 1 and 2 are the behaviors of simple PEO polymer

electrolyte with different salts, conventional $LiCF_3SO_3$, and perfluorosulphonimide, $Li[(CF_3SO_2)_2N]$.[334] $Li[(CF_3SO_2)_2N]$ is an organic anion based salt and the relatively big and non-coordinating anion has extensive degree of charge delocalization. Due to this effect, electrolyte of PEO with $Li[(CF_3SO_2)_2N]$ has an order of magnitude of ionic conductivity than that of PEO with $LiCF_3SO_3$ in the temperature range of above 20^oC . Second, effect of blending different polymers to obtain lower T_g: blending of different polymers can overcome the shortcomings of individual polymer and enhance the mobility of the polymer electrolyte. As a result, the new complex has lower T_g. The new electrolyte complex shows improved behavior of ionic conductivity as shown in curve 3, compared to curve 1. Third, effect of small amount of organic liquid, i.e., plasticizer: normally, amount of 10 to 25% plasticzer as additive is added to solid polymer electrolyte.[335] As mentioned previously, these additives can act as chain lubricants to make segmental motion of polymer easier and to provide liquid-like feature of lithium ion transport. Therefore, ionic conductivity of the modified polymer electrolyte can be further enhanced to the amount of an order of magnitude, as shown in curve 4 (compared to curve 3), even though this might bring the issues of leakage of liquid solvent and compromise of the mechanical stability of polymer electrolyte. Fourth, effect of large amount of liquid solvent or solvent mixtures, in the range of 60-95% liquid solvent, i.e., gel-type polymer electrolyte: two fabrications of conventional gel-type electrolyte (curve 7) and Bellcore process (curve 10) are listed. From the point view of behavior of ionic conductivity, Bellcore process gel-type electrolyte over-performs the conventional gel-type electrolyte. The ionic conductivity of both type

electrolytes is less than an order of magnitude than that of organic liquid electrolytes, as shown in curve 7 and 9 correspondingly.[336]

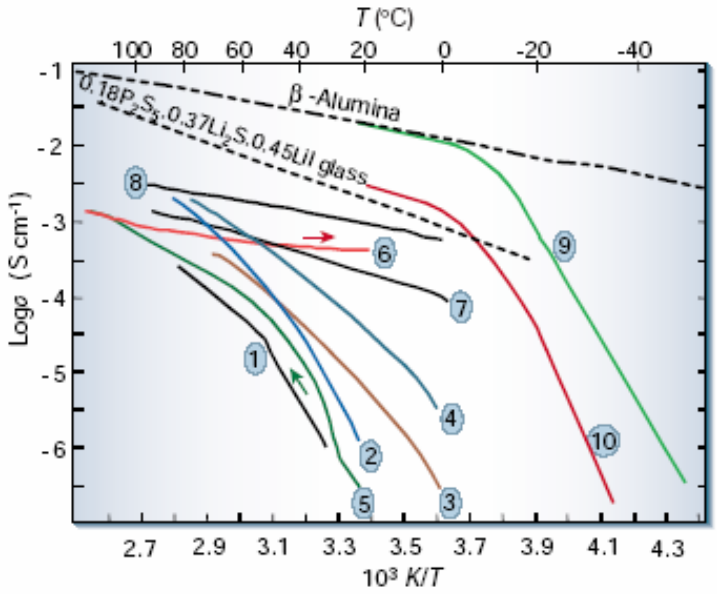

Figure 7.5. Arrhenius polt of conductivity for various solid electrolytes. (1) First-generation PEO-$LiCF_3SO_3$; (2) new solutes with high-dissociation PEO-$Li[(CF_3SO_2)_2N]$; (3) low-T_g combination polymer; (4) plasticized polymer electrolyte PEO-$Li[(CF_3SO_2)_2N]$ + 25 % w/w PEG-dimethylether (molecular weight, 250); (5) heating curves of liquid crystalline polymer electrolytes; (6) cooling curves of liquid crystalline polymer electrolytes; (7) gel-type polymer (X-linked PEO-dimethacrylate-$Li[(CF_3SO_2)_2N]$-PC 70 %; (8) liquid electrolyte PC/DME-$LiCF_3SO_3$; (9) liquid electrolyte EC/DMC-$LiPF_6$ at low temperature; (10) gel electrolyte P(VdF-HFP)/EC/DMC-$LiPF_6$ (Adapted by permission from Macmillan Publishers Ltd: Nature, 414, 2001, 359-367[203], copyright 2001)

7.2.3 Solid state non-polymer ionic electrolytes

7.2.3.1 Features of solid state ionic electrolytes

In principle, we know that all-solid-state battery systems are most promising in the view of improving the safety and reliability. It is clear that solid electrolytes are the key materials for the application of such devices. Generally speaking, very few solid electrolytes are suitable for application in solid-state lithium batteries, because ionic conductivity of lithium ion conductive solid electrolyte is only $1/10 \sim 1/10^5$ of that of organic liquid conductivity.[337] Many researches have focused on the developments of solid ionic electrolytes. Generally, these ionic electrolytes can be categorized into two types, crystalline ion conductor, amorphous or glassy ion conductor.

7.2.3.2 Crystalline ion conductor

Mechanism of ionic transport in solids arises from the atomic disorder/defects in real crystals, including vacancies and interstitial ions. The crystal contains different sites where ions are located and these sites are energetically nearly equivalent.[338] This is the most important requirement and feature of the ionic conductors. Solid compounds as pure ionic conductors have been a long history.[339,340] But their developments and applications did not gain much interest until last 30 years, during the period many solid electrolytes with high ionic conductors and high chemical stability at room temperature were discovered.[341,342] For example, ZrO_2, sodium-β/β"-alumina were used as solid electrolyte (and separator as well) in batteries.[343]

Even though not any crystalline lithium ionic conductor with high ionic conductivity and other desirable properties has been developed for use in practical

lithium batteries, the research for searching lithium ion conductor is promising.[337,344] These conductors include LISICON-type materials (LISICON: lithium super ionic conductor), [345-347] Li^+- β-alumina, [348] perovskite materials, [349,350] thio-LISICON materials, [351-358] crystalline inorganic chalcogenides, [359] and $LiNO_3$-mixed $(Gd_{0.9}La_{0.1})_2O_3$.[360] Table 7.5 shows the conductivity and other properties of these lithium ion conductor materials. Generally speaking, those crystal materials contain oxygen ions, for example LISICON-type materials, Li^+- β-alumina, and perovskite materials, have relatively low ionic conductivity below 10^{-3} S cm^{-1} at room temperature. These materials cannot be used as solid electrolyte in lithium batteries. Fortunately, material design based on the idea of the structural criteria for crystalline ion conductors proposed by West [361] has been progress. These criteria include, (i) mobile ions should have a suitable size and the lattice has easy conduction pathways. This idea is reflected in the design of crystalline inorganic chalcogenides [359] and $LiNO_3$-mixed $(Gd_{0.9}La_{0.1})_2O_3$ [360]. Inorganic chalcogenide frameworks (ICF-m, m is the number related to the type of framework topology and followed by elemental symbols) integrate zeolite-like architecture with open-framework and have open channels as the paths for fast lithium ion transport. ICF-22 InS-Li was reported with specific conductivity of 1.1×10^{-2} S cm^{-1} at 24°C under 31.7% relative humidity.[359] Tamura et al. [360]followed the idea of design of potassium ion conducting solid based on the rare earth oxides [347,362,363] and developed crystal $0.325(Gd_{0.9}La_{0.1})_2O_3$-$_{0.35}LiNO_3$ with the C-type rare earth structure, Gd_2O_3, possessing large open space for lithium ion transport. (ii) there should be disorder/defects in a mobile ion sublattice. Substitution of multivalent cations with

monovalent cations introduces interstitial lithium ions or vacancies lead to high lithium ion mobility.[359,361] (iii) highly polarizable mobile ions and anion sublattices are more favorable. A lot of works have been in this field, including ICF-m [359] and thio-LISICON [351-358]. The substitution of oxygen ions by sulfide ions in the crystal is the main idea in these solid electrolytes. The increasing ion conductivity arises from the fact of larger ionic radii and more polarizable of sulfides. The interaction between Li-S is weaker than that of Li-O. As the result, lithium ion conductivity of 2.2×10^{-2} S cm-1 was reported at 25°C in a new thio-LISICON, $Li_{4-x}Ge_{1-x}P_xS_4$ (x=0.75).[351]

Table 7.5: Conductivities (at 25°C unless noted), activation enthalpies of fast lithium-ion solid conductors

Solid electrolyte	σ (S cm^{-1})	E_A(eV)	Ref.
LiI (40 mole % Al_2O_3)	10^{-5} (total)	0.43 (total)	364 365
Li_4SiO_4-Li_3PO_4	3.7×10^{-6} (total)	0.52 (total)	366
$Li_{1.3}Al_{0.3}Ti_{1.7}(PO_4)_3$	7×10^{-4} (total)	0.35 (total)	367
$Li_{0.34}La_{0.51}TiO_{2.94}$	10^{-3} (bulk) 7.5×10^{-5} (grain-b)	0.40 (bulk) 0.42 (grain-b)	368-370
0.5$LiTaO_3$-0.5$SrTiO_3$	5×10^{-4} (bulk)	0.33 (bulk)	371
0.5Li_4SiO_4-0.5Li_5AlO_4	2.3×10^{-7} (total)	0.55 (total)	372
$Li_{3.25}Ge_{0.25}P_{0.75}S_4$	2.2×10^{-3} (total)		351
ICF-22 InS-Li	1.1×10^{-2} (total)		359
0.325$(Gd_{0.9}La_{0.1})_2O_3$- 0.35$LiNO_3$	2.02×10^{-1} (total) (773K)		360

7.2.3.3 Glass ion conductor

Glass materials are the other important class of ion conductors investigated for lithium ion conductors. Normally, there are two ways to prepare the glass electrolytes:

the melt quenching method and the mechanical milling technique.[373] The glass electrolytes have greater variation in composition than crystalline materials (and are easier to design desired electrolyte materials with higher ionic conductivity and higher stability).[374-379] Besides, ionic diffusion pathways in glass electrolyte are isotropic due to the feature of the glass electrolyte itself and the resistance at grain boundary is thus small. [337] Glass electrolytes can be classified into two groups: oxides and sulfides, which are similar to the idea of the crystalline electrolytes. Oxide glasses consist of a network former (such as SiO_2, P_2O_5, or B_2O_3) and a network modifiers (such as Na_2O, Li_2O or CaO). The network former breaks bridging bonds, such as Si-O-Si, and form non-bridging oxygen atoms, such as $Si\text{-}O^{-}\text{-}Li^{+}$. [380] Network modifiers can modify the channel network and increase the ionic conductivity. In oxide glass electrolytes, oxide ions are covalently bonded to the glass network and only lithium ions are mobile.[337] Generally, due to the stronger interaction between oxygen ions and lithium ions, the ionic conductivity of the oxide electrolyte is in the order of 10^{-6} S cm^{-1}, which is too low for the practical use in lithium batteries. On the other hand, sulfide glass electrolytes increase the ionic conductivity because of the larger polarizability of sulfide ion. Sulfide glass electrolyte normally include glass formers, such as P_2S_5, B_2S_3, SiS_2, GeS_2, Al_2S_3, and As_2S_3, and modifiers, like Li_2S, Na_2S, and Ag_2S, and dopants, such as lithium halide [380] and Li_3PO_4[369,381,382]. The ionic conductivity of lithium ions in these glass electrolytes has been reported in the order of 10^{-3} S cm^{-1}.[357,380,383,384] Table 7.6 shows lithium ionic conductivity in glass electrolytes based on sulfides.

Table 7.6: Lithium ionic conductivity in glass electrolytes based on sulfides

Glass composition	Ionic conductivity ($S\ cm^{-1}$)	Remarks	Ref.
Li_2O-B_2O_3	4×10^{-7}	Oxide glass	380
xLi_2S-$(1-x)GeS_2$ ($0<x<0.5$)	4×10^{-5}	Conventional quenching	385
xLi_2S-$(1-x)GeS_2$ ($0<x<0.63$)	2×10^{-4}	Twin roller quenching	386
xLi_2S-$(1-x)P_2S_5$ ($0.63<x<0.68$)	3×10^{-4}	Conventional quenching	387
$0.5Li_2S$-$0.5SiS_2$	3×10^{-4}	Conventional quenching	388
$0.6Li_2S$-$0.4SiS_2$	5×10^{-4}	Liquid nitrogen quenching	389
$0.33Li_2S$-$0.67As_2S_3$	3×10^{-9}	Conventional quenching	390
xLi_2S-$(1-x)SiS_2$ ($0.3<x<0.6$)	5×10^{-4}	Twin roller quenching	391
$0.42Li_2S$-$0.28SiS_2$-0.30LiI	1.3×10^{-3}	Liquid nitrogen quenching	380
$0.47Li_2S$-$0.14SiS_2$-$0.09P_2S_5$-0.30LiI	2.1×10^{-3}	Liquid nitrogen quenching	380
$0.30Li_2S$-$0.21SiS_2$-$0.08Li_2CO_3$-0.10LiBr	1.2×10^{-3}	Liquid nitrogen quenching	380
$0.60Li_2S$-$0.38SiS_2$-$0.02Li_3PO_4$	7.4×10^{-4}	Liquid nitrogen quenching	381
$0.63Li_2S$-$0.36SiS_2$-$0.01Li_3PO_4$	1.8×10^{-3}	Liquid nitrogen quenching	381

Three main systems, Li_2S-SiS_2 system, Li_2S-P_2S_5 system, and glass-ceramics electrolyte system are extensively studied for application in lithium batteries. Sulfide glasses in the systems Li_2S-SiS_2 and Li_2S-P_2S_5 prepared by melt-quenching method were reported to have ionic conductivities over 10^{-4} S cm^{-1} at room temperature.[387,392,393] A second former can increase ionic conductivity of glass electrolyte, stability of glass electrolyte against the anode, and allow fine-tuning of the physical properties of the

glass electrolyte.[380,382,389,394] Dopants can improve the ionic conductivity of glass electrolytes. The doping of Li_3PO_4 to the system of Li_2S-SiS_2 was studied by Takada et al. [381] and ionic conductivity of 7.4×10^{-4} S cm^{-1} for composition of $0.02Li_3PO_4$-$0.60Li_2S$-$0.38SiS_2$ and 1.8×10^{-3} S cm^{-1} for $0.01Li_3PO_4$-$0.63Li_2S$-$0.36SiS_2$ at ambient temperature are reported.

On the other hand, glass-ceramics electrolytes in the Li_2S-P_2S_5 system have been found to have higher ionic conductivities than corresponding glass materials, [351,354,357,395]although crystallization of glassy materials normally have lower conductivities.[396] In Li_2S-P_2S_5 system, the enhancement of the ionic conductivity is attributed to the formation of metastable superionic crystal phases in the system.[344,354] X-ray diffraction (XRD) patterns of the $67Li_2S$-$33PS_{2.5}$ samples before and after being heat up to 240^oC show crystalline structure similar to the superionic conducting crystalline phases of $Li_{4-x}Ge_{1-x}P_xS_4$ ($0.6<x<0.8$).[351] Ionic conductivities of about 10^{-3} S cm^{-1} for glass-ceramic solid electrolytes at ambient temperature have been achieved.[344,373,383,397]

7.3 Objectives of this project

From the overview of previous sections, we know that an excellent electrolyte should have high ionic conductivity, high mechanical, chemical and electrochemical stability over a wide range of potential window. By careful design, crystalline materials can have higher ionic conductivity.[351] Solid electrolyte is the key component for the development and practical application of solid state lithium batteries. Developments of

solid electrolyte are promising and more materials are being investigated currently. As we see the issue, the concepts of single ion conduction mechanism and appropriate lithium ion conduction pathways/channels are very important factors for solid state electrolyte of lithium batteries.

Based on these concepts, the objectives of this proposal are to investigate a new solid electrolyte as the potential application in the solid state lithium batteries. For single ion conduction mechanism, anions of the materials are expected to be immobile and the transfer number of lithium ion will be unity. Thus anions should have relatively large size. Regarding the lithium ion conduction pathways/channels in the materials, the selected electrolyte should possess an appropriate space and the space should somehow be connected to each other in certain way to facilitate lithium ion transport.

The material we investigate in this proposal is di-lithium phathlocyanine (Li_2Pc).[398-402] Through the self-assembly of Li_2Pc molecules, ion conducting channels are formed for lithium ion transport. Besides, the delocalization of negative charge on macromolecule decreases the effective interaction between lithium ion and anion. Lithium ion conductivity can thus be enhanced. The high bulk ion conductivity itself is not enough for the criteria of good electrolyte. Good transport properties at the interface with the electrode is also an important problem that needs to be addressed. Small activation energy through electrolyte and into electrode or no build-up of lithium ions at the interface is desired when brought these two solid-solid phases into contact. This proposal first uses computational methods to obtain the structural information of the crystalline Li_2Pc and lithium ion transport at the interface at the atomic level. Static and

dynamics properties of the systems with bulk and interface systems are calculated to investigate the potential of Li_2Pc as a solid electrolyte for lithium batteries.

Beyond understanding the lithium ion transport through electrolyte-electrode interface, the ultimate goal of this proposal is to understand the factors that affect the ion transport in solid materials. General rules for design and modification of materials to improve ion transport in solids is expected an additional outcome of this work.

CHAPTER VIII

METHODOLOGY AND COMPUTATIONAL / SIMULATIONAL DETAILS

8.1 Overview

Computational modeling and simulation have been important tools in battery design and material research as well. At the system design level, computational modeling with more complex and accurate mathematical models can predict the effect of cell design, electrode thickness, electrode morphology, new packaging techniques, and numerous other factors.[403] There are several reviews [403-406] and papers [407-417] which focus on the modeling of lithium secondary batteries. Optimization of battery performance for safer, higher-energy design of new systems and mechanism of cell degradation and failure have been achieved successfully by computational modeling.

Instead of computational modeling of the cell design, this proposal focuses on computational simulation on material chemistry, including characterization of solid electrolyte and lithium ion transport through interface. Computational chemistry has been an efficient tool between theories and experiments in the field of material research in the field of lithium secondary batteries. It provides more detailed information on an atomic level to understand and explain experimental results, for example, new materials for electrolyte and electrode, lithium ion transport during charge and discharge processes.[227,398,401-403,418-442] Computational simulation methods include molecular dynamics,

quantum chemistry, and Monte Carlo simulation. This project will employ molecular dynamics and quantum chemistry to investigate the self-assembly of solid electrolyte and lithium ion transport from electrolyte into cathode.[398,402]

8.2 MD simulations of crystalline Li_2Pc

8.2.1 Initial configurations

Four primitive unit cells (designated as α-, β-, ε-, and χ-forms) of dilithium phthalocyanine were built based on several sources of data for this and related systems: 1) the analysis of experimental X-ray spectra of crystalline Li_2Pc, [443](for the ε-form); 2) the experimental density of solid Li_2Pc at room temperature [444] (for the α-, β-, and χ-forms); 3) the reported polymorphism of various metal phthalocyanines [445-447] (for the α-, β-, and χ-forms). The cell parameters of the four configurations are shown in Table 8.1. Among these polymorphs, the α-, β-, and ε-form structures have monoclinic unit cells, and the χ-form has a tetragonal unit cell. The primitive unit cells for the α-, β-, and χ-forms have the same dimensions as the reported structures for the polymorphs of LiPc except that the shortest cell dimension was elongated to fit the experimental density of Li_2Pc (1.40 g/cm^3). The cell parameters of the ε-form were chosen to match the crystal d-spacing that best reproduces the experimental X-ray data, as calculated with the powder indexing program CRYSFIRE 2002.[448]

Table 8.1: Cell parameters of α, β, ε, and χ forms of Li_2Pc used in MD simulations

Crystalline structure	a (Å)	b (Å)	c (Å)	α (°)	β (°)	γ (°)
α	26.2	4.0	23.9	90.0	94.5	90.0
β	19.4	5.1	14.6	90.0	120.4	90.0
ε	5.1	14.0	18.3	118.2	90.0	90.0
χ	13.8	13.8	6.5	90.0	90.0	90.0

Dilithium phthalocyanine has molecular formula of $Li_2C_{32}N_8H_{16}$. Figure 8.1 shows the molecular structure of Li_2Pc, including side view and top view. The starting configurations for the MD simulations of the α, β, ε and χ crystalline forms are shown in Figure 8.2. All initial configurations were set in staggered arrangements, and in the χ-form molecules in subsequent layers are rotated with respect to each other by an angle of 30° (Figure 8.3) according to structures reported for pthalocyanines [449] and also based in our ab initio calculations of Li_2Pc dimers.[398,450]

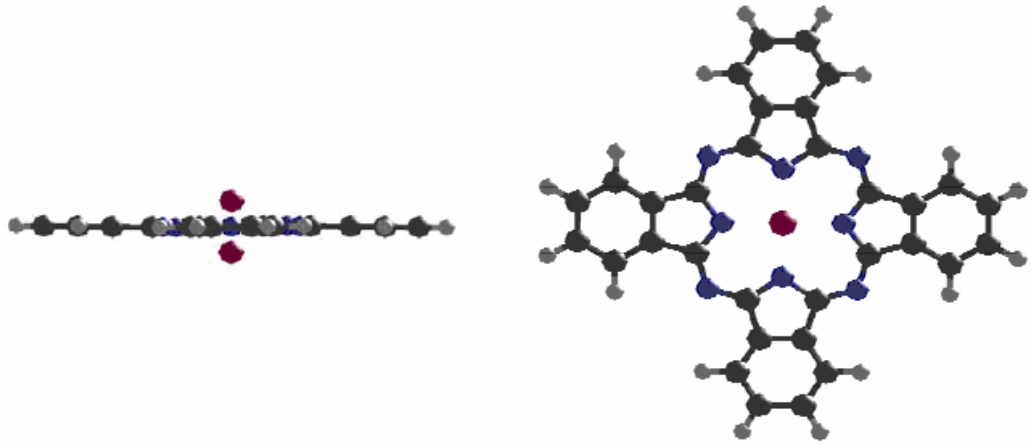

(a) (b)

Figure 8.1. Structure of Li_2Pc molecule. (a) side view, (b) top view

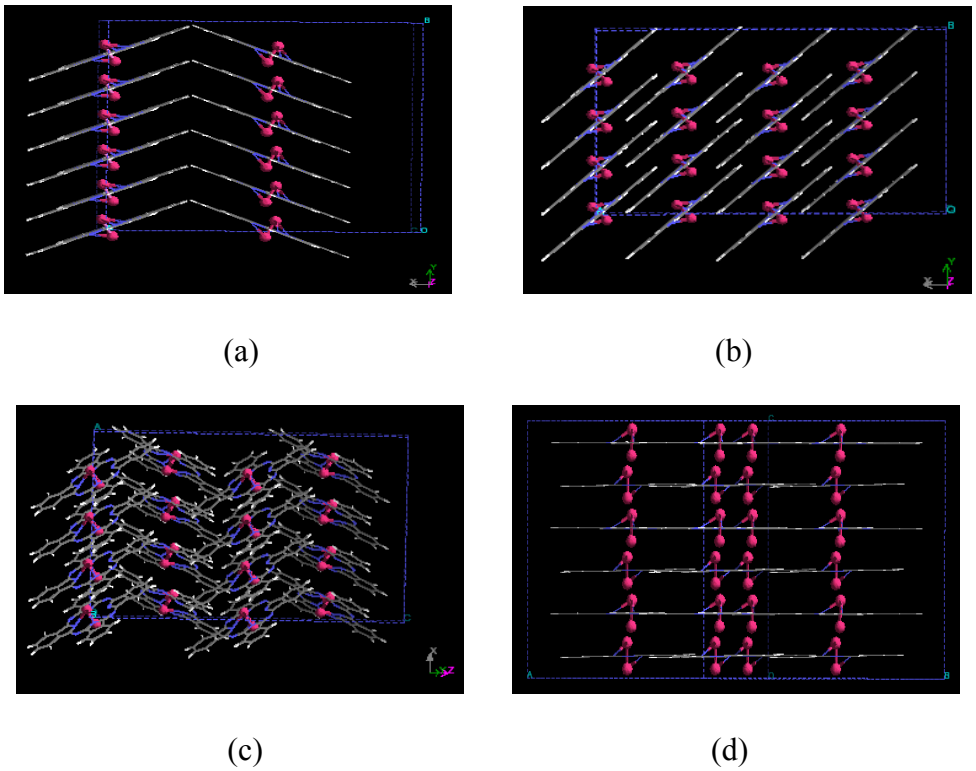

Figure 8.2. Initial configuration of the unit cells for molecular dynamics simulations. (a) α-form, (b) β-form, (c) ε-form, (d) χ-form

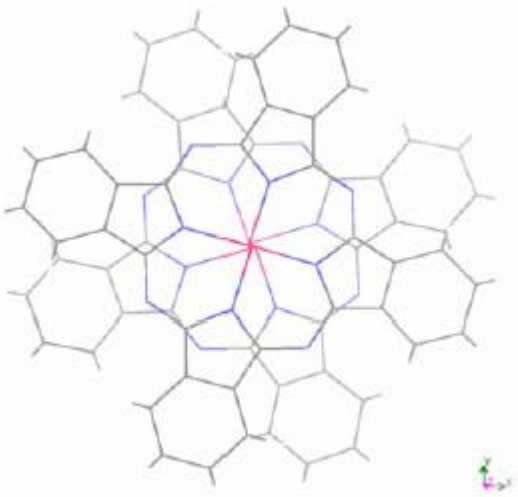

Figure 8.3. Rotation of two dilithium phthalocyanine molecules used for initial configuration of χ-form

The initial geometry of the individual Li_2Pc molecules used in the MD simulations was taken from the DFT optimized structure of a single molecule (B3PW91/6-311G). The unit cells shown in Table 8.1 were duplicated along the shortest cell length to define the initial MD simulation cell for each of the Li_2Pc forms. As a result, MD simulation cells of the α- and χ-forms contained 24 Li_2Pc molecules, whereas those of β-form and ε-form contained 32 Li_2Pc molecules (Figure 8.2). To minimize strain of the initial configurations, a total energy minimization was performed previous to the MD simulations using the UFF force field, [182]and a combination of minimization methods (steepest descent, adopted basis Newton Raphson, Quasi Newton and Truncated Newton) were applied as provided in the Cerius^2 3.0 package.[157] The minimized ensembles were used as input to the DL-POLY program, [166] to perform MD simulations using the force fields described in the next section.

8.2.2 Force fields

8.2.2.1 Intramolecular terms

The selected force field contains intramolecular and intermolecular terms. The *intramolecular* potential includes the following two terms:

(1) Bond potential:

$$U(r_{ij}) = \frac{1}{2} k_{ij} (r_{ij} - r_{ij,0})^2, \tag{8.1}$$

(2) Valence angle potential:

$$U(\theta_{jik}) = A_{jik}[1 + \cos(m_{jik}\theta_{jik} - \delta_{jik})], \tag{8.2}$$

In these formulae $k_{ij,}$ and A_{jik} are force constants relating atoms *i*, *j*, and *k*, r_{ij} is the distance between atoms *i* and *j* ($r_{ij}= \left|\bar{r}_i - \bar{r}_j\right|$), $r_{ij,0}$ is the corresponding equilibrium distance, θ_{jik} is the angle between bond vectors $\bar{r}_{ij}$ and $\bar{r}_{ik}$.

The force constants for the potential terms were evaluated according to the following equations [182] where the parameters θ_0 and $r_{ij,0}$, (Tables 8.2 and 8.3) were obtained averaging over all atoms (bonds, or angles) of the same type from the optimized geometry of Li_2Pc calculated with B3PW91/6-311G, [398]whereas the parameter z_i^* was taken from effective charge of different atoms[182]:

$$k_{ij} = 664.12 \frac{z_i^* z_j^*}{r_{ij,0}^3} \frac{kcal}{mol}, \tag{8.3}$$

$$A_{ijk} = \frac{664.12}{r_{ij,0} r_{jk,0}} \frac{z_i^* z_k^*}{r_{IK}^5} r_{ij,0} r_{jk,0} \left[3 r_{ij,0} r_{jk,0} (1 - \cos^2 \theta_0) - r_{IK}^2 \cos\theta_0\right] \frac{kcal}{mol}, \tag{8.4}$$

$$r_{IK} = (r_{ij,0}^2 + r_{jk,0}^2 - 2 r_{ij,0} r_{jk,0} \cos\theta_0)^{1/2}, \tag{8.5}$$

where

$$m = \frac{\pi}{\pi - \theta_0},$$

$$\delta = -\pi + \frac{\pi\theta_0}{\pi - \theta_0},$$

Table 8.2: Selected force field equilibrium angles θ_0 (degrees) averaged over all bonds and angles of the same type, from the values obtained from Li_2Pc optimization (B3PW91/6-311G). The atom numbers correspond to Figure 8.4

i j k	Atom numbers for group i-j-k	θ_0
C C H	48-21-7, 32-47-1, 40-19-15, 26-35-10 39-23-5, 42-25-12, 20-31-4, 43-44-8	120.68
C C H	24-21-7, 41-47-1, 30-19-15, 38-35-10 34-23-5, 28-25-12, 29-31-4, 17-44-8	121.69
C C H	21-24-9, 47-41-2, 19-30-6, 35-38-13 23-34-14, 25-28-3, 31-29-16, 44-17-11	119.67
C C H	41-24-9, 24-41-2, 38-30-6, 30-38-13 28-34-14, 34-28-3, 17-29-16, 29-17-11	119.14
C C C	22-48-21, 36-32-47, 46-40-19, 45-26,35 18-39-23, 27-42-25, 33-20-31, 37-43-44	132.71
C C C	22-48-32, 36-32-48, 46-40-26, 45-26-40 18-39-42, 27-42-39, 33-20-43, 37-43-20	106.11
C C C	21-48-32, 47-32-48, 19-40-26, 35-26-40 23-39-42, 25-42-39, 31-20-43, 44-43-20	121.18
C C C	48-21-24, 32-47-41, 40-19-30, 26-35-38 39-23-34, 42-25-28, 20-31-29, 43-44-17	117.63
C C C	21-24-41, 47-41-24, 19-30-38, 35-38-30 23-34-28, 25-28-34, 31-29-17, 44-17-29	121.19
C C N	48-22-55, 43-37-55, 32-36-56, 40-46-56 26-45-52, 39-18-52, 42-27-51, 20-33-55	122.38
C C N	48-22-54, 32-36-54, 40-46-50, 26-45-50 39-18-49, 42-27-49, 20-33-53, 43-37-53	110.22
N C N	55-22-54, 56-36-54, 56-46-50, 52-45-50 52-18-49, 51-27-49, 51-33-53, 55-37-53	127.40
C N C	37-55-22, 46-56-36, 33-51-27, 45-52-18	122.55
C N C	22-54-36, 46-50-45, 18-49-27, 33-53-37	107.34

Table 8.3. Selected force field equilibrium distances $r_{ij,0}$ (Å) and angles θ_0 (degrees) averaged over all bonds and angles of the same type, from the values obtained from Li_2Pc optimization (B3PW91/6-311G). The atom numbers correspond to Figure 8.4

i j	Atom numbers for pair i-j	$r_{ij,0}$
H C	9-21, 2-41, 6-30, 13-38, 14-34, 3-28, 11-17, 16-29	1.086
H C	7-21, 1-47, 15-19, 10-35, 8-44, 4-31, 12-25, 5-23	1.085
C C	17-29, 24-41, 28-34, 30-38	1.405
C C	43-20, 32-48, 40-26, 39-42	1.401
C C	17-44, 29-31, 24-21, 41-47, 30-19, 38-35, 23-34, 25-28	1.389
C C	43-44, 20-31, 21-48, 32-47, 19-40, 26-35, 23-39, 25-42	1.392
C C	37-43, 20-33, 27-42, 18-39, 26-45, 40-46, 32-36, 22-48	1.455
C N	22-54, 36-54, 46-50, 45-50, 18-49, 27-49, 33-53, 37-53	1.370
C N	36-56, 46-56, 45-52, 18-52, 27-51, 33-51, 37-55, 22-55	1.324

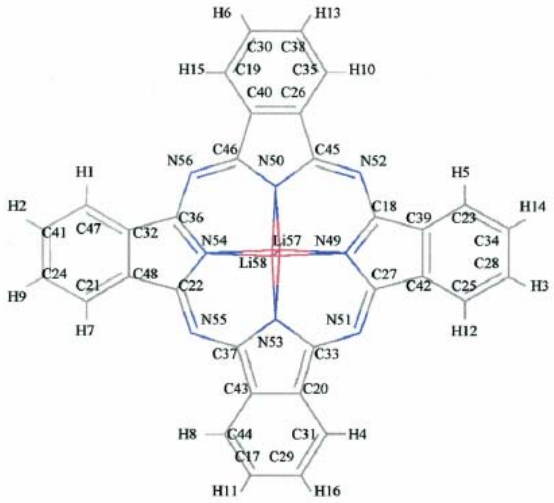

Figure 8.4. Labeled Li_2Pc

8.2.2.2 Intermolecular terms

In order to allow the migration of lithium ions from the molecule, neither the bond potential between Li and N, nor the valence angle potentials among Li-N-Li, and N-Li-N, were included. Instead, the Li-N interaction was represented by a combination of 12-6

Lennard-Jones (LJ) and Coulombic site-site potential functions with parameters reported in Tables 8.4 and 8.5. The DFT optimized (B3PW91/6-311G) Li-N bond length is 2.18 Å, which can be compared with the value 2.17 Å obtained with this model, while the UFF [182] 12-6 LJ potential yields 2.15 Å. Although an accurate description of the van der Waals interactions are certainly critical for these types of compounds, the Li-N is the most critical bond distance since an explicit harmonic bond potential between Li and N is not present in our model.

The intermolecular potentials include two terms:

(1) A short-ranged LJ (12-6) potential:

$$U(r_{ij}) = 4\varepsilon\left[\left(\frac{\sigma}{r_{ij}}\right)^{12} - \left(\frac{\sigma}{r_{ij}}\right)^{6}\right] \tag{8.6}$$

where ε is the LJ well depth in kJ/mol and σ is the LJ length parameter in Å. The well-depth and van der Waals length parameters for interactions between H, N, and C atoms of the same type were selected as in the Dreiding force field.[451] For Li-Li interactions we used the LJ parameters reported by Heizinger [452] (Table 8.4). The LJ parameters between atoms of different species were calculated with the Lorentz-Berthelot rule.[164]

Table 8.4: Values of LJ 12-6 parameters

atom	ε (kJ/mol)	σ (Å)
H	6.35×10^{-2}	2.846
C	3.98×10^{-1}	3.473
N	7.74×10^{-1}	3.263
Li	1.50×10^{-1}	2.370

(2) The Ewald sum [164] was used to incorporate long-range corrections to the usual electrostatic (Coulombic) potential. For molecular systems, the Ewald sum replaces a potentially infinite sum in real space with two finite sums: one in real space and one in reciprocal space; and the self energy correction.[164,166] The Mulliken[453-455] atomic charges used for the Coulombic terms were obtained from DFT optimized geometries (B3PW91/6-311G) for one Li_2Pc molecule; they are shown in Table 8.5.[401]

Table 8.5: Mean values (averaged over all atoms of the same type) of the Mulliken atomic charges from B3PW91/6-311G optimization of Li_2Pc. The atom numbers correspond to Figure 8.4

Atom type	Atom number	Charge
H	1, 4, 5, 7, 8, 10, 12, 15	0.21
	2, 3, 6, 9, 11, 13, 14, 16	0.20
C	17, 24, 28, 29, 30, 34, 38, 41	-0.20
	19, 21, 23, 25, 31, 35, 44, 47	-0.17
	20, 26, 32, 39, 40, 42, 43, 48	-0.08
	18, 22, 27, 33, 36, 37, 45, 46	0.39
N	49, 50, 53, 54	-0.63
	51, 52, 55, 56	-0.40
Li	57, 58	0.66

8.2.3 MD procedure

The DL_POLY program,[166] version 2.13, was used in all simulations. MD simulations were run in the microcanonical ensemble (NVE) for 1200 ps with a time step of 0.001 ps at 300 K. Equilibration runs of 500 ps were performed before collecting averages in production runs of 700 ps. During the equilibration phase, the interval for scaling velocities according to the selected temperature was set to 0.002 ps, in the production phase the scaling is disconnected, but the temperature remains about constant. The cutoff radius, beyond which intermolecular interactions of the real space part of the long-range electrostatic and the van der Waals potentials were set to zero, was chosen as 10.0 Å, which corresponds to half the minimum cell length.

8.3 Ab initio calculations and molecular dynamics simulations of interphase

8.3.1 Ab initio calculations of a simplified Li_2Pc model in contact with a pyrite cluster

As a solid state electrolyte, Li_2Pc exhibits ion conducting channels through which lithium ions diffuse.[398,456] In such systems, the most important interaction is set by the lithium ions immersed in the negative electrostatic potential field formed by the nitrogen atoms. Based on this we simplified the system achieving a size computationally manageable, while keeping the main features of the system of interest. Thus, a simplified Li_2Pc model, with molecular formula $Li_2C_8N_8H_8$, is used to determine its main interactions with the surface of pyrite, modeled as a cluster. In the simplified Li_2Pc model (Figure 8.5), four outside benzene rings of Li_2Pc are replaced by eight hydrogen atoms, while the anion matrix of Li_2Pc able to form lithium ion conducting channels is

still present. The validation of such simplified model will be discussed in later section. Full optimizations of $Li_2C_8N_8H_8$ monomer and dimer are performed at Hartree-Fock (HF/6-311G) and density functional theory (DFT) (B3PW91/6-311G) levels, in order to compare the geometry, charge distribution, and binding energy with those of Li_2Pc, and $(Li_2Pc)_2$ respectively.[398,450] The pyrite surface is modeled as a 24-atom stoichiometric cluster, Fe_8S_{16}, and optimized at the HF level, with a pseudopotential LANL2DZ basis set.[457] The 24-atom pyrite cluster is chosen because it preserves the S_2 dimer and the S-Fe-S triple layer, which are present in the bulk structure of pyrite, whereas the outmost two S atoms are coordinated by 2 Fe atoms and one S atom respectively. Previous work[458] reported results of a fixed 27-atom pyrite cluster, used to study the oxidation mechanisms of O_2 and H_2O on the pyrite (100) surface.

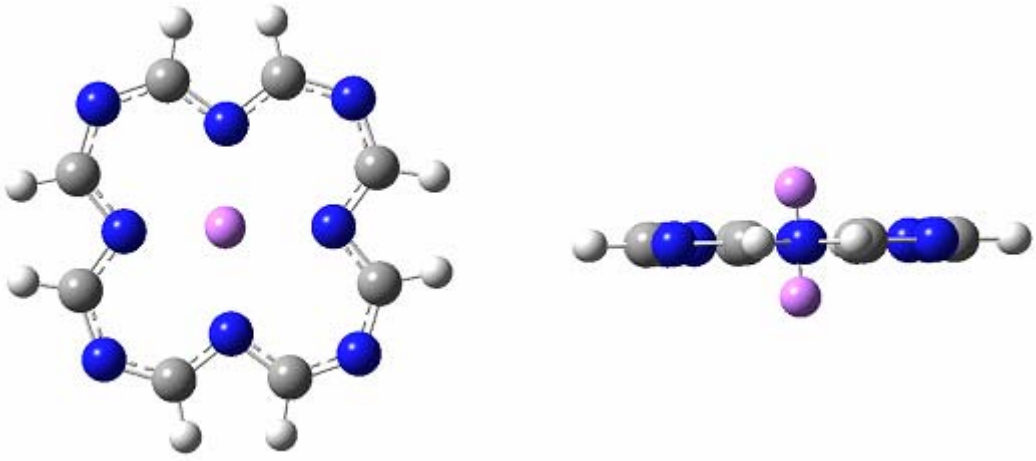

(a) (b)

Figure 8.5. Simplified model of dilithium phthalocyanine, $Li_2C_8N_8H_8$

To investigate the interfacial region, the simplified model of Li_2Pc is located on top of the model 24-atom pyrite cluster, and optimized at the HF/3-21G level. The equilibrium structures of all the involved species are fully optimized using Gaussian 98.[459] The results from the interaction between the Li_2Pc model ($Li_2C_8N_8H_8$) and the 24-atom pyrite cluster provided the charge distribution and the distance between lithium ions and the active sites of the pyrite surface, which were used to build an effective force field for MD simulations as discussed in the next section.

8.3.2 Ab initio calculations of full Li_2Pc molecule in contact with a pyrite cluster

The complex of a full Li_2Pc molecule with pyrite cluster is also being studied with ab initio calculations. Due to the bigger surface of full Li_2Pc molecule than that of simplified Li_2Pc model, a bigger cluster of pyrite model with 48 atoms has been used. The cluster of pyrite alone and the complex have been fully optimized at the level of HF/3-21G and B3LYP/3-21G respectively using Gaussian 03. The results are to validate the reliability of the simplified model.

8.3.3 MD simulations

8.3.3.1 χ-form Li_2Pc

In our MD simulations, full Li_2Pc molecules are used. In previous section we discussed that Li_2Pc may have four possible crystalline structures, the α-, β- ε- and χ-form. Among these four polymorphs, Li_2Pc molecules are assembled in staggered configurations in the α- and β-forms, and in shifted configurations in the ε- and χ-forms. Energetically, the χ-form crystalline structure has the lowest energy and thus is the most

stable structure.[398] For this reason, the χ-form was initially selected to investigate the interactions of Li_2Pc with a pyrite (100) surface.

8.3.3.2 Thin film growth of Li_2Pc on pyrite (100) surface

To investigate the self-assembly of Li_2Pc on a pyrite (100) surface, we considered a system consisting of a 5-layer slab of pyrite (100) surface in contact with a mono-layer, a bi-layer, or multi-layers of Li_2Pc located in a tetragonal unit cell, subjected to periodic boundary conditions (PBC) in the three spatial directions, with the XY plane parallel to the interface and the Z axis perpendicular to it. The initial configurations of pyrite slab for MD simulations can be seen in Figure 8.6, as an indication of how we build the cell describe following. The 5-layer pyrite slab contains 250 FeS_2 groups.

During a first set of simulations, the entire pyrite slab is fixed, while the motion of the Li_2Pc atoms is not restricted. In order to apply PBC along both the X-and Y-axes in the combined systems containing the χ-form crystalline Li_2Pc and the pyrite slab, five pyrite unit cells (each unit cell has dimensions 5.42 Å × 5.42 Å in the XY plane) were repeated in both X- and Y-directions; and two χ-form crystalline Li_2Pc unit cells (each unit cell has dimensions 13.85 Å × 5.42 Å in XY plane) were repeated also in both X- and Y-directions. As a result, two differently oriented crystals would each be periodic on the XY plane. In order to avoid the interaction between Li_2Pc with the pyrite slab on the next periodic cell when PBC are applied, a vacuum space of about 15 to 30 Å (depending on the number of Li_2Pc molecules in the cell) along the Z-axis was added above the Li_2Pc phase. The dimensions of the simulation cell were 27.14 Å × 27.14 Å × 50.00 Å.

Two orientations of the χ-form Li_2Pc were used as initial configurations, with the initial stacking axis of Li_2Pc either perpendicular or parallel to the pyrite (100) surface respectively. In the first case, systems containing 1, 2, 4, 8, and 16 Li_2Pc molecules were introduced in the simulation cell, each layer containing a maximum number of four Li_2Pc molecules. A separation of 2.5 Å between the phthalocyanine rings in contact with the pyrite surface was initially set. In the low density systems containing one or two Li_2Pc molecules, the pyrite surface is only partially covered. For the high density cases containing 8 or 16 Li_2Pc molecules, additional layer(s) were added, with separations of 3.25 Å between phthalocyanine rings. This separation was set based on those found in the bulk χ-form of the crystalline Li_2Pc structure. The initial configurations of the system of pyrite slab with 4 Li_2Pc molecules are shown in Figure 8.6. 4 Li_2Pc molecules are distributed on a single layer above the pyrite slab. Other systems containing different number of Li_2Pc molecules are not shown, but their configurations can be easily imaged from Figure 8.6. For the system contains 1 Li_2Pc molecule, only one of any of these 4 Li_2Pc molecules exists in the cell; for the system contains 2 Li_2Pc molecules, two neighbor Li_2Pc molecules are distributed at the same layer; for the system containing 8 or 16 Li_2Pc molecules, additional layer(s) of one or three is(are) added to the top of these four Li_2Pc molecules, respectively.

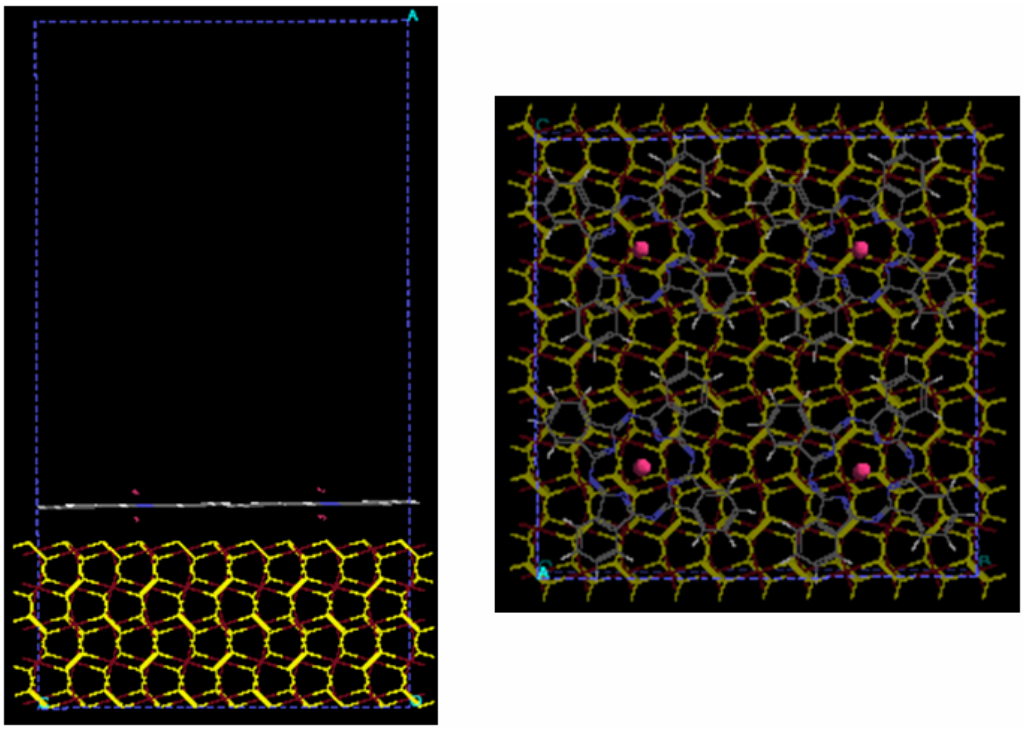

(a) (b)

Figure 8.6. Initial configurations of complex of five-layer pyrite slab (100) and 4 Li_2Pc molecules, with stacking axis perpendicular to (100) surface. (a) side view, (b) top view

In the series of simulations where the stacking axis of Li_2Pc was initially located parallel to the pyrite (100) surface, four cases of systems containing 1, 2, 8 and 16 Li_2Pc molecules were simulated, where each layer can contain up to 16 Li_2Pc molecules to fully cover the surface. Only the initial configurations of system with 8 Li_2Pc molecules are shown in Figure 8.7. Other systems are not shown, but can be image from the configurations of system with 8 Li_2Pc. For the case of system containing 1 Li_2Pc, only a single of any 8 molecules is left; for the case of system containing 2 Li_2Pc; only two neighbor Li_2Pc molecules of these 8 molecules are left; while for the case of system

containing 16 molecules, another 8 Li_2Pc molecules occupy on the other side of cell, if viewed from the Figure 8.7 (b).

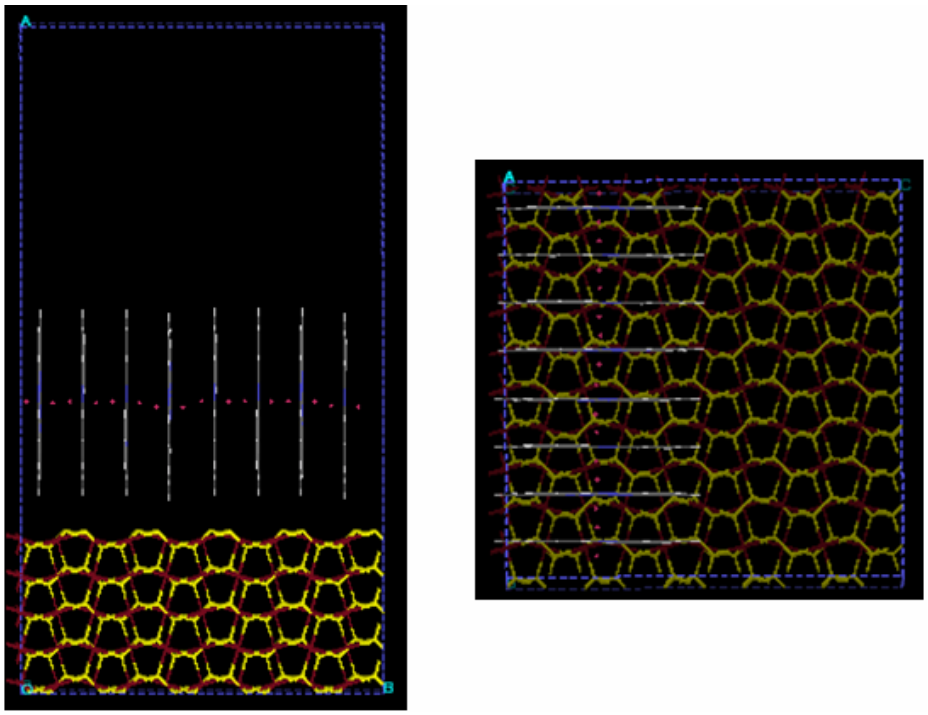

(a) (b)

Figure 8.7. Initial configurations of complex of five-layer pyrite slab (100) and eight Li_2Pc molecules, with stacking axis parallel to (100) surface. (a) side view, (b) top view

8.3.3.3 Diffusion of lithium ions with electric field

To investigate the effect of motion of the surface atoms, new simulations were performed for systems containing a 5-layer pyrite slab, with the two top 2 layers left unfixed. A six-layer χ-form of crystalline Li_2Pc (each layer containing four Li_2Pc molecules) was initially set with the stacking axis perpendicular to pyrite (100) surface,

and the bottom four Li_2Pc layers were left unfixed. That is, atoms close to the interface on both sides were unfixed. The fixed layers are used to mimic the bulk properties of Li_2Pc and pyrite, respectively. The resulting simulation cell has dimensions of 27.14 Å × 27.14 Å × 100 Å. In such system, an external electric field was applied in order to promote lithium ion transport through the interface during the time scale of the simulation. The initial configuration is shown in Figure 8.8.

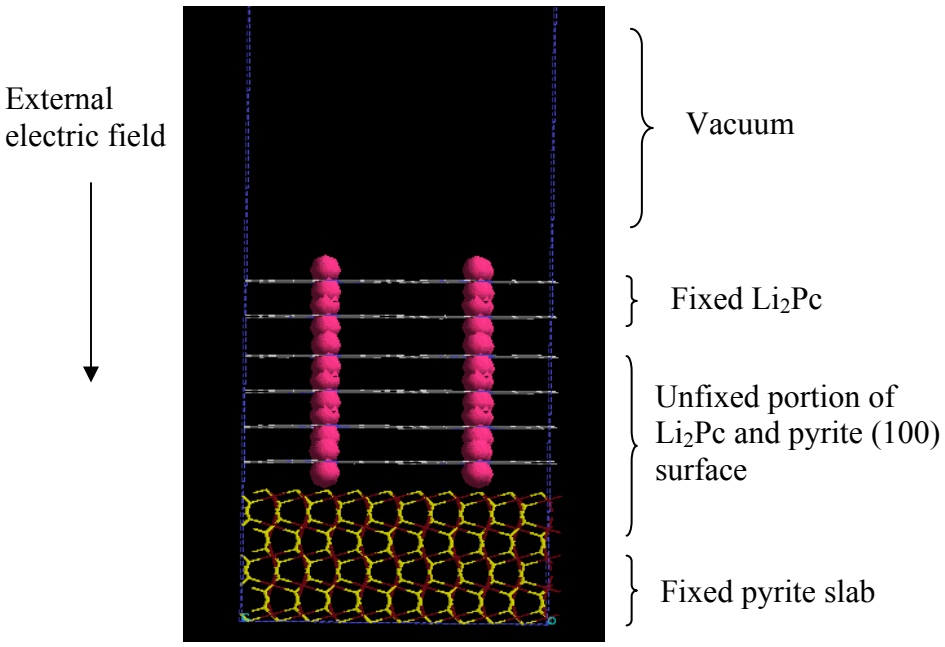

Figure 8.8. Initial configurations of complex of five-layer pyrite slab (100) with six-layer Li_2Pc for motion of lithium ions

8.3.3.4 Force fields

The selected force fields contain intramolecular and intermolecular terms. The model and parameters for Li_2Pc were the same as in previous section. For the pyrite slab,

intramolecular terms include bond potentials of Fe-S and S-S pairs and valence angle potential of the S-S-Fe term. The intermolecular terms include the short-range Lennard-Jones (LJ) potential and the long-range electrostatic (Coulombic) potential. The LJ parameters for pyrite were taken from the literature.[460] The Ewald sum[164] was used to incorporate long-range corrections to the usual electrostatic potential function. The interactions between Li_2Pc and pyrite are two-body pair potentials of any combinations of two of Li, C, N, H, Fe, and S atoms, including short-range LJ potential and long-range electrostatic potential.

The charge equilibration method of Rappe & Goddard[461], which takes into account the geometry and the electronegativities of the various atoms, rendered average charges on each of the Fe atoms of +0.64, and –0.32 on each of the S atoms.[462] These charges were verified with the ab initio calculations reported in the previous section. These charges are fixed during our MD simulations.

8.3.3.5 MD procedure

The DL_POLY program,[166] version 2.14, was used in all MD simulations. MD simulations were run in the microcanonical ensemble (NVE) for the study of the deposition of Li_2Pc over pyrite surface, and in the canonical (NVT) ensemble with the Evans thermostat for the analysis of the lithium ion transport through the Li_2Pc/pyrite interface with and without an external applied electric field.

All simulations were run for 800 ps with a time step of 0.001 ps. Equilibration runs of 300 ps were performed before collecting averages in production runs of 500 ps. During the equilibration phase, the velocities were scaled according to the selected

temperature at intervals of 0.002 ps; in the production phase the scaling was disconnected, but the temperature remained approximately constant. The simulations were performed at 300 K. The cutoff radius, beyond which intermolecular interactions of the real space part of the long-range electrostatic and the Van der Waals potentials were set to zero, was chosen as 10.0 Å.

CHAPTER IX

MD SIMULATION OF Li_2Pc

9.1 Introduction

Di-lithium phthalocyanine (Li_2Pc) has been proposed as a solid electrolyte for lithium-ion batteries, with the expected advantage of providing single-ion transport characteristics for lithium ions. [456]Molecular self-assembly may lead to the formation of lithium ion conducting channels, where the anion matrix of di-lithium phthalocyanine, an unsaturated macrocyclic compound, forms the channel. When such self-assembled structure is used as solid electrolyte of lithium-ion batteries, lithium ion transport may depend on the electric field gradient established between the electrodes, instead of being a function of polymer segmental motion as that observed for oxygen-based solid polymer electrolytes, and therefore, it is expected that the temperature dependence for lithium ion conduction will be minimized. Also, voltage drop across the electrolyte will be minimized even at high current loads because of the single-ion transport characteristics. The performance of Li_2Pc as electrolyte in an all-solid state electrochemical cell has been recently reported.[444]

In view of the potential advantages of the use of Li_2Pc as a solid electrolyte, understanding the lithium-ionic transport mechanisms in solid Li_2Pc becomes essential. However, little is known about its crystalline structure. Other metal phthalocyanines are known to be polymorphic.[445-447,449,463-469] Particularly, a great deal of research has been

done on the polymorphism of lithium phthalocyanine because of its potential use as an oximetry probe and its interesting electrical and magnetic behavior.[445,446] Depending on the preparation conditions, LiPc can crystallize in three different structures, namely, α-, β-, and χ-forms. The α- and β-forms of LiPc show monoclinic unit cells with parameters a = 2.57 nm, b = 0.38 nm, c = 2.36 nm, and β = 91.0° and space group C2/c, [470]and a = 1.94 nm, b = 0.49 nm, c = 1.40 nm, and β = 120.36° and space group $P2_{1/c}$,[471] respectively. The χ-form shows a tetragonal unit cell with parameters $a = b$ = 1.385 nm and c = 0.65 nm and the space group P4/mcc.[466] These three polymorphs showed different properties correlated to the nature of molecular packing.[447]

X-ray spectra of Li_2Pc were obtained at Argonne National Laboratory [443] and at the Air Force Laboratory where Li_2Pc solid state density was also determined.[444] We have used this information to formulate models that, in conjunction with ab initio data for the single molecule and dimers, are input for classical molecular dynamics (MD) simulations used to investigate self-assembled structures and determine their corresponding X-ray spectra. We focus on the characterization of structural and dynamical properties of a self-assembly of Li_2Pc and its potential to provide lithium-ion conducting channels for lithium-ion batteries. Calculated X-ray spectra and lithium-ion diffusion coefficients are compared to experimental results. The possibility of existence of ion-channels in the solid state structure is investigated through analyses of configurations derived from the MD simulations.

9.2 MD simulations at 300 K

9.2.1 Structures

9.2.1.1 Final configurations

The final structures (after 1200 ps total simulation length) of the four forms of Li_2Pc are shown in Figure 9.1. The corresponding Li-Li intramolecular distance (for α-, β-, ε-, and χ-forms) are also computed as averages and reported in Table 9.1. The MD results (Figure 9.1) indicate that molecules in ε-form and χ-form are shifted from each other in two adjacent layers, while those in the α-form and β-form are staggered. In the shifted structure, lithium atoms locate between the ring center of one molecule and one of the benzene rings of the second molecule, whereas in the staggered structure, both lithium atoms locate between the ring centers of the two molecules. In other words, if we see these two dimer complexes, the overlapped portion of dimer complex is larger in the staggered structure than in the shifted structure. The separations between layers (Table 9.1) have been computed (from the last MD configuration of each case) as averages over measured distances between all the equivalent two adjacent layers within the simulation cell. Comparison of these distances (Table 9.1) with those of $(Li_2Pc)_2$ calculated by B3LYP/6-31G(d) (3.72 Å for the staggered form and 3.77 Å for the shifted form)[398] indicates good agreement between MD and DFT regarding the staggered forms, whereas shorter distances are found by MD in the shifted configurations.

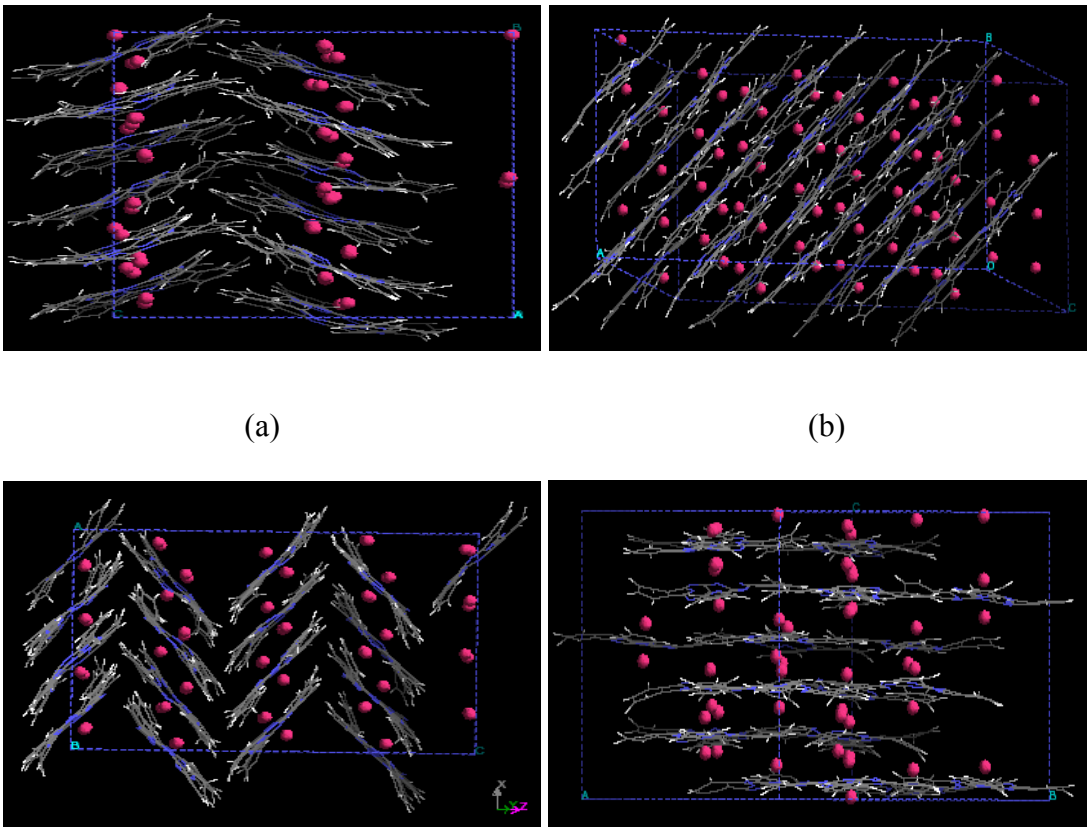

(a) (b)

(c) (d)

Figure 9.1. Structures resulting from MD after 1200ps of production time. (a) α-form, (b) β-form, (c) ε-form, (d) χ-form

Table 9.1: Average parameters of Li_2Pc self-assembled structures after 1200 ps of MD

Li_2Pc polymorphs	α-form	β-form	ε-form	χ-form
Structure	staggered	staggered	shifted	shifted
Density (g/cm^3)	1.40	1.40	1.51	1.40
Interplanar distance (Å)*	3.75	3.52	3.17	3.25
Li-Li intramolecular distance (Å)*	2.67	2.68	2.45	2.47
Energy (kJ/mol)	-1850.50	-1853.44	-1852.31	-1856.71
Energy fluctuation (kJ/mol)	8.10	9.07	9.12	8.05
Temperature (K)	285.60	279.26	280.68	285.05
Temperature fluctuation (K)	4.33	3.66	3.70	4.30

* According to B3LYP/6-31G(d) optimizations, the interplanar separations in the staggered form of the dimer is 3.72 Å, and 3.77 Å for the shifted form. The Li-Li intramolecular distance in the dimer is 2.56 Å (staggered), 2.23 Å (shifted), and 1.99 Å in the monomer. [398]

Another difference between the DFT dimer structures and the MD results arises from the intramolecular distance between two lithium atoms, which are elongated after MD (2.2-2.6 Å for ε-, and χ-forms, and 2.4-2.9 Å for α-, and β-forms, note that average values are listed in Table 9.1), whereas 1.99 Å, 2.23 Å, and 2.56 Å separations were found after B3LYP/6-31G(d) geometry optimization of a single molecule as well as in the shifted and staggered dimers, respectively.[398] The longer Li-Li intramolecular distances obtained from the MD simulations in comparison with the DFT results point to the influence of collective effects of the much larger ensemble of molecules in the MD simulations, but also they may be a reflection of a weakening of the Li-N bonds which would facilitate the mobility of the lithium atoms in the self-assembled structure. On the other hand, the small energy difference found between the average total energies shown in Table 9.1 is an indication of possible polymorphism of Li_2Pc.

9.2.1.2 Radial distribution functions

Radial distribution functions (rdf's), $g_{XY}(r)$, are indicators of local structure, defined as the ratio of the local density (at position r) of atoms Y surrounding a central atom X, with respect to the bulk density, where the local density is evaluated in spherical shells surrounding the central atom.

Rdfs between Li and H, C, N, and Li respectively are shown in Figure 9.2. The first peak of the $g_{LiLi}(r)$ corresponds to intramolecular Li-Li distances (Figure 9.2 (a)). For the ε- and χ-forms (shifted) these peaks are sharper and more intense than those of the staggered forms, and they are centered at 2.45 and 2.47 Å respectively. For the staggered α- and β-forms the first peak is slightly shifted to larger distances, centered at about 2.67 Å. Note however, that the first peak of $g_{LiLi}(r)$ for the α-form presents a small shoulder approximately at 2.45 Å which may indicate that the α-form is composed by a combination of shifted and staggered structures. The second and third Li-Li peaks of $g_{LiLi}(r)$ also provide a good indication of the difference between staggered and shifted structures. The second peak of each form corresponds to two lithium atoms between two consecutive Pc rings, whereas the third peak of each form corresponds to Li57-Li57', or Li58-Li58' (see Figure 8.4). The staggered structures have their second peak located at 3.8 to 4 Å for the β- and α-forms respectively, and a clear third peak is located at about 5 Å. In contrast, the second and third Li-Li peaks of the shifted structures are located at longer distances, about 5 and 6 Å respectively for the ε-form, whereas less long-range order is observed for the χ-form.

Figure 9.2 (b) displays the Li-N rdfs, where the first peak corresponds to Li-N intramolecular interactions. The first peak at 2.3 Å in $g_{LiN}(r)$ (Figure 9.2 (b)) corresponds to lithium atoms to N49, N50, N53, and N54 (see Figure 8.4), while the second peak at 3.6 Å to lithium atoms to N51, N52, N55, N56; the position of both peaks agree for all the crystalline forms, but the second peak is less intense for the staggered structures, and a third peak is also clearly defined for all cases. The broadening of the first peak may be attributed to the contributions from two alternative structures in the staggered forms.

$g_{LiX}(r)$s (X=C, H) of the ε- and χ-forms (Figures 9.2 (c) and (d)) are similar, and similarity also exists between those of the α- and β-forms. As we discussed before, in the shifted system, lithium atoms are located between the ring center of one molecule and one of the benzene rings of the second molecule. Thus, the first peak of $g_{LiX}(r)$ (X=C, H) (Figures 9.2 (c) and (d)) in the ε- and χ-forms corresponds to lithium atoms interacting with C and H atoms respectively on the benzene ring mentioned above.

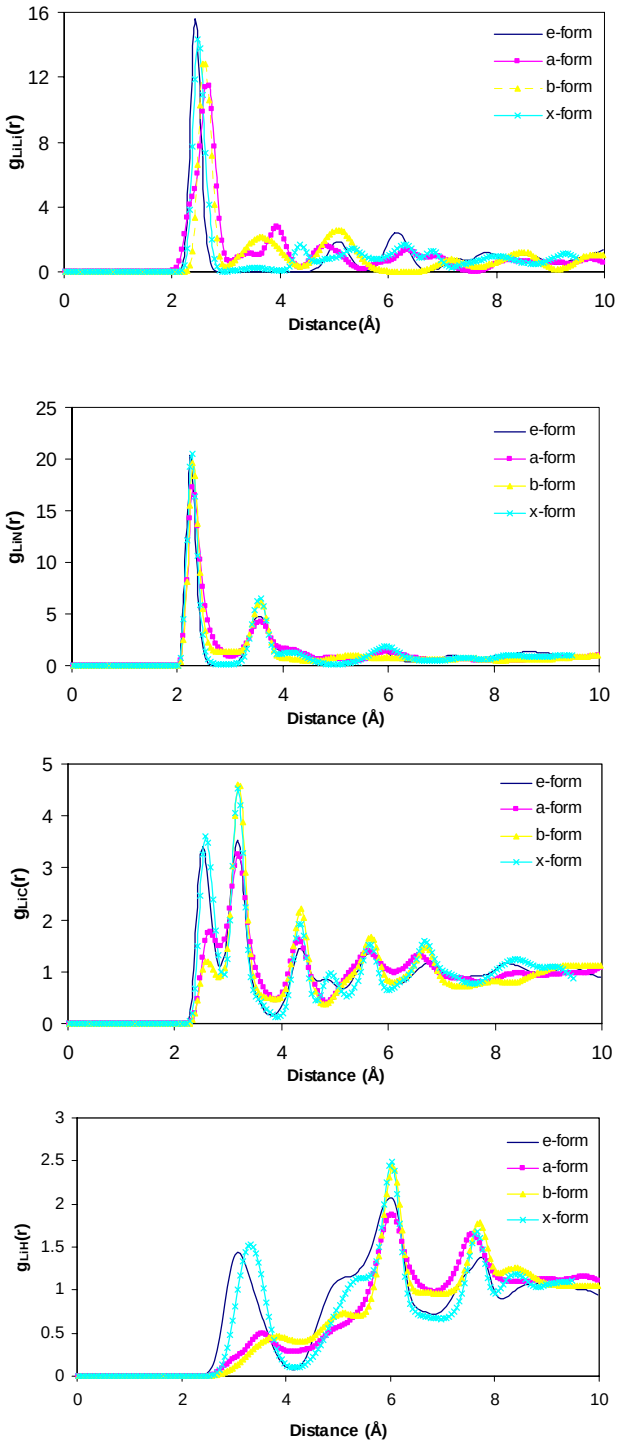

Figure 9.2. Partial radial distribution functions. (a) Li-Li; (b) Li-N; (c) Li-C; (d) Li-H

In the staggered system, lithium atoms are located between the centers of two phthalocyanine rings. Thus in the α- and β-forms, the first peak of g_{LiC}(r) mainly corresponds to lithium atoms interacting with part of C atoms of the inner Pc ring, their intensity is much lower than that of the ε- and χ-forms, probably because there is a small degree of shifting that causes the Li ion not to be centered on the Pc ring, therefore we detect a combination of shorter Li-C and longer Li-C intramolecular distances. Both the first and second peaks are much sharper and better defined for the shifted than for the staggered structures. Also, because of the different location of lithium atoms in the shifted and staggered systems, the first peak of $g_{LiH}(r)$ is centered at 3.2 Å in the ε- and χ-forms (where the Li atom is on top of the benzene ring), whereas a very low density peak is found at 3.7 Å in the α- and β-forms.

9.2.2 X-ray spectra

PowderCell Version 1.0,[472] a program for exploring and manipulating crystal structures and calculating X-ray powder patterns was used to calculate X-ray spectra corresponding to the simulated structures. This program uses as input primitive cell parameters and structure (atomic positions) and simulates an X-ray pattern using Bragg's law, weighting the contributions of each atom with calculated structure factors. We used as input the coordinates from the final molecular structure of the MD simulations in the primitive cells of each of the four crystalline forms, along with their respective primitive cell parameters, to obtain simulated X-ray powder diffractograms.

Figures 9.3 (a) and (b) show experimental X-ray diffraction spectra of Li_2Pc synthesized in Argonne National Laboratory (dried at 220 ^oC in vacuum), and received

from Aldrich (dried at 160 ^{o}C in vacuum) respectively.[398] Comparing the two experimental spectra, we observe that in 9.3 (a) several sharp peaks appear at an angle 2θ around 20^{o}, but only a broad peak is detected in Figure 9.3 (b), where some small peaks disappear. We speculate that the experimental X-ray spectra may reflect a mixture of Li_2Pc polymorphs, some of them less crystalline than others; the presence of impurities may also add new features to the spectrum, as observed in other metal phthalocyanines.[469,473] In addition, different methods to synthesize Li_2Pc may give different mixtures of Li_2Pc polymorphs. It is also possible that structural changes may exist because of the different drying temperatures.

Figures 9.3 (c) to (f) show the simulated X-ray spectra for the four investigated crystalline forms. In our comparative analysis, we notice that internal molecular reorientations of the Li_2Pc molecules in a primitive cell may cause enhancement, reduction, or even disappearance of some of the peaks that would arise because of the primitive cell dimensions, and the possible influence of polymorphism in the experimental data may obscure a direct comparison of the calculated and experimental structures. However, we perform a direct comparison of each of the calculated spectrum to the experimental data (Figs. 9.3 (a) and (b)), assuming that the latter are single crystalline phases.

A reasonable agreement in the peak positions is found for the ε-form (Figure 9.3 (e)), not surprisingly since the parameters of the primitive cell of the ε-form were selected to reproduce the d-spacing of the experimental diffractogram of Figure 9.3 (a); however the agreement is less satisfactory for angles $2\theta > 20^{o}$. The correspondence is

much better for the β-form which has similar dimensions to the ε-cell. Moreover, comparison between the relative intensities of the simulated diffraction peaks with the experimental ones, points to a better agreement of the β-form over the ε-form. The experimental spectra in Figures 9.3 (a) and (b), and that of the calculated β-phase (Figure 9.3 (d)) show also a close similarity to the reported spectra for the β-phase of H_2Pc [473] and MgPc.[469]

On the other hand, the simulated X-ray spectrum of the α-form of Li_2Pc exhibits few and rather broad diffraction peaks, compared to other three Li_2Pc simulated polymorphs. This feature is indicative of a low crystallinity of the α-form, which was also observed for the α-forms of other metal phthalocyanines.[445,474] The fusion of the two peaks appearing in the range $5 < 2\theta < 10^{o}$ is another characteristic of the α–phase, also detected in other metal and non-metal phthalocyanines. [469,473]In comparison with Figures 9.3 (a) and (b), we discard the contribution of the α-phase to the experimental spectrum.

The simulated X-ray spectrum of the χ-form shows a well defined crystalline structure. However, although some peaks appear at the same position of the experimental ones, most of them do not, and probably the χ-form is not the predominant form that contributed to the experimental data. However, the peak of highest intensity for this structure appears a value 2θ of 18.8 ^{o} in coincidence with the broad peak of Figure 9.3 (b) that makes the main difference between the experimental structures Figures 9.3 (a) and (b). This aspect points out to the possibility of a mixture of the most-likely β-form with the χ-form in the experimental (Figure 9.3 (b)) spectrum.

In summary, the results in Figure 9.3 indicate that the best agreement between experimental and calculated results is found for the β-phase.

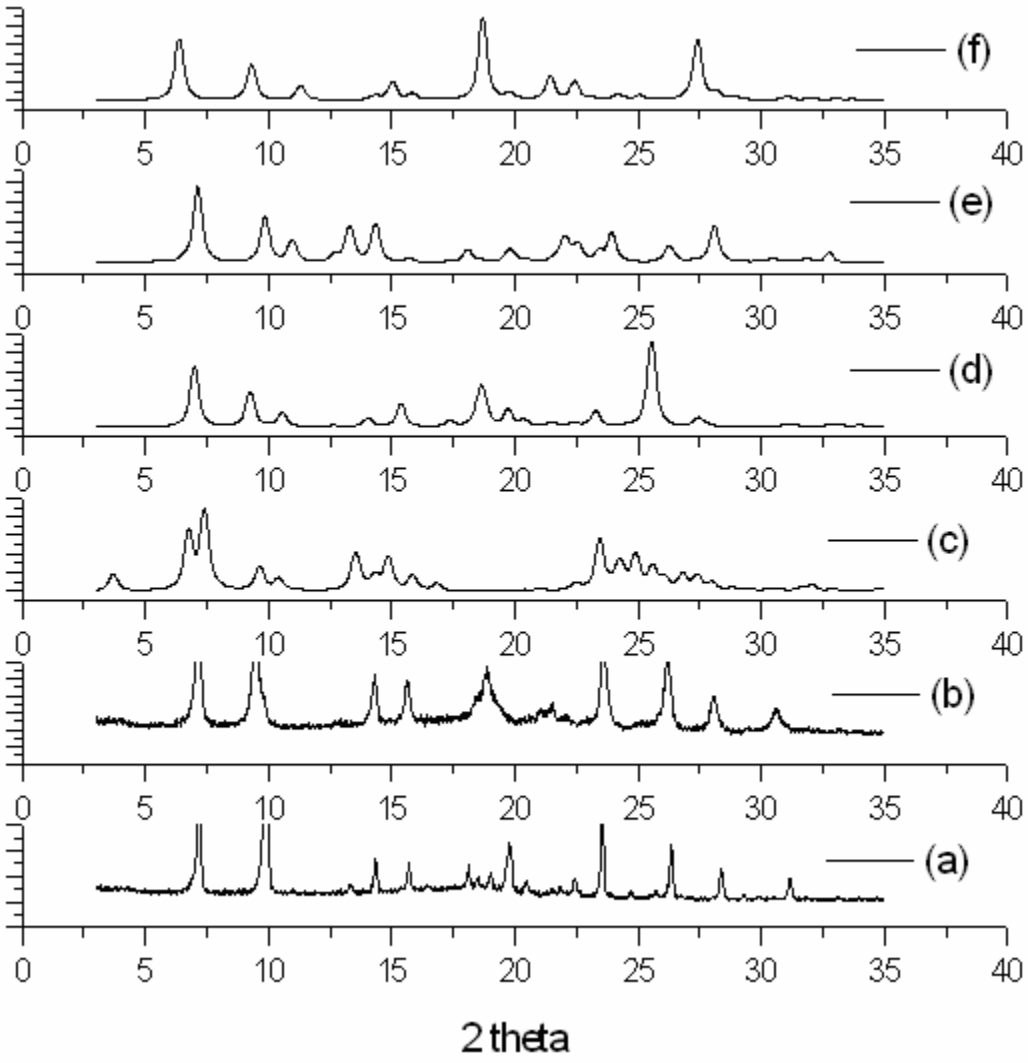

Figure 9.3. Comparison of simulated X-ray with experimental data. (a) Li_2Pc synthesized in Argonne National Laboratory (dried at 220 ^oC vacuum), (b) Li_2Pc from Aldrich (dried at 160 ^oC vacuum), (c) α-form, (d) β-form, (e) ε-form, (f) χ-form

9.2.3 Ion channel formation and ionic diffusion

Looking at the self-assembly molecular organization, an alignment of lithium ions is found that can be associated with the expected lithium ion conducting channels. We can visualize these conducting channels in α-form, β-form, and ε-form when combining the top (not shown) and side (Figure 9.1) views of the unit cells, or rotating the unit cell of χ-form, as shown in Figure 9.4. For clarity, lithium ions are highlighted as purple ball model. These chains of ions are oriented along the same direction across layers. From the view of selected, we can clearly see the aggregation of lithium ions near the center of the macro-center ring of Li_2Pc molecules. The distribution and orientation of lithium ions in these structures are quite similar to the distribution and orientation of lithium ions in other crystalline lithium ionic conductors, like $LiAlCl_4$, $Li_{029}La_{0.57}TiO_3$ etc.[338] At this point, the pathways for lithium ion transport are clear in all these four crystalline forms. This satisfies one requirement for lithium ion conductor about the pathway. The next concern is how fast lithium ions can transport along these pathways.

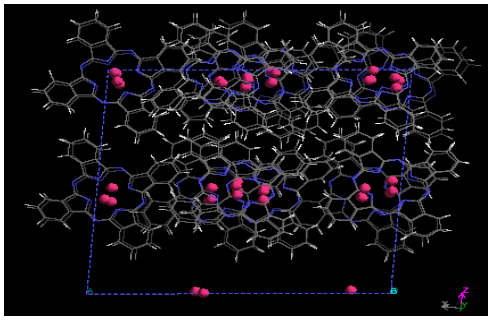

(a)

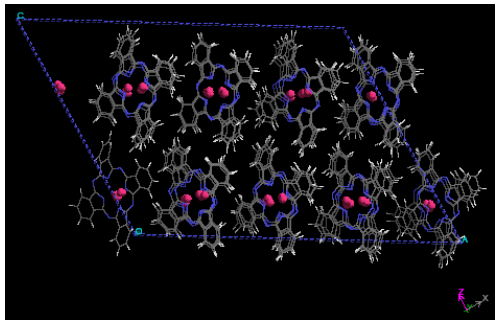

(b)

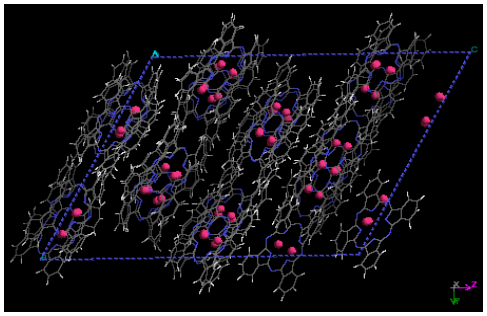

(c)

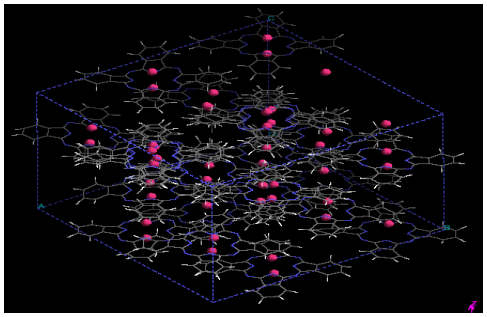

(d)

Figure 9.4. Structure obtained from MD showing the lithium ions diffusion channel. (a) α-form, (b) β-form, (c) ε-form, (d) χ-form

9.2.4 Self-diffusion coefficient

To investigate lithium mobility, we calculated the velocity autocorrelation function (VAF), which is related to the macroscopic, phenomenological, self-diffusion coefficient *D* through the Green-Kubo formula,[475] written as the time integral of a microscopic time-correlation function:

$$D = \int_0^\infty \langle v(t).v(t_0) \rangle_{t_0} \, dt \tag{9.1}$$

where the function in brackets is a measure of the projection of the particle velocity at time t onto its initial value, averaged over all initial conditions t_0. Figure 9.5 shows the VAF for lithium ions of Li_2Pc in each of the crystalline forms, at 300K. The velocity autocorrelation function of lithium ions shows oscillations in the time domain, indicating the rattling motion of lithium ions in the "cage" of their nearest neighbors. The corresponding conductivity of lithium ions was calculated via the Nernst-Einstein equation,

$$\kappa = \frac{cDz^2F^2}{RT} \tag{9.2}$$

where the *c* is the concentration of lithium ions, *D* is the ionic diffusion coefficient, *z* is the charge on lithium ions, *F* is the Faraday constant, *R* is the gas constant, and *T* is the absolute temperature.

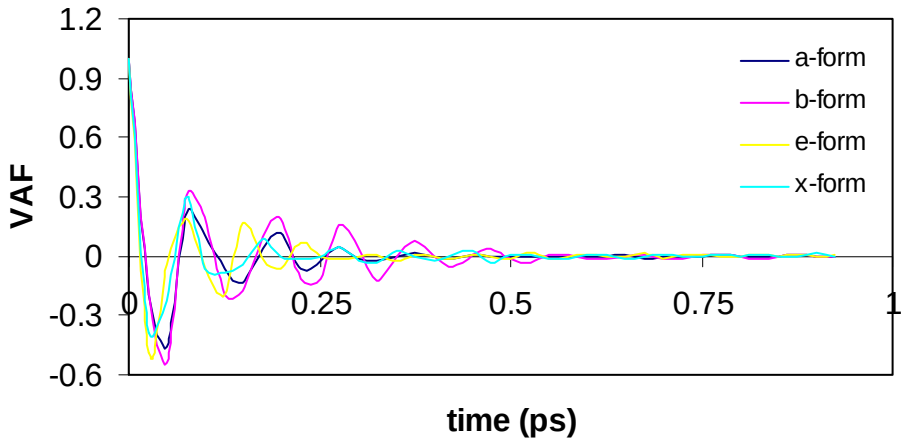

Figure 9.5. VAF plots for lithium ions

Table 9.2: **Calculated diffusion coefficient and conductivity of lithium ions in various Li_2Pc crystalline forms**

Li_2Pc crystalline form	Diffusion coefficient (cm^2/s)	Conductivity* (S/cm)
α	5.94×10^{-9}	2.65×10^{-5}
β	1.35×10^{-8}	6.03×10^{-5}
ε	2.04×10^{-8}	9.79×10^{-5}
χ	1.88×10^{-8}	8.40×10^{-5}

*Experimental ionic conductivities of 5.1 to 8.9 $\times10^{-4}$ S/cm were obtained at 300 K.[444]

The results shown in Table 9.2 illustrate the differences in ionic mobility imposed by the various crystal structures, with the less crystalline α-form having the smallest self-diffusion coefficient and the ε-form the highest. A transport mechanism for lithium ions in Li_2Pc has been suggested, whereby instead of depending on polymer segmental motion as in the PEO system, [476] the lithium ion diffusion would depend mainly on the electric field gradient in the system. Values of diffusion of lithium ions in PEO/$LiClO_4$ mixtures were reported to be 5.2 x 10^{-9} cm^2/s at 349 K, [477]which are below our

calculated values at 300 K. Compared to the experimental ionic conductivity in Li_2Pc (Table 9.2), the simulated lithium ion conductivity results are about one order of magnitude smaller. This difference is explained considering that in the simulation ions move via self-diffusion determined by the field created by the self-assembly of Li_2Pc molecules, while in the experiment diffusion across the electrolyte/electrode interface is driven by a difference of chemical potential and by an electric field gradient established between the electrodes of an electrochemical cell. Work to incorporate the effect of an electric field in the simulations is in progress, and will be reported in next chapter. Further, we note that equation (9.1) has the implicit assumption that ions at low concentrations do not interact with each other and therefore their motion is uncorrelated. However, this is an oversimplification of this system that has a strong long-range Coulombic component. A more accurate equation would relate the conductivity to the charge flux autocorrelation function,[478] where the charge flux is calculated by the sum of charge times velocity for each ion. Alternatively, one could calculate Maxwell-Stefan diffusion coefficients, where the mass fluxes are linearly related to the gradient of chemical potential instead of being proportional to the gradient of concentration. [479]

9.3 Temperature effects

Molecular dynamics simulations of polymorphs of Li_2Pc at higher temperature of 373 K and 473 K are also investigated. Compared to configurations of these polymorphs at 300 K, formation of lithium ion channels is similar at higher temperatures. Figures of these configurations are not shown due to the similarity. But, main radial distribution

functions of these polymorphs are listed. Figure 9.6 to Figure 9.9 show radial distribution functions of Li-N (a), Li-Li (b), and Li-C (c) at temperatures of 300 K, 373 K, and 473 K for α-form, β-form, ε-form, and χ-form Li_2Pc, respectively. From Figure 9.7 to Figure 9.9, no clear difference among the same function in individual form of Li_2Pc at different temperatures is found, except for the small difference on the peak intensities. These functions together with their final configurations (not shown) indicate that these three forms are relatively stable up to the temperature studied. On the other hand, the radial distribution functions of α-form at different temperatures show some difference, especially the function of Li-Li as in Figure 9.6 (b). The function at 300 K is different from those at higher temperature of 373 K and 473 K. As we discussed previously, the first peak corresponds to the Li-Li pair attached to the same phthalocyanine ring, one above and the other below. This peak is broader at 300 K than that of at higher temperatures. The second, third, and forth peaks of Li-Li at 300 K correspond to the Li-Li pairs from different phthalocyanine ring. These peaks merge to a single peak centered at about 4.3 Å at 373 K and 473 K. Recall the X-ray at 300 K, we know that a low crystallinity of the α-form was observed. This indicates that the crystallinity of the α-form at higher temperature is enhanced. As at 300 K, α-form with low crystallinity has only half conductivity of other three forms, the enhanced crystallinity of the α-form might increase the conductivity at higher temperatures.

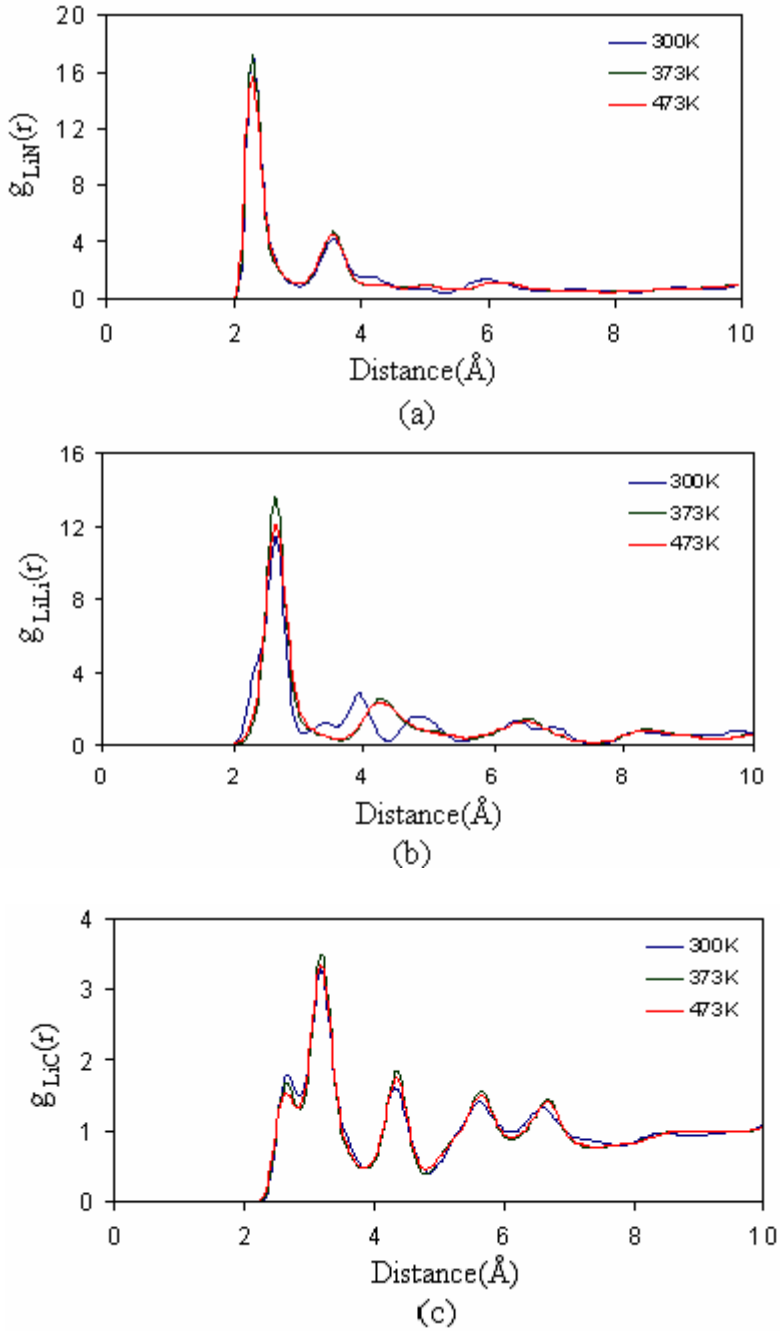

Figure 9.6. Radial distribution function of α-form Li_2Pc at different temperatures. (a) $g_{LiN}(r)$, (b) $g_{LiLi}(r)$, (c) $g_{LiC}(r)$

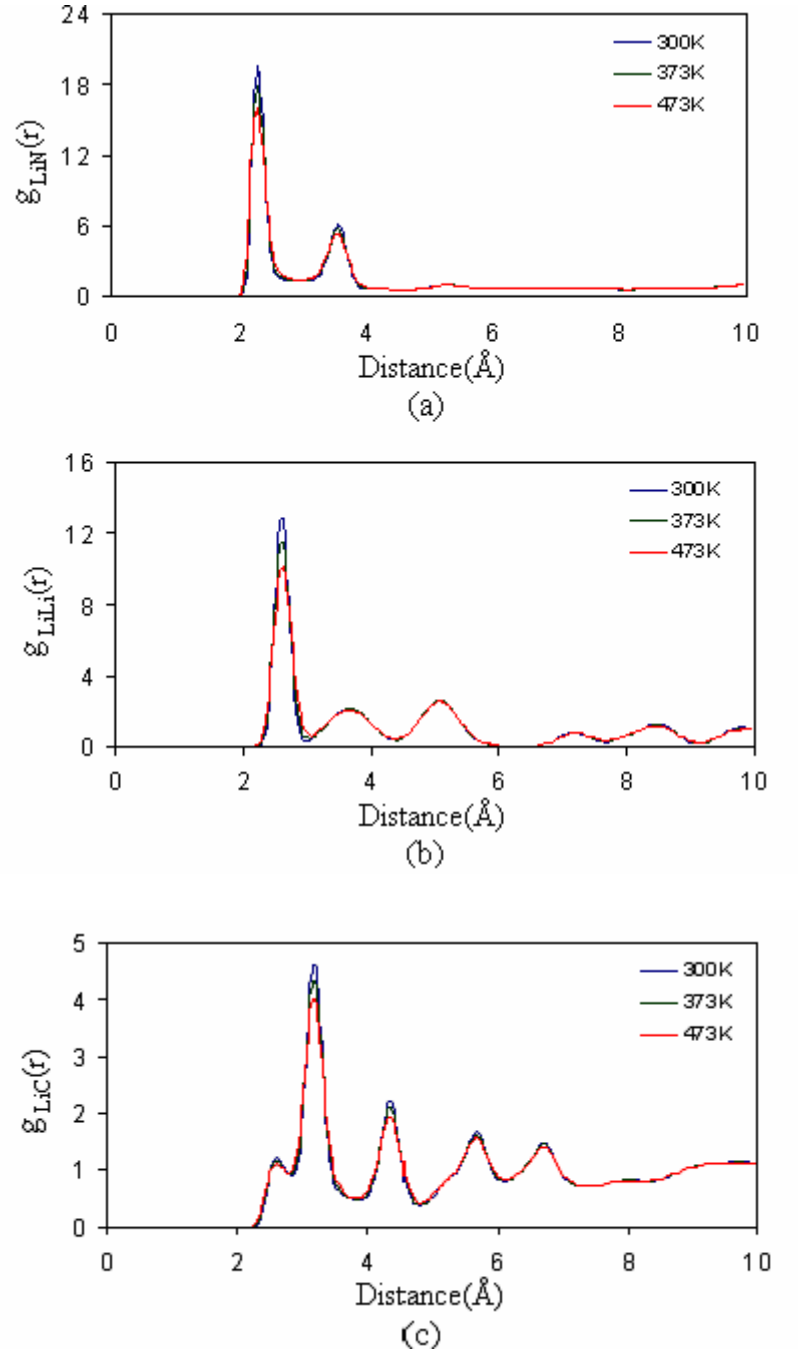

Figure 9.7. Radial distribution function of β-form Li_2Pc at different temperatures. (a) $g_{LiN}(r)$, (b) $g_{LiLi}(r)$, (c) $g_{LiC}(r)$

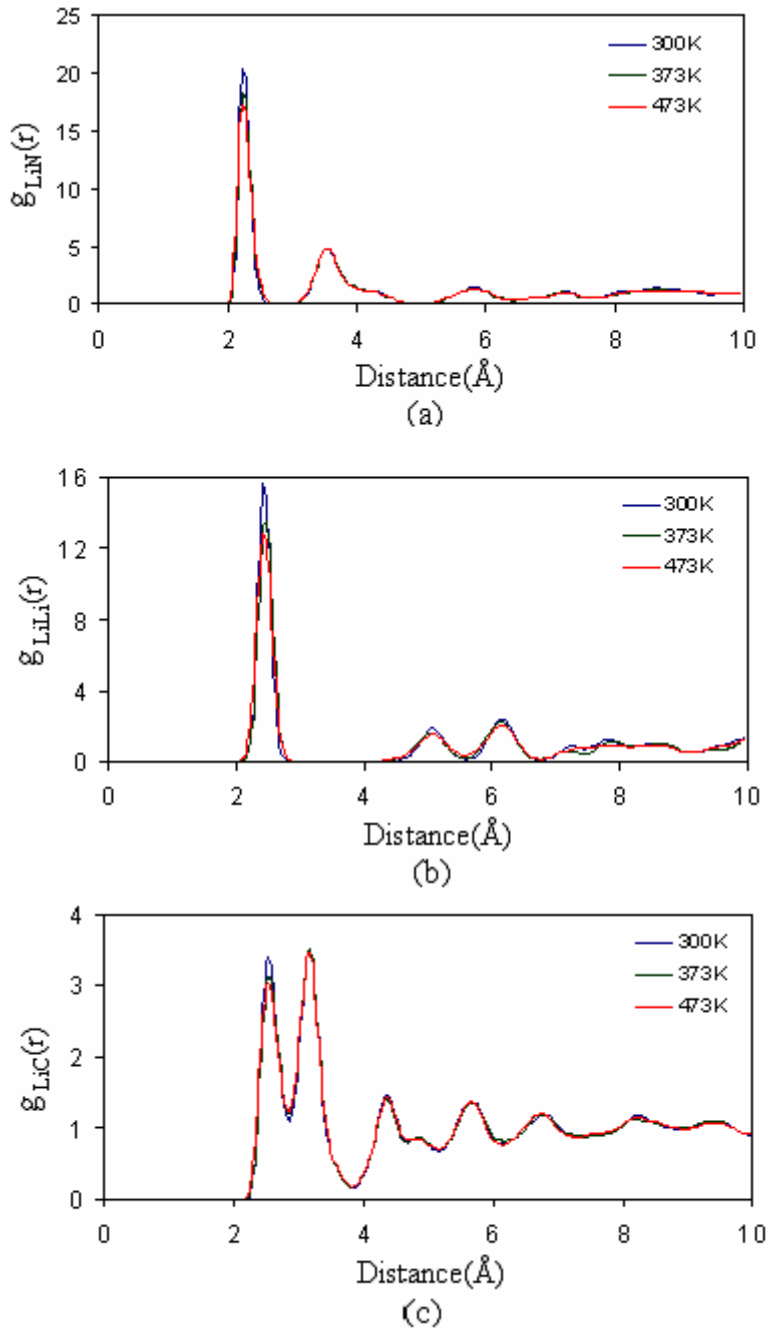

Figure 9.8. Radial distribution function of ε-form Li_2Pc at different temperatures. (a) $g_{LiN}(r)$, (b) $g_{LiLi}(r)$, (c) $g_{LiC}(r)$

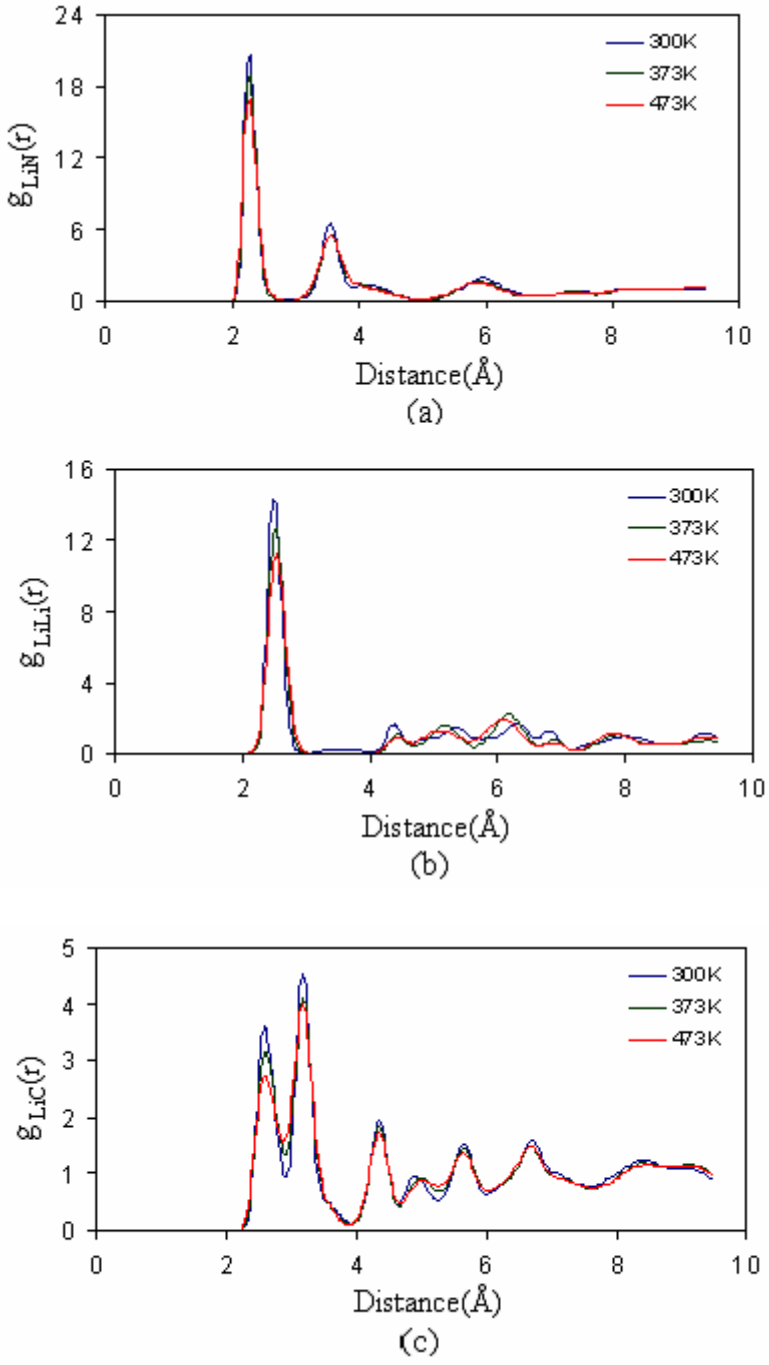

Figure 9.9. Radial distribution function of χ-form Li_2Pc at different temperatures. (a) $g_{LiN}(r)$, (b) $g_{LiLi}(r)$, (c) $g_{LiC}(r)$

9.4 Conclusions

MD simulations show the viability of using a large array of molecules to form a lithium ion conducting channel via molecular self-assembly. The elongation of the Li-Li intramolecular distances based on the MD simulations illustrate collective effects provided by the self-assembled structure and their importance for facilitating fast ionic transport with the channel.

The close values of the calculated energies of MD suggest the ease of formation of various polymorphs simultaneously during material preparation. The comparison of the simulated and experimental X-ray data indicates the possibility of a mixture of the most-likely β-form with the χ-form in the experimental spectrum. On the other hand, calculated ionic conductivities are one order of agnitude below the experimental values, which is primarily attributed to the absence of an external driving force for ionic diffusion in the simulated self-assembled structures.

CHAPTER X

AB INITIO CALCULATIONS/MD SIMULATIONS OF INTERPHASE

10.1 Introduction

Solid state lithium ion batteries have been of interest for microbattery applications for decades [209,480,481] and new materials including electrodes and solid electrolytes are constantly being tested.[450,482-484] Poly(ethylene oxide) (PEO) –based materials are favored materials for solid electrolytes.[485] However, they exhibit low ionic conductivity when operated below their crystallization temperature. Suggested strategies to improve the ionic conductivity at ambient temperature include composition and molecular structure modifications to preempt crystallization, [486,487]and polymer networking, such as chemical cross-linking, which consists of adding a suitable ionically conducting liquid to a polymer matrix.[314,429] These approaches effectively improve the ionic conductivities at the desired temperatures, but in such battery design, a separator or supporting matrix is required because of the liquid-like nature of the electrolyte.

Thus, solid electrolytes with good ionic conductivity are actively investigated. Among them, the crystalline structure and self-assembly characteristics of di-lithium phthalocyanine (Li_2Pc) as well as its bulk properties as ion conductor in an electrochemical cell, where Li_2Pc is used as the solid state electrolyte, have been

analyzed.[398,450] The main advantage of this solid electrolyte is that the anion matrix of di-lithium phthalocyanine, an unsaturated macrocyclic compound, forms continuous ion conducting channels for lithium-ion transport. The conductivity of Li_2Pc is about 10^{-4} S/cm, [402] which is not far from the value required for moderate-rate power sources (10^{-3} S/cm at room temperature). Another advantage is that the transference number for lithium when Li_2Pc is used as solid electrolyte is equal to unity, compared to the small lithium ion transference number of polymer electrolytes.

High energy density, compatibility with the electrolyte, low cost, availability and favorable physical properties, such as nontoxicity and non-flammability are the main important factors for cathode materials. Natural pyrite (iron disulfide) is a very attractive cathode material because of its low cost at \$0.5/Kg (vs. other artificially lithiated metal oxides at \$30/kg to \$80/kg), and its high theoretical specific energy of Li/FeS_2 (1273 Wh/kg based on $4e/FeS_2$).[488] As a result, pyrite has been used in commercial lithium primary cells [489] to power cameras, computers and watches. Recently there has been a renewed research interest in and efforts to improve the performance of the Li-Fe-S system for secondary cells.[488,490,491] In these investigations, lithium ion intercalations have been analyzed from charge-discharge processes, cyclic voltammograms, X-ray spectroscopy, Scanning Electron Microscopy (SEM), Electrochemical Impedance Spectroscopy (EIS). Yet, the properties at the interfaces between cathode and electrolyte are still not as well understood as the bulk properties of the individual components. In fact, it is very difficult to obtain experimental data of the interface structure and behavior at an atomistic level. On the other hand, computational

techniques have proven to be effective methods to understand interfacial phenomena.[430,492-496] In this work, ab initio and molecular dynamics simulations are used to analyze the Li_2Pc/pyrite interface by characterizing the structure of a self-assembled Li_2Pc electrolyte film in contact with a pyrite (100) surface. Structural and dynamical properties are analyzed, including radial distribution functions, adsorption of Li_2Pc on the pyrite (100) surface, and intercalation of lithium ions into the model pyrite structure under an applied external electric field.

10.2 Ab initio/DFT calculations of interactions of Li_2Pc with pyrite (100)

10.2.1 Interactions of the pyrite cluster with the simplified Li_2Pc model ($Li_2C_8N_8H_8$)

10.2.1.1 Characterization of the simplified Li_2Pc model ($Li_2C_8N_8H_8$)

Figure 10.1 shows the B3PW91/6-311G optimized structure of $Li_2C_8N_8H_8$. Table 10.1 shows the charge distribution of $Li_2C_8N_8H_8$, in comparison to those of the atoms in similar positions in Li_2Pc obtained with the same method.[398]

The optimized structure of $Li_2C_8N_8H_8$ exhibited a planar ring structure with two lithium ions located in the middle axis of the ring, one above and the other below, as observed in Li_2Pc.[398] The atomic charges at similar positions in $Li_2C_8N_8H_8$ and Li_2Pc agree reasonably well, especially for the Li and N atoms. The charge on C atoms is less positive in $Li_2C_8N_8H_8$ than in Li_2Pc as a result of the substitution of the benzene rings by H atoms. However, the -CH groups in $Li_2C_8N_8H_8$ have an average positive charge of ~ +0.29, which is similar to the charge of $–C_4H_2$ groups (+ 0.35) in Li_2Pc located at the same position regarding the phthalocyanine ring. The distance between two Li atoms in

$Li_2C_8N_8H_8$ is 2.14 Å, and the average distance between Li and N1 is 2.34 Å, slightly elongated in comparison to those in Li_2Pc, 1.99 Å and 2.18 Å respectively. However, the central ring structure of $Li_2C_8N_8H_8$ did not change much compared to that of Li_2Pc. The distances for N1-C and N2-C are 1.36 Å and 1.32 Å. In Li_2Pc calculated with the same method, these two distances are 1.37 Å and 1.32 Å, respectively.

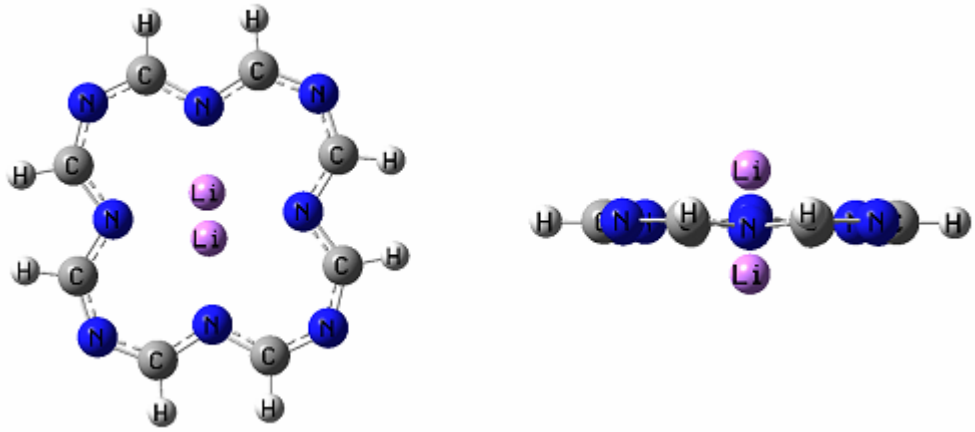

(a) (b)

Figure 10.1. Optimized structure (B3PW91/6-311G) of $Li_2C_8N_8H_8$. (a) Top view; (b) Side view

Table 10.1: Mean values (averaged over all atoms of the same type) of the Mulliken atomic charges from B3PW91/6-311G optimization of $Li_2C_8N_8H_8$. N1 represents each of the four nitrogen atoms located close to ring center, and N2 corresponds to the other four nitrogen atoms located farther from the ring center (Figure 10.1 (a))

	Atom type				
	H	C	N1	N2	Li
Charge in $Li_2C_8N_8H_8$	0.17	0.12	-0.59	-0.36	0.74
Charge in Li_2Pc[398]	0.20	0.39	-0.63	-0.40	0.66

Both ab initio and DFT yield $Li_2C_8N_8H_8$ dimers in shifted configurations, as shown in Figure 10.2. This is similar to the results for $(Li_2Pc)_2$,[398,450] where the shifted dimer configurations are energetically more stable than the staggered ones. Electronic and binding energies are summarized in Table 10.2. Binding energies are calculated as the difference between the energy of the complex and the sum of the individual energies of the reactant molecules, calculated with the same level of theory and basis set. Both configurations of $Li_2C_8N_8H_8$ shifted dimers yielded an average distance between the two rings of about 3.7 Å, compared to 3.77 Å for shifted $(Li_2Pc)_2$. The lithium atoms between two rings were separated by 4.72 Å according to the HF calculation, and by 5.34 Å from the DFT results. The intramolecular distance between two lithium atoms was in the range of 2.36 to 2.50 Å. All these distances agree well with those found in the shifted $(Li_2Pc)_2$ configuration.[398] Thus, it was concluded that $Li_2C_8N_8H_8$ retains the main features of Li_2Pc and therefore it was used to calculate its interactions with a model pyrite surface.

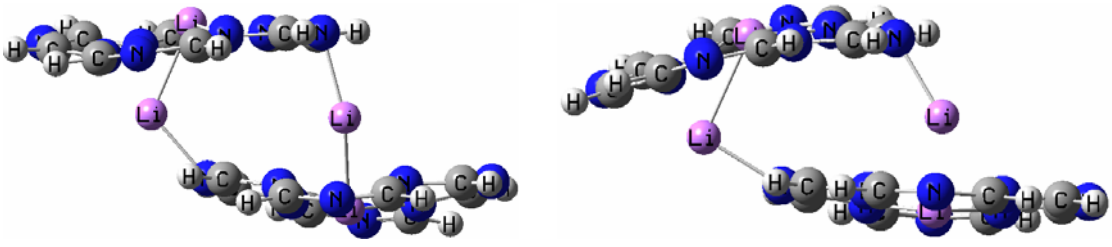

(a) (b)

Figure 10.2. Optimized structures of $Li_2C_8N_8H_8$ dimers. (a) HF/6-311G, (b) B3PW91/6-311G

Table 10.2: Optimized energies (Hartrees), BSSE corrections (Hartrees) and binding energies (B.E.) with BSSE corrections (kcal/mol), and spin multiplicity (m) for $Li_2C_8N_8H_8$ and $(Li_2C_8N_8H_8)_2$, pyrite cluster, and $Li_2C_8N_8H_8$/pyrite cluster complex

System	Method	Basis set	m	Electronic Energies	BSSE corrections	B.E.
$Li_2C_8N_8H_8$	HF	3-21G	1	-753.84505		
	HF	6-311G	1	-757.89215		
	B3PW91	6-311G	1	-762.40450		
$Li_2C_8N_8H_8$ dimer	HF	6-311G	1	-1515.86196		48.73
	B3PW91	6-311G	1	-1524.87332		40.36
24-atom pyrite	HF	LANL2DZ	1	-1138.79315		
cluster			3	-1138.84851		
$Li_2C_8N_8H_8$/pyrite	HF	3-21G/	1	-1892.77312	0.03049	65.58
cluster		LANL2DZ	3	-1892.81469	0.07147	31.16

10.2.1.2 Pyrite bulk and (100) structure

Pyrite has a simple cubic structure with space group Pa3 and cell parameter of 5.42 Å,[497] with four FeS_2 molecules in the primitive unit cell. In bulk pyrite, each Fe is coordinated by six S atoms and each S is coordinated by three Fe atoms and one S atom. In the pyrite (100) surface, Fe is coordinated by five S atoms and S by two Fe atoms and one S atom. The configurations of pyrite bulk unit cell and pyrite (100) surface are shown in Figure 10.3. Compared to the bulk structure, on the (100) surface no sulfur dimer pair is broken and the S-Fe-S triple layer is kept intact as well. Singlet and triplet multiplicities were used for the 24-atom pyrite cluster model and for the interfacial complex. Geometry optimization of the pyrite cluster alone (not shown) with HF/LANL2DZ for spin multiplicities of 1 and 3 both yielded four threefold-coordinated S sites on the surface, as found in the uppermost surface S sites of a pyrite (100) surface. The corresponding energies are shown in Table 10.2. It is found that the triplet cluster

has lower energy compared to the singlet. Corner Fe sites are coordinated by three S atoms, while side Fe sites are coordinated by four S atoms. These corner and side Fe sites are the undersaturated environment in the cluster, utilized as a basic model for surface "defect" sites.[458] This is consistent with S-deficient defects which can be present on the (100) surface to an appreciable degree.[498-501]

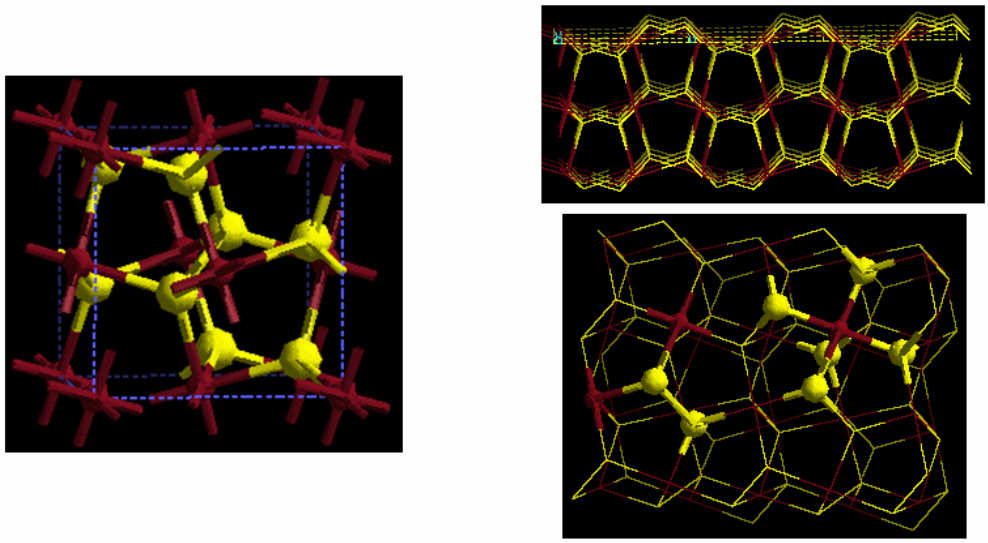

(a) (b)

Figure 10.3. Configurations of pyrite bulk and (100) surface. (a) pyrite bulk, (b) top view (right top) and side view (right bottom) of pyrite (100) surface. Fe marked as dark red and S marked as yellow. Some selected atoms are highlighted for the purpose to clearly see the coordination of Fe and S ions

10.2.1.3 Interaction of the simplified Li_2Pc model with pyrite cluster

Figure 10.4 shows the optimized structure of the singlet $Li_2C_8N_8H_8$/pyrite cluster calculated at the HF level. $Li_2C_8N_8H_8$ preferentially adsorbs to the pyrite cluster through Li-S, and N-Fe interactions with a total energy decrease (including the BSSE correction)

of 65.58 kcal/mol at HF/LANL2DZ for Fe and S atoms and HF/3-21G for $Li_2C_8N_8H_8$. The stable adsorption geometry shows one lithium atom attached to two of the threefold-coordinated S sites on the surface, the distances between Li and S are 2.51 Å and 2.53 Å. Mulliken population analysis shows that the adsorbed lithium atom has higher positive charge (+0.77) than the lithium atom embedded in the ring (+0.58). One N2 atom, with –0.36 charge (Table 10.1), is attached to one corner Fe site, at a distance of 2.05 Å. This adsorbed nitrogen has higher negative charge (-0.96) than the rest of nitrogen atoms in the ring (-0.55 to -0.82). We did not observe a third adsorption site of either lithium ion or nitrogen atoms on the pyrite cluster. The ring structure of the simplified Li_2Pc model is very stable as in Li_2Pc, and as a result the ring itself tends to extend as a planar configuration.

The same interactions Li-S and N-Fe are observed for the triplet, but the binding energy after BSSE correction is much lower, 31.16 kcal/mol. However, both binding energies (singlet and triplet) suggest that the interaction of the complex with the cluster is relatively strong, which indicates the possibility of good surface contact required for transport of Li ions. The distances found for the triplet multiplicity are 2.56 Å for Li-S and 2.03 Å for N-Fe. Mulliken population analysis yields similar charges for the main atoms as in the singlet case, +0.82 for the adsorbed Li and +0.38 for the embedded Li, –0.98 for the adsorbed N and the charges of the rest of the N atoms are in the range of –0.63 to –0.82.

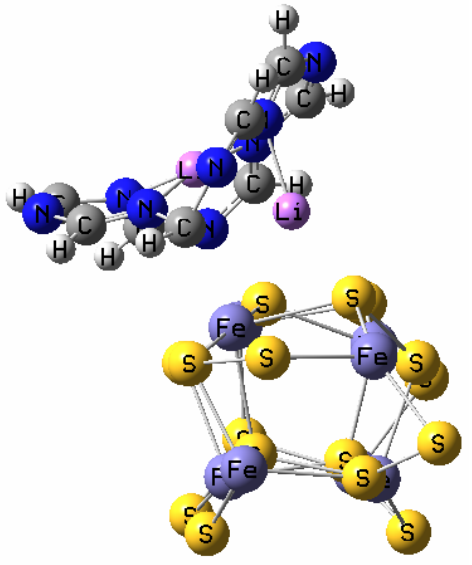

Figure 10.4. Optimized geometry of the singlet $Li_2C_8N_8H_8$/pyrite cluster at HF level with 3-21G for simplified Li_2Pc model and LANL2DZ for the pyrite cluster

After the first two adsorption sites, it is difficult to have a third atom to adsorb on the pyrite cluster because of the tendency of $Li_2C_8N_8H_8$ to form a planar structure and the electronic repulsion between the Li-Fe and N-S pairs. Therefore, finding only two predominant binding sites confirmed that the main attractive interactions of the system were those of Li-S and Fe-N. Thus, the continuous negative electrostatic potential field – lithium ion conducting channel realized in bulk Li_2Pc in our previous study might be extended to the pyrite surface.

10.2.2 Interactions of the pyrite cluster with full Li_2Pc

Li_2Pc has significant bigger surface area compared to the simplified Li_2Pc model. In order to study the interaction of pyrite cluster with full Li_2Pc, a bigger size of pyrite

cluster is needed to bring contact with whole Li_2Pc molecule. As a result, a cluster with 16 units of FeS_2, $(FeS_2)_{16}$, is chosen. Figure 10.5 shows the optimized configurations of $(FeS_2)_{16}$ cluster alone and complex of $(FeS_2)_{16}$ cluster interacted with Li_2Pc at the level of B3LYP, with 3-21G basis set for Li_2Pc and LanL2DZ for $(FeS_2)_{16}$ cluster. Table 10.3 shows the corresponding electronic energies of different systems and calculated binding energy of the complex of $(FeS_2)_{16}$ cluster and Li_2Pc. From the top view of the optimized structure of complex, pyrite cluster with Li_2Pc, it is clear that the bottom lithium ion is adsorbed to one of the surface sulfur ion. The distance between lithium ion and sulfur ion is 2.72 Å calculated by HF and 2.64 Å calculated by B3LYP. Due to the interaction of pyrite cluster with Li_2Pc, especially lithium ions, lithium ions are not distributed symmetrically above or below regarding to the PC ring. Instead, both lithium ions tend to move closer to pyrite cluster. Calculated by B3LYP, the distance between these two lithium ions is 2.12 Å and these two lithium ions are not at the center of PC ring. While, the bottom lithium ion is about 1.27 Å below the PC ring and the top lithium ion is about 0.80 Å above the PC ring. The bottom lithium ion has positive charge of 2.06 and the top lithium ion has negative charge of 0.681. The sulfur ion where the bottom lithium ion attached to has negative charge of 0.108 and the nitrogen ions of PC ring have negative charge in the range of –0.634~-0.696. The binding energy calculated with B3LYP is about –41.82 kcal/mol, as shown in Table 10.3. In the complex of full Li_2Pc with pyrite cluster, not other adsorption size is observed other than the bottom lithium ion to the one surface sulfur ion.

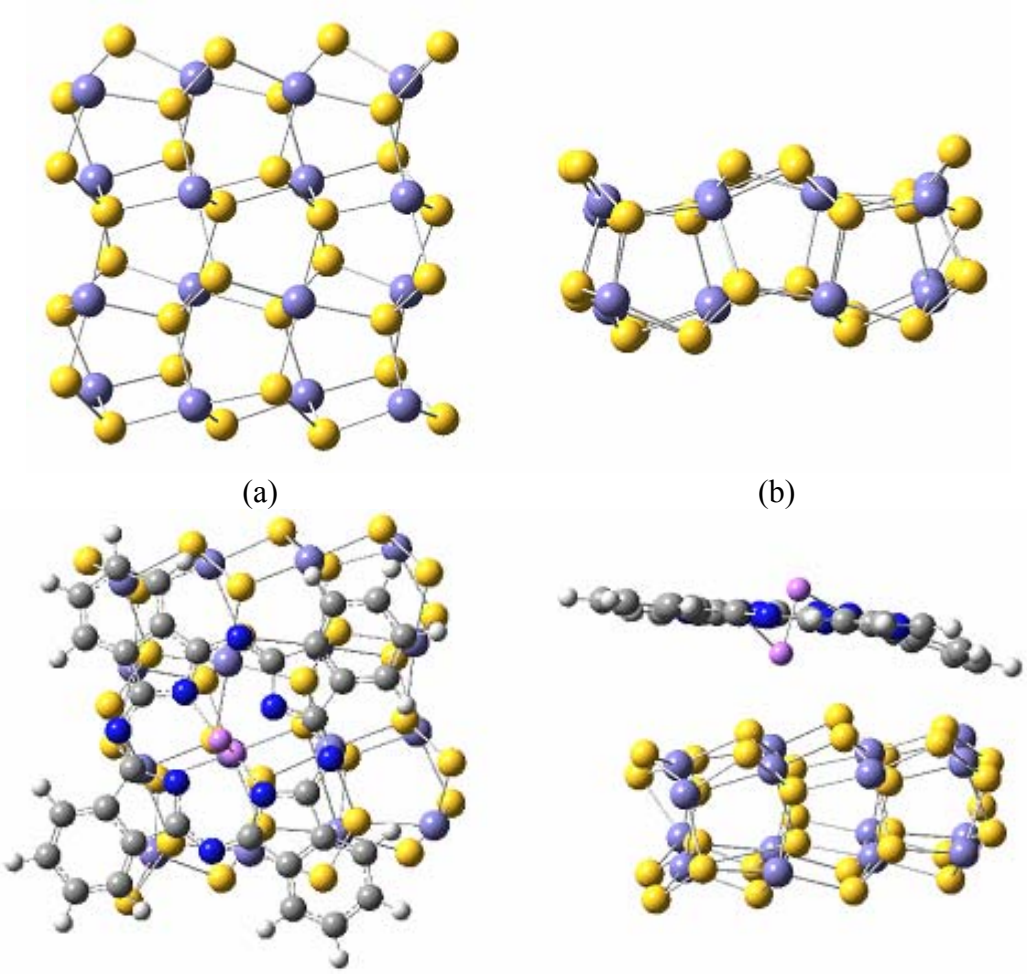

Figure 10.5. Optimized configurations of $(FeS_2)_{16}$ cluster and complex of cluster with Li_2Pc at the level of B3LYP, with 3-21G for Li_2Pc and LanL2DZ for $(FeS_2)_{16}$ cluster. (a) top view of $(FeS_2)_{16}$ cluster, (b) side view of $(FeS_2)_{16}$ cluster, (c) top view of $(FeS_2)_{16}$ cluster and Li_2Pc, (d) side view of $(FeS_2)_{16}$ cluster and Li_2Pc. Li colored as pink, N colored as blue, C colored as grey, H colored as white, Fe colored as purple, and S colored as yellow

Table 10.3: Electronic energy (Hatrees) and binding energy (kcal/mol) of interaction of $(FeS_2)_{16}$ cluster and Li_2Pc

System	Electronic Energy		Binding Energy	
	HF	B3LYP	HF	B3LYP
Li_2Pc	-1662.43689	-1673.06456		
$(FeS_2)_{16}$	-2277.90344	-2298.92944		
$(FeS_2)_{16}$- Li_2Pc	-3940.40421	-3972.06064	-40.09	-41.82

10.3 MD simulations of the self-assembly of Li_2Pc on a pyrite (100) surface

10.3.1 Initial stacking axis of Li_2Pc perpendicular to the pyrite (100) surface

10.3.1.1 Final configuraitons

The pyrite (100) surface is very stable because it retains intact the S_2 dimer and the S-Fe-S triple layer configuration, maintaining the same environment as in bulk pyrite. For this reason, to investigate the self-assembled deposition of Li_2Pc over a pyrite surface using MD simulations, the pyrite slab is kept fixed, whereas in the space above the pyrite slab, there is enough vacuum space to allow Li_2Pc molecules to move freely during the simulations, so the self-assembly of Li_2Pc molecules on the pyrite surface can be observed. Figure 10.6 shows an instantaneous side view of equilibrated systems containing one to sixteen Li_2Pc molecules. The mean separation distance between the phthalocyanine ring and the pyrite (100) surface increases from an initial value of 2.5 Å to 3.5 Å after system equilibration. By carefully measuring the closest distance between Li and S atoms, we find an average value of about 2.6 Å. The value agrees very well with the results obtained from the ab initio calculations of the pyrite cluster interacting with $Li_2C_8N_8H_8$. The separation of the Li_2Pc molecules from the surface may be due to a balance among the main electrostatic interactions between pyrite and Li_2Pc, the

attractions between Fe and N, Li and S, Li and N atoms, as well as the repulsions between Fe-Li, S-N, and Li-Li pairs. For systems containing more than one Li_2Pc molecule, shifted dimers were formed, as shown in Figure 10.6 (b), and at higher densities, a four-layer Li_2Pc film as depicted by Figure 10.6 (e), with a structure similar to the bulk χ-form Li_2Pc crystalline structure,[398] as confirmed by the analysis of radial distribution functions, g_{LiX}(X:Li, C, N, H) (not shown).

Top views of some of the systems in Figure 10.6 are shown in Figure 10.7. For better visualization, only the top layer of pyrite surface is shown and lithium atoms are highlighted (in Figure 10.7 (a), only the bottom four of total eight Li2Pc are shown and four closest Li ions to the pyrite surface are highlighted). The lithium atoms which are the closest to the pyrite (100) surface adsorb on sites close to the outmost S surface atoms. It is understandable that they are not exactly adsorbed on the top of S atoms, considering the size of the Li_2Pc molecule and thus the overall repulsion and attraction interactions between different atom pairs. This result is in agreement with that from the ab initio calculation in section 10.2.1, where one lithium ion from $Li_2C_8N_8H_8$ adsorbs on the bridge site connecting two outmost surface S atoms. Figure 10.7 (b) shows potential conducting channels visualized by using four neighbor simulation cells. The existence of the ion conducting channels in the interface is important when the solid electrolyte and the cathode are brought in contact. The continuity of such ion conducting channels through the interface would enhance lithium ion transport under the effect of applied fields that would act as driving forces for ion migration.

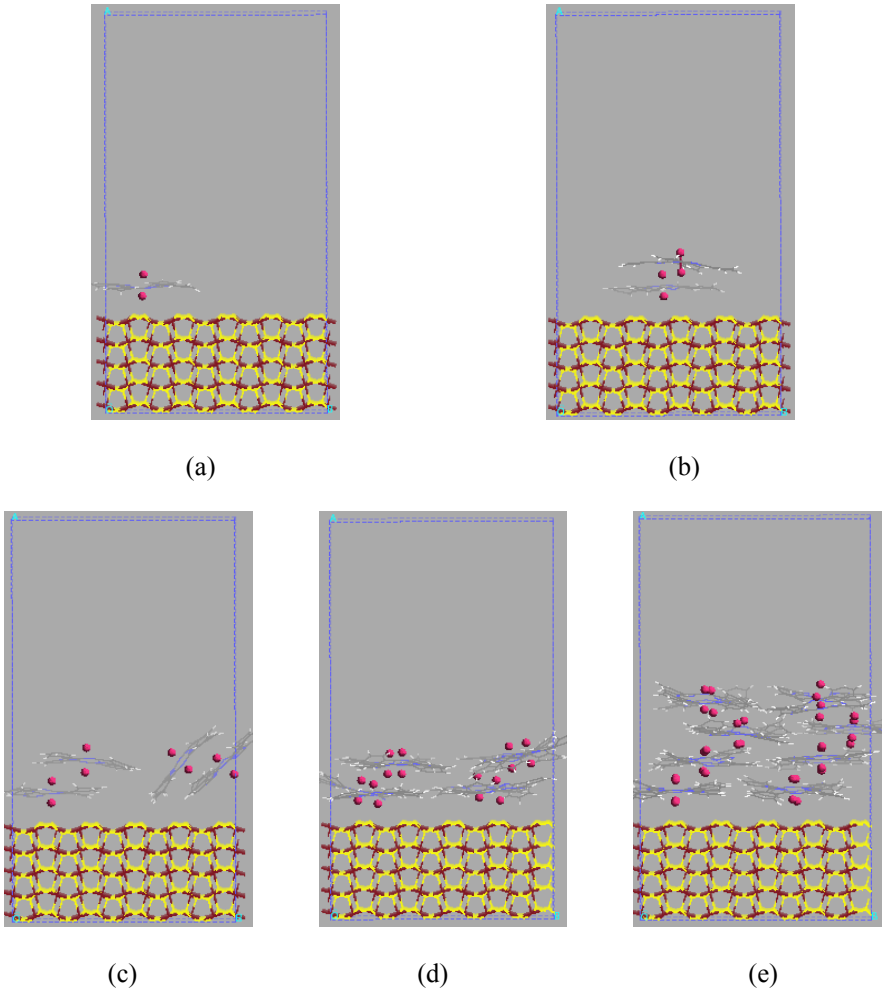

Figure 10.6. Snapshots from MD simulations after 500 ps of production time for systems with stacking axis of Li_2Pc initially perpendicular to the pyrite (100) surface for systems containing increasing number (n) of Li_2Pc molecules. (a) n = 1, (b) n = 2, (c) n = 4, (d) n = 8, (e) n = 16

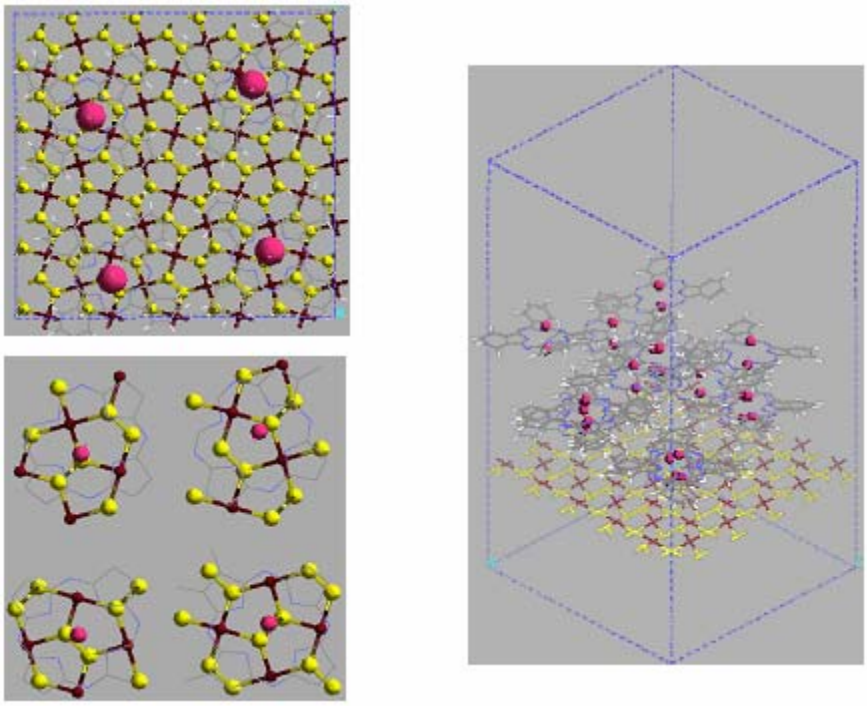

(a) (b)

Figure 10.7. (a) Top view of a configuration containing eight Li_2Pc molecules arranged in two layers; (b) View of potential lithium ion conducting channels of a system with sixteen Li_2Pc molecules. For better visualization, only top layer of pyrite slab is shown, and in (a), four bottom Li_2Pc of total eight molecules are shown and only four bottom Li ions which are close to the pyrite surface are highlighted

10.3.1.2 Radial distribution functions

Figures 10.8 (a) and (b) show the radial distribution functions (*RDF*) of Li-S and Fe-N at various Li_2Pc densities. *RDF*s are indicators of local structure defined as the ratio of the local density (at position r) of a second atom surrounding at a central atom. The first peak of the Li-S *RDF* (Figure 10.8 (a)) corresponds to the interaction between the closest Li-S pairs in the interface region revealing an average shortest distance of 2.65 Å. The decrease of the first peak magnitude is due to the relatively smaller atomic fraction of Li atoms on the surface as the Li_2Pc density increases. The position of the

first peak shifts to a lower value as the density of Li_2Pc increases, indicating enhanced S-Li interactions. The negatively charged N atoms of Li_2Pc interact with the positively charged Fe atoms of the substrate (Figure 10.8 (b)); however, the shortest distance Fe-N is larger than 4 Å, showing that the molecule attaches to the surface via the Li-S interaction.

This result differs from that obtained from the ab initio calculation, where strong adsorption was found via Li-S and Fe-N pairs as well. This may be explained by the fact that the small cluster exposes Fe defect sizes especially in the corners, where 3-coordinated Fe can openly interact with N atoms. In a surface containing 5-coordinated Fe sites the Fe-N interaction strength decreases because the accessibility to the Fe sites becomes more difficult. Another reason that might lead to more difficult Fe-N contacts is the enhanced S-N repulsions.

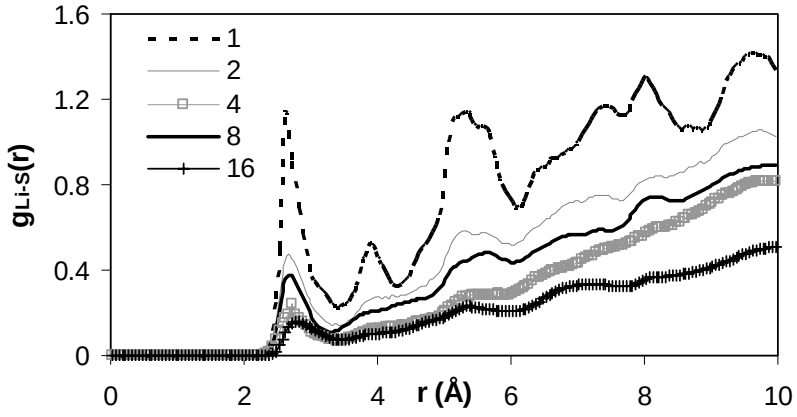

(a)

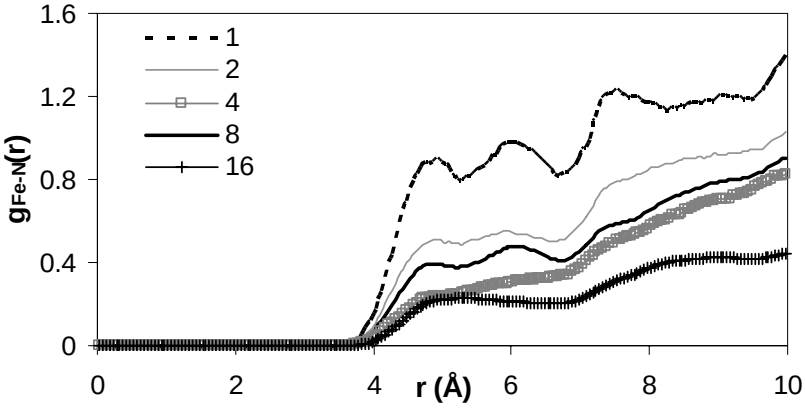

(b)

Figure 10.8. Radial distribution functions of systems with initial Li_2Pc stacking axis perpendicular to the pyrite (100) surface. (a) Li-S, (b) Fe-N

10.3.1.3 Formation of shifted Li_2Pc dimers

In order to prove that the formation of shifted Li_2Pc dimers above the pyrite surface is not caused by the small size of the pyrite (100) surface in the simulation, another system containing a 5-layer pyrite slab with $(FeS_2)_{640}$ and four Li_2Pc molecules

was tested, where the surface has the dimensions of 43.42 ×43.42 Å. Initially, four Li_2Pc molecules were located on the same plane parallel to the pyrite (100) surface, with the same separation distance of 2.5 Å between the phthalocyanine ring and the surface as in the previous simulations. In this system, the surface is only partially covered by four Li_2Pc molecules. The final configuration (not shown) indicated that one of the Li_2Pc molecules moved away from the surface and formed a second layer, while the other three Li_2Pc molecules remained in the first layer in contact with the pyrite surface. The Li-Li intermolecular distance from two Li_2Pc molecules in two different layers is 5.28 Å, which agrees with the intermolecular Li-Li distance of the shifted Li_2Pc dimer according to the B3LYP/6-31g(d) optimized structure.[398] The other two Li-Li pairs are separated by distances higher than 10 Å. Thus, the formation of a stable shifted dimer is favorable, in agreement with our previous DFT calculations.[398,450]

10.3.2 Initial stacking axis of Li_2Pc parallel to the pyrite (100) surface

10.3.2.1 Final configuraions

H. Xiang and coworkers[502] found that most di-lithium octacyanophthalocyanine [$Li_2Pc(CN)_8$] molecules in a Langmuir-Blodgett film were stacked in a face-to-face aggregated state with the stacking axis parallel to an indium tin oxide (ITO) surface. Similarly, we investigated cases where the stacking axis of the Li_2Pc molecules is parallel to the pyrite (100) surface. In systems at low or intermediate Li_2Pc density, the surface is only partially covered, so Li_2Pc molecules are free to rotate and migrate. At the highest density, Li_2Pc molecules might not able to rotate, but they are free to move to an energetic favorable configuration. Figure 10.9 (a) through (d) show the final

configurations of the systems with one, two, eight, and sixteen Li_2Pc molecules respectively. For the systems at low Li_2Pc density (Figures 10.9 (a) and (b)), the final configurations show that the whole ring of Li_2Pc rotates and the stacking axis changed from parallel to perpendicular position with respect to the pyrite surface. This is due to the strong interaction between Li and S atoms, as well as the available free space for Li_2Pc molecules to rotate, suggesting that a self-assembly of Li_2Pc with a stacking axis perpendicular to the pyrite (100) surface is more stable. Also, we clearly observed the formation of a shifted Li_2Pc dimer for the system with two Li_2Pc molecules per cell (Figure 10.9 (b)). However, for the higher density systems containing 8 and 16 Li_2Pc molecules per cell, the change of the stacking axis from a parallel to a perpendicular position is not observed. Li_2Pc molecules in a system containing eight Li_2Pc molecules showed a slight rotation and the Pc rings were no longer completely perpendicular to the pyrite surface, but have an edge-on configuration on the pyrite surface (Figure 10.9 (c)). The configuration of Li_2Pc in this system is similar to the previously proposed β-form crystalline structure.[398] For the highest density system (Figure 10.9 (d)), the Pc rings of the final configuration remain relatively perpendicular to the pyrite surface. Although the strong interaction between Li and S atoms would favor the rotation of Li_2Pc, the unavailability of free space is the main reason why Li_2Pc cannot rotate due to its large volume. In the final configuration, the crystalline structure of Li_2Pc in this system is the χ-form.[398]

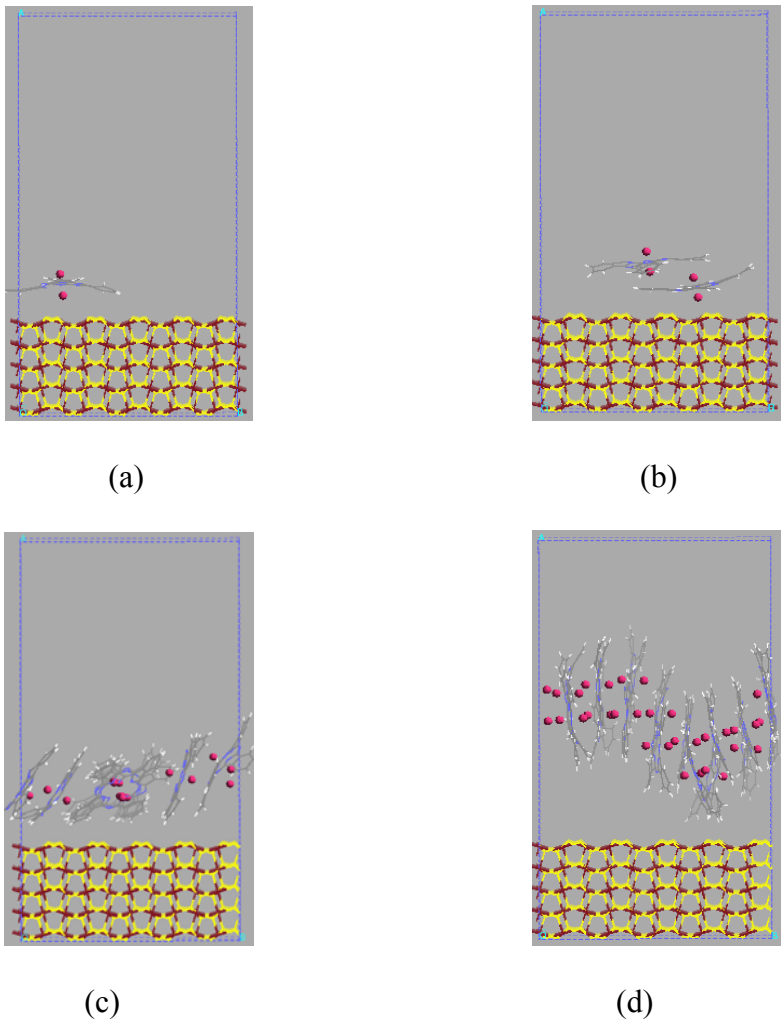

Figure 10.9. Snapshots after MD simulations with initial stacking axis of Li_2Pc parallel to the pyrite (100) surface using various numbers (n) of Li_2Pc molecules in the simulation cell. (a) n = 1, (b) n = 2, (c) n = 8, (d) n = 16

10.3.2.2 Radial distribution functions

Figures 10.10 (a) and (b) show the radial distribution functions of Li-S and Fe-N at various densities of Li_2Pc. The average position of the Li ions with respect to the S atoms on the surface remains equal to 2.65 Å for the low-density systems (Figure 10.10 (a)). At higher densities of Li_2Pc, a clear change is observed in the interfacial

configuration of the Li_2Pc assembly, as evidenced by the N atoms interacting with Fe atoms with shortest distances found at about 4.5 Å (Figure 10.10 (b)). In the highest density cases (Figures 10.10 (c) and (d)), the interfacial contact between solid electrolyte and electrode is very limited. Lithium ion conducting channels are not found to continue from the Li_2Pc phase to the pyrite phase. Thus, this configuration would hinder the diffusion of lithium ions from the electrolyte phase into the cathode.

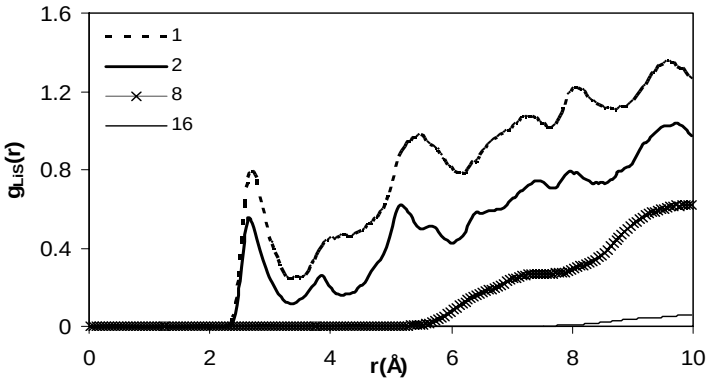

(a)

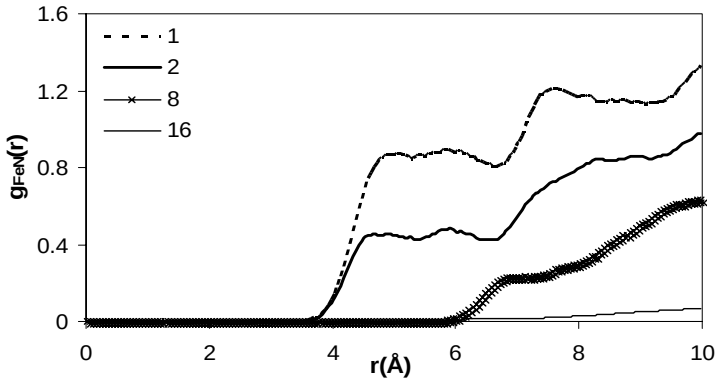

(b)

Figure 10.10. Radial distribution functions from MD simulations where in the initial configuration the Li_2Pc stacking axis was parallel to the pyrite (100) surface. (a) Li-S, (b) Fe-N

To determine which configuration dominates the Li_2Pc self-assembly on a pyrite surface, the total energy of the high Li_2Pc density systems with stacking axis arranged parallel to the surface is compared to that of perpendicular orientation. The MD calculated total energies are $-1.46x10^4$ kcal/mol for the system with stacking axis perpendicular to the pyrite surface and $-1.45x10^4$ kcal/mol for that with stacking axis parallel to the pyrite surface. Thus, the higher interaction between Li-S pairs in the former case makes it energetically favorable.

10.4 Li_2Pc/pyrite interfacial phenomena with/without electric field

10.4.1 Interfacial phenomena at 300 K

10.4.1.1 Final configurations and formation of ion conducting channles

When a self-assembled Li_2Pc film is used as a solid electrolyte of lithium ion batteries, lithium ion transport may depend on the electric field gradient established between electrodes.[398,456] In this section, an external electric field is applied to the system. Typical electric field values in an electrochemical environment range from 10^9 V/m to 10^{11}V/m.[503-506] In an electrochemical cell, when a potential of 1V is applied, the electric field in the double layer takes an approximate value of $5x10^9$ V/m.[507] We applied a field of 2.07×10^{10} V/m in a direction perpendicular to the surface, along the stacking axis of Li_2Pc, which is also the direction of the ion conducting channels in self-assembled Li_2Pc (Figures 10.6 and 10.7). This value is based on the practical lithium batteries with voltage of about 4 V between two electrodes. Snapshots obtained after 800 ps total simulation length of the χ-form Li_2Pc/pyrite interface without and with the

existence of external electric field are shown in Figure 10.11. For clarity, the top vacuum portion of the simulation cell is not shown in the figure and lithium ions are highlighted. Without the existence of an external electric field, intercalation of lithium ions through the interface to the pyrite slab is not detected (Figure 10.11 (a)). In contrast, with the additional driving force imposed by the electric field, eleven lithium ions (34.4% of the number of ions in the unfixed layers) diffused through the interface into the relaxed first layer of the pyrite slab. We did not observe any lithium ion diffusing into the unrelaxed portion of the pyrite slab. We found that the lithium ions diffusing in the Li_2Pc phase (Figure 10.11 (b)) are located only around the center axis of each phthalocyanine molecule. Figure 10.12 shows snapshots of the configuration in the Li_2Pc phase corresponding to Figure 10.11 (b); only the center unsaturated macro-rings of half of the phthalocyanine molecules are shown. The unsaturated macro-rings partially overlap, offering continuous channels for lithium ion transport. The lithium ion channels are not linear, but spiral along the Z-axis. The possible pathways for lithium ions are shown as dot lines. More detail about this lithium ion channels will be studied separately.

Figure 10.11 (b) illustrates that under the applied field, no lithium ions remained in the interfacial region. After 1200 ps (Figure 10.11 (c)) no further migration of lithium ions was observed. We speculate that saturation of the first slab layer might have been achieved under these conditions, impeding migration of additional ions through the interface, and at the same time the presence of these ions in the first slab layer would

generate repulsion forces that repel the presence of ions in the interfacial region. The particular pattern is due to the artificial restrictions imposed in the system.

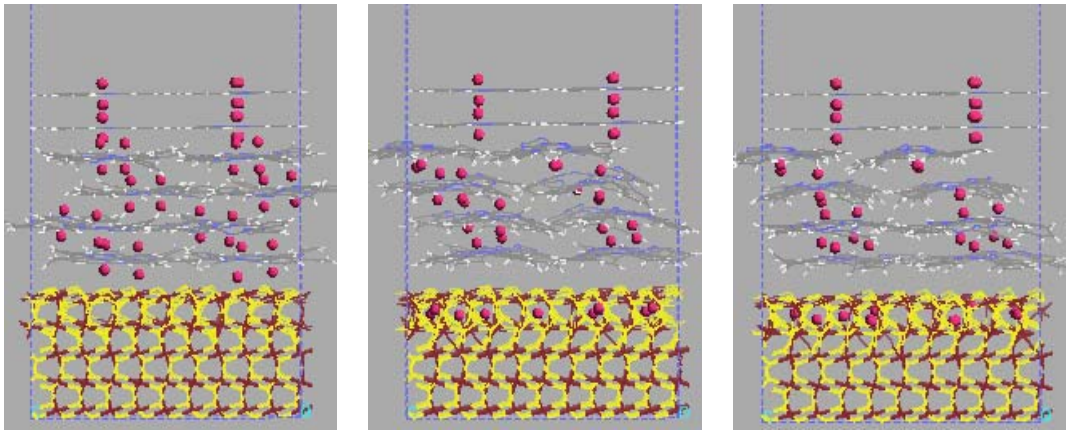

(a) (b) (c)

Figure 10.11. Snapshots of the simulated pyrite/Li_2Pc interface. The two top layers of the electrolyte phase and the two bottom layers of the slab are fixed. (a) Without electric field applied, after 800 ps, (b) Under an applied electric field of $2.07x10^{10}$V/m, after 800 ps, (c) With electric field of $2.07x10^{10}$V/m, after 1200 ps

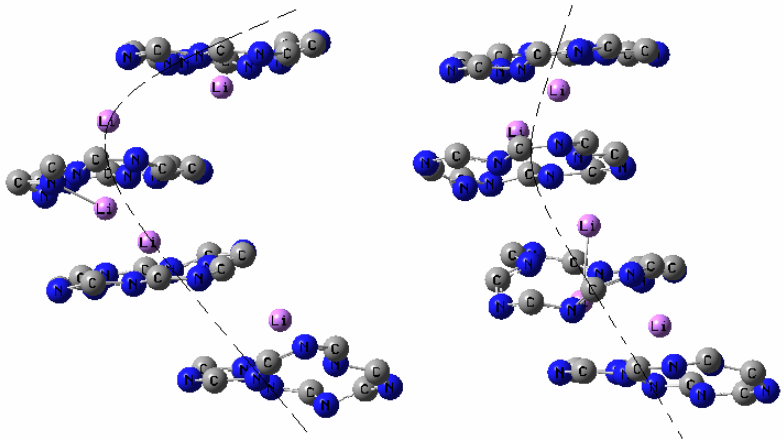

Figure 10.12. Li ion conducting channels in the Li_2Pc phase. For clarity, peri-benzene rings of Li_2Pc are not shown. Two dot lines show the possible transport paths of Li ions

10.4.1.2 Radial distribution functions

Radial distribution functions between pairs involving Li, N, Fe, and S are shown in Figure 10.13. Comparing the *RDF*s of Li-Li and Li-N with those in the χ-form of bulk crystalline Li_2Pc,[398] it is found that the peak positions are located almost at the same distance in these cases, though the peaks intensities are reduced due to the migration of lithium ions into pyrite slab. These two *RDF*s confirmed that lithium ions in electrolyte phase maintain their relative same positions with respect to the phthalocyanine molecules, even with the existence of an electric field. This proves our speculation that the lithium ion transport takes place through the ion conducting channels only, as we stated above. The phthalocyanine anions are not affected by the existence of the electric field, as illustrated by the $g_{NX}(r)$ (X:Fe, S), which do not show any obvious difference with respect to those without the applied electric field, whereas significant changes are observed for the *RDF*s of Li-Fe and Li-S, due to intercalation of lithium ions into pyrite slab. The intercalation of lithium ions enhanced the interactions between Li and S, and in lesser degree that of Li and Fe. The first peak position of Li-S changed from 2.25 Å to 1.60 Å. The shorter distance between Li and Fe was partially due to the strong increased interaction of Li-S, which brought lithium ions into the slab. The broad peak of $g_{LiFe}(r)$ between 2 to 4 Å split into several peaks, and peak positions also shifted to a lower value.

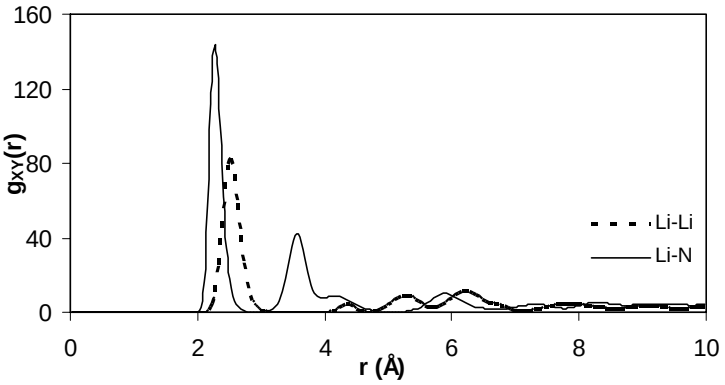

(a)

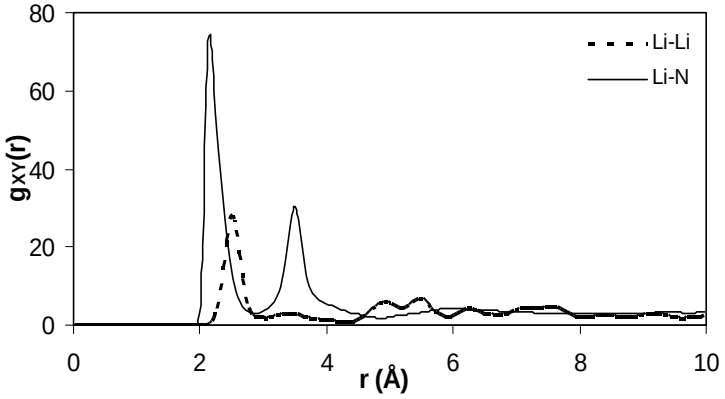

(b)

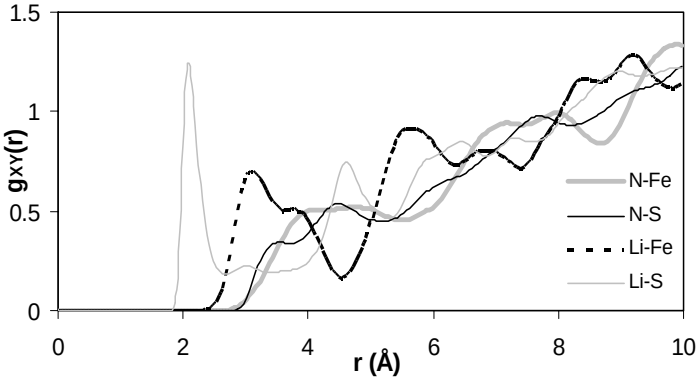

(c)

Figure 10.13. Radial distribution functions. (a) RDFs of Li-X (X: Li, N) without EF; (b) RDFs of Li-X (X: Li, N) with EF = 2.07×10^{10}V/m; (c) RDFs of X-Y (X: Li, N; Y: Fe, S) without EF; (b) RDF of Li-X (X: Li, N) RDFs of X-Y (X: Li, N; Y: Fe, S) with EF = 2.07×10^{10}V/m

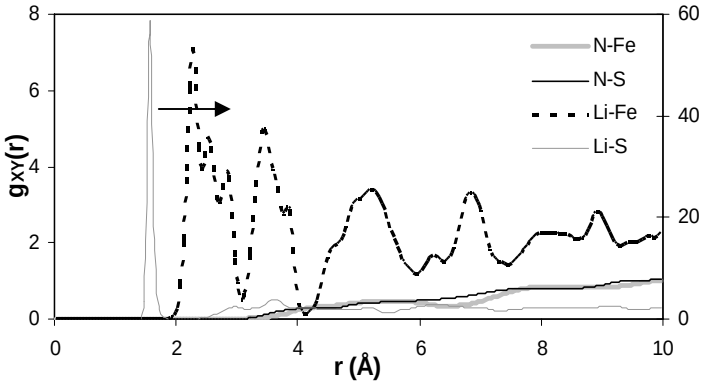

(d)

Figure 10.13 Continued.

The *RDF*s (not shown) calculated for longer simulations (1200 ps) under the external electric field (Figure 10.11 (c)) showed almost the same behavior as those of Figure 10.11 (b).

10.4.1.3 Coordinations of lithium ion inside pyrite slab

Careful examination of the pyrite slab after intercalation of lithium ions shows that in the first two layers of the slab, Fe and S atoms vibrate around their equilibrium states. Figure 10.14 shows three of the twelve unfrozen lithium ions, surrounded by Fe and S atoms.

The distance between Li and S is about 1.55-1.65 Å, which corresponds the first peak of the *RDF* of Li-S in Figure 10.13 (b); and about 2.30 Å for Li and Fe1, ~ 2.50 Å for Li and Fe2, which corresponds to the first two peaks of the *RDF* of Li-Fe in Figure 10.13 (b). These data reveal a predominant S-Li interaction.

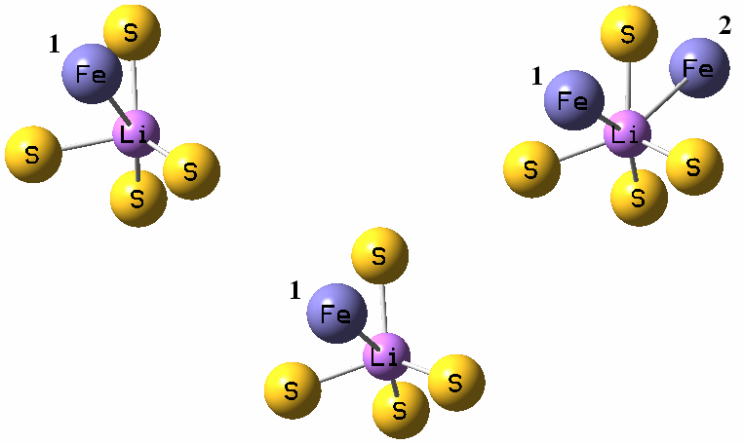

Figure 10.14. Coordination of Li^+ after intercalation into the pyrite slab

10.4.2 Interfacial phenomena at different temperatures and electric fields

10.4.2.1 Electric field effects

In previous section, we have discussed the interfacial phenomena of lithium ion transport with/without external electric field at 300 K. With the presence of external electric field, Li ions intercalate into the relaxed layer of pyrite slab, but not into the fixed layer. From the activation energy point, this can be explained that during the diffusion of lithium ions from Li_2Pc phase to relaxed pyrite layer the activation energy is relatively low, while for the process from relaxed pyrite layer to fixed pyrite layer, the activation energy is high. To verify this, we further unfix the middle two layers of pyrite slab, which brings a total of four of five layers unfixed. At the mean time, additional two layers of Li_2Pc are added to Li_2Pc phase to see the continuous formation of lithium ion conducting channels. Overall, the system contains eight layer Li_2Pc (4 Li_2Pc

molecule each layer) and five layer pyrite slab, while top two layers of Li_2Pc and bottom layer of pyrite are fixed. The initial configuration (not shown) is similar to as shown in Figure 8.8. As we mentioned before, that external electric field is the driving force of the lithium ion transport. In this study, MD simulations are performed in three different cases: without EF, with EF of $2.07x10^9$V /m and $2.07x10^{10}$ V/m. In each case, the system is studied at temperatures of 273 K, 300 K, and 323 K. Each simulation runs for 800 ps based on previous experience.

Figure 10.15 shows the snapshots of the final configurations of these systems at 300 K with different driving forces. Without the applied electric field to the system, no intercalation of lithium ions into pyrite slab is observed, as shown in Figure 10.15 (a). This is same as what we discussed in previous section. On the other hand, the spiral shape of conducting channels can be visualized. With electric field of $2.07x10^9$ V/m, we start to see a few lithium ions that intercalate into pyrite slab, but only to the first layer. No lithium ion in deeper layer is observed. As the electric field increases to $2.07x10^{10}$ V/m, more lithium ions intercalate into pyrite slab and lithium ions transport to different layers of relaxed slabs. At temperatures of 273 K and 323 K, the results are similar to the case of 300 K with the same driving force. Thus, figures of snapshots for these cases are not shown. With these results, it can be concluded that, (1) electric field is indeed the driving force of lithium ion intercalation; (2) the activation energy of lithium ion diffusion through the interphase (from Li_2Pc phase to first layer of pyrite slab) is smaller than that of through pyrite phase (from first layer into deeper layer), since at lower value of driving force no lithium ion is observed in deeper layer, while at stronger driving

force, intercalation into deeper layers happens; (3) temperature is not the important factor on the diffusion of lithium ions.

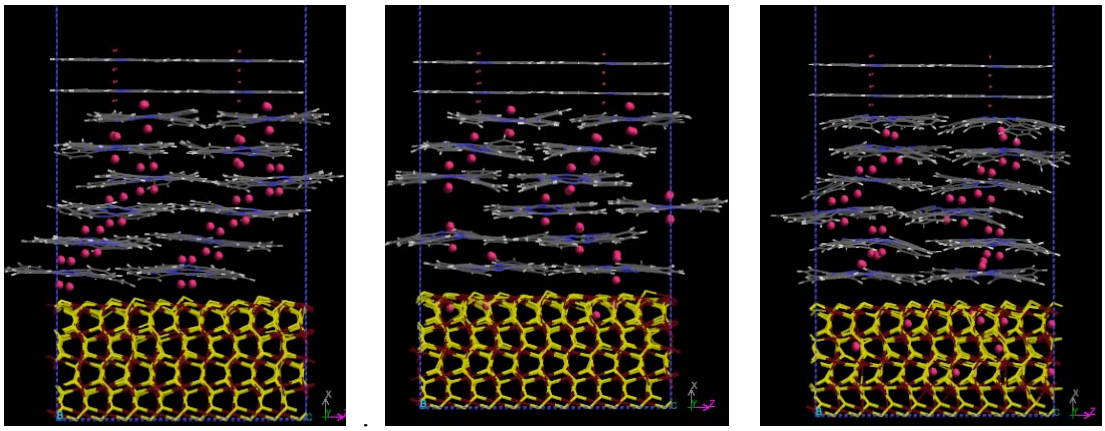

(a) (b) (c)

Figure 10.15. Snapshots of the simulated pyrite/Li_2Pc interface. The two top layers of the electrolyte phase and the bottom layer of the slab are fixed. (a) Without electric field applied, 300 K, (b) Under an applied electric field of $2.07x10^9$ V/m, 300 K, (c) Under an applied electric field of $2.07x10^{10}$ V/m, 300 K

10.4.2.2 Temperature effects

The interactions of Li-S and Li-Fe are important for the intercalation of lithium ions into pyrite slab and diffusions of lithium ions through pyrite slab. Radial distribution functions between Li-S and Li-Fe can give some indications of these interactions. Figure 10.16 through Figure 10.18 show the radial distribution functions of Li-S and Li-Fe at different temperatures for the case of without EF, EF of $2.07x10^9$ V/m, and EF of $2.07x10^{10}$ V/m, respectively. Without the existence of EF, as shown in Figure 10.15 (a), no lithium ions are found inside the pyrite slab and thus the first peak of Li-S

and Li-Fe are corresponding to lithium ions (which locate in the region between first layer of pyrite slab and bottom layer of Li_2Pc phase) to S and Fe ions at (100) surface, respectively. Without the driving force, i.e. EF, temperature is the only factor of affecting interfacial interaction. As temperature increases from 273 K to 300 K, the first two peaks of Li-Fe appear at slightly short distance and the peak intensities increase a little bit. At the temperature of 323 K, these two peaks merge into a single peak with higher intensity. For RDF of Li-S, the first peak does not change much. However, the shoulder at the right side of the first peak appears to a shorter distance as the temperature increases and the intensity of the shoulder increases also. RDFs indicate that the interactions between lithium ions and pyrite (100) are enhanced as the temperature increases.

As EF is applied to the system, lithium ions start to transport into pyrite slab, shown as in Figure 10.15 (b) and (c). The interactions between lithium ions and Fe and S ions are significantly increased due to the relocation of lithium ions inside the pyrite slab. The corresponding first two peaks of Li-Fe and first peak of Li-S all appear at clear shorter distance that those of without existence of EF. At the mean time, these peaks become narrower, especially at higher value of EF, 2.07×10^{10} V/m. These functions can be clearly seen from Figure 10.17 and 10.18. The difference of radial distribution functions of Li-Fe and Li-S indicates the structural change of pyrite slab once the intercalation of lithium ions. The change of the structure of pyrite slab can be obtained from the radial distribution function of S-Fe.

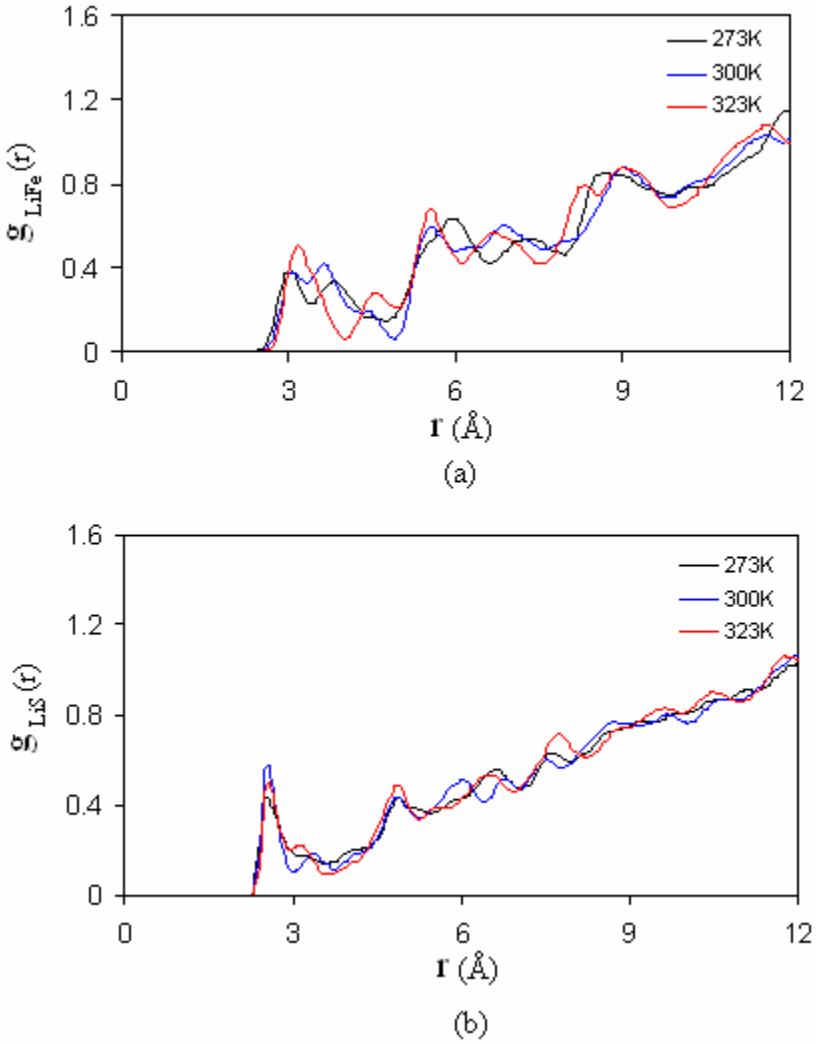

Figure 10.16. Radial distribution functions at different temperatures without EF. (a) $g_{LiFe}(r)$, (b) $g_{LiS}(r)$

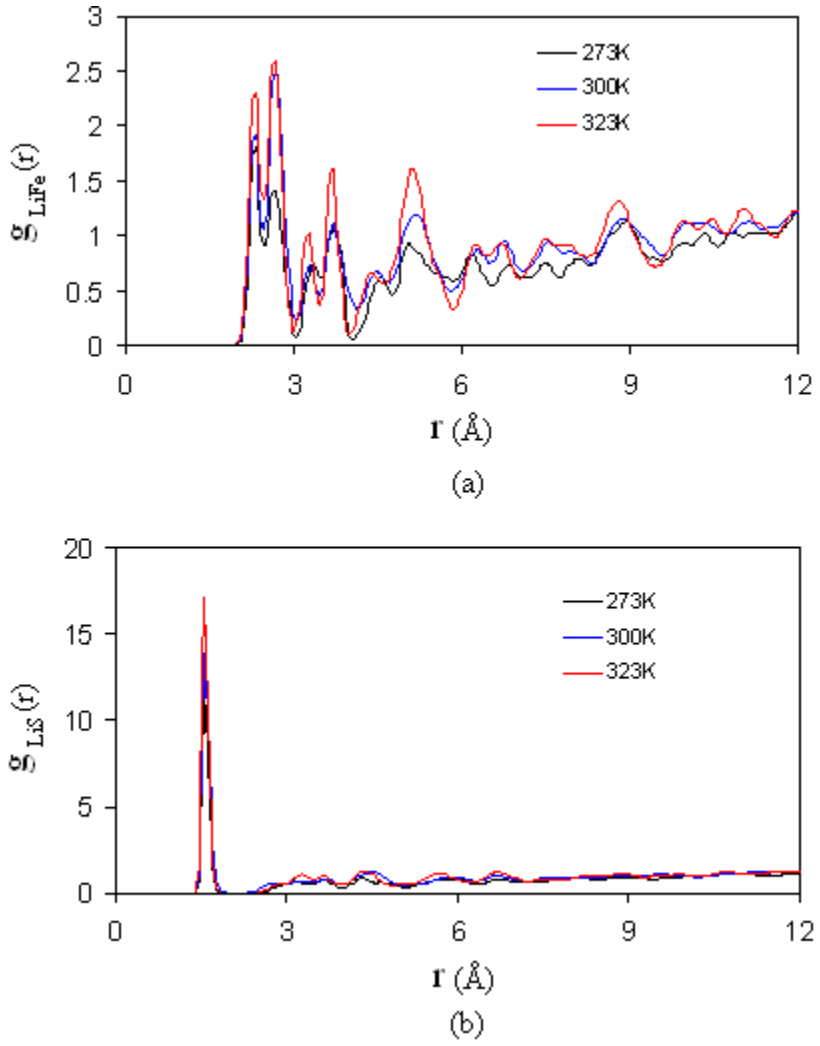

Figure 10.17. Radial distribution functions at different temperatures with EF of 2.07×10^9 V/m. (a) $g_{LiFe}(r)$, (b) $g_{LiS}(r)$

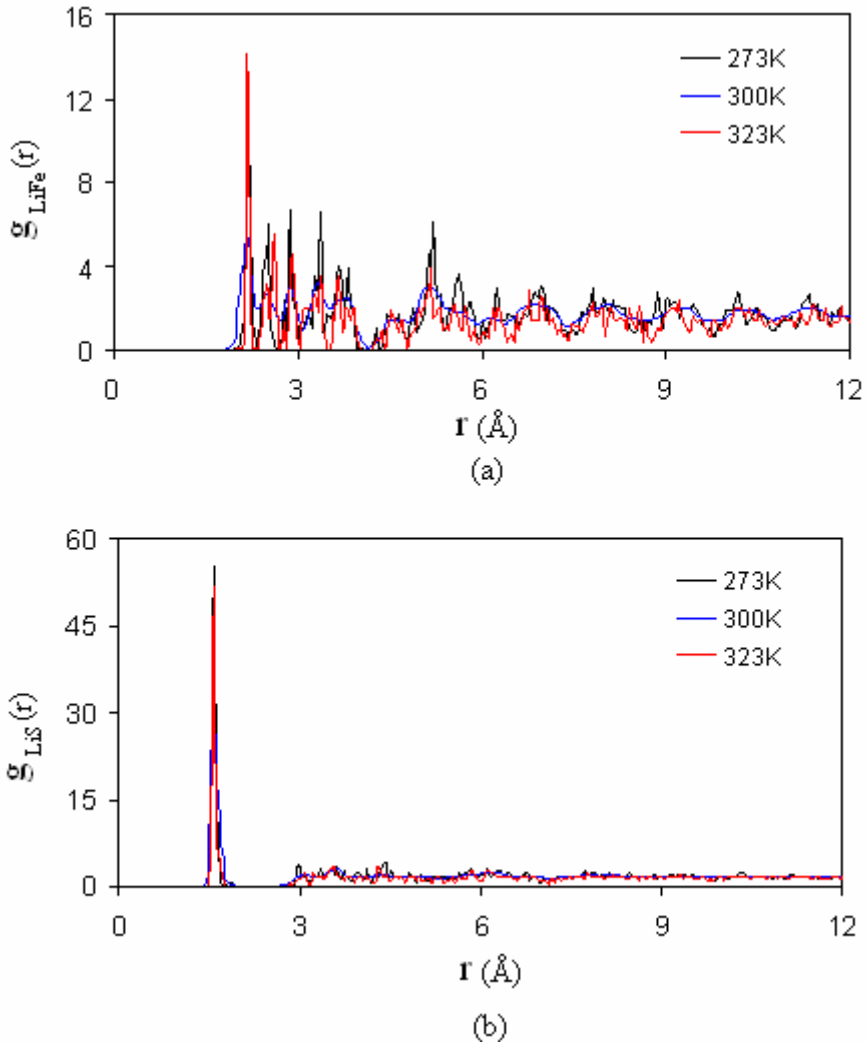

Figure 10.18. Radial distribution functions at different temperatures with EF of $2.07x10^{10}$ V/m. (a) $g_{LiFe}(r)$, (b) $g_{LiS}(r)$

In each case of without the existence of EF, or EF of $2.07x10^{9}$ V/m and $2.07x10^{10}$ V/m, the radial distribution functions of S-Fe are the same at the different temperatures from 273 K to 323 K. Figure 10.19 shows the radial distribution function of S-Fe at 300 K for without EF and different values of EF. Recall the fact that only a few lithium ions transfer into first layer of pyrite slab at the value EF of $2.07x10^{9}$ V/m, the RDFs of S-Fe

do not show much difference to that of without existence of EF. Pyrite slab still keeps the bulk crystalline structure, with Fe and S vibrating around their equilibrium positions. When EF increases to $2.07x10^{10}$ V/m, the RDF of S-Fe changes, especially at short distance lower than 5 Å. The change of structure of pyrite phase at higher value of EF is related to the intercalation of lithium ions deep into pyrite slab. Intercalation of lithium ions enhances the interaction of lithium ions with Fe and S ions, and also the interaction of Fe and S ions. The structural change at high value of EF might decrease the activation energy of diffusion of lithium ions through pyrite slab.

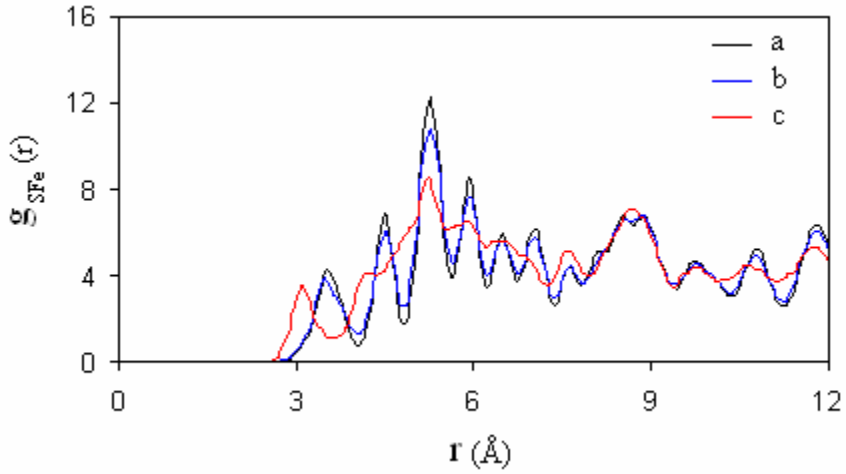

Figure 10.19. Radial distribution function of S-Fe at 300 K. (a) without EF, (b) with EF of $2.07x10^{9}$ V/m, (c) with EF of $2.07x10^{10}$ V/m

10.5 Conclusions

Ab initio calculations of a simplified Li_2Pc model and full Li_2Pc interacting with a pyrite cluster and MD simulations of the interface between pyrite/Li_2Pc indicate that the interaction is dominated by the attraction between lithium and sulfur atoms. MD

simulations suggest the possibility of existence of at least two different orientations for the self-assembly of Li2Pc over the pyrite (100) surface. At low Li_2Pc densities, shifted dimers are favorable and more stable. As the density increases, both β- and χ-form structures are found in different orientations. At the highest Li_2Pc density, only the χ-form structure is found. Energetically, self-assembled structures with the stacking axis perpendicular to the surface are more favorable than those where the stacking axis is parallel to the surface, because they maximize the Li–S interactions, although the energy difference is not very significant. The orientation with stacking axis perpendicular to the pyrite surface promotes a good interfacial contact and ionconducting channels are open to the interface.

When an electric field is applied in the direction perpendicular to the surface, transport of lithium ions diffusing through the ion channels is facilitated through the interface into the pyrite slab. As the driving force, the magnitude of the electric field directly affects the number of the lithium ions and the path of the lithium ion transport intercalated into pyrite slab.

CHAPTER XI

CONCLUSIONS AND RECOMMENDATIONS FOR FUTURE WORK

11.1 Conclusions

11.1.1 Hydrogen adsorption

The major conclusions of the hydrogen adsorption on corannulene-based materials are listed as followings.

- It is shown that corannulene has potential advantages as hydrogen storage material over planar graphite and even carbon nanotubes. Such advantages are derived from the specific geometric and electronic characteristics of corannulene which enhances the interaction with hydrogen molecules. These enhanced interactions are due to the permanent dipole moment of corannulene which can induce dipole-dipole interactions with hydrogen and also to the electronic density distribution between corannulene molecules that duplicate the binding energy per hydrogen molecule and may favor adsorbate-adsorbate cooperative interactions.
- Lithium atoms are more favorable to dope over the six-member ring on the concave side of corannulene. A stable ratio of lithium atom to carbon atoms is between 1:3 and 1:4. The doping of lithium atoms enhances the hydrogen adsorption due to three factors. Lithium atoms doped corannulene complexes

have higher dipole moment and thus enhance the induced dipole-dipole interaction with hydrogen molecules. Also, the interaction between lithium atom and hydrogen is stronger than the interaction between carbon atom and hydrogen. Besides, the doping of lithium atoms provides more space in the doping complexes for hydrogen adsorption.

- Pore volume of the adsorbents is important for hydrogen adsorption. Modification of corannulene, which tends to increase the pore volume of the modified corannulene, can enhance hydrogen adsorption. With two organic linker of $(-C\equiv C-CH=CH-C\equiv C-)$ connecting two symmetry carbon pairs of corannulene, 1,5-biscorannulenecyclophane has large pore volume for hydrogen adsorption. 1,5-biscorannulenecyclophane as hydrogen storage material significantly increases the hydrogen adsorption capacity compared to corannulene at the same conditions of temperature and pressures. According to the prediction, DOE target of 6.5 wt% can be reached at 294 bar at 273 K, and 309 bar at 300 K.

11.1.2 Lithium ion conducting channels

The major conclusions of studies on lithium ion conducting channels are listed as followings.

- Polymorphs of crystalline Li_2Pc are predicted. Li_2Pc molecules may be distributed in two shifted and two staggered crystalline configurations with very similar total energies. Lithium ion conducting channels are realized in all these crystalline forms. Comparison of simulated X-ray spectra with experimental X-

ray data suggests the mixtures of β– (staggered) and χ–(shifted) crystalline forms in the experimental samples.

- Self-diffusion coefficients of lithium ions in these four crystallines are one order of magnitude less than experimental data at 300 K. This is probably due to the lack of driving force for lithium ion transport in simulations.
- Li_2Pc as solid electrolyte has relatively good surface contact with the pyrite (100) surface. The interaction between lithium ion and sulfur ion is the main cause of the good surface contact. Lithium ions intercalate into pyrite slab with the existence of the electric field as the driving force. As the driving force, the magnitude of the electric field directly affects the number of the lithium ions and the path of the lithium ion transport intercalated into pyrite slab.

11.2 Recommendations for future work

11.2.1 Molecular transport in solid

The main recommendations on molecular transport in solid for future work include as the followings.

- Modification of corannulene increases the pore volume for hydrogen adsorption. Experimental measurement of hydrogen adsorption on corannulene at 72 bar and 298 K was in good agreement with MD simulation result on corannulene at its equilibrium ILD (4.8 Å). Experimental measurements of hydrogen adsorption on 1,5-biscorannulenecyclophane can be studied as suggested by the reported predictions. For further improvement of hydrogen adsorption, doping of lithium

atoms on 1,5-biscorannulenecyclophane could be investigated with MD simulations to verify if there is an enhancement of the interaction between hydrogen and the adsorbent in the presence of lithium.

- This work proposes hydrogen adsorption on corannulene and modification of corannulene, either by doping of lithium atoms or bridging of two corannulene with two organic linkers. It may be extended to other gas adsorption on carbon materials, such as methane adsorption on carbon materials.

11.2.2 Ionic transport in solid

The main recommendations on ionic transport in solid for future work include as the followings.

- Four different crystalline forms of Li_2Pc are predicted. Diffusion coefficient of lithium ions in these crystalline structures is still not high enough, compared to liquid organic electrolytes. Addition of small amount of organic solvent is expected to have higher lithium ion diffusion coefficient. Experimentally, a battery using Li_2Pc with small amount of water and acetone trapped has been assembled with a lithium metal foil anode and a composite cathode with manganese dioxide and is being tested at the Air Force Research Lab. But the mechanism and role of solvent are not clear yet. The content of water needs to be removed or replaced by other solvent. Lithium ion conductivity can be obtained by performing MD simulations of Li_2Pc with organic solvent, such as EC and/or PC. The relationship of the conductivity vs. composition of solvent can suggest an improved solid electrolyte for solid state batteries.

- Activation energy of lithium transport through interface is qualitatively predicted as easily to overcome for lithium ions, based on the fact that no lithium build-up in the interphase is observed during MD simulations. Classic MD simulations are not able to obtain activation energy quantitatively. However, ab initio molecular dynamics, such as DFT and Car-Parrinello molecular dynamics (CPMD) of model systems, can be used to estimate the energy barrier following the lithium ion transport through the interface. With the system of pyrite (100) and Li_2Pc, the activation energy of lithium ion transport can be obtained in electrolyte phase, interface, and cathode phase. Quantitatively measurements of activation energy of lithium ion transport in solid electrolyte phase, interface, and cathode phase are helpful for modification of system to achieve enhanced diffusion of lithium ions.

REFERENCES

(1) Dutton, G., Bristow, A., Page, M., Kelly, C., Watson, J. Tetteh, A., The hydrogen energy economy: its long-term role in greenhouse gas reduction, 2005. http://www.earthscape.org/frames/searchframe.html.

(2) Verne, J. *The Mysterious Island*; Signet Classics: New York, 1986.

(3) U.S. Department of Energy, The changing structure of the electric power industry: an update. United States Department of Energy, Washington, DC, 1996.

(4) Gray, J. L. Early decisions in the development of the CANDU program, 1987. http://www.cns-snc.ca/history/pioneers/jl_gray/earlydecisions.html.

(5) Minnesota Department of Commerce, The hydrogen potential: hydrogen technology and Minnesota opportunities, 2003. http://www.state.mn.us/ mn/externalDocs/Commerce/Hydrogen_Potential_090803021706_HydrogenReport4.pdf.

(6) Armstrong, P. Hydrogen power: science fact or science fiction, 1996. http://www.borderlands.com/journal/h2.htm.

(7) Hoffmann, P. Tomorrow's energy: hydrogen, fuel cells, and the prospects for a clearner planet, 2001. http://www.earthscape.org/r3/hop01/hop01.html.

(8) Braun, H. Hydrogen-fueled aircraft, 2004. http://www.braunf orpresident.us/headlines/policy_briefs/pbpdf/HydrodgenFueledAircraft.pdf.

(9) Bellis, M. Hydrogen fuel cells - innovation for the 21st century, 2000. http://inventors.about.com/od/fstartinventions/a/Fuel_Cells.htm.

(10) New York State Energy Research and Development Authority, Hydrogen fact sheet. History of hydrogen, 2005. http://www.getenergysmart.org/Files/ HydrogenEducation/3HistoryofHydrogen.pdf

(11) Greene, D. L.; Jones, D. W.; Leiby, P. N. The outlook for US oil dependence. *Energy Policy* **1998**, *26*, 55.

(12) Veziroglu, T. N., Basar O., Dynamics of a universal hydrogen energy system and world parameters, In *Proceedings of the Hydrogen Economy Miami Energy (THEME) Conference*, Miami Beach, FL, March 1974, p156.

(13) Roberts, P. *The End of Oil: on the Edge of a Perilous New World,* Houghton Mifflin Company: New York, 2004.

(14) Rifkin, J. *The Hydrogen Economy: the Creation of the Worldwide Energy Web and the Redistribution of Power on Earth,* Penguin Group (USA) Inc.: New York, 2003.

(15) U.S. Department of Energy, The Department of Energy Strategic Plan: protecting national, energy, and economic security with advanced science and technology and ensuring environmental cleanup, 2003. http://strategicplan.doe.gov/ full.pdf.

(16) State of the Union Address, President's hydrogen fuel initiative: a clean and secure energy future, 2003. http://www.hydrogen.energy.gov/presidents_ initiative.html.

(17) Arenofsky, J., The hydrogen house: fueling a dream, 2005. http://www.emagazine.com/view/?2992.

(18) Yamasaki, A. An overview of CO_2 mitigation options for global warming-emphasizing CO_2 sequestration options. *J. Chem. Eng. Japan* **2003**, *36*, 361.

(19) Hanisch, C. The pros and cons of carbon dioxide dumping. *Environmental Science and Technology* **1998**, *32*, 20A.

(20) Hishida, M.; Fumizawa, M.; Inaba, Y.; Aritomi, M.; Nomura, S.; Kosaka, S.; Yamada, S.; Ogata, K. Nuclear energy conversion systems for arresting global warming. *Energy Conversion and Management* **1997**, *38*, 1365.

(21) Penner, S. S.; Haraden, J.; Mates, S. Long-term global energy supplies with acceptable environmental impacts. *Energy* (Oxford, United Kingdom) **1992**, *17*, 883.

(22) U.S. Department of Energy, A national vision of America's transition to a hydrogen economy - to 2030 and beyond," United States Department of Energy, Washington, DC, 2002.

(23) U.S. Department of Energy, Hydrogen posture plan: an integrated research, development, and demonstration plan, United States Department of Energy, Washington, DC, 2004.

(24) United Nations Industrial Development Organization - International Centre for Hydrogen Energy Technologies (UNIDO-ICHET), Why hydrogen: the hydrogen economy, 2000. http://www.unido-ichet.org/hydrogen_world.php..

(25) Purcell, R. Jr., Why hydrogen? 1999. http://www.rmi.org/sitepages/pid540.php.

(26) U.S. Department of Energy, National hydrogen energy roadmap: production, delivery, storage, conversiton, applicaitons, public education and outreach, United States Department of Energy, Washington, DC, 2002.

(27) Schlapbach, L.; Zuttel, A. Hydrogen-storage materials for mobile applications. *Nature* **2001**, *414*, 353.

(28) Sauer, H. Light-weight container for storage of hydrogen with comparable diffusion stability to conventional products. *Ger. Offen.* **2005**, p 8.

(29) Zuettel, A. Materials for hydrogen storage. *Materials Today,* **2003**, *6*, 24.

(30) Ovshinsky, S. R.; Young, R.; Huang, B. Atomically engineered hydrogen storage alloys having extended storage capacity at high pressures and high pressure hydrogen storage units containing variable amounts thereof; Energy Conversion Devices, Inc., Troy, MI, 2003; 33 pp.

(31) Sherif, S. A.; Zeytinoglu, N.; Veziroglu, T. N. Liquid hydrogen: potential, problems, and a proposed research program. *Int. J. Hydrogen Energy* **1997**, *22*, 683.

(32) Stange, M.; Maehlen, J. P.; Yartys, V. A.; Norby, P.; van Beek, W.; Emerich, H. In situ SR-XRD studies of hydrogen absorption-desorption in $LaNi_{4.7}Sn_{0.3}$. *J. Alloys and Compounds* **2005**, *404-406*, 604.

(33) Jiang, Z.; Dougal, R. A.; Liu, S.; Gadre, S. A.; Ebner, A. D.; Ritter, J. A. Simulation of a thermally coupled metal-hydride hydrogen storage and fuel cell system. *J. Power Sources* **2005**, *142*, 92.

(34) Kohno, T.; Yoshida, H.; Kanda, M. Hydrogen storage properties of $La(Ni_{0.9}M_{0.1})_3$ alloys. *J. Alloys and Compounds* **2004**, *363*, 249.

(35) Gadre, S. A.; Ebner, A. D.; Al-Muhtaseb, S. A.; Ritter, J. A. Practical modeling of metal hydride hydrogen storage systems. *Ind. Eng. Chem. Res.* **2003**, *42*, 1713.

(36) Esayed, A. Y. Metal hydrides. *Energy Sources* **2001**, *23*, 257.

(37) Guther, V.; Otto, A. Recent developments in hydrogen storage applicaitons based on metal hydrides. *J. Alloys and Compounds* **1999**, *293-295*, 889.

(38) Hahne, E.; Kallweit, J. Thermal conductivity of metal hydride materials for storage of hydrogen: experimental investigation. *Int. J. Hydrogen Energy* **1998**, *23*, 107.

(39) Vanhanen, J. P.; Lund, P. D.; Hagstrom, M. T. Feasibility study of a metal hydride hydrogen store for a self-sufficient solar hydrogen energy system. *Int. J. Hydrogen Energy* **1996**, *21*, 213.

(40) Hagstrom, M. T.; Lund, P. D.; Vanhanen, J. P. Metal hydride hydrogen storage for near-ambient temperature and atmospheric pressure applications, a PDSC study. *Int. J. Hydrogen Energy* **1995**, *20*, 897.

(41) Sandrock, G.; Thomas, G. The IEA/DOE/SNL on-line hydride databases. *Appl. Phys. A* **2001**, *72*, 153.

(42) Reilly, J. J.; Wiswall, R. H., Jr. Formation and properties of iron titanium hydride. *Inorg. Chem.* **1974**, *13*, 218.

(43) Selvam, P.; Viswanathan, B.; Swamy, C. S.; Srinivasan, V. Magnesium and magnesium alloy hydrides. *Int. J. Hydrogen Energy* **1986**, *11*, 169.

(44) Liu, F.-J.; Suda, S. A method for improving the long-term storability of hydriding alloys by air/water exposure. *J. Alloys and Compounds* **1995**, *231*, 411.

(45) Bogdanovic, B.; Schwickardi, M. Ti-doped alkali metal aluminum hydrides as potential novel reversible hydrogen storage materials. *J. Alloys and Compounds* **1997**, *253-254*, 1.

(46) Jensen, C. M.; Zidan, R.; Mariels, N.; Hee, A.; Hagen, C. Advanced titanium doping of sodium aluminim hydride: segue to a practical hydrogen storage material? *Int. J. Hydrogen Energy* **1999**, *24*, 461.

(47) Wang, J.; Ebner, A. D.; Prozorov, T.; Zidan, R.; Ritter, J. A. Effect of graphite as a co-dopant on the dehydrogenation and hydrogenation kinetics of Ti-doped sodium aluminum hydride. *J. Alloys and Compounds* **2005,** *395*, 252.

(48) Bellosta-von-Colbe, J. M.; Felderhoff, M.; Bogdanovic, B.; Schueth, F.; Weidenthaler, C. One-step direct synthesis of a Ti-doped sodium alanate hydrogen storage material. *Chem. Commun.* **2005**, *37*, 4732.

(49) Haiduc, A. G.; Stil, H. A.; Schwarz, M. A.; Paulus, P.; Geerlings, J. J. C. On the fate of the Ti catalyst during hydrogen cycling of sodium alanate. *J. Alloys and Compounds* **2005**, *393*, 252.

(50) Iniguez, J.; Yildirim, T.; Udovic, T. J.; Sulic, M.; Jensen, C. M. Structure and hydrogen dynamics of pure and Ti-doped sodium alanate. *Phys. Rev. B* **2004**, *70*, 060101/1.

(51) Felderhoff, M.; Klementiev, K.; Gruenert, W.; Spliethoff, B.; Tesche, B.; Bellosta-von-Colbe, J. M.; Weidenthaler, C. Combined TEM-EDX and XAFS studies of Ti-doped sodium alanate. *Phys. Chem. Chem. Phys.* **2004**, *6*, 4369.

(52) Kircher, O.; Fichtner, M. Hydrogen exchange kinetics in $NaAlH_4$ catalyzed in different decomposition states. *J. Appl. Phys.* **2004**, *95*, 7748.

(53) Schuth, F.; Bogdanovic, B.; Felderhoff, M. Light metal hydrides and complex hydrides for hydrogen storages. *Chem. Commun.* **2004**, *20*, 2249.

(54) Dymova, T. N.; Dergachev, Y. M.; Sokolov, V. A.; Grechanaya, N. A. Dissociation pressure of sodium tetrahydroaluminate and trisodium hexahydroaluminate. *Dokl. Akad. Nauk. S.S.S.R.* **1975**, *224*, 591.

(55) Dymova, T. N.; Eliseeva, N. G.; Bakum, S. I.; Dergachev, Y. M. Direct synthesis of alkali metal tetrahydroaluminates in melts. *Dokl. Akad. Nauk. S.S.S.R.* **1974**, *215*, 1369.

(56) Argonne National Laboratory, Basic research needs for the hydrogen economy, Argonne National Laboratory, Argonne, IL 2004.

(57) O'Keeffe, M., The archetypical MOF, 1999, http://www.public.asu.edu/~rosebudx/MOF-5N.jpg.

(58) Dillon, A. C.; Parilla, P. A.; Gennett, T.; Gilbert, K. E. H.; Blackburn, J. L.; Kim, Y.-H.; Zhao, Y.; Zhang, S. B.; Alleman, J. L.; Jones, K. M.; McDonald, T.; Heben, M. Hydrogen storage in carbon based materials, 2004. http://www.hydrogen.energy.gov/pdfs/progress04/iiid1_heben.pdf

(59) Dillon, A. C.; Jones, K. M.; Bekkedahl, T. A.; Kiang, C. H.; Bethune, D. S.; Heben, M. J. Storage of hydrogen in single-walled carbon nanotubes. *Nature* **1997**, *386*, 377.

(60) Dillon, A. C.; Gennett, T.; Alleman, J. L.; Jones, K. M.; Parilla, P. A.; Heben, J. J., Carbon nanotube materials for hydrogen storage, 2000. http://www.eere.energy.gov/hydrogenandfuelcells/pdfs/28890kkk.pdf

(61) Dillon, A. C.; Heben, M. J. Hydrogen storage using carbon adsorbents: past, present, and future. *Appl. Phys. A* **2001**, *72*, 133.

(62) Ye, Y.; Ahn, C. C.; Witham, C.; Fultz, B.; J. Liu, J.; Rinzler, A. G.; Colbert, D.; Smith, K. A.; Smalley, R. E. Hydrogen adsorption and cohesive energy of single-walled carbon nanotubes. *Appl. Phys. Lett.* **1999**, *74*, 2307.

(63) Liu, C.; Fan, Y. Y.; Liu, M.; Cong, H. T.; Cheng, H. M.; Dresselhaus, M. S. Hydrogen storage in single-walled carbon nanotubes at room temperature. *Science* **1999**, *286*, 1127.

(64) Gao, H.; Wu, X.; Li, J.; Wu, G.; Lin, J.; Wu, K.; Xu, D. Hydrogen adsorption of open-tipped insufficiently graphitized multiwalled carbon nanotubes. *Appl. Phys. Lett.* **2003**, *83*, 3389.

(65) Gundiah, G.; Govindaraj, A.; Rajalakshmi, N.; Dhathathreyan, K. S.; Rao, C. N. R. Hydrogen storage in carbon nanotubes and related materials. *J. Mat. Chem.* **2003**, *13*, 209.

(66) Yamanaka, S.; Fujikane, M.; Uno, M.; Murakami, H.; Miura, O. Hydrogen content and desorption of carbon nano-structures. *J. Alloys and Compounds* **2004**, *366*, 264.

(67) Poirier, E.; Chahine, R.; Benard, P.; Cossement, D.; Lafi, L.; Melancon, E.; Bose, T. K.; Desilets, S. Storage of hydrogen on single-walled carbon nanotubes and other carbon structures. *Appl. Phys. A* **2004**, *78*, 916.

(68) Sudan, P.; Zuttel, A.; Mauron, P.; Emmenegger, C.; Wenger, P.; Schlapbach, L. Physisorption of hydrogen in single-walled carbon nanotubes. *Carbon* **2003**, *41*, 2377.

(69) Furuya, Y.; Hashishin, T.; Iwanaga, H.; Motojima, S.; Hishikawa, Y. Interaction of hydrogen with carbon coils at low temperature. *Carbon* **2004**, *42*, 331.

(70) Ritschel, M.; Uhlemann, M.; Gutfleisch, O.; Leonhardt, A.; Graff, A.; Taschner, C.; Fink, J. Hydrogen storage in different carbon nanostructures. *Appl. Phys. Lett.* **2002**, *80*, 2985.

(71) Kajiura, H.; Tsutsui, S.; Kadono, K.; Kakuta, M.; Murakami, Y. Hydrogen storage capacity of commercially available carbon materials at room temperature. *Appl. Phys. Lett.* **2003**, *82*, 1105.

(72) Hirscher, M.; Becher, M.; Haluska, M.; Dettlaff-Weglikowska, U.; Quintel, A.; Duesberg, G. S.; Choi, Y.; Downes, P.; Hulman, M.; Roth, S.; Stepanek, I.; Bernier, P. Hydrogen storage in sonicated carbon materials. *Appl. Phys. A: Mater. Sci. & Proc.* **2001**, *72*, 129.

(73) Hirscher, M.; Becher, M.; Haluska, M.; Quintel, A.; Skakalova, V.; Choi, Y.-M.; Dettlaff-Weflikowska, U.; Roth, S.; Stepanek, I.; Bernier, P.; Leonhardt, A.; Fink, J. Hydrogen storage in carbon nanostructures. *J. Alloys and Compounds* **2002**, *330-332*, 654.

(74) Meregalli, V.; Parrinello, M. Review of theoretical calculations of hydrogen storage in carbon-based materials. *Appl. Phys. A* **2001**, *72*, 143.

(75) Froudakis, G. E. Why alkali-metal-doped carbon nanotubes posses high hydrogen uptake. *Nano Lett.* **2001**, *1*, 531.

(76) Wang, Q.; Johnson, J. K. Optimization of carbon nanotube arrays for hydrogen adsorption. *J. Phys. Chem. B* **1999**, *103*, 4809.

(77) Wang, Q.; Johnson, J. K. Hydrogen adsorption on graphite and in carbon slit pores from path integral simulations. *Mol. Phys.* **1998**, *95*, 299.

(78) Simonyan, V. V.; Diep, P.; Johnson, J. K. Molecular simulaiton of hydrogen adsorption in charged single-walled carbon nanotubes. *J. Chem. Phys.* **1999**, *111*, 9778.

(79) Simonyan, V. V.; Johnson, J. K. Hydrogen storage in carbon nanotubes and graphitic nanofibers. *J. Alloys and Compounds* **2002**, *330-332*, 659.

(80) Gauy, P.; Stansfield, B. L.; Rochefort, A. On the control of carbon nanostructures for hydrogen storage applicaitons. *Carbon* **2004**, *42*, 2187.

(81) Yin, Y. F.; Mays, T. J.; McEnaney, B. Molecular simulations of hydrogen storage in carbon nanotube arrays. *Langmuir* **2000**, *16*, 10521.

(82) Cao, D.; Feng, P.; Wu, J. Molecular simulation of novel carbonaceous materials for hydrogen storage. *Nano Lett.* **2004**, *4*, 1489.

(83) Ma, Y. C.; Xia, Y. Y.; Zhao, M. W.; Wang, R. J.; Mei, L. M. Effective hydrogen storage in single-wall carbon nanotubes. *Phys. Rev. B* **2001**, *63*, 115422.

(84) Dubot, P.; Cenedese, P. Modeling of molecular hydrogen and lithium adsorption on single-wall carbon nanotubes. *Phy. Rev. B* **2001**, *63*, 241402/1.

(85) Lee, S. M.; Lee, Y. H. Hydrogen storage in single-walled carbon nanotubes. *Appl. Phys. Lett.* **2000**, *76*, 2877.

(86) Nauschlicher, C. W. High coverage of hydrogen on a (10,0) carbon nanotube. *Nano Lett.* **2001**, *1*, 223.

(87) Liu, C.; Cheng, H.-M. Carbon nanotubes for clean energy applicaitons. *J. Phys. D: Appl. Phys* **2005**, *38*, R231.

(88) Shaijumon, M. M.; Ramaprabhu, S. Synthesis of carbon nanotubes by pyrolysis of acetylene using alloy hydride materials as catalyst and their hydrogen adsorption studies. *Chem. Phys. Lett.* **2003**, *374*, 513.

(89) Smith, M. R.; Bittner, E. W.; Shi, W.; Johnson, J. K.; Bochrath, B. C. Chemical activation of single-walled carbon nanotubes for hydrogen adsorption. *J. Phys. Chem. B* **2003**, *107*, 3752.

(90) Ci, L. J.; Zhu, H. W.; Wei, B. Q.; Xu, C. L.; Wu, D. H. Annealing amorphous carbon nanotubes for their application in hydrogen storage. *Appl. Surf. Sci.* **2003**, *205*, 39.

(91) Hou, P. X.; Xu, S. T.; Ying, Z.; Yang, Q. H.; Liu, C.; Cheng, H. M. Hydrogen adsorption/desorption behavior of multi-walled carbon nanotubes with different diameters. *Carbon* **2003**, *41*, 2471.

(92) Zhou, Y. P.; Feng, K.; Sun, Y.; Zhou, L. Adsorption of hydrogen on multiwalled carbon nanotubes at 77 K. *Chem. Phys. Lett.* **2003**, *380*, 526.

(93) Lueking, A. D.; Yang, R. T.; Rodriguez, N. M.; Baker, R. T. K. Hydrogen storage in graphite nanofibers: effect of synthesis catalyst and preteratment conditions. *Langmuir* **2004**, *20*, 714.

(94) Anson, A.; Callejas, M. A.; Benito, A. M.; Maser, W. K.; Izquierdo, M. T.; Rubio, B.; Jagiello, J.; Thommes, M.; Parra, J. B.; Martinez, M. T. Hydrogen adsorption studies on single wall carbon nanotubes. *Carbon* **2004**, *42*, 1243.

(95) Bacsa, R.; Laurent, C.; Morishima, R.; Suzuki, H.; Lay, M. L. Hydrogen storage in high surface area carbon nanotubes produced by catalytic chemical vapor deposition. *J. Phys. Chem. B* **2004**, *108*, 12718.

(96) Shiraishi, M.; Takenobu, T.; Yamada, A.; Ata, M.; Kataura, H. Hydrogen storage in single-walled carbon nanotube bundles and peapods. *Chem. Phys. Lett.* **2002**, *358*, 213.

(97) Callejas, M. A.; Anson, A.; Benito, A. M.; Maser, W.; Fierro, J. L. G.; Sanjuan, M. L.; Martinez, M. T. Enhanced hydrogen adsorption on single-wall carbon nanotubes by sample reduction. *Mat Sci Eng B-Solid* **2004**, *108*, 120.

(98) Takagi, H.; Hatori, H.; Soneda, Y.; Yoshizawa, N.; Yamada, Y. Adsorptive hydrogen storage in carbon and porous materials. *Mater. Sci. Eng. B* **2004**, *108*, 143.

(99) Lawrence, J.; Xu, G. High pressure saturation of hydrogen stored by single-walled carbon nanotubes. *Appl. Phys. Lett.* **2004**, *84*, 918.

(100) Tarasov, B. P.; Maehlen, J. P.; Lototshk, M. V.; Muradyan, V. E.; Yartys, V. A. Hydrogen sorption properties of arc generated single-wall carbon nanotubes. *J. Alloys and Compounds* **2003**, *356-357*, 510.

(101) Liu, F.; Zhang, X. B.; Cheng, J. P.; Kong, F. Z.; Huang, W. Z.; Chen, C. P. Preparation of short carbon nanotubes by mechanical ball milling and their hydrogen adsorption behavior. *Carbon*, **2003,** *41*, 2527.

(102) Zhang, H. Y.; Chen, Y. M.; Li, S. H.; Fu, X. J.; Zhu, Y. J.; Yi, S. P.; Xue, X. M.; He, Y. Y.; Chen, Y. L. Hydrogen storage for carbon nanotubes synthesized by the pyrolysis method using lanthanum nickel alloy as catalyst. *J. Appl. Phys.* **2003**, *94*, 6417.

(103) Ning, G. Q.; Wei, F.; Luo, G. H.; Wang, Q. X.; Wu, Y. L.; Yu, H. Hydrogen storage in multi-wall carbon nanotubes using samples up to 85 g. *Appl. Phys. A* **2004**, *78*, 955.

(104) Gupta, B. K.; Tiwari, R. S.; Srivastava, O. N. Studies on synthesis and hydrogenation behavior of graphitic nanofibers prepared through palladium catalyst assisted thermal carcking of acetylene. *J. Alloys and Compounds* **2004**, *381*, 301.

(105) Kowalczyk, P.; Tanaka, H.; Holyst, R.; Kaneko, K.; Ohmori, T.; Miyamoto, J. Storage of hydrogen at 303 K in graphite slitlike pores from grand canonical Monte Carlo simulation. *J. Phys. Chem. B* **2005**, *109*, 17174.

(106) Zhang, X. R.; Cao, D. P.; Chen, J. F. Hydrogen adsorption storage on single-walled carbon nanotube arrays by a combination of classical potential and density functional theory. *J. Phys. Chem. B* **2003**, *107*, 4942.

(107) Hu, N.; Sun, X.; Hsu, A. Monte Carlo simulations of hydrogen adsorption in alkali-doped single-walled carbon nanotubes. *J. Chem. Phys.* **2005**, *123*, 044708/1.

(108) Volpe, M.; Cleri, F. Role of surface chemistry in hydrogen adsorption in single-wall carbon nanotubes. *Chem. Phys. Lett.* **2003**, *371*, 476.

(109) Deng, W.; Xu, X.; Goddard, W. A. New alkali doped pillared carbon materials designned to achieve practical reversible hydrogen storage for transportation. *Phys. Rev. Lett.* **2004**, *92*, 166103.

(110) Rosi, N. L.; Eckert, J.; Eddaoudi, M.; Vodak, D. T.; Kim, J.; O'Keeffe, M.; Yaghi, O. M. Hydrogen storage in microporous metal-organic frameworks. *Science* **2003**, *300*, 1127.

(111) Ward, M. D. Materials science: molecular fuel tanks. *Science* **2003**, *300*, 1104.

(112) Kesanli, B.; Cui, Y.; Smith, M. R.; Bittner, E. W.; Brockrath, B. C.; Lin, W. Highly interpenetrated metal-organic frameworks for hydrogen sotrage. *Angew. Chem. Int. Ed.* **2005**, *44*, 72.

(113) Yang, Q.; Zhong, C. Molecular simulation of adsorption and diffusion of hydrogen in metal-organic frameworks. *J. Phys. Chem. B* **2005**, *109*, 11862.

(114) Sagara, T.; Klassen, J.; Ortony, J.; Ganz, E. Binding energies of hydrogen molecules to isoreticular metal-orgainc framework materials. *J. Chem. Phys.* **2005**, *123*, 014701/1.

(115) Rowsell, J. L. C.; Yaghi, O. M. Strategies for hydrogen storage in metal-organic frameworks. *Angew. Chem. Int. Ed.* **2005**, *44*, 4670.

(116) Perles, J.; Iglesias, M.; Martin-Luengo, M.-A.; Monge, M. A.; Ruiz-Valero, C.; Snejko, N. Metal-orgainc scandium framework: useful material for hydrogen storage and catalysis. *Chem. Mat.* **2005**, *17*, 5837.

(117) Bordiga, S.; Vitillo, J. G.; Ricchiardi, G.; Regli, L.; Cocina, D.; Zecchina, A.; Arstad, B.; Bjorgen, M.; Hafizovic, J.; Lillerud, K. P. Interaction of hydrogen with MOF-5. *J. Phys. Chem. B* **2005**, *109*, 18237.

(118) Sagara, T.; Ortony, J.; Ganz, E. New isoreticular metal-orgainc framework materials for high hydrogen storage capacity. *J. Chem. Phys.* **2005**, *123*, 214707/1.

(119) Yildirim, T.; Hartman, M. R. Direct observation of hydrogen adsorption sites and nanocage formation in metal-organic frameworks. *Phys. Rev. Lett.* **2005**, *95*.

(120) Li, Y.; Yang, R. T. Significantly enhanced hydrogen storage in metal-organic frameworks via spillover. *J. Am. Chem. Soc.* **2006**, *128*, 726.

(121) Rowsell, J. L. C.; Millward, A. R.; Park, K. S.; Yaghi, O. M. Hydrogen sorption in functionalized metal-organic frameworks. *J. Am. Chem. Soc.* **2004**, *126*, 5666.

(122) Chae, H. K.; Aiberio-Perez, D. Y.; Kim, J.; Go, Y. B.; Eddaoudi, M.; Matzger, A. J.; O'Keeffe, M. A route to high surface area porosity and inclusion of large molecules in crystals. *Nature* **2004**, *427*, 523.

(123) Pan, L.; Sander, M. B.; Huang, X.; Li, J.; Smith, M.; Bittner, E.; Bockrath, B.; Johnson, J. K. Microporous metal organic materials: promising candidates as sorbents for hydrogen storage. *J. Am. Chem. Soc.* **2004**, *126*, 1308.

(124) Eddaoudi, M.; Kim, J.; Rosi, N.; Vodak, D.; Wachter, J.; O'Keeffe, M.; Yaghi, O. M. Systematic design of pore size and functionality in isoreticular MOFs and their application in methane storage. *Science* **2002**, *295*, 469.

(125) Ferey, G.; Latroche, M.; Serre, C.; Millange, F.; Loiseau, T.; Percheron-Guegan, A. Hydrogen adsorption in the nanoporous metal-benzene dicarboxylate $M(OH)(O_2C\text{-}C_6H_4\text{-}CO_2)$ ($M = Al^{3+}$, Cr^{3+}), MIL-53. *Chem. Commun.* **2003**, *24*, 2976.

(126) Loiseau, T.; Serre, C.; Huguenard, C.; Fink, G.; Taulelle, F.; Henry, M.; Bataille, T.; Ferey, G. A rationale for the large breathing of the porous aluminum terephthalate (MIL-53) upon hydration. *Chem. Eur. J.* **2004**, *10*, 1373.

(127) Dybtsev, D. N.; Chun, H.; Yoon, S. H.; Kim, D.; Kim, K. Microporous manganese formate: a simple metal-organic porous material with high framework stability and highly selective gas sorption properties. *J. Am. Chem. Soc.* **2004**, *126*, 32.

(128) Lee, E. Y.; Suh, M. P. A robust porous material constructed of linear coordination polymer chains: Reversible single-crystal to single-crystal transformations upon dehydration and rehydration. *Angew. Chem. Int. Ed.* **2004**, *43*, 2798.

(129) Dybtsev, D. N.; Chun, H.; Kim, K. Rigid and flexible: a highly porous metal-organic framework with unusual guest-dependent dynamic behavior. *Angew. Chem. Int. Ed.* **2004**, *43*, 5033.

(130) Zhao, X.; Xiao, B.; Fletcher, A.; Thomas, K. M.; Bradshaw, D.; Rosseinsky, M. J. Hysteretic adsorption and desorption of hydrogen by nanoporous metal-organic frameworks. *Science* **2004**, *306*, 1012.

(131) Kubota, Y.; Takata, M.; Matsuda, R.; Kitaura, R.; Kitagawa, S.; Kato, K.; Sakata, M.; Kobayashi, T. C. Direct observation of hydrogen molecules adsorbed onto a microporous coordination polymer. *Angew. Chem. Int. Ed.* **2005**, *44*, 920.

(132) Chen, B.; Ockwig, N. W.; Andrew, A. R.; Contreras, D. S.; Yaghi, O. M. High H_2 adsorption in a microporous metal-organic framework with open metal sites. *Angew. Chem. Int. Ed.* **2005**, *44*, 4745.

(133) Barth, W. E. Synthesis of corannulene (dibenzo[ghi,mno]-fluoranthene), Ph.D. Dissertation, Univ. of Michigan, Ann Arbor, MI, 1967.

(134) Lawton, R. G.; Barth, W. E. Synthesis of corannulene. *J. Am. Chem. Soc.* **1971**, *93*, 1730.

(135) Davy, J. R.; Iskander, M. N.; Reiss, J. A. Cyclophanes XIII, approaches to the synthesis of corannulene. *Australian J. Chem.* **1979**, *32*, 1067.

(136) Houk, K. N.; Li, Y. Corannulene: a convenient new synthesis. *Chemtracts: Org. Chem.* **1991**, *4*, 401.

(137) Borchardt, A.; Fuchicello, A.; Kilway, K. V.; Baldridge, K. K.; Siegel, J. S. Synthesis and dynamics of the corannulene nucleus. *J. Am. Chem. Soc.* **1992**, *114*, 1921.

(138) Mehta, G.; Panda, G. A new synthesis of corannulene. *Tetrahedron Lett.* **1997**, *38*, 2145.

(139) Seiders, T. J.; Elliott, E. L.; Grube, G. H.; Siegel, J. S. Synthesis of corannulene and alkyl derivatives of corannulene. *J. Am. Chem. Soc.* **1999**, *121*, 7804.

(140) Knolker, H.-J.; Braier, A.; Brocher, D. J.; Jones, P. G.; Piotrowski, H. Transition metal complexes in organic synthesis, Part 55. Synthesis of corannulene via an iron-mediated [2+2+1] cycloaddition. *Tetrahedron Lett.* **1999**, *40*, 8075.

(141) Jones, C. S.; Elliott, E.; Siegel, J. S. Synthesis and properties of monosubstituted ethynylcorannulenes. *Synlett* **2004**, 187.

(142) Chen, P.; Wu, X.; Lin, J.; Tan, K. L. High H_2 uptake by alkali-doped carbon nanotubes under ambient pressure and moderate temperatures. *Science* **1999**, *285*, 91.

(143) Zhu, Z. H.; Lu, G. Q.; Smith, S. C. Comparative study of hydrogen storage in Li- and K-doped carbon materials-theoretically revisited. *Carbon* **2004**, *42*, 2509.

(144) Goddard, W. A., III; Deng, W.; Xu, X. Carbon-based compositions for reversible hydrogen storage. *PCT Int. Appl.* 2004, pp 33.

(145) Deng, W.-Q.; Xu, X.; Goddard, W. A. New alkali doped pillared carbon materials designed to achieve practical reversible hydrogen storage for transportation. *Phys. Rev. Lett.* **2004**, *92*, 166103/1.

(146) Skakalova, V.; Quintel, A.; Choi, Y. M.; Roth, S.; Becher, M.; Hirscher, M. Chemical processes during solid state reaction of carbon with alkali salts prepared for gravimetric hydrogen storage measurements. *Chem. Phys. Lett.* **2002**, *365*, 333.

(147) Pinkerton, F. E.; Wicke, B. G.; Olk, C. H.; Tibbetts, G. G.; Meisner, G. P.; Meyer, M. S.; Herbst, J. F. Thermogravimetric measurement of hydrogen absorption in alkali-modified carbon materials. *J. Phys. Chem. B* **2000**, *104*, 9460.

(148) Yang, R. T. Hydrogen storage by alkali-doped carbon nanotubes - revisited. *Carbon* **2000**, *38*, 623.

(149) Cabria, I.; Lopez, M. J.; Alonso, J. A. Enhancement of hydrogen physisorption on graphene and carbon nanotubes by Li doping. *J. Chem. Phys.* **2005**, *123*, 204721.

(150) Lee, H. B.; Sharp, P. R. Nickel and platinum s-bonded derivatives of corannulene. *Organometallics* **2005**, *24*, 4875.

(151) Elliott, E. L. The synthesis and properties of corannulene and novel corannulene derivatives. Dissertation, University of California, San Diego, 2003.

(152) Grube, G. H.; Elliott, E. L.; Steffens, R. J.; Jones, C. S.; Baldridge, K. K.; Siegel, J. S. Synthesis and properties of sym-pentasubstituted derivatives of corannulene. *Org. Lett.* **2003**, *5*, 713.

(153) Marcinow, Z.; Sygula, A.; Ellern, A.; Rabideau, P. W. Lowering inversion barriers of buckybowls by benzannelation of the rim: synthesis and crystal and molecular structure of 1,2-dihydrocyclopenta[b,c]dibenzo[g,m]corannulene. *Org. Lett.* **2001**, *3*, 3527.

(154) Vainer, G. E.; Stankevich, I. V.; Chistyakov, A. L. Corannulene derivatives as models for calculations of fullerene derivatives. *Russian Chem. Bull. (Translation of Izvestiya Akademii Nauk, Seriya Khimicheskaya)* **1997**, *46*, 1211.

(155) Seiders, T. J.; Baldridge, K. K.; Elliott, E. L.; Grube, G. H.; Siegel, J. S. Synthesis and quantum mechanical structure of sym-pentamethylcorannulene and decamethylcorannulene. *J. Am. Chem. Soc.* **1999**, *121*, 7439.

(156) Frisch, M. J.; Trucks, G. W.; Schlegel, H. B.; Scuseria, G. E.; Robb, M. A.; Cheeseman, J. R.; Montgomery, J. A.; Vreven, T.; Kudin, K. N.; Burant, J. C.; Millam, J. M.; Iyengar, S. S.; Tomasi, J.; Barone, V.; Mennucci, B.; Cossi, M.; Scalmani, G.; Rega, N.; Petersson, G. A.; Nakatsuji, H.; Hada, M.; Ehara, M.; Toyota, K.; Fukuda, R.; Hasegawa, J.; Ishida, M.; Nakajima, T.; Honda, Y.; Kitao, O.; Nakai, H.; Klene, M.; Li, X.; Knox, J. E.; Hratchian, H. P.; Cross, J. B.; Bakken, V.; Adamo, C.; Jaramillo, J.;

Gomperts, R.; Stratmann, R. E.; Yazyev, O.; Austin, A. J.; Cammi, R.; Pomelli, C.; Ochterski, J. W.; Ayala, P. Y.; Morokuma, K.; Voth, G. A.; Salvador, P.; Dannenberg, J. J.; Zakrzewski, V. G.; Dapprich, S.; Daniels, A. D.; Strain, M. C.; Farkas, O.; Malick, D. K.; Rabuck, A. D.; Raghavachari, K.; Foresman, J. B.; Ortiz, J. V.; Cui, Q.; Baboul, A. G.; Clifford, S.; Cioslowski, J.; Stefanov, B. B.; Liu, G.; Liashenko, A.; Piskorz, P.; Komaromi, I.; Martin, R. L.; Fox, D. J.; Keith, T.; Al-Laham, M. A.; Peng, C. Y.; Nanayakkara, A.; Challacombe, M.; Gill, P. M. W.; Johnson, B.; Chen, W.; Wong, M. W.; Gonzalez, C.; Pople, J. A. *GAUSSIAN 03*; Revision C.02; Gaussian, Inc.: Wallingford, CT, 2004.

(157) *Molecular Simulations, Inc.*; CERIUS 2: San Diego, CA, 1997.

(158) *Gaussian, Inc*.; GAUSSVIEW 03W: Wallingford, CT, 2003.

(159) Martin, J. M. L.; Alsenoy, C. V. Structure and vibrational spectra of the azabenzenes. a density functional study including exact exchange contributions. *J. Phys. Chem.* **1996**, *100*, 6973.

(160) Baldridge, K. K.; Siegel, J. S. Corannulene-based fullerene fragments $C_{20}H_{10}$-$C_{50}H_{10}$. When does a buckybowl become a buckytube? *Theor. Chem. Acc.* **1997**, *97*, 67.

(161) Frash, M. V.; Hopkinson, A. C.; Bohme, D. K. Corannulene as a Lewis base: computational modeling of protonation and lithium cation binding. *J. Am. Chem. Soc.* **2001**, *123*, 6687.

(162) Jursic, B. S. Density functional theory and complete basis set ab initio evaluation of proton affinity for some selected chemical systems. *THEOCHEM* **1999**, *487*, 193.

(163) Rapaport, D. C. *The Art of Molecular Dynamics Simulation*, 2nd ed.; Cambridge University Press: Cambridge, 2004.

(164) Allen, M. P.; Tildesley, D. J. *Computer Simulation of Liquids*; Oxford University Press: Oxford, 1990.

(165) Allen, M. P. Introduction to Molecular Dynamics Simulation. In *Computational Soft Matter: From Synthetic Polymers to Proteins, Lecture Notes*; Attig, N., Binder, K., Grubmuller, H., Kremer, K., Eds.; http://www.fz-juelich.de/nic-series/volume23/allen.pdf: Julich, 2004.

(166) Smith, W.; Forester, T. R. DL_POLY; Daresbury Laboratory: Daresbury, Cheshire UK, 1996.

(167) Zhao, X. B.; Xiao, B.; Fletcher, A. J.; Thomas, K. M. Hydrogen adsorption on functionalized nanoporous activated carbons. *J. Phys. Chem. B* **2005**, *109*, 8880.

(168) Hanson, J. C.; Nordman, C. E. The crystal and molecular structure of corannulene, $C_{20}H_{10}$. *Acta Cryst.* **1976**, *B32*, 1147.

(169) Guay, P.; Stanfield, B. L.; Rochefort, A. On the control of carbon nanostructures for hydrogen storage applications. *Carbon* **2004**, *42*, 2187.

(170) Darkrim, F.; Levesque, D. High adsorptive property of opened carbon nanotubes at 77 K. *J. Phys. Chem. B* **2000**, *104*, 6773.

(171) Ayalon, A.; Sygula, A.; Cheng, P.-C.; Rabinovitz, M.; Rabideau, P. W.; Scott, L. T. Stable high-order molecular sandwiches: hydrocarbon polyanion pairs with multiple lithium ions inside and out. *Science* **1994**, *265*, 1065.

(172) Gordon, P. A.; Saeger, R. B. Molecular modeling of adsorptive energy storage: hydrogen storage in single-walled carbon nanotubes. *Ind. Eng. Chem. Res.* **1999**, *38*, 4647.

(173) Wang, Q.; Johnson, J. K.; Broughton, J. Q. Thermodynamic properties and phase equilibrium of fluid hydrogen from path integral simulations. *Mol. Phys.* **1996**, *89*, 1105.

(174) Novaco, A. D.; Wroblewski, J. P. Rotational states of H_2, HD, and D_2 on graphite. *Phy. Rev. B* **1989**, *39*, 11364.

(175) Diep, P.; Johnson, J. K. An accurate H_2-H_2 interaction potential from first principles. *J. Chem Phys.* **2000**, *112*, 4465.

(176) Okamoto, Y.; Miyamoto, Y. Ab initio investigation of physisorption of molecular hydrogen on planar and curved graphenes. *J. Phys. Chem. B* **2001**, *105*, 3470.

(177) Cheng, H.; Cooper, A. C.; Pez, G. P.; Kostov, M. K.; Piotrowski, P.; Stuart, S. J. Molecular dynamics simulations on the effects of diameter and chirality on hydrogen adsorption in single walled carbon nanotubes. *J. Phys. Chem. B* **2005**, *109*, 3780.

(178) Scanlon, L. G. Personal Comunications, June 2005.

(179) Prausnitz, J. M.; Lichtenthaler, R. N.; Azevedo, E. G. *Molecular Thermodynamics of Fluid Phase Equilibria*, 3rd ed.; Pretice Hall: Upper Saddle River, NJ, 1999.

(180) Gray, C. G.; Gubbins, K. E. *Theory of Molecular Fluids*, Vol. 1, Clarendon Press: Oxford, England, 1984.

(181) Matsuzawa, N.; Dixon, D. A. Semiempirical calculations of the polarizability and second-order hyperpolarizability of C_{60}, C_{70}, and model aromatic compounds. *J. Phys. Chem.* **1992**, *96*, 6241.

(182) Rappe, A. K.; Casewit, C. J.; Colwell, K. S.; Goddard, W. A.; Skiff, W. M. UFF, a full periodic table force field for molecular mechanics and molecular dynamics simulations. *J. Am. Chem. Soc.* **1992**, *114*, 10024.

(183) Gready, J. E.; Bacskay, G. B.; Hush, N. S. Finite-field method calculations of molecular polarisabilities. I. Theoretical basis and limitations of SCF and Galerkin treatments. *Chem. Phys.* **1977**, *22*, 141.

(184) Lovas, F. J.; McMahon, R. J.; Grabow, J.-U.; Schnell, M.; Mack, J.; Scott, L. T.; Kuczkowski, R. L. Interstellar chemistry: a strategy for detecting polycyclic aromatic hydrocarbons in space. *J. Am. Chem. Soc.* **2005**, *127*, 4345.

(185) Janot, R.; Conard, J.; Guerard, D. Ball milling: a new route for the synthesis of superdense lithium GICs. *Carbon* **2001**, *39*, 1931.

(186) Kang, H. S. Density functional study of lithium -- aromatic sandwich compounds and their crystals. *J. Phys. Chem. A* **2005**, *109*, 478.

(187) Zhao, Y.; Truhlar, D. G. Multicoefficient extrapolated density functional theory studies of pi-pi interactions: the benzene dimer. *J. Phys. Chem. A* **2005**, *109*, 4209.

(188) Dewar, M. J. S.; Zoebisch, E. G.; Eamonn, F.; Healy, E. F. Development and use of quantum mechanical molecular models. 76. AM1: a general purpose quantum mechanical molecular model. *J. Am. Chem. Soc.* **1985**, *107*, 3902.

(189) Scanlon, L. G.; Balbuena, P. B.; Zhang, Y.; Sandi, G.; Back, C. K.; Feld, W. A.; Mack, J.; Rottmayer, M. A.; Riepenhoff, J. L. Investigation of corannulene for molecular hydrogen storage via computational chemistry and experimentation. *J. Phys. Chem. B.* **2006**, Accepted.

(190) Zhao, Y. L.; Zhang, R. Q.; Wang, R. S. The role of lithium in hydrogen storage in aromatic carbon materials. *Chem. Phys. Lett.* **2004**, *398*, 62.

(191) Zhu, Z. H.; Lu, G. Q.; Smith, S. C. Comparative study of hydrogen storage in Li- and K-doped carbon materials -- theoretically revisited. *Carbon* **2004**, *42*, 2509.

(192) Turker, L. AM1 treatment of $(Li+nH_2)@C_{60}$ (n=0-5) systems. *Int. J. Hydrogen Energy* **2003**, *28*, 223.

(193) Turker, L.; Gumus, S. A quire behavior of $(Li+nH_2)@C_{58}$ systems - an AM1 treatment. *J. Mol. Struct.* **2004**, *684*, 205.

(194) Challet, S.; Azais, P.; Pellenq, R. J. M.; Isnard, O.; Soubeyroux, J. L.; Duclaux, L. Hydrogen adsorption in microporous alkali-doped carbons - (activated carbon and single wall nanotubes). *J Phys Chem Solids* **2004**, *65*, 541.

(195) Sygula, A.; Sygula, R.; Fronczek, F. R.; Rabideau, P. W. Addition of organolithium reagents to corannulene and conformational preferences in 1-Alkyl-1,2-dihydrocorannulenes. *J. Org. Chem.* **2002**, *67*, 6487.

(196) Sygula, A.; Sygula, R.; Rabideau, P. W. Barrelene-semibullvalene rearrangement induced by visible light synthesis of dicorannuleneosemibullyalene dimethyl dicarboxylate. *Tetrahedron Lett.* **2005**, *46*, 1189.

(197) Dinadayalane, T. C.; Deepa, S.; Reddy, A. S.; Sastry, G. N. Density functional theory study on the effect of substitution and ring annelation to the rim of corannulene. *J. Org. Chem.* **2004**, *69*, 8111.

(198) Kavitha, K.; Manoharan, M.; Venuvanalingam, P. 1,3-dipolar reactions involving corannulene: how does its rim and spoke addition vary. *J. Org. Chem.* **2005**, *70*, 2528.

(199) Shabtai, E.; Hoffman, R. E.; Cheng, P.-C.; Bayrd, E.; Preda, D. C.; Scott, L. T.; Rabinovitz, M. Reduced corannulenes: 1,8-dicorannulenyloctane anions, a supramolecular octaaanion. *J. Chem. Soc., Perkin Trans.* **2000**, *2*, 129.

(200) Scanlon, L. G., Personal Communication, November 2005.

(201) Buchmann, I., Basics: every battery user should know, 2003. http://www.batteryuniversity.com/.

(202) Dell, R. M. Batteries: fifty years of materials development. *Sol. St. Ionics* **2000**, *134*, 139.

(203) Tarascon, J.-M.; Armand, M. Issues and challenges facing rechargeable lithium batteries. *Nature* **2001**, *414*, 359.

(204) Wakihara, M. Recent developments in lithium ion batteries. *Mater. Sci. Eng. B* **2001**, *R33*, 109.

(205) Dresselhaus, M. S.; Thomas, I. L. Alternative energy technologies. *Nature* **2001**, *414*, 332337.

(206) Vincent, C. A. Lithium batteries: a 50-year perspective, 1959-2009. *Sol. St. Ionics* **2000**, *134*, 159.

(207) Schalkwijk, W. A. V.; Scrosati, B. *Advances in Lithium-ion Batteries*; Plenum Publishers: New York, 2002.

(208) Berndt, D., Development of the battery, 1999. http://www.varta-automotive.com/eng/index2.php?p=6&s=3&content%20=knowhow/batterielexikon/entwicklung.html.

(209) Whittingham, M. S. Chemistry of intercalation compounds: metal guests in chalcogenide hosts. *Prog. Sol. St. Chem.* **1978**, *12*, 41.

(210) Mizushima, K.; Jones, P. C.; Wiseman, P. J.; Goodenough, J. B. Lithium cobalt oxide(Li_xCoO_2) ($0<x<1$): a new cathode material for batteries of high energy density. *Mater. Res. Bull.* **1980**, *15*, 783.

(211) Henston, T. A.; Chamberland, B. L. A survey of first-row ternary oxides: lithium metal oxide ($LiMO_2$) (M = scandium-copper). *J. Phys. Chem. Solids* **1987**, *48*, 97.

(212) Delmas, C.; Saadoune, L. Electrochemical and physical properties of the $Li_xNi_{1-y}Co_yO_2$ phases *Sol. St. Ionics* **1992**, *53-56*, 370.

(213) Armstrong, A. R.; Bruce, P. G. Synthesis of layered $LiMnO_2$ as an electrode for rechargeable lithium batteries. *Nature* **1996**, *381*, 499.

(214) Armstrong, A. R.; Huang, H.; Richard, R. A.; Bruce, P. G. $Li_{0.44}MnO_2$: an intercalation electrode with a tunnel structure and excellent cyclability. *J. Mat. Chem.* **1998**, *8*, 255.

(215) Thackeray, M. M. Manganese oxides for lithium batteries. *Prog. Solid State Chem.* **1997**, *25*, 1.

(216) Tarascon, J. M.; Guyomard, D. Li metal free rechargeable batteries based on $Li_{1+x}Mn_2O_4$ cathodes ($0<x<1$) and carbon anodes. *J. Electrochem. Soc* **1991**, *138*, 2865.

(217) Tarascon, J. M.; Guyomard, D. The $Li_{1+x}Mn_2O_4$/C rocking chair system: a review. *Electrochim. Acta* **1993**, *38*, 1221.

(218) Tarascon, J. M.; Guyomard, D. An update of the Li metal free rechargeable battery based on $Li_{1+x}Mn_2O_4$ cathodes and carbon anodes. *J. Power Sources* **1993**, *43-44*, 689.

(219) Guyomard, D.; Tarascon, J. M. Li metal-free rechargeable $LiMn_2O_4$/carbon cells: their understanding and optimization. *J. Electrochem. Soc.* **1992**, *139*, 937.

(220) Darling, R.; Newman, J. Modeling side reactions in composite $LiMn_2O_4$ electrodes. *J. Electrochem. Soc.* **1998**, *145*, 990.

(221) Guyomard, D.; Tarascon, J. M. The carbon/$LiMn_2O_4$ system. *Electrochim. Acta* **1993**, *38*, 1221.

(222) Peramunage, D.; Abraham, K. M.; Willstaedt, E. B. Lithium-ion batteries based on overlithiated $LiMn_2O_4$. Paper presented at *13th Annual Battery Conference on Applications and Advances*, 1998, Long Beach, CA.

(223) Yamada, A.; Tanaka, M. Jahn-Teller structural phase transition around 280 K in $LiMn_2O_4$. *Mat. Res. Bul.* **1995**, *30*, 715.

(224) Coociantelli, J. M.; Menetrier, M.; Delmas, C.; Doumerc, J. P.; Pouchard, M.; Hagenmuller, P. Electrochemical and structural characterization of lithium intercalation and deintercalation in the lithium vanadate (g-LiV_2O_5) bronze. *Sol. St. Ionics* **1992**, *50*, 99.

(225) Cocciantelli, J. M.; Doumerc, J. P.; Pouchard, M.; Broussely, M.; Labat, J. Crystal chemistry of electrochemically inserted lithium vanadium oxide ($Li_xV_2O_5$). *J. Power Sources* **1991**, *34*, 103.

(226) Leroux, F.; Goward, G.; Power, W. P.; Nazar, L. F. Electrochemical Li insertion into conductive polymer/ V_2O_5 nanocomposites. *J. Electrochem. Soc.* **1997**, *144*, 3886.

(227) Garcia, M. E.; Webb, E.; Garofalini, S. H. Molecular dynamics simulation of V_2O_5/Li_2SiO_3 interface. *J. Electrochem. Soc.* **1998**, *145*, 2155.

(228) Kim, J.; Manthiram, A. Synthesis and lithium intercalation properties of nanocrystalline lithium iron oxides. *J. Electrochem Soc.* **1999**, *146*, 4371.

(229) Okada, S.; Arai, H.; Yamamoto, J. Iron complex cathodes. *Denki Kagaku oyobi Kogyo Butsuri Kagaku* **1997**, *65*, 802.

(230) Padhi, A. K.; Nanjundaswamy, K. S.; Masquelier, C.; Okada, S.; Goodenough, J. B. Effect of structure on the Fe^{3+}/Fe^{2+} redox couple in iron phosphates. *J. Electrochem Soc.* **1997**, *144*.

(231) Linden(Ed.), D. *Handbook of Batteries*, 2nd ed.; McGraw-Hill: New York, 1995.

(232) Besenhard(Ed.), J. O. *Handbook of Battery Materials*; Wiley-VCH: New York, 1999.

(233) Broussely, M.; Archdale, G. Li-ion batteries and portable power source prospects for the next 5-10 years. *J. Power Sources* **2004**, *136*, 386.

(234) Takamura, T. Trends in advanced batteries and key materials in the new centery. *Sol. St. Ionics* **2002**, *152-153*, 19.

(235) Ohzuku, T.; Ueda, A.; Kouguchi, M. Synthesis and characterization of $LiAl_{1/4}Ni_{3/4}O_2$ for lithium-ion (shuttlecock) batteries. *J. Electrochem Soc.* **1995**, *142*, 4033.

(236) Ueda, A.; Ohzuku, T. Solid-state redox reactions of $LiNi_{1/2}Co_{1/2}O_2$ for 4 volt secondary lithium cells. *J. Electrochem Soc.* **1994**, *141*, 2010.

(237) Gitzendanner, R. L.; Russell, P. G.; Marsh, C.; Marsh, R. A. Design and development of a 20 Ah Li-ion prismatic cell *J. Power Sources* **1999**, *81-82*, 847.

(238) Padhi, A. K.; Nanjundaswamy, K. S.; Goodenough, J. B. Phospho-olivines as positive-electrode materials for rechargeable lithium batteries. *J. Electrochem Soc.* **1997**, *144*, 1188.

(239) Amine, K.; Yasuda, H.; Yamachi, M. β-FeOOH, a new positive electrode material for lithium secondary batteries. *J. Power Sources* **1999**, *81-82*, 221.

(240) Tanaka, K.; Ueda, M.; Koike, T.; Yamabe, T.; Yata, S. X-ray diffraction studies of pristine and heavily-doped polyacenic materials. *Synthetic Metals* **1988**, *25*, 265.

(241) Yata, S.; Tanaka, K.; Yamabe, T. Polyacene (PAS) batteries. *Mat. Res. Soc. Symp. Proc.* **1998**, *496*, 15.

(242) Hara, M.; Satoh, A.; Takami, N.; Ohsaki, T. Structural and electrochemical properties of lithiated polymerized aromatics. Anodes for lithium-ion cells. *J. Phys. Chem.* **1995**, *99*, 16638.

(243) Zheng, T.; McKinnon, W. R.; Dahn, J. R. Hysteresis during lithium insertion in hydrogen-containing carbons. *J. Electrochem Soc.* **1996**, *143*, 2137.

(244) Nishijima, M.; Kagohashi, T.; Takeda, Y.; Imanishi, M.; Yamamoto, O. Electrochemical studies of a new anode material, $Li_{3-x}M_xN$ (M = Co, Ni, Cu). *J. Power Sources* **1997**, *68*, 510.

(245) Wilson, A. M.; Dahn, J. R.; Xue, J. S.; Gao, Y.; Feng, X. H. Carbonaceous materials containing silicon as anodes for lithium-ion cells. *Mat. Res. Soc. Symp. Proc.* **1995**, *393*, 305.

(246) Fey, G. T.-K.; Chen, C.-L. High-capacity carbons for lithium-ion batteries prepared from rice husk. *J. Power Sources* **2001**, *97-98*, 47.

(247) Sato, K.; Noguchi, M.; Demachi, A.; Oki, N.; Endo, M. A Mechanism of lithium storage in disordered carbons. *Science* **1994**, *264*, 556.

(248) Ohzuku, T.; Iwakoshi, Y.; Sawai, K. Formation of lithium-graphite intercalation compounds in nonaqueous electrolytes and their application as a negative electrode for a lithium ion (shuttlecock) cell. *J. Electrochem. Soc.* **1993**, *140*, 2490.

(249) Mabuchi, A.; Tokumitsu, K.; Fujimoto, H.; Kasuh, T. Charge-discharge characteristics of the mesocarbon microbeads heat-treated at different temperatures. *J. Electrochem. Soc.* **1995**, *142*, 1041.

(250) Dahn, J. R.; Fong, R.; Spoon, M. J. Suppresion of staging in lithium-intercalated carbon by disorder in the host. *Phys. Rev. B* **1990**, *42*, 6424.

(251) Dahn, J. R. Phase diagram of Li_xC_6. *Phys. Rev. B* **1991**, *44*, 9170.

(252) Shu, Z. X.; McMillan, R. S.; Murray, J. J. Electrochemical interaction of lithium into graphite. *J. Electrochem. Soc.* **1993**, *140*, 922.

(253) Zheng, T.; Xue, J. S.; Dahn, J. R. Lithium insertion in hydrogen-containing carbonaceous materials. *Chem. Mat.* **1996**, *8*, 389.

(254) Endo, M.; Kim, C.; Karaki, T.; Nishimura, Y.; Matthews, M. J.; Brown, S. D. M.; Dresselhaus, M. S. Anode performance of a Li ion battery based on graphitized and B-doped milled mesophase pitch-based carbon fibers. *Carbon* **1999**, *37*, 516.

(255) Nishi, Y. Performance of the first lithium ion battery and its process technology. In *Lithium Ion Batteries;* Wakihara, M., Yamamoto, O., Eds.; Kodansha: Tokyo, Japan, 1998, p 181.

(256) Takamura, T.; Sumiya, K.; Suzuki, J.; Yamada, C.; Sekine, K. Enhancement of Li doping/undoping reaction rate of carbonaceous materials by coating with an evaporated metal film. *J. Power Sources* **1999**, *81-82*, 368.

(257) Tatsumi, K.; Zaghib, K.; Sawada, Y.; Abe, H.; Ohsaki, T. Anode performance of vapor-grown carbon fibers in secondary lithium-ion batteries. *J. Electrochem Soc.* **1995**, *145*, A1423.

(258) Takeda, Y.; Nishijima, M.; Yamahata, M.; Takeda, K.; Imanishi, N.; Yamamoto, O. Lithium secondary batteries using a lithium cobalt nitride, $Li_{2.6}Co_{0.4}N$, as the anode. *Sol. St. Ionics* **2000**, *130*, 61.

(259) Yang, J.; Takeda, Y.; Imanishi, N.; Yamamoto, O. Novel composite anodes based on nano-oxides and $Li_{2..6}Co_{0.4}N$ for lithium ion batteries. *Electrchim. Acta* **2001**, *46*, 2659.

(260) Liu, Y.; Horikawa, K.; Fujiyosi, M.; Imanishi, N.; Hirano, A.; Takeda, Y. The effect of doped elementals on the electrochemical behavior of hexagonal $Li_{2..6}Co_{0..4}N$. *J. Electrochem Soc.* **2004**, *151*, A1450.

(261) Liu, Y.; Yang, J.; Imanishi, N.; Hirano, A.; Takeda, Y.; Yamamoto, O. Composite anode containing nano-$SiO_{1.1}$ and $Li_{2..6}Co_{0..4}N$ with solid PEO electrolytes for lithium-ion batteries. *J. Power Sources* **2005**, *146*, 376.

(262) Besenhard, J. O.; Yang, J.; Winter, M. Will advanced lithium-alloy anodes have a chance in lithium-ion batteries? *J. Power Sources* **1997**, *68*, 87.

(263) Nagayama, M.; Morita, T.; Ikuta, H.; Wakihara, M.; Takano, M.; Kawasaki, S. A new anode material $SnSO_4$ for lithium secondary battery. *Sol. St. Ionics* **1998**, *106*, 33.

(264) Kim, S.-S.; Ikuta, H.; Wakihara, M. Synthesis and characterization of MnV_2O_6 as a high capacity anode material for a lithium secondary battery. *Sol. St. Ionics* **2001**, *139*, 57.

(265) Idota, Y.; Kubota, T.; Matsufuji, A.; Maekawa, Y.; Miyasaka, T. Tin-based amorphous oxide: a high-capacity lithium-ion-storage material. *Science* **1997**, *276*, 1395.

(266) Denis, S.; Baudrin, E.; Orsini, F.; Ouvrard, G.; Touboul, M.; Tarascon, J.-M. Synthesis and electrochemical properties of numerous classes of vanadates *J. Power Sources* **1999**, *81-82*, 79.

(267) Yin, J.; Wada, M.; Yoshida, S.; Ishihara, K.; Tanase, S.; Sakai, T. New Ag-Sn alloy anode materials for lithium-ion batteries. *J. Electrochem Soc.* **2003**, *150*, A1129.

(268) Sakaguchi, H.; Honda, H.; Akasaka, Y.; Esaka, T. Ce-Sn intermetallic compounds as new anode materials for rechargeable lithium batteries. *J. Power Sources* **2003**, *119-121*, 50.

(269) Doublet, M.-L.; Lemoigno, F.; Gillot, F.; Monconduit, L. The Li_xVPn_4 ternary phases (Pn = P, As): rigid networks for lithium intercalation/deintercalation. *Chem. Mat.* **2002**, *14*, 4126.

(270) Rom, I.; Wachtler, M.; Papst, I.; Schmied, M.; Besenhard, J. O.; Hofer, F.; Winter, M. Electron microscopical characterization of Sn/SnSb composite electrodes for lithium-ion batteries. *Sol. St. Ionics* **2001**, *143*, 329.

(271) Yang, J.; Takeda, Y.; Li, Q.; Imanishi, N.; Yamanoto, O. Solid polymer electrolyte cells using $SnSb/Li_{2.6}Co_{0.4}N$ composite anodes. *J. Power Sources* **2001**, *97-98*, 779.

(272) Hamon, Y.; Brousse, T.; Jousse, F.; Topart, P.; Buvat, P.; Schleich, D. M. Aluminum negative electrode in lithium ion batteries. *J. Power Sources* **2001**, *97-98*, 185.

(273) Zhao, X. B.; Gao, G. S.; Lu, C. P.; Zhang, L. J.; Hu, S. H.; Zhu, T. J.; Zhou, B. C. Electrochemical properties of some Sb or Te based alloys for candidate anode materials of lithium-ion batteries. *J. Alloys and Compounds* **2001**, *315*, 265.

(274) Wachtler, M.; Besenhard, J. O.; Winter, M. Tin and tin-based intermetallics as new anode materials for lithium-ion cells. *J. Power Sources* **2001**, *94*, 189.

(275) Peled, E. Chapter 3: Lithium stability and film formation in organic and inorganic electrolyte for lithium battery systems. *Lithium Batteries*; Gabano, J. P., Ed.; Academic Press: New York, 1983; 43.

(276) Morita, M.; Ishikawa, M.; Matsuda, Y. Organic electrolytes for rechargeable lithium ion batteries. *Lithium Ion Batteries*; Wakihara, M., Yamamoto, O., Eds.; Kodansha: Tokyo, 1998; 156.

(277) Blomgren, G. E. Properties, structure and conductivity of organic and inorganic electrolytes for lithium battery systems. In *Lithium Batteries*; Gabano, J. P., Ed.; Academic Press: New York, 1983; p 13.

(278) Matsuda, Y.; Satake, H. Mixed electrolyte solutions of propylene carbonate and dimethoxyethane for high energy density batteries. *J. Electrochem Soc.* **1980**, *127*, 877.

(279) Gutmann, V. *The Donor-Acceptor Approach to Molecular Interactions*; Plenum: New York, 1978.

(280) Besenhard, J. O.; Fritz, H. P. Cathodic reduction of graphite in organic solutions of alkali and NR^{4+} salts. *J. Electroanal. Chem. and Inter. Electrochem.* **1974**, *53*, 329.

(281) Shu, Z. X.; McMillan, R. S.; Murray, J. J.; Davidson, I. J. Use of chloroethylene carbonate as an electrolyte solvent for a lithium ion battery containing a graphitic anode. *J. Electrochem Soc.* **1995**, *142*, L161.

(282) Jehoulet, C.; Biensan, P.; Bodet, J. M.; Broussely, M.; Tessier-Lescorret, C. Batteries for portable applications and electric vehicles; *Proc. Electrochem. Soc.*, **1997**, *97*, 18.

(283) Wrodnigg, G. H.; Besenhard, J. O.; Winter, M. Ethylene sulfite as electrolyte additive for lithium-ion cells with graphitic anodes. *J. Electrochem Soc.* **1999**, *146*, 470.

(284) Wrodnigg, G. H.; Wrodnigg, T. M.; Besenhard, J. O.; Winter, M. Propylene sulfite as film-forming electrolyte additive in lithium ion batteries. *Electrochem. Comm.* **1999**, *1*, 148.

(285) Wrodnigg, G. H.; Lie, L. H.; Winter, M.; Besenhard, J. O. Ethylene sulfite as new film-forming agent for LiC_n-anodes. *Adv. Sci. Tech.* **1999**, *24*, 131.

(286) Wrodnigg, G. H.; Reisinger, C.; Besenhard, J. O.; Winter, M. Cyclic and linear sulfites as electrolyte solvents and electrolyte additives for lithium ion cells with graphitic anodes. *ITE Batt. Lett.* **1999**, *1*, 110.

(287) Aurbach, D.; Ein-Eli, Y.; Markovsky, B.; Zaban, A.; Luski, S.; Carmeli, Y.; Yamin, H. The study of electrolyte solutions based on ethylene and diethyl carbonates for rechargeable Li batteries. II. graphite electrodes *J. Electrochem Soc.* **1995**, *142*, 2882.

(288) Ohta, A.; Koshina, H.; Okuno, H.; Murai, H. Relationship between carbonaceous materials and electrolyte in secondary lithium-ion batteries *J. Power Sources* **1995**, *54*, 6.

(289) Blomgren, G. E. Liquid electrolytes for lithium and lithium-ion batteries. *J. Power Sources* **2003**, *119-121*, 326.

(290) Armand, M. Polymer solid electrolytes: an overview. *Sol. St. Ionics* **1983**, *9-10*, 745.

(291) Scrosati, B.; Neat, R. J. *Lithium Polymer Batteries*; Chapman & Hall: London, 1993.

(292) Dias, F. B.; Plomp, L.; Veldhuis, J. B. J. Treads in polymer electrolytes for secondary lithium batteries. *J. Power Sources* **2000**, *88*, 169.

(293) Scrosati, B. Lithium ion plastic batteries. In *Lithium Ion Batteries*; Wakihara, M., Yamamoto, O., Eds.; Wiley-VCH: Tokyo, 1998; p 218.

(294) Armand, M.; Sanchez, J. Y.; Gauthier, M.; Choquette, Y. Polymeric materials for lithium batteries. In *Electrochemistry of Novel Materials*; Lipkowski, J., Ross, P. N., Eds.; VCH: New York, 1994; p 65.

(295) Scrosati, B. Power sources for portable electronics and hybrid cars: lithium batteries and fuel cells. *Chem. Rec.* **2005**, *5*, 286.

(296) Scrosati, B. Lithium polymer electrolytes. In *Advances in Lithium-Ion Batteries*; Schalkwijk, W. A. V., Scrosati, B., Eds.; Kluwer Academic/Plenum: New York, 2002; p 251.

(297) Fenton, D. E.; Parker, J. M.; Wright, P. V. Complexes of alkali metal ions with poly(ethylene oxide). *Polymer* **1973**, *14*, 589.

(298) Armand, M. B.; Chabagno, J. M.; Duclot, M. J. Polyethers as solid electrolytes. In *Fast Ion Transport in Solids: Electrodes Electrolytes*; Elsevier North Holland: New York, 1979, p 131.

(299) Mitsubishi Corp., Ionic conduction mechanism of polymeric electrolyte, 2004. http://www.sankonol.com/eng/intro/intro_eng.htm.

(300) Ratner, M. A.; Johansson, P.; Shriver, D. F. Polymer electrolytes: ionic transport mechanisms and relaxation coupling. *MRS Bull.* **2000**, *25*, 31.

(301) Scrosati, B.; Vincent, C. A. Polymer electrolytes: the key to lithium polymer batteries. *MRS Bull.* **2000**, *25*, 28.

(302) Gray, F.; Armand, M. Polymer electrolytes. In *Handbook of Battery Materials*; Besenhard, J. O., Ed.; Wiley-VCH: Weinheim, 1999; p 499.

(303) Krawiec, W.; Scanlon, L. G.; Fellner, J. P.; Vaia, R. A.; Vasudevan, S.; Giannelis, E. P. Polymer nanocomposites: a new strategy for synthesizing solid electrolytes for rechargeable lithium batteries. *J. Power Sources* **1995**, *54*, 310.

(304) Wieczorek, W.; Stevens, J. R.; Florijanzayk, Z. Composite polyether based solid electrolytes: the lewis acid-base approach. *Sol. St. Ionics* **1996**, *85*, 67.

(305) Croce, F.; Appetecchi, G. B.; Persi, L.; Scrosati, B. Nanocomposite polymer electrolytes for lithium batteries. *Nature* **1998**, *394*, 456.

(306) Kumar, B.; Scanlon, L. G. Composite electrolytes for lithium rechargeable batteries. *J. Electroceram.* **2000**, *5*, 127.

(307) Kumar, B.; Scanlon, L. G.; Marsh, A.; Mason, R.; Higgins, R.; Baldwin, S. Structural evolution and conductivity of PEO:$LiBF_4$-MgO composite electrolytes. *Electrchim. Acta* **2001**, *46*, 1515.

(308) Morita, M.; Fujisaki, T.; Yoshimoto, N.; Ishikawa, M. Ionic conductance behavior of polymeric composite solid electrolytes containing lithium aluminate. *Electrchim. Acta* **2001**, *46*, 1565.

(309) Bloise, A. C.; Tambelli, C. C.; Franco, R. W. A.; Donoso, J. P.; Magon, C. J.; Souza, M. F.; Rosario, A. V.; Pereira, E. C. Nuclear magnetic resonance study of PEO-based composite polymer electrolytes. *Electrchim. Acta* **2001**, *45*, 1571.

(310) Scrosati, B.; Croce, R.; Panero, S. Progress in lithium polymer battery R&D. *J. Power Sources* **2001**, *100*, 93.

(311) Nest, J. F. L.; Callens, S.; Gandini, A.; Armand, M. A new polymer network for ionic conduction. *Electrchim. Acta* **1992**, *37*, 1595.

(312) Nishimoto, A.; Watanabe, M.; Lkeda, Y.; Kohjiya, S. High ionic conductivity of new polymer electrolytes based on high molecular weight polyether comb polymers. *Electrchim. Acta* **1998**, *43*, 1177.

(313) Blonsky, P. M.; Shriver, D. F.; Austin, P.; Allcock, H. R. Complex formation and ionic conductivity of polyphosphazene solid electrolytes. *Sol. St. Ionics* **1986**, *18-19*, 258.

(314) Soo, P. P.; Huang, B.; Jang, Y.-I.; Chiang, Y.; Sadowa, D. R.; Mayes, A. M. Rubbery block copolymer electrolyte for solid-state rechargeable lithium batteries. *J. Electrochem. Soc.* **1999**, *146*, 32.

(315) Watanabe, M.; Endo, T.; Nishimoto, A.; Miura, K.; Yanagida, M. High ionic conductivity and electrode interface properties of polymer electrolytes based on high molecular weight branched polyether *J. Power Sources* **1999**, *81-82*, 786.

(316) York, S.; Kellam, E. C.; Allcock, H. R.; Frech, R. A vibrational spectroscopic study of lithium triflate in polyphosphazenes with linear oligoethyleneoxy side-chains of different lengths. *Electrchim. Acta* **2001**, *46*, 1553.

(317) Silva, R. A.; Silva, G. G.; Furtado, C. A.; Moreira, R. L.; Pimenta, M. A. Structure and conductivity in polydioxolane/$LiCF_3SO_3$ electrolytes. *Electrchim. Acta* **2001**, *46*, 1493.

(318) Matsui, S.; Muranaga, T.; Higobashi, H.; Inoue, S.; Sakai, T. Liquid-free rechargeable Li polymer battery. *J. Power Sources* **2001**, *97-98*, 772.

(319) Ruzette, A.-V. G.; Soo, P. P.; Sadoway, D. R.; Mayes, A. M. Melt-formable block copolymer electrolytes for lithium rechargeable batteries. *J. Electrochem Soc.* **2001**, *148*, A537.

(320) Wieczorek, W.; Florjanczyk, Z.; Stevens, J. R. Composite polyether based solid electrolytes. *Electrchim. Acta* **1995**, *40*, 2251.

(321) Tanaka, R.; Sakurai, M.; Sekiguchi, H.; Mori, H.; Murayama, T.; Ooyama, T. Lithium ion conductivity in polyoxyethylene/polyethylenimine blends. *Electrchim. Acta* **2001**, *46*, 1709.

(322) Feuillade, G.; Perche, P. Ion-conductive macromolecular gels and membranes for solid lithium cells. *J. Appl. Electrochem.* **1975**, *5*, 63.

(323) Abraham, K. M.; Alamgir, M. Ambient temperature rechargeable polymer-electrolyte batteries. *J. Power Sources* **1993**, *43*, 195.

(324) Abraham, K. M.; ALamgir, M. Lithium ion-conductive solid polymer electrolytes with liquid-like conductivity. *J. Electrochem Soc.* **1990**, *137*, 1657.

(325) Nagasubnramanian, G.; Attia, A. I.; Halpert, G. A polyacrylonitrile-based gelled electrolyte: electrochemical kinetic studies. *J. Appl. Electrochem.* **1994**, *24*, 298.

(326) Gray, F. M. *Polymer Electrolytes*; Royal Soc. Chem.: Cambridge, 1997.

(327) Appetecchi, G. B.; Romagnoli, P.; Scrosati, B. Composite gel membranes: a new class of improved polymer electrolytes for lithium batteries. *Electrochem. Comm.* **2001**, *3*, 281.

(328) Gozdz, A. S.; Tarascon, J.-M.; Gebizlioglu, O. S.; Schmutz, C. N.; Warren, P. C.; Shokooyi, F. K. A new hybrid polymer electrolyte for lithium-ion rechargeable batteries. *Proc. Electrochem. Soc.*, **1995**, *94-28*, 400.

(329) Gozdz, A. S.; Schmutz, C. N.; Tarascon, J. M.; Warren, P. C. Polymeric electrolytic cell separator membrane. 1995 US Patent 5296318, 11 pp.

(330) Tarascon, J. M.; Gozdz, A. S.; Schmutz, C.; Shokoohi, F.; Warren, P. C. Performance of Bellcore's plastic rechargeable Li-ion batteries. *Sol. St. Ionics* **1996**, *86-88*, 49.

(331) Wright, P. V. Developments in polymer electrolytes for lithium batteries. *MRS Bull.* **2002**, *27*, 597.

(332) Boudin, F.; Andrieu, X.; Jehoulet, C.; Olsen, I. I. Microporous PVdF gel for lithium-ion batteries. *J. Power Sources* **1999**, *81-82*, 804.

(333) Brodd, R. J.; Tagawa, K. Lithium-ion cell production processes. In *Advances in Lithium-Ion Batteries*; Schalkwijk, W. A. V., Scrosati, B., Eds.; Kluwer Academic/Plenum: New York, 2002; p 267.

(334) Armand, M.; Gorecki, W.; Andreani, R. Perfluorosulfonimide salts as solute for polymer electrolytes. In *Second International Meeting on Polymer Electrolytes*; Scrosati, B., Ed.; Elsevier: London, 1989; p 91.

(335) Fauteux, D. *Polymer Electrolyte Review-2*; Elsevier Applied Science: London, 1989.

(336) Stallworth, P. E.; Fontanella, J. J.; Wintersgill, M. C.; Scheidler, C. D.; Immel, J. J.; Greenbaum, S. G.; Gozdz, A. S. NMR, DSC and high pressure electrical conductivity studies of liquid and hybrid electrolytes *J. Power Sources* **1999**, *81-82*, 739.

(337) Kondo, A. All solid-state lithium secondary battery with highly ion conductive galssy electrolyte. In *Lithium Ion Batteries*; Wakihara, M., Yamamoto, O., Eds.; Wiley-VCH: Weinheim, 1998; p 199.

(338) Birke, P.; Weppner, W. Solid electrolytes. In *Handbook of Battery Materials*; Besenhard, J. O., Ed.; Wiley-VCH: Weinheim, Germany, 1999; p 525.

(339) Warburg, E. Solid ionic conductor. *Wiedemann. Ann. Phys.* **1884**, *21*, 622.

(340) Warburg, E.; Tegetmeyer, F. Development of future ionic conductor. *Wiedemann. Ann. Phys.* **1888**, *32*, 455.

(341) Rickert, H. *Electrochemistry of Solids: an Introduction*; Springer-Verlag: Berlin, 1982.

(342) Kudo, T.; Fueki, K. *Solid State Ionics*; VCH: Weinheim, 1990.

(343) Mennicke, S. Development and status of sodium sulfer batteries, *Sol. St. Ionics, Proc. Symp. A2 Int. Conf. Adv. Mater.* (1992), Meeting Date 1991, 3-15, Heidelberg, Germany.

(344) Minami, T.; Tatsumisago, M.; Wakihara, M.; Iwakura, C.; Kohjiya, S.; Tanaka, I. *Sol. St. Ionics for Batteries*; Springer-Verlag: Tokyo, 2005.

(345) Hong, H. Y.-P. Crystal structure and ionic conductivity of $Li_{14}Zn(GeO_4)_4$ and other new Li^+ superionic conductiors. *Mat. Res. Bul.* **1978**, *13*, 117.

(346) Alpen, U. V.; Bell, M. F.; Wichelhaus, W.; Cheung, K. Y.; Dudley, G. J. Ionic conductivity of $Li_{14}Zn(GeO_4)_4$ (Lisicon). *Electrochim. Acta* **1978**, *23*, 1395.

(347) Adachi, G.-Y.; Imanaka, N. The binary rare earth oxides. *Chem. Rev.* **1998**, *98*, 1479.

(348) Farrington, G. C.; Dunn, B. S.; Briant, J. L. Lithium(1+) and divalent ion conductivity in b- and b"-alumina. *Sol. St. Ionics* **1981**, *3-4*, 405.

(349) Inaguma, Y.; Matsui, Y.; Yu, J.; Shan, Y.; Nakamura, T.; Itoh, M. Effect of substitution and pressure on lithium ion conductivity in perovskites $Ln_{1/2}Li_{1/2}TiO_3$ (Ln = La, Pr, Nd and Sm). *J. Phys. Chem. Sol.* **1997**, *58*, 843.

(350) Latie, L.; Villeneuve, G.; Conte, D.; Flem, G. L. Ionic conductivity of oxides with general formula $Li_xLn_{1/3}Nb_{1-x}Ti_xO_3$ (Ln = La, Nd). *J. Sol. St. Chem.* **1984**, *51*, 293.

(351) Kanno, R.; Murayama, M. Lithium ionic conductor thio-LISICON: the Li_2S-GeS_2-P_2S_5 system. *J. Electrochem. Soc.* **2001**, *148*, A742.

(352) Kanno, R.; Hata, T.; Kawamoto, Y.; Irie, M. Synthesis of a new lithium ionic conductor, thio-LISICON-lithium germanium sulfide system. *Sol. St. Ionics* **2000**, *130*, 97.

(353) Murayama, M.; Kanno, R.; Irie, M.; Ito, S.; Hata, T.; Sonoyama, N.; Kawaoto, Y. Synthesis of new lithium ionic conductor thio-LISICON - lithium silicon sulfides system. *J. Sol. St. Chem.* **2002**, *168*, 140.

(354) Murayama, M.; Sonoyama, N.; Yamada, A.; Kanno, R. Material design of new lithium ionic conductor, thio-LISICON, in the Li_2S-P_2S_5 system. *Sol. St. Ionics* **2004**, *170*, 173.

(355) Kobayashi, T.; Inada, T.; Sonoyama, N.; Yamada, A.; Kanno, R. ll solid-state batteries using super ionic conductor, thio-LISICON - electrode/electrolyte interfacial design. *Mat. Res. Soc. Symp. Proc.* **2005**, *835*, 333.

(356) Murayama, M.; Kanno, R.; Kawamoto, Y.; Kamiyama, T. Structure of thio-LISICON, $Li_4Ge_4S_4$. *Sol. St. Ionics* **2002**, *154-155*, 789.

(357) Hayashi, A.; Hama, S.; Minami, T.; Tatsumisago, M. Formation of superionic crystals from mechanically milled Li_2S-P_2S_5 glasses. *Electrchem. Commu.* **2003**, *5*, 111.

(358) Ohta, N.; Takada, K.; Osada, M.; Zhang, L.; Sasaki, T.; Watanabe, M. Solid electrolyte, thio-LISICON, thin film prepared by pulsed laser deposition. *J. Power Sources* **2005**, *146*, 707.

(359) Zheng, N.; Bu, X.; Feng, P. Synthetic design of crystalline inorganic chalcogenides exhibiting fast-ion conductivity. *Nature* **2003**, *426*, 428.

(360) Tamura, S.; Mori, A.; Imanaka, N. Li^+ ion conduction in $(Gd,La)_2O_3$-$LiNO_3$ system. *Sol. St. Ionics* **2004**, *175*, 467.

(361) West, A. R. *Basic Solid State Chemistry*, 2nd ed.; John Wiley & Sons: Chichester, UK, 1999.

(362) Kim, Y. W.; Masui, T.; Oda, A.; Tamura, S.; Imanaka, N. Solution of potassium nitrate into gadolinium oxide lattice. *Phys. Status Solid A: Appl. Res.* **2003**, *198*, 369.

(363) Kim, Y. W.; Oda, A.; Imanaka, N. Extraordinary high potassium ion conducting polycrystalline solids based on gadolinium oxide-potassium nitrite solid solution. *Electrchem. Commu.* **2003**, *5*, 94.

(364) Liang, C. C. Conduction characteristics of the lithium iodide-aluminum oxide solid electrolytes. *J. Electrochem. Soc.* **1973**, *120*, 1289.

(365) Weppner, W. Electronic transport properties and electrically induced p-n junction in zirconium oxide + 10 m/o yttrium oxide. *J. Sol. St. Chem.* **1977**, *20*, 305.

(366) Hu, Y. W.; Raistrick, I. D.; Huggins, R. A. Ionic conductivity of lithium orthosilicate-lithium phosphate solid solutions. *J. Electrochem Soc.* **1977**, *124*, 1240.

(367) Aono, H.; Sugimoto, E.; Sadaoka, Y.; Imanaka, N.; Adachi, G. Ionic conductivity of solid electrolytes based on lithium titanium phosphate. *J. Electrochem Soc.* **1990**, *137*, 1023.

(368) Inaguma, Y.; Chen, L.; Itoh, M.; Mitsuru, N.; Nakamura, T.; Uchida, T.; Ikuta, H.; Wakihara, M. High ionic conductivity in lithium lanthanum titanate. *Sol. St. Commu.* **1993**, *86*, 689.

(369) Aotani, N.; Iwamoto, K.; Takada, K.; Kondo, S. Synthesis and electrochemical properties of lithium ion conductive glass, Li_3PO_4- Li_2S - SiS_2. *Sol. St. Ionics* **1994**, *68*, 35.

(370) Kawai, H.; Kuwano, J. Lithium ion conductivity of A-site deficient perovskite solid solution $La_{0.67-x}Li_{3x}TiO_3$. *J. Electrochem Soc.* **1994**, *141*, L78.

(371) Inaguma, Y.; Matsui, Y.; Shan, Y.-J.; Itoh, M.; Nakamura, T. Lithium ion conductivity in the perovskite-type $LiTaO_3$-$SrTiO_3$ solid solution. *Sol. St. Ionics* **1995**, *79*, 91.

(372) Neudecker, B. J.; Weppner, W. Li_9SiAlO_8: a lithium ion electrolyte for voltages above 5.4 V. *J. Electrochem Soc.* **1996**, *143*, 2198.

(373) Ohtomo, T.; Mizuno, F.; Hayashi, A.; Tadanaga, K.; Tatsumisago, M. Mechanochemical synthesis of lithium ion conducting glasses and glass-ceramics in the system Li_2S-P-S. *Sol. St. Ionics* **2005**, *176*, 2349.

(374) Hirai, K.; Tatsumisago, M.; Minami, T. Thermal and electrical properties of rapidly quenched glasses in the systems Li_2S-SiS_2-Li_xMO_y (Li_xMO_y = Li_4SiO_4, Li_2SO_4). *Sol. St. Ionics* **1995**, *78*, 269.

(375) Iwamoto, K.; Aotani, N.; Takada, K.; Kondo, S. Application of Li_3PO_4-Li_2S-SiS_2 glass to the solid state secondary batteries. *Sol. St. Ionics* **1995**, *79*, 288.

(376) Takada, K.; Iwamoto, K.; Kondo, S. Lithium iron sulfide as an electrode material in a solid state lithium battery. *Sol. St. Ionics* **1999**, *117*, 273.

(377) Morimoto, H.; Yamashita, H.; Tatsumisago, M.; Masahiro, M.; Minami, T. Mechanochemical synthesis of the high lithium ion conductive amorphous materials in the systems Li_2S-SiS_2 and Li_2S-SiS_2-Li_4SiO_4. *J. Ceramic Soc. Japan* **2000**, *108*, 128.

(378) Bartholomew, R. F.; Young, D. M.; Ellison, A. J. G. Electrical properties of new glasses based on the Li_2S-SiS_2 system. *J. Non-Crystal. Solids* **1999**, *256-257*, 242.

(379) Iwamoto, K.; Aotani, N.; Takada, K.; Kondo, S. Rechargeable solid state battery with lithium conductive glass, Li_3PO_4---Li_2S---SiS_2 *Sol. St. Ionics* **1994**, *70-71*, 658.

(380) Kennedy, J. H.; Zhang, Z.; Eckert, H. Ionically conductive sulfide-based lithium glasses. *J. Non-Crystal. Solids* **1990**, *123*, 328.

(381) Takada, K.; Aotani, N.; Kondo, S. Electrochemical behaviors of Li^+ ion conductor, Li_3PO_4-Li_2S-SiS_2 *J. Power Sources* **1993**, *43*, 135.

(382) Kondo, S.; Takada, K.; Yamamura, Y. New lithium ion conductors based on Li_2S-SiS_2 system *Sol. St. Ionics* **1992**, *53-56*, 1183.

(383) Hayashi, A.; Ishikawa, Y.; Hama, S.; Minami, T.; Tatsumisago, M. Fast lithium-ion conducting glass-ceramics in the system Li_2S-SiS_2-P_2S_5. *Electrochem. Sol. St. Lett.* **2003**, *6*, A47.

(384) Tatsumisago, M. Glassy materials based on Li_2S for all-solid-state lithium secondary batteries. *Sol. St. Ionics* **2004**, *175*, 13.

(385) Souquet, J. L.; Robinel, E.; Barrau, B.; Ribes, M. Glass formation and ionic conduction in the M_2S---GeS_2 (M = Li, Na, Ag) systems *Sol. St. Ionics* **1981**, *3-4*, 317.

(386) Pradel, A.; Pagnier, T.; Ribes, M. Effect of rapid quenching on electrical properties of lithium conductive glasses *Sol. St. Ionics* **1985**, *17*, 147.

(387) Mercier, R.; Malugani, J. P.; Fahys, B.; Robert, G. Superionic conduction in lithium sulfide-phosphorus sulfide-lithium iodide glasses. *Sol. St. Ionics* **1981**, *5*, 663.

(388) Sahami, S.; Shea, S. W.; Kennedy, J. H. Preparation and conductivity measurements of SiS_2-Li_2S-LiBr lithium ion conductive glasses. *J. Electrochem Soc.* **1985**, *132,* 985.

(389) Kennedy, J. H.; Yang, Y. Glass-forming region and structure in SiS_2---Li_2S---LiX (X = Br, I). *J. Solid State Chem.* **1987**, *69*, 252.

(390) Visco, S. J.; Spellane, P. J.; Kennedy, J. H. Complex plane and (7)Li NMR studies of arsenic sulfide-based lithium glasses. *J. Electrochem Soc.* **1985**, *132*, 1766.

(391) Pradel, A.; Ribes, M. Electrical properties of lithium conductive silicon sulfide glasses prepared by twin roller quenching *Sol. St. Ionics* **1986**, *18-19*, 351.

(392) Kennedy, J. H. Ionically conductive glasses based on silicon disulfide. *Mat. Chem. Phys.* **1989**, *23*, 29.

(393) Minami, T.; Hayashi, A.; Tatsumisago, M. Preparation and characterization of lithium ion-conducting oxysulfide glasses. *Sol. St. Ionics* **2000**, *136-137*, 1015.

(394) Pradel, A.; Ribes, M. Lithium chalcogenide conductive glasses. *Mat. Chem. and Phys.* **1989**, *23*, 121.

(395) Hayashi, A.; Hama, S.; Morimoto, H.; Tatsumisago, M.; Minami, T. High lithium ion conductivity of glass-ceramics derived from mechanically milled glassy powders. *Chem. Lett.* **2001**, *9*, 872.

(396) Minami, T.; Machida, N. Preparation of new glasses with high ionic conductivities. *Mater. sci. Eng. B* **1992**, *13*, 203.

(397) Kanno, R.; Murayama, M.; Inada, T.; Kobayashi, T.; Sakamoto, K.; Sonoyama, N.; Yamada, A.; Kondo, S. A self-assembled breathing interface for all-solid-state ceramic lithium batteries. *Electrochem. Sol. St. Lett.* **2004**, *7*, A455.

(398) Zhang, Y.; Alonso, P. R.; Martinez-Limia, A.; Scanlon, L. G.; Balbuena, P. B. Crystalline structure and lithium-ion channel formation in self-assembled di-lithium phtalocyanine: theory and experiments. *J. Phys. Chem. B* **2004**, *108*, 4659.

(399) Zhang, Y.; Scanlon, L. G.; Balbuena, P. B. Computational study of the structure of di-lithium phthalocyanine/pyrite interface; Paper presented at *228th ACS National Meeting*, 2004, Philadelphia, PA, United States.

(400) Zhang, Y.; Scanlon, L. G.; Balbuena, P. B. Analysis of the structure of di-lithium phthalocyanine/pyrite interface; Paper presented at *AICHE national meeting*, 2004, Austin, TX.

(401) Zhang, Y.; Balbuena, P. B. Analysis of the structure and dynamics of di-lithium phthalocyanine: a molecular dynamics study. Paper presented at *ACS 77th Colloid and Surface Science Symposium*, June 2003, Altanta, GA

(402) Zhang, Y.; Wang, Y.; Scanlon, L. G.; Balbuena, P. B. Ab initio and classical molecular dynamics studies of the di-lithium phthalocyanine/pyrite interfacial structure. *J. Electrochem Soc.* **2005,** *152*, A1955.

(403) Ceder, G.; Doyle, M.; Arora, P.; Fuentes, Y. Computational modeling and simulation for rechargeable batteries. *MRS Bull.* **2002**, *27*, 619.

(404) Botte, G. G.; Subramanian, V. R.; White, R. E. Mathematical modeling of secondary lithium batteries. *Electrochim. Acta* **2000**, *45-46*, 2595.

(405) Thomas, K. E.; Newman, J.; Darling, R. M. Mathematical modeling of lithium batteries. In *Adcances in Lithium-Ion Batteries*; Schalkwijk, W. A. V., Scrosati, B., Eds.; Kluwer Academic/Plenum: New York, 2002.

(406) Doyle, M.; Newman, J. The use of mathematical modeling in the design of lithium/polymer battery systems *Electrochim. Acta* **1995**, *40*, 2191.

(407) Doyle, M.; Fuller, T. F.; Newman, J. Modeling of galvanostatic charge and discharge of the lithium/polymer/insertion cell. *J. Electrochem. Soc.* **1993**, *140*, 1527.

(408) Doyle, M.; Newman, J.; Reimers, J. A quick method of measuring the capacity versus discharge rate for a dual lithium-ion insertion cell undergoing cycling. *J. Power Sources* **1994**, *52*, 211.

(409) Doyle, M. Design and simulation of lithium rechargeable batteries. Ph. D. Dissertation, University of California, Berkeley, 1995.

(410) Doyle, M.; Newman, J. Modeling the performance of rechargeable lithium-based cells: design correlations for limiting cases. *J. Power Sources* **1995**, *54*, 46.

(411) Doyle, M.; Newman, J.; Gozdz, A. S.; Schmutz, C. N.; Tarascon, J. M. Comparison of modeling predictions with experimental data from plastic lithium ion cells. *J. Electrochem. Soc.* **1996**, *143*, 1890.

(412) Ploehn, H. J.; Ramadass, P.; White, R. E.; Altomare, D.; Balbuena, P. B. Continuum and statistical mechanics-based models for solid electrolyte interfaces in lithium-ion batteries. *Lithium-Ion Batteries: Solid-Electrolyte Interphase*; Balbuena, P. B., Wang, Y., Eds.; Imperial College Press: London, 2004.

(413) Yeu, T.; White, R. E. Mathematical model of a lithium/polypyrrole cell. *J. Electrochem. Soc.* **1990**, *137*, 1327.

(414) Arora, P.; White, R. E.; Doyle, M. Capacity fade mechanisms and side reactions in lithium-ion batteries. *J. Electrochem. Soc.* **1998**, *145*, 3647.

(415) Johnson, B. A.; White, R. E. Characterization of commercially available Li-ion batteries. *J. Power Sources* **1998**, *70-71*, 48.

(416) Spotnitz, R. M.; Zuckerbrod, D.; Johnson, S. L.; Lundquist, J. T.; White, R. E. Mathematical modeling of grace Li-TiS_2 cells; In *Proceedings of the Symposium*

on Modeling of Batteries and Fuel Cells, White, R. E., Verbrugge, M. W., Stockel, J. F., Eds.; 1991, p 145.

(417) Spotnitz, R. Simulation of capacity fade in lithium-ion batteries. *J. Power Sources* **2003**, *113*, 72.

(418) Ceder, G.; Chiang, Y. M.; Sadoway, D. R.; Aydinol, M. K.; Jang, Y. I.; Huang, B. Identification of cathode materials for lithium ion batteries guided by first-principles calculations. *Nature* **1998**, *392*, 694.

(419) Aydinol, M. K.; Kohan, A. F.; Ceder, G.; Cho, K.; Joannopoulos, J. Ab initio study of lithium intercalation in metal oxides and metal dichalcogenides. *Phys. Rev. B* **1997**, *56*, 1354.

(420) VanderVen, A.; Aydinol, M. K.; Ceder, G. First-principles evidence for stage ordering in Li_xCoO_2. *J. Electrochem. Soc.* **1998**, *145*, 2149.

(421) Ota, H.; Sato, T.; Suzuki, H.; Usami, T. TPD-GC/MS analysis of the solid electrolyte interface (SEI) on a graphite anode in the propylene carbonate/ethylene sulfite electrolyte system for lithium batteries. *J. Power Sources*, **2001**, *97-98*, 107.

(422) VanderVen, A.; Ceder, G. Lithium diffusion mechanisms in layered interclation compounds. *J. Power Sources* **2001**, *97-8*, 529.

(423) Marianetti, C. A.; Morgan, D.; Ceder, G. First-principles investigation of the cooperative Jahn-Teller effect for octahedrally coordinated transition-metal ions. *Phys. Rev. B* **2001**, *6322*, 4304.

(424) Wu, E. J.; Ceder, G. Computational investigation of dielectric absorption at microwave frequencies in binary oxides. *J. Appl. Phys.* **2001**, *89*, 5630.

(425) deDomPablo, M. E. A. Y.; Marianetti, C.; VanderVen, A.; Ceder, G. Jahn-Teller mediated ordering in layered Li_xMO_2 compounds. *Phys. Rev. B* **2001**, *14*, 4107.

(426) Reed, J.; Ceder, G.; VanderVen, A. Layered to spinel phase transition in Li_xMnO_2. *Electrochem. Sol. St. Lett.* **2001**, *6*, A78.

(427) VanderVen, A.; Marianetti, C.; Morgan, D.; Ceder, G. Phase transformations and volume changes in spinel $Li_xMn_2O_4$. *Sol. St. Ionics* **2000**, *135*, 21.

(428) Song, J. K.; Tsubouchi, M.; Suzuki, T. Femtosceond photoelectron imagin on pyrzine: Spectroscopy of 3s and 3p Rydberg states. *J. Chem Phys.* **2001**, *115*, 8810.

(429) Li, W.; Garofalini, S. H. Molecular dynamics simulation of lithium diffusion in Li_2O-Al_2O_3-SiO_2 glasses. *Sol. St. Ionics* **2004**, *166*, 365.

(430) Garofalini, S. H.; Shadwell, P. Molecular dynamics simulations of cathode/glass interface behavior effect of orientation on phase transformation, Li migration, and interface relaxation. *J. Power Sources* **2000**, *89*, 190.

(431) Balbuena, P. B.; Wang, L.; Li, T.; Derosa, P. Ab initio and molecular dynamics studies of cation-water interactions. *Theor. Comp. Chem.* **1999**, *7*, 431.

(432) Li, T.; Balbuena, P. B. Theoretical studies of lithium perchlorate in ethylene carbonate, propylene carbonate, and their mixtures. *J. Electrochem. Soc.* **1999**, *146*, 3613.

(433) Li, T.; Marquez, A.; Balbuena, P. B. First principles calculations of energetics and diffusion at the carbon-lithium anode/electrolyte interface. Paper presented at *93rd meeting of the Electrochemical Society*, 1998, San Diego, CA.

(434) Marquez, A.; Li, T.; Balbuena, P. B. Computational studies of lithium/benzene and lithium-perchlorate/ethylene-carbonate interactions. Paper presented at *AIChE National Meeting*, 1998, Miami, FL.

(435) Li, T.; Balbuena, P. B. Ab initio studies of surface reactions in lithium/graphite electrodes. Paper presented at *195th Meeting of the Electrochemical Society*, 1999, Seattle, WA.

(436) Li, T.; Balbuena, P. B. Theoretical studies of the chemical reduction of ethylene carbonate. *Chem. Phys. Lett.* **2000**, *317*, 422.

(437) Wang, Y.; Nakamura, S.; Ue, M.; Balbuena, P. B. Theoretical studies to understand surface chemistry on carbon anodes for lithium-ion batteries: Reduction mechanisms of ethylene carbonate. *J. Am. Chem. Soc.* **2001**, *123*, 11708.

(438) Balbuena, P. B.; Wang, Y.; Nakamura, S.; Ue, M. Solvent reduction and SEI layer formation: theory and experiments; 2001 Joint International Meeting of ECS and ISE, 2001, San Francisco, CA.

(439) Wang, Y.; Nakamura, S.; Tasaki, K.; Balbuena, P. B. Theoretical studies to understand surface chemistry on carbon anodes for lithium-ion batteries: How does vinylene carbonate play its role as an electrolyte additive? *J. Am. Chem. Soc.* **2002**, *124*, 4408.

(440) Wang, Y.; Balbuena, P. B. Associations of alkyl carbonates: intermolecular CH···O interactions. *J. Phys. Chem. A* **2001**, *105*, 9972.

(441) Wang, Y.; Balbuena, P. B. Associations of lithium alkyl dicarbonates through O-Li-O interactions. *J. Phys. Chem. A* **2002**, 106, 9582.

(442) Wang, Y.; Balbuena, P. B. Theoretical insights into the reductive decompositions of propylene carbonate and vinylene carbonate: a density functional theory study. *J. Phys. Chem. B* **2002**, *106*, 4486.

(443) Johnson, C., Private communication, December 2003.

(444) Scanlon, L. G., Private communication, December 2003.

(445) Brinkmann, M.; Chaumont, C.; Wachtel, H.; Andre, J. J. Polymorphism in powders and thin films of lithium phthalocyanine. An X-ray, optical and electron spin resonance study. *Thin Sol. Films* **1996**, *283*, 97.

(446) Andre, J. J.; Brinkmann, M. Molecular semiconductors for magnetometry and oximetry: lithium phthalocyanine radical. *Synthetic Metals* **1997**, *90*, 211.

(447) Ilangovan, G.; Zweier, J. L.; Kuppusamy, P. Electrochemical preparation and EPR studies of lithium phthalocyanine: evaluation of the nucleation and growth mechanism and evidence for potential-dependent phase formation. *J. Phys. Chem. B* **2000**, *104*, 4047.

(448) Shirley, R. *The CRYSFIRE System for Automatic Powder Indexing: User's Manual*, The Lattice Press: Guildford, Surrey, England, 2000.

(449) Sugimoto, H.; Mori, M.; Masuda, H.; Taga, T. Synthesis and molecular structure of a lithium complex of phtalocyanine radical. *J. Chem. Soc., Chem. Commun.* **1986**, 962.

(450) Scanlon, L. G.; Lucente, L. R.; Feld, W. A.; Sandi, G.; Balbuena, P. B.; Alonso, P. R.; Turner, A. Composite cathode with Li_2Pc. *J. Electrochem. Soc.* **2004**, *151*, A1338.

(451) Mayo, S. L.; Olafson, B. D.; Goddard, W. A. Dreiding: a generic force field for molecular simulations. *J. Phys. Chem.* **1990**, *94*, 8897.

(452) Heizinger, K., The structure of aqueous electrolyte solutions as derived from MD (molecular dynamics) simulations, *Pure Appl. Chem.* **1985**, *57*, 1031.

(453) Mulliken, R. S. Electronic population analysis on LCAO-MO molecular wave functions. *J. Chem. Phys.* **1955**, *23*, 1833.

(454) Mulliken, R. S. Electronic population analysis on LCAO-MO molecular wave functions. II. Overlap populations, bond orders, and covalent bond energies. *J. Chem. Phys.* **1955**, *23*, 1841.

(455) Mulliken, R. S. Electronic population analysis on LCAO-MO molecular wave functions. III Effects of hybridization on overlap and gross AO populations. *J. Chem. Phys.* **1955**, *23*, 2338.

(456) Scanlon, L. G.; Lucente, L. R.; Feld, W. A.; Sandi, G.; Campo, D.; Turner, A.; Johnson, C.; Marsh, R. Lithium-ion conducting channel. *Proceedings of the International Workshop on Electrochemical Systems*; Landgrebe, A. R., Klingler, R. J., Eds., 2000; Vol. 36; pp 326.

(457) Hay, P. J.; Wadt, W. R. Ab initio effective core potentials for molecular calculations. Potentials for the transition metal atoms Sc to Hg. *J. Chem. Phys.* **1985**, *82*, 270.

(458) Rosso, K. M.; Becker, U.; Hochella, M. F. Jr. The interaction of pyrite (100) surfaces with O_2 and H_2O: fundamental oxidation mechanisms. *American Mineralogist* **1999**, *84*, 1549.

(459) Frisch, M. J.; Trucks, G. W.; Schlegel, H. B.; Scuseria, G. E.; Robb, M. A.; Cheeseman, J. R.; Zakrzewski, V. G.; Montgomery, J. A.; Stratmann, R. E.; Burant, J. C.; Dapprich, S.; Millam, J. M.; Daniels, A. D.; Kudin, K. N.; Strain, O. F. M. C.; Tomasi, J.; Barone, B.; Cossi, M.; Cammi, R.; Mennucci, B.; Pomelli, C.; Adamo, C.; Clifford, S.; Ochterski, J.; Petersson, G. A.; Ayala, P. Y.; Cui, Q.; Morokuma, K.; Malick, D. K.; Rabuck, A. D.; Raghavachari, K.; Foresman, J. B.; Ciolovski, J.; Ortiz, J. V.; Stefanov, V. V.; Liu, G.; Liashensko, A.; Piskorz, P.; Komaroni, I.; Gomperts, R.; Martin, R. L.; Fox, D. J.; Keith, T.; Al-Laham, M. A.; Peng, C. Y.; Nanayakkara, A.; Gonzalez, C.; Challacombe, M.; Gill, P. M. W.; Johnson, B.; Chen, W.; Wong, M. W.; Andres, J. L.; Head-Gordon, M.; Replogle, E. S.; Pople, J. A. *GAUSSIAN 98*, Revision A.11; Gaussian Inc.: Pittsburgh, PA, 1998.

(460) Philpott, M. R.; Goliney, I. Y.; Lin, T. T. Molecular dynamics simulation of water in a contact with an iron pyrite FeS_2 surface. *J. Chem. Phys.* **2004**, *120*, 1943.

(461) Rappe, A. K.; Goddard, W. A. Charge equilibration algorithm for molecular dynamics simulations. *J. Phys. Chem.* **1991**, *95*, 3358.

(462) Molecular Simulation Inc. (MSI), Force-field based simulations, San Diego, 1997. http://www.accelrys.com/about/history/msi.html

(463) Fischer, M. S.; Templeton, D. H.; Zalkin, A.; Calvin, M. Structure and chemistry of the porphyrins. The crystal and molecular structure of the monohydrated dipyridinated magnesium phthalocyanin complex. *J. Am. Chem. Soc.* **1971**, *93*, 2622.

(464) Diel, B. N.; Inabe, T.; Lyding, J. W.; K. F. Schoch, J.; Kannewurf, C. R.; Marks, T. J. Cofacial asembly of partially oxidized metallomacrocycles as an approach to controlling lattice architecture in low-dimensional molecular solids. Cemical, structural, oxidation state, transport, magnetic and optical properties of halogen-doped $[M(phthalocyaninato)O]_n$ macromolecules, where M=Si, Ge, and Sn. *J. Am. Chem. Soc.* **1983**, *105*, 1551.

(465) Dirk, C. W.; Inabe, T.; K. F. Schoch, J.; Marks, T. J. Cofacial assembly of partially oxidized metallomacrocycles as an approach to controlling lattice architecture in low-dimensional molecular solids. Chemical and architectural properties of the "face-to-face" polymers $[M(phthalocyaninato)O]_n$ where M=Si, Ge, and Sn. *J. Am. Chem. Soc.* **1983**, *105*, 1539.

(466) Brinkmann, M.; Turek, P.; Andre, J. J. EPR study of the x, a and b structures of lithium phthalocyanine. *J. Mat. Chem.* **1998**, *8*, 675.

(467) Kimura, T.; Sumimoto, M.; Sakaki, S.; Fujimoto, H.; Hashimoto, Y.; Matsuzaki, S. Electronic structure of lithium phthalocyanine studied by ultraviolet photoemission spectroscopy. *Chem. Phys.* **2000**, *253*, 125.

(468) Yanagi, H.; Manivannan, A. Epitaxial growth of molecular magnetic thin films of lithium phthalocyanine. *Thin Sol. Films* **2001**, *393*, 28.

(469) Janczak, J.; Kubiak, R. X-ray single crystal investigations of magnesium phthalocyanine. The 4+1 coordination of the Mg ion and its consequence. *Polyhedron* **2001**, *20*, 2901.

(470) Wachtel, H.; Wittmann, J. C.; Lotz, B.; Petit, M. A.; Andre, J. J. Anisotropic spin transport in oriented lithium phthalocyanine thin films. *Thin Sol. Films* **1994**, *250*, 219.

(471) Homborg, H.; Teske, C. L. Lithium phthalocyanines: preparation and characterization of the monoclinic and tetragonal modifications of LiPc and the halogen adducts LiPcX (X = Cl, Br, I). *Z. Anorg. Allg. Chem.* **1985**, *527*, 45.

(472) Kraus, W.; Nolze, G. PowderCell for Windows; Federal Institute for Materials Research and Testing: Berlin, Germany, 1997.

(473) Kubiak, R.; Janczak, J.; Ejsmont, K. On polymorphic and non-polymorphic conversions of phthalocyanines. *Chem. Phys. Lett.* **1995**, *245*, 249.

(474) Assour, J. M.; Harrison, S. E. Electron spin resonance of concentrated copper phthalocyanine crystals. *Phys. Rev.* **1964**, *136*, 1368.

(475) Hansen, J.-P.; McDonald, I. R. *Theory of Simple Liquids*, 2nd ed.; Academic Press: San Diego, CA, 1990.

(476) Kuppa, V.; Manias, E. Computer simulation of PEO/layered-silicate nanocomposites: 2. lithium dynamics in PEO/Li^+ montmorillonite intercalates. *Chem. Mater.* **2002**, *14*, 2171.

(477) Gorecki, W.; Andreani, R.; Berthier, C.; Mali, M.; Roos, J.; Brinkmann, D. NMR, DSC, and conductivity study of a poly(ethylene oxide) complex electrolyte: $PEO(LiClO_4)_x$. *Sol. St. Ionics* **1986**, *18-19*, 295.

(478) Muller-Plathe, F.; vanGunsteren, W. F. Computer simulation of a polymer electrolyte: lithium iodide in amorphous poly(ethylene oxide). *J. Chem. Phys.* **1995**, *103*, 4745.

(479) Thompson, A. P.; Heffelfinger, G. S. Direct molecular simulation of gradient-driven diffusion of large molecules using constant pressure. *J. Chem. Phys.* **1999**, *110*, 10693.

(480) Kanehori, K.; Matsumo, K.; Miyauchi, K.; Kudo, T. Thin-film solid electrolyte and its application to secondary lithium cell. *Sol. St. Ionics* **1983**, *9-10*, 1445.

(481) Jones, S. D.; Akridge, J. R.; Shokoohi, F. K. Thin film rechargeable Li batteries. *Sol. St. Ionics* **1994**, *69*, 357.

(482) Hernan, L.; Morales, J.; Sanchez, L.; Santos, L. Use of Li-M-Mn-O [M = Co, Cr, Ti] spinels prepared by a sol-gel method as cathodes in high-voltage lithium batteries. *Sol. St. Ionics* **1999**, *118*, 179.

(483) Dudney, N. J.; Bates, J. B.; Zuhr, R. A.; Young, S.; Robertson, J. D.; Jun, H. P.; Hackney, S. A. Nanocrystalline $Li_xMn_{2-y}O_4$ cathodes for solid-state thin-film rechargeable lithium batteries. *J. Electrochem. Soc.* **1999**, *146*, 2455.

(484) Neudecker, B. J.; Zuhr, R. A.; Bates, J. B. Lithium silicon tin oxynitride (Li_ySiTON): high-performance anode in thin-film lithium-ion batteries for microelectronics. *J. Power Sources* **1999**, *81-82*, 27.

(485) MacCallum, J. R.; Vincent, C. A. *Polymer Electrolyte Reviews*; Elsevier: Amsterdam, 1987; Vol. 1.

(486) Wang, Y.; Balbuena, P. B. Combined ab initio quantum mechanics and classical molecular dynamics studies of polyphosphazene polymer electrolytes: competitive solvation of Li^+ and $LiCF_3SO_3$. *J. Phys. Chem. B* **2004**, *108*, 15694.

(487) Abraham, K. M. Directions in secondary lithium battery research and development. *Electrochim. Acta* **1993**, *38*, 1233.

(488) Golodnitsky, D.; Peled, E. Pyrite as cathode insertion material in rechargeable lithium/composite polymer electrolyte batteries. *Electrochim. Acta* **1999**, *45*, 335.

(489) Clark, M. B. *Lithium-Iron Disulfide Cells*; Academic: London, UK, 1983.

(490) Shao-Horn, Y.; Osmialowski, S.; Horn, Q. C. Reinvestigation of lithium reaction mechanisms in FeS_2 pyrite at ambient temperature. *J. Electrochem. Soc.* **2002**, *149*, A1547.

(491) Montoro, L. A.; Rosolen, J. M. Gelatin/DMSO: a new approach to enhancing the performance of a pyrite electrode in a lithium battery. *Sol. St. Ionics* **2003**, *159*, 233.

(492) Marquez, A.; Balbuena, P. B. Molecular dynamics study of graphite/electrolyte interfaces. *J. Electrochem. Soc.* **2001**, *148*, A624.

(493) Garcia, M. E.; Webb, E.; Garofalini, S. H. Molecular dynamics simulation of V_2O_5/Li_2SiO_3 interface. *J. Electrochem. Soc.* **1998**, *145*, 2155.

(494) Kulp, D. T.; Garofalini, S. H. Molecular dynamics studies of lithium injection in model cathode/electrolyte systems. *J. Electrochem. Soc.* **1996**, *143*, 2211.

(495) Li, W.; Garofalini, S. H. Molecular dynamics simulations of Li insertion in a nanocrystalline V_2O_5 thin film cathode. *J. Electrochem Soc.* **2005**, *152*, A364.

(496) Li, W.; Garofalini, S. H. Molecular dynamics simulations of lithium diffusion in silica-doped nanocrystalline V_2O_5. *J. Electrochem Soc.* **2005**, *152*, A1860.

(497) Stevens, E. D.; DeLucia, M. L.; Coppens, P. Experimental observation of the effect of crystal field splitting on the electron density distribution of iron pyrite. *Inorg. Chem.* **1980**, *19*, 813.

(498) Birkholz, M.; Fiechter, S.; Hartmann, A.; Tributsh, H. Sulfur deficiency in iron pyrite (FeS_{2-x}) and its consequences for band-structrue models. *Phy. Rev. B* **1991**, *43*, 11926.

(499) Guevremont, J. M.; Strongin, D. R.; Schoonen, M. A. A. Effects of surface imperfections on the binding of CH_3OH and H_2O on FeS_2(100): using adsorbed Xe as a probe of mineral surface structure. *Sur. Sci.* **1997**, *391*, 109.

(500) Guevremont, J. M.; Strongin, D. R.; Schoonen, M. A. A. Photoemission of adsorbed xenon, X-ray photoelectron spectroscopy, and temperature-programmed desorption studies of H_2O on FeS_2(100). *Langmuir* **1998**, *14*, 1361.

(501) Karthe, S.; Szargan, R.; Suoninen, E. Oxidation of pyrite surfaces: a photoelectron spectroscopic study. *Appl. Surf. Sci.* **1993**, *72*, 157.

(502) Xiang, H.-Q.; Tanaka, K.; Takahara, A.; Kajiyama, T. Spectroscopic and electrochemical characterizations of dilithium octacyanophthalocyanine Langmuir-Blodgett films. *Langmuir* **2002**, *18*, 2223.

(503) Markovits, A.; Minot, C. Theoretical study of the acetonitrile flip-flop with the electric field orientation. Adsorption on a Pt(111) electrode surface. *Cata. Lett.* **2003**, *91*, 225.

(504) Pacchioni, G.; Bagus, P. S. Point-charge effects on the vibrational frequency of CO chemisorbed on Cu and Pd clusters: a model for CO with ionic coadsorbates. *Phy. Rev. B* **1989**, *40*, 6003.

(505) Yuan, S.; Zhang, Y.; Li, Y. Molecular simulation study of alkyl-modified silicon crystal under the external electric field. *Chem. Phys. Lett.* **2004**, *389*, 155.

(506) Zangi, R.; Mark, A. E. Electrofreezing of confined water. *J. Chem. Phys.* **2004**, *120*, 7123.

(507) Bockris, J. O. M.; Reddy, A. K. N. *Modern Electrochemistry*; Plenum Press: New York, 1973.

VITA

Yingchun Zhang received his Bachelor of Science in chemistry from Xiamen University, Xiamen, China in 1997. He then continued his graduate study and received his Master of Science in chemistry at the same university in 2000. He entered the graduate program in Department of Chemistry at University of Missouri at Columbia in August, 2000.

In August 2002, he joined Dr. Balbuena's research group as a Ph.D. student in chemical engineering. Since then, he has worked in the area of computational simulations on material science. He received his Ph.D. in May 2006.

Mr. Zhang may be reached at 3122 TAMU, Department of Chemical Engineering, College Station, TX 77843. His email address is yingchun.zhang@chemail.tamu.edu.